

# Relationship between microstructure and ionic conductivity in oxygen-substituted Li-thiophosphate glasses and glass ceramics

Zur Erlangung des akademischen Grades eines

DOKTORS DER NATURWISSENSCHAFTEN

(Dr. rer. nat.)

von der KIT-Fakultät für Chemie und Biowissenschaften

des Karlsruher Instituts für Technologie (KIT)

genehmigte

DISSERTATION

Von

M. Sc. Ramon Zimmermanns

1. Referent: Prof. Dr. Helmut Ehrenberg

2. Referent: Prof. Dr. Dominic Bresser

Tag der mündlichen Prüfung: 15.07.2024



This document is licensed under a Creative Commons Attribution 4.0 International License (CC BY 4.0): <https://creativecommons.org/licenses/by/4.0/deed.en>

## **Selbständigkeitserklärung**

Hiermit versichere ich, dass ich die vorliegende Arbeit selbstständig verfasst habe, dass ich keine anderen als die angegebenen Quellen und Hilfsmittel benutzt habe, dass ich die wörtlich oder inhaltlich übernommenen Stellen als solche gekennzeichnet habe und dass ich die Satzung des KIT zur Sicherung guter wissenschaftlicher Praxis in der jeweils gültigen Fassung beachtet habe.

Karlsruhe, den 10.06.2024

Ramon Zimmermanns



# Inhalt

<b>LIST OF FIGURES</b> .....	<b>III</b>
<b>LIST OF TABLES</b> .....	<b>VII</b>
<b>LIST OF ABBREVIATIONS</b> .....	<b>VIII</b>
<b>DANKSAGUNG</b> .....	<b>IX</b>
<b>ZUSAMMENFASSUNG</b> .....	<b>XI</b>
<b>1 THEORETICAL BACKGROUND &amp; INTRODUCTION</b> .....	<b>1</b>
1.1 ALL SOLID STATE BATTERIES .....	1
1.2 MECHANOCHEMICAL SYNTHESIS .....	7
1.3 STRUCTURE ANALYSIS .....	9
1.3.1 <i>Diffraction</i> .....	10
1.3.2 <i>Local environment analysis techniques</i> .....	12
1.3.3 <i>Pair Distribution Function Analysis</i> .....	14
1.3.4 <i>Reverse Monte Carlo</i> .....	17
1.4 CHEMICAL ANALYSIS .....	19
1.4.1 <i>X-ray Photo Spectroscopy</i> .....	19
1.4.2 <i>Scanning Electron Microscopy &amp; Energy Dispersive X-ray Spectroscopy</i> .....	20
1.5 ANALYSIS OF ION DYNAMICS .....	20
1.5.1 <i>Impedance spectroscopy</i> .....	20
1.5.2 <i>Nuclear Magnetic Resonance Spectroscopy</i> .....	24
<b>2 MOTIVATION</b> .....	<b>28</b>
<b>3 RESULTS AND DISCUSSION</b> .....	<b>29</b>
3.1 THE INFLUENCE OF OXYGEN SUBSTITUTION ON THE ATOMIC STRUCTURE AND IONIC CONDUCTIVITY OF LI OXY-SULFIDE GLASSES .....	29
3.1.1 <i>Experimental</i> .....	30
3.1.2 <i>Synthesis</i> .....	32
3.1.3 <i>Structure Analysis</i> .....	37
3.1.4 <i>Electrochemical analysis</i> .....	48
3.1.5 <i>Neutron total scattering</i> .....	55
3.1.6 <i>Structure model refinement with RMC</i> .....	61
3.1.7 <i>Summary and conclusion</i> .....	67
3.2 INFLUENCE OF OXYGEN SUBSTITUTION ON THE CRYSTALLISATION BEHAVIOUR OF LI OXY-SULFIDE GLASSES .....	69
3.2.1 <i>Experimental</i> .....	69
3.2.2 <i>Introduction Crystal Phases of LPS</i> .....	69
3.2.3 <i>Temperature-dependent structure analysis</i> .....	71
3.2.4 <i>Electrochemical analysis</i> .....	80
3.2.5 <i>High-temperature Impedance spectroscopy</i> .....	83
3.2.6 <i>Summary and conclusion</i> .....	91
3.3 OPTIMISATION OF THE MECHANOCHEMICAL SYNTHESIS PROCEDURE .....	92
3.3.1 <i>Experimental</i> .....	92
3.3.2 <i>Synthesis Parameter Optimisation</i> .....	92
3.3.3 <i>Fabrication of metastable Phases</i> .....	96
<b>4 CONCLUSION &amp; OUTLOOK</b> .....	<b>100</b>
<b>5 APPENDIX</b> .....	<b>102</b>
<b>REFERENCES</b> .....	<b>122</b>



## List of Figures

<b>1:</b> Comparison of the basic construction of a commercial Li-ion battery and an all-solid-state battery. ....	2
<b>2:</b> Radar diagrams to visualise the properties of different types of solid electrolyte materials; oxides (red), sulphides (yellow), halides (blue), and polymers (green) .....	4
<b>3:</b> Overview of reported conductivity values for LPS and LPSO from ball milling synthesis. Black squares: amorphous LPS, red circles: amorphous LPSO, blue triangles: glass-ceramic LPS with a small amount of crystallites, green triangle: mainly $\beta$ -LPS phase. ....	6
<b>4:</b> Explanation of parameters affecting different aspects of the diffractogram. Adapted from Dinnebier 2008.[66] .....	11
<b>5:</b> Examples for two simple equivalent circuits used in battery analysis (Randles cell (B), diffusion extended Randles cell (E)) and their representation as Nequist (A, D) and Bode (C, F) plots. ....	23
<b>6:</b> Example of a simple pulse sequence for PFG-NMR experiments. Red arrows represent the magnetisation vectors. ....	25
<b>7:</b> Example of a simple pulse sequence for $T_1$ relaxometry experiments. Red arrows represent the magnetisation vectors. ....	26
<b>8:</b> Schematic overview of the two compared synthesis routes. ....	33
<b>9:</b> X-ray diffractograms of LIO3 ( $x = 20$ ) at progressing time steps during ball milling synthesis (A) and all LIO samples after 195 h total milling time (B). Diffractograms of the LIPSO series for comparison (C) reprinted with permission from[44]. ....	35
<b>10:</b> fraction of P - S and P - O bonds calculated from XPS analysis for LIO samples (A) and LIPSO samples (B). B is reprinted with permission from[44]. ....	36
<b>11:</b> SEM of all LIO samples (A-F) and EDX maps of P(green), O(blue) and S(cyan) for LIO4 (G). ....	37
<b>12:</b> Synchrotron PDF of LIPSO (A), with zoom-in on the low $r$ region (B) and LIO (C) with zoom-in to low $r$ and detailed peak assignment (D). ....	38
<b>13:</b> PDF of LIPSO sample with 30 % LPO (black) with PDFgui fit of the $\beta$ -LPO phase (red) and the difference curve (green) compared to the LIO sample with the same oxygen content (brown, dotted) A: low and mid $r$ region, B: mid and high $r$ region. ....	41
<b>14:</b> Raman and $^{31}\text{P}$ MAS-NMR spectra of LIO (A, B) and LIPSO (C, D), with the assignment of the main bands and sketches of PS43-, PO43-, and P2S64- structural units. Blue arrows in the NMR plots point to the peaks of mixed PO $_x$ Sy3- units. C and D are reprinted with permission from [44]. ....	42
<b>15:</b> MAS-NMR fits for LIPSO (A) and LIO (B) samples with 25 % oxygen substitution. As well as bar diagrams representation of the relative quantities of structural units in the LIPSO sample (C), LIO sample (D), and a calculated statistical distribution of oxygen (E) .....	44
<b>16:</b> EIS measurements of LIO, LIPSO and mixed LPS/LPO samples (A), LIPSO and a repetition series (B) and LIO and a repetition series (C). .... <b>Fehler! Textmarke nicht definiert.</b>	
<b>17:</b> Left: Comparison of conductivity trends and fraction of high oxygen substituted tetrahedral of the LIO samples (A), LIPSO samples (C), and the repetition LIPSO series (E).	

Right: Comparison of conductivity trends and fraction of amorphous $[\text{PO}_4]^{3-}$ units of the LiO samples (B), LIPSO samples (D), and the repetition LIPSO series (F). .....	50
<b>18:</b> Results for temperature-dependent ion dynamic measurements with EIS (A), PFG-NMR (B) and comparison of the derived room temperature conductivities (D).... <b>Fehler! Textmarke nicht definiert.</b>	
<b>19:</b> Activation energies for the LiO series determined by different analytical methods (A) and $T_1$ relaxometry of three representative samples (B).....	53
<b>20:</b> Peak assignment for the neutron PDFs (A) with schematic illustration of the distortions for mixed tetrahedral (B) and corresponding distances in the glasses (C).....	58
<b>21:</b> Comparison of neutron PDF at 100K (A), neutron PDF at 300K (B), and synchrotron PDF at RT (C). .....	59
<b>22:</b> Schematic illustration of angle deformation in mixed tetrahedra. ....	61
<b>23:</b> Neutron (left) and synchrotron (right) data and simulations from RMC refined structures for oxy-sulfide glasses with 0 (A, B), 10 (C,D), 20 (E, F) and 30 % (G, H) oxygen substitution. Red boxes mark the region that was used in the RMC simulation. ....	65
<b>24:</b> Histograms of calculated angles between nearest $\text{PO}_x\text{S}_{4-x}$ tetrahedra for structures with 0 (A), 10 (B), 20 (C) and 30% (D) oxygen substitution. Two nearest tetrahedra are placed on top of each other and the smallest angle between each pair of bonds is calculated (A inset). ....	66
<b>25:</b> Li - S (A) and Li - O (B) partial $G(r)$ s calculated from the refined structure models. ....	67
<b>26:</b> $[\text{PS}_4]^{3-}$ tetrahedra orientation and crystal structure of $\gamma$ -LPS (A), $\beta$ -LPS (B) and $\alpha$ -LPS (C). .....	71
<b>27:</b> Temperature-dependent XRD of LIO samples. Percentages denote the level of oxygen substitution. ....	72
<b>28:</b> Cell parameter (A-C) and unit cell volume (D) versus Temperature for $\beta$ -LPS.....	73
<b>29:</b> Evolution of Crystalline domain size (A) cell parameters (B, C) and unit cell volume (D) for the LGPS-type phase in all oxysulfide samples with 0 to 30 % oxygen substitution. The results were retrieved from Rietveld refinement of the x-ray diffractograms. ....	75
<b>30:</b> Evolution of phase fractions with temperature for oxysulfides with 0 to 30 % oxygen substitution. The values were retrived from Rietveld refinement of the x-ray diffractograms. ....	76
<b>31:</b> Structure of LGPS-type $\text{Li}_3\text{PO}_x\text{S}_{4-x}$ . Oxygen-containing tetrahedra are coloured pink. ....	77
<b>32:</b> Temperature-dependent synchrotron PDF measurements on samples with 0 (A, B), 10 (C, D), and 15 % oxygen substitution (E, F). The extended $G(r)$ s up to 75 Å are displayed on the left. The low $r$ region up to 8 Å is presented on the right.....	79
<b>33:</b> T-dependent Impedance measurements of LIO samples heated to 300 °C (A), activation energies of heat-treated samples (B), and comparison of Li-Ion conductivities of oxy-sulfide glasses and glass-ceramics with reference data from [45] (C). .... <b>Fehler! Textmarke nicht definiert.</b>	
<b>34:</b> Schematic illustration of the high-temperature impedance spectroscopy measurement cell (A) and pictures of the c parts (B), the fully assembled cell (C), and the contacted cell in the furnace (D) .....	85



<b>35:</b> Temperature-dependent x-ray diffractograms of LPS mixed with Al (A), Ti (B), CuS (C), MoS <sub>2</sub> (D) and Ni (E).....	87
<b>36:</b> Li-ion conductivity development for samples with 0 (A), 15 (B) and 25 % (C) oxygen substitution during heating up to 500 °C in the HT-impedance cell. Red data points indicate the first measurement after the furnace has been heated to the next higher temperature.	88
<b>37:</b> Investigation of temperature development during ball milling synthesis. A: Photo of the closed ball-milling jar. B: plot of temperature development over time for different sets of milling and cooling times with 10 mm balls (red) and 3 mm balls (blue).....	93
<b>38:</b> Conductivity response for all DoE experiments (A), correlation of the three investigated factors (B), and 2D response surface for 15 h of milling time with 75 g milling media (C) and 100 g milling media (D). .....	96
<b>39:</b> X-ray diffractograms of all DoE samples sorted by their ion conductivity with zoom in the low angle region (A). .....	97
<b>40:</b> Photos of milling jars with 75 g of 15 mm balls (a), and 100 of 20 mm balls (b).....	99
<b>41:</b> Overview over reported conductivity values for LPS and LPSO from ball milling synthesis. Black squares: amorphous LPS, red circles: amorphous LPSO, blue triangles: glass-ceramic LPS with small amount of crystallites, green triangle: mainly β-LPS phase.....	100
<b>42:</b> X-ray diffractograms of each sample from the LIO series in between milling cycles. ....	103
<b>43:</b> SEM images of all samples. ....	103
<b>44:</b> EDX maps for P(green), O(blue) and S(cyan) of all LIO samples. ....	104
<b>45:</b> Rietveld refinements of the LIPSO samples. Only β-Li <sub>3</sub> PO <sub>4</sub> phase was refined. ....	105
<b>46:</b> PDF of LIPSO samples (black) with PDFgui fit of the β-LPO phase (red) and the difference curve (green) compared to the LIO sample with the same oxygen content (brown, dotted). .....	106
<b>47:</b> MAS-NMR fits of LIO (left) and LIPSO (right) samples with 10, 15 and 20 % oxygen. ....	107
<b>48:</b> MAS-NMR fits of LIO (left) and LIPSO (right) samples with 25, 30 and 40 % oxygen. ....	108
<b>49:</b> Simulated neutron PDFs for the starting models compared the the data. ....	109
<b>50:</b> Neutron and sychrotron F(Q) data and simulated F(Q)s from RMC refined structure models for 0 (A, B), 10 (C, D), 20 (E, F) and 30 % (G, H) oxygen substitution. ....	110
<b>51:</b> Rietveld refinement of Temperature-dependent x-ray diffractograms from the sample with 0 % oxygen substitution. ....	111
<b>52:</b> Rietveld refinement of Temperature-dependent x-ray diffractograms from the sample with 10 % oxygen substitution. ....	112
<b>53:</b> Rietveld refinement of Temperature-dependent x-ray diffractograms from the sample with 15 % oxygen substitution. ....	113
<b>54:</b> Rietveld refinement of Temperature-dependent x-ray diffractograms from the sample with 20 % oxygen substitution. ....	114
<b>55:</b> Rietveld refinement of Temperature-dependent x-ray diffractograms from the sample with 25 % oxygen substitution. ....	115
<b>56:</b> Rietveld refinement of Temperature-dependent x-ray diffractograms from the sample with 30 % oxygen substitution. ....	116

<b>57:</b> Evolution of lattice parameters with temperature for the sample with 10 % oxygen substitution.....	116
<b>58:</b> Evolution of lattice parameters with temperature for the sample with 15 % oxygen substitution. ....	117
<b>59:</b> Evolution of lattice parameters with temperature for the sample with 20 % oxygen substitution. ....	117
<b>60:</b> Evolution of lattice parameters with temperature for the sample with 25 % oxygen substitution. ....	117
<b>61:</b> Evolution of lattice parameters with temperature for the sample with 30 % oxygen substitution. ....	118
<b>62:</b> SEM image of the LPS pellet after test run in the HT-impedance cell (A) and EDX mapping for phosphorous (B), sulfur (C), iron (D) and chrome (E).....	118
<b>63:</b> Rietveld refinement of LPS mixed with Al (A) and Ti (B) at 500 °C. ....	118

## List of Tables

<b>Table 1:</b> Overview over LIO samples.....	34
<b>Table 2:</b> Fractions of different structural units found in oxy-sulfide glasses based on NMR analysis and calculated statistical distribution.....	47
<b>Table 3:</b> Neutron and x-ray scattering coefficients for $\text{Li}_3\text{POS}_3$ . Green values are the pairs with the strongest coefficients, yellow values are about one third of the strongest one and red values are less than one tenth of the strongest coefficient.....	56
<b>Table 4:</b> overview of DoE experiments with values for investigated factors .....	94
<b>Table 5</b> Neutron and x-ray scattering coefficients for $\text{Li}_3\text{PS}_4$ .....	119
<b>Table 6</b> Neutron and X-ray scattering coefficients for $\text{Li}_3\text{PO}_{0.4}\text{S}_{3.6}$ .....	119
<b>Table 7</b> Neutron and X-ray scattering coefficients for $\text{Li}_3\text{PO}_{0.6}\text{S}_{3.4}$ .....	120
<b>Table 8</b> Neutron and X-ray scattering coefficients for $\text{Li}_3\text{PO}_{0.8}\text{S}_{3.2}$ .....	120
<b>Table 9</b> Neutron and X-ray scattering coefficients for $\text{Li}_3\text{POS}_3$ .....	121
<b>Table 10</b> Neutron and X-ray scattering coefficients for $\text{Li}_3\text{PO}_{1.2}\text{S}_{2.8}$ .....	121

## List of Abbreviations

DFT:	Density functional theory
eD:	Electron diffraction
EDX:	Energy dispersive x-ray spectroscopy
EIS:	Electrical impedance spectroscopy
EV:	Electric vehicle
EXAFS:	Extended x-ray absorption fine structure
LGPS:	$\text{Li}_{10}\text{GeP}_2\text{S}_{12}$
LPS:	Lithium thiophosphate ( $\text{Li}_3\text{PS}_4$ )
MAS-NMR:	Magic angle spinning – nuclear magnetic resonance
MD:	Molecular dynamics
ML:	Machine learning
NMR:	Nuclear magnetic resonance
nPD:	Neutron powder diffraction
PDF:	Pair distribution function
RMC:	Reverse Monte Carlo
RT:	Room temperature
SE:	Solid electrolyte
SEM:	Scanning electron microscope(y)
TEM:	Transmission electron microscope(y)
XAS:	X-ray absorption spectroscopy
XANES:	X-ray absorption near edge structure
XPS:	X-ray photon spectroscopy
XRD:	X-ray diffraction

## Danksagung

Im Verlauf meiner Doktorarbeit wurde ich von vielen Menschen begleitet und unterstützt, ohne deren Hilfe diese Arbeit so nicht möglich gewesen wäre. Mein besonderer Dank gilt:

Prof. Dr. Helmut Ehrenberg für Aufnahme als Doktorand am IAM-ESS, für die Übernahme des Gutachtens und das Korrekturlesen des Manuskripts.

Prof. Dr. Dominic Bresser für die Übernahme des Zweitgutachtens.

Dr. Anna-Lena Hansen für die Betreuung und Anleitung sowie zahlreicher hilfreicher Diskussionen. Dazu die Durchführung von PDF Messungen am DESY und das Korrekturlesen des Manuskripts.

Dr. Michael Knapp für die Betreuung, die hilfreichen Diskussionen und die stets offene Tür. Außerdem für das Korrekturlesen des Manuskripts.

Dr. Xianlin Luo für seine Unterstützung beim Einarbeiten im Labor und für die Durchführung und Auswertung der XPS Messungen.

Dr. Sylvio Indris für hilreiche Diskussionen über NMR sowie die Durchführung der  $^{31}\text{P}$  MAS-NMR Messungen und das Korrekturlesen der entsprechenden Passagen im Manuskript.

Dr. Mareen Schaller für die Durchführung und Auswertung der PFG-NMR und  $T_1$  Messungen und die Hilfe bei der Interpretation der Daten sowie das Korrekturlesen der entsprechenden Passagen im Manuskript.

Dr. Daniel Weber für zahlreiche hilfreiche Diskussionen und spannende Zusammenarbeit im Labor.

Daniel Hilscher für die Arbeit zur Syntheseoptimierung im Rahmen seiner Masterarbeit (3. Kapitel)

Dr. Marcel Sadowsky für die produktive Kooperation und das Erstellen der MD Glas Modelle, welche essenziell für die RMC Simulationen waren.

Liuda Mereacre für Hilfe und Unterstützung bei allen Fragen des alltäglichen Arbeiten im Labor.

Almut Kriese für die Hilfe bei allen administrativen Aufgaben.

Dominik Rotzler und Jialiang Liu für ihre Unterstützung als wissenschaftliche Hilfskräfte.

Bettina Huntzinger für die SEM aufnahmen.

Luis Sanchez Neudeck für IT Support.

Heinz Göbel für die Hilfe beim Verschicken von Proben um die halbe Welt.

Dr. Mattew Tucker for the admission and supervision at ORNL the ongoing help with RMC modelling and analysis and interpretation of neutron PDF data.

Dr. Michelle Everett for help with nrd measurements.

Paul Cullier, Dr. Yuanpeng Zhang, Ida Nielsen, Dayton Kizzire for help with RMC simulations and coding python scripts and good times in d around Oak Ridge.

Meinen Kollegen im Geb. 441/1 und darüber hinaus für die angenehme Arbeitsatmosphäre und die vielen Aktivitäten auf und neben dem Campus.

Besonders auch meinen Freunden und meiner Familie für ihre bedingungslose Unterstützung und Zuversicht während meiner gesamten Studiums und Promotionszeit!

Außerdem danke ich dem Bundesministerium für Bildung und Forschung für die Finanzierung im Rahmen des Festbatt II Projekts (03XP0433A)

Fulbright Germany für die Finanzierung meines Aufenthalts in Oak Ridge durch das Fulbright Stipendium

Teile der Ergebnisse wurden durch Messzeiten der Synchrotron Beamline PETRA III (Beamline P02.1), DESY, (danke an Martin Etter und Volodymyr Baran) und der Spallations Neutronen Quelle am ORNL (Instrument: NOMAD) erlangt.

## Zusammenfassung

In dieser Arbeit wurde der Einfluss von Sauerstoffsubstitution in Li-thiophosphat Gläsern und Glas-Keramiken untersucht, welche als Feststoffelektrolyten in Li-Feststoffbatterien verwendet werden können. Analysiert wurden die Einflüsse auf die atomare Struktur bzw. Nahordnung, die ionische Leitfähigkeit und das Kristallisationsverhalten der Gläser mit dem Ziel, Zusammenhänge zwischen atomarer Struktur und ionischer Leitfähigkeit zu identifizieren. Zu diesem Zweck wurde zunächst eine Reihe von Li-thiophosphat Gläsern mit variierender Sauerstoffsubstitution durch mechano-chemisches Kugelmahlen hergestellt. Mithilfe verschiedener Analysetechniken wurden die atomare Struktur der erhaltenen Materialien untersucht. Mittels Röntgen- und Neutronendiffraction mit anschließender Paarverteilungsfunktionsanalyse (PDF Analyse) in Kombination mit Raman und Magnet-Resonanz-Spektroskopie (NMR) konnten die einzelnen Struktureinheiten identifiziert und ihre Anordnung im Material sowie die Sauerstoffverteilung ermittelt werden. In Kooperation mit der Arbeitsgruppe von Karsten Albe, TU Darmstadt, wurden Strukturmodelle anhand der experimentellen Daten erstellt, welche mittels Reverse Monte Carlo (RMC) Simulationen weiter verfeinert werden konnten. Zusätzlich zu der strukturellen Analyse der Materialien wurde die Li-Ionen Dynamik auf verschiedenen Längenskalen untersucht. Die makroskopische Li-Ionen Leitfähigkeit wurde durch elektrochemische Impedanz Spektroskopie (EIS) ermittelt. Zudem wurden ausgewählte Proben mit gepulster  $^7\text{Li}$ -Feldgradienten (PFG)-NMR und Spin-Gitter ( $T_1$ )-Relaxometrie untersucht, um die lokalen Sprungprozesse zu beleuchten. Aus den ermittelten Daten und durch Vergleiche mit früheren Untersuchungen aus der Gruppe konnte aufgeklärt werden, dass neben der Sauerstoffkonzentration auch die Verteilung der Sauerstoffatome im Material einen erheblichen Einfluss auf die ionische Leitfähigkeit haben und eine bessere Verteilung zu einer geringeren Leitfähigkeitsreduktion führt. Um diese Verteilung zu erreichen, sollten Synthesebedingungen und Edukte so gewählt werden, dass eine effektive Reaktion aller Edukte gewährleistet ist.

Zudem wurde das Kristallisationsverhalten der synthetisierten Gläser mithilfe von temperaturabhängigen Röntgendiffraktionsmessungen untersucht. Dabei wurden verschiedene kristalline Phasen identifiziert und der Einfluss der Sauerstoffsubstitution über einen großen Konzentrationsbereich (10 - 30 %) quantifiziert. In allen Sauerstoff enthaltenden Proben wurde eine LGPS analoge Kristallstruktur als dominierende Phase festgestellt, welche eine verbesserte Leitfähigkeit im Vergleich zum Glas aufweist. Dadurch ist es möglich, hohe Sauerstoffkonzentrationen (bis 15 %) zu erreichen, ohne signifikante Verschlechterung der Li-Ionen Leitfähigkeit hinnehmen zu müssen. Eine Hochtemperatur Impedanz Messzelle wurde entwickelt, um den Einfluss von Nebenphasen und Änderungen der Zellparameter während des Kristallisationsprozesses auf die ionische Leitfähigkeit direkt beobachten zu können. Es ist jedoch weitere Optimierung erforderlich, um eine zuverlässige Interpretation der Daten zu gewährleisten.

Zuletzt wurden die Synthesebedingungen für das Kugelmahlen mittels „Design of Experiment“ (DoE) Ansatz optimiert, um den Einfluss der verwendeten Parameter auf die Kristallstruktur des Products besser zu verstehen und ein verbessertes Syntheseprotokoll zu entwickeln. Im Rahmen der Analyse konnte durch die gezielte Erhöhung der Kollisionsenergie zum ersten Mal die Hochtemperatur  $\text{Li}_3\text{PS}_4$  Alpha-Phase durch eine Raumtemperatur Synthese direkt

hergestellt werden. Die Analyse durch EIS bestätigte eine signifikante Erhöhung der Leitfähigkeit von 0.2 auf 0.7 mS/cm. Zudem konnte die Reaktionszeit drastisch reduziert werden von mehreren Tagen auf 15 h.



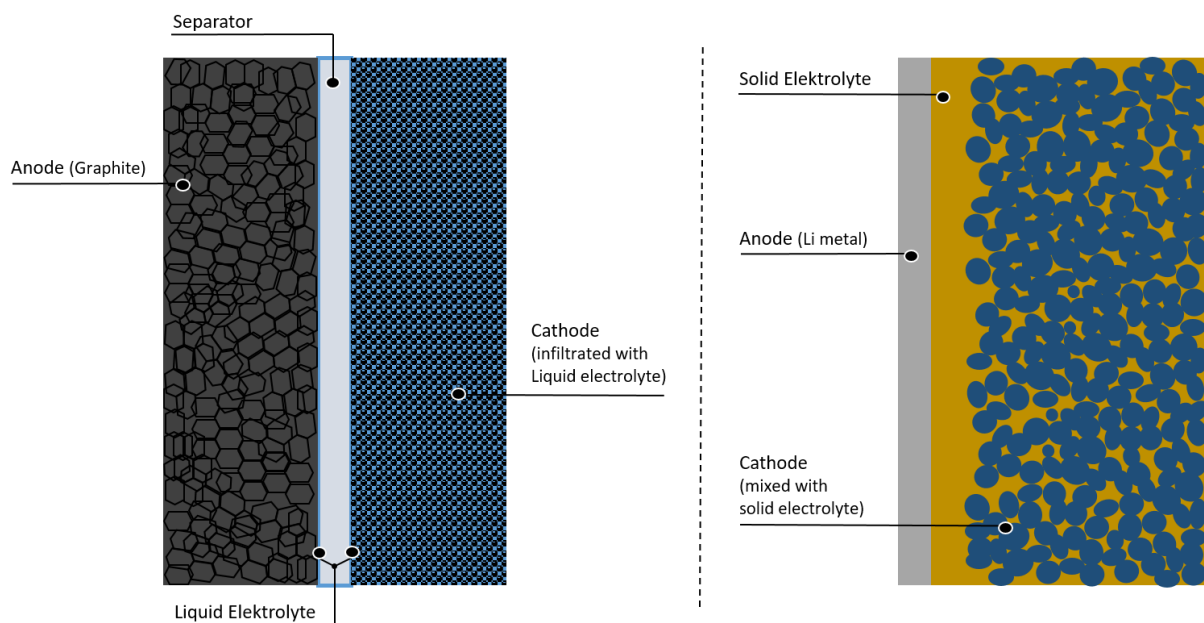
# 1 Theoretical Background & Introduction

## 1.1 All Solid State Batteries

The global shift from fossil fuels to renewable energy sources is one of the greatest challenges facing our society. Energy from renewable sources limits our dependence on oil and gas, which, in the current situation, often means dependence on politically unstable regions. Furthermore, the transition marks a critical step towards mitigating climate change and achieving sustainable energy systems. However, this transition poses significant challenges, particularly in terms of energy storage. Renewable energy sources, such as solar and wind power, are intermittent and require efficient storage solutions to ensure a steady and reliable supply of energy.[1] Furthermore, the electrification of transportation is a cornerstone of this energy transition. Electric vehicles (EVs) are increasingly replacing internal combustion engine vehicles, reducing dependence on fossil fuels and cutting greenhouse gas emissions. Several European countries, including Germany and France, have already announced a ban on internal combustion engine vehicles in the near future.[2] However, the widespread adoption of EVs hinges on advancements in battery technology to further increase the capacity (driving range) and fast charging capabilities and to reduce the cost of batteries.[3] Lithium-ion batteries have been the leading technology for energy storage, especially for EVs, due to their high energy density and efficiency. But other areas of modern life have also been shaped by the development of rechargeable Li-ion batteries as almost all wireless and handheld electronic devices are currently powered by such batteries.[4] However, Li-ion batteries are approaching their physical limits in terms of energy capacity and safety.[5] The search for better battery technologies has led to the exploration of several alternative technologies, such as other metal-ion batteries (Na, Mg, Al,...), metal-air batteries, or redox flow batteries[6] just to name a few.

Another concept to further advance Li-ion battery technology is the All-Solid-State Battery (ASSB). ASSBs offer several advantages over traditional lithium-ion batteries, including higher energy density, improved safety, and potentially longer lifespans as well as fast charging capabilities.[7] The concept of an ASSB is similar to that of a commercial Li-ion battery, both are illustrated in Figure 1. The key difference is the replacement of the liquid electrolyte for a solid electrolyte (SE), which simultaneously serves as the separator to avoid shortcuts.

Currently used liquid electrolytes for Li-ion batteries are commonly composed of a Li salt, dispersed in an organic solvent. In particular, the combination of the organic solvent, which decomposes into flammable components, and the oxygen-releasing electrode materials pose a major safety risk when the battery goes into a thermal runaway due to damage or mishandling.[8] Introducing a solid electrolyte should reduce the risk of a thermal runaway by reducing side reactions and increasing the thermal stability of the electrolyte. Furthermore, a solid electrolyte potentially enables the use of Li metal or silicon anodes, which have the potential to significantly increase the capacity and energy density of the battery.[9]

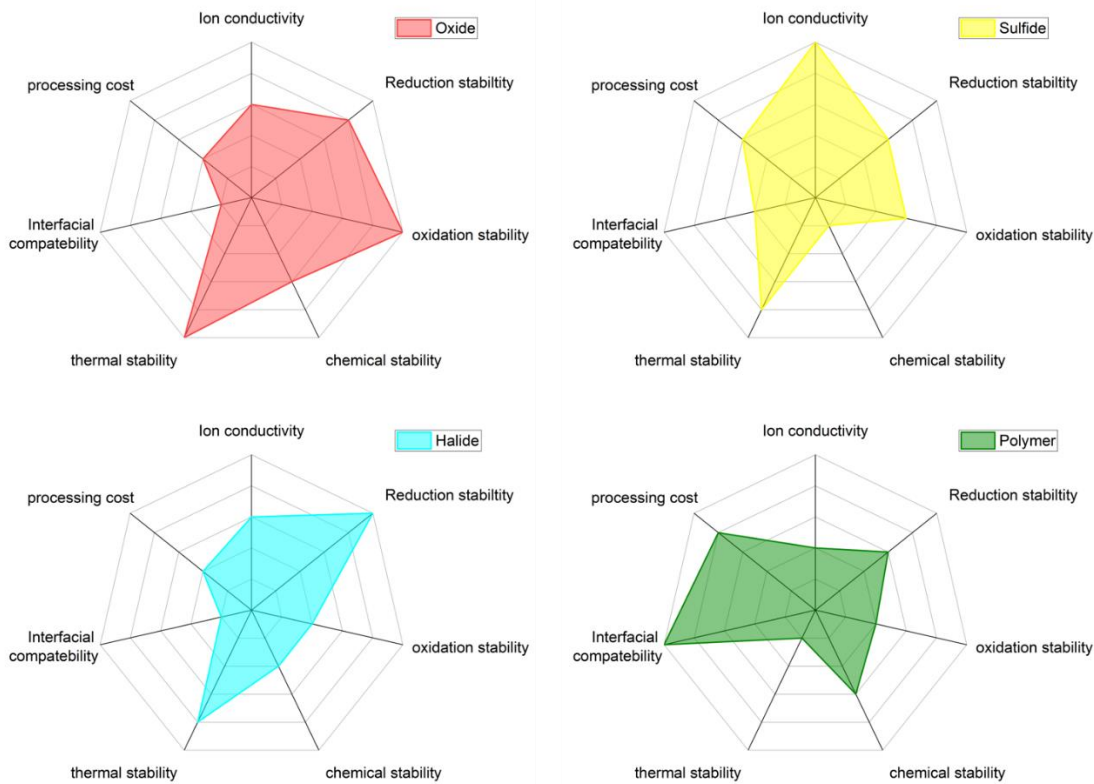


1: Comparison of the basic construction of a commercial Li-ion battery and an all-solid-state battery.

ASSBs are not limited to lithium; the concept is transferable to other alkali metals such as sodium (Na)[10] and potassium (K),[11] and is being actively researched, broadening the scope of application and accessibility of raw materials. Other battery concepts such as Li-S or Li-air batteries also benefit from the development of solid-state electrolytes.[12]

The key component in ASSBs is the solid electrolyte (SE), which facilitates ion transport between the electrodes. There are three main categories of ASSBs, which differ mainly in the electrolyte material used; inorganic, polymer, and hybrid. The inorganic electrolytes can be divided into oxides, sulphides, and halides and can be further separated by their crystal structure.[13] The hybrid concepts typically combine inorganic and polymer electrolytes either by dispersing inorganic particles in a polymer matrix[14] or by stacking several layers of

individual electrolytes to reduce contact resistances and side reactions between components. The latter can also be used to combine different inorganic materials.[15] All of these material classes have different advantages and challenges as summarised in the radar diagrams in Figure 2. Polymer electrolytes are soft and have good interfacial compatibility because of their ability to respond to volume changes of the electrodes during cycling. Their electrochemical stability is also good and the wide variety of available chemistry opens up a plethora of options for tailored materials. On the downside, these tailor-made polymers can increase the cost of the material, besides, their ionic conductivity and thermal stability are comparatively low. Inorganic electrolytes on the other hand are typically cheaper to produce and have higher ionic conductivities and thermal stability. However, due to their mechanical integrity, the main drawback is their Interfacial compatibility as volume changes of the electrodes can lead to build-up pressure or contact loss in the electrode/electrolyte interface. Among the inorganic electrolytes, there are further distinctions depending on the type of material; oxides typically have a high oxidation, and excellent thermal stability, but suffer from lower ionic conductivities. In addition, the fabrication process typically requires thermal treatment at high temperatures, increasing the energy cost of the production. The Halides have excellent reduction stability but are prone to oxidation and also lag in ionic conductivity. For sulphides, on the other hand, their ionic conductivity is their main selling point as it is the highest of all solid electrolytes accompanied by easy processability at room temperature. The main disadvantage for this group of SEs is their chemical and electrochemical instability.[1, 16]



2: Radar diagrams to visualise the properties of different types of solid electrolyte materials; oxides (red), sulphides (yellow), halides (blue), and polymers (green)

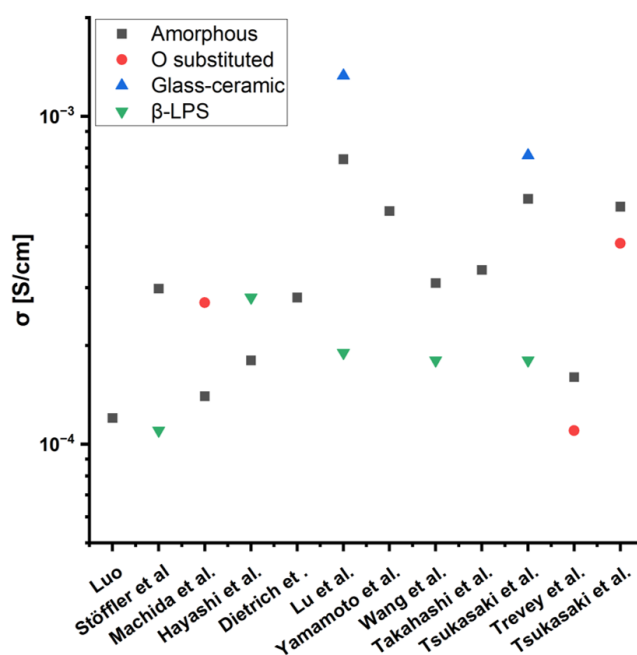
Hybrid concepts attempt to combine the advantages of several types of electrolytes to overcome their weaknesses. Typical challenges for these concepts arise from the additional interphases between the individual electrolytes.[17] More recently, the combination of solid electrolytes with liquids has been proposed to mitigate the contact issues for SEs, leading to an almost solid-state battery.[18]

As mentioned above, sulphide-based solid electrolytes have emerged as promising candidates due to their excellent ionic conductivity, which rivals, and in some cases, exceeds that of conventional liquid electrolytes.[7, 19, 20] This high conductivity is attributed to their unique structural properties. The low electronegativity of the bulky sulphur atom reduces the interaction between Li ions and the anion network compared to oxides for instance, facilitating rapid lithium-ion transport. However, the adoption of sulphide solid electrolytes is not without challenges. One of the primary issues is their sensitivity to moisture and air, leading to rapid degradation and the formation of toxic byproducts.[21] Furthermore, the interface between sulphide electrolytes and electrodes poses significant challenges. Stability

and compatibility at this interface are crucial for the overall performance and longevity of ASSBs. Issues such as interfacial resistance and chemical reactivity at the electrolyte-electrode interface have been focal points of recent research.[22, 23] To address the issue of sulphide solid electrolyte stability, several strategies have been developed and investigated. A number of studies focus on different coatings of the electrolyte or the electrode particles to form an artificial solid electrolyte interphase (SEI), others propose hybrid concepts with polymer buffer layers to avoid direct contact of the sulphide electrolyte with the electrode material.[24] Oxygen substitution has been explored as another viable strategy to enhance sulphide SE stability. The aim is to combine the good chemical stability of the oxides with the excellent ionic conductivity of the sulphides. Several studies indeed report lower H<sub>2</sub>S evolution upon contact with humid air as well as enhanced cycle stability for oxygen sulphide SEs.[25–28] This approach, however, often comes at the cost of reduced conductivity, thus, the right strategy needs to be found to get the best compromise between conductivity and stability.

The most prominent candidates of sulphide-based SEs are the LGPS-like structures, the thio-LISICONs, Argyrodites, and the LPS glasses and glass ceramics.[21] LGPS was named after the Li<sub>10</sub>GeP<sub>2</sub>S<sub>12</sub> compound which, at the time it was found, had the highest conductivity of any solid lithium ion conductor with 0.12 S cm<sup>-1</sup>, and the first that could rival liquid electrolytes.[29] The materials crystallise in the tetragonal space group *P4<sub>2</sub>/nmc* and typically exhibit fast 1D conduction channels along the c-axis. Other examples of this class of materials include Li<sub>10</sub>SnP<sub>2</sub>S<sub>12</sub> (LSnPS)[30] and Li<sub>7</sub>SiPS<sub>8</sub> (LiSiPS)[31]. The highest ever recorded Li-ion conductivity with 0.25 S cm<sup>-1</sup> was reported for Li<sub>9.54</sub>Si<sub>1.74</sub>P<sub>1.44</sub>S<sub>11.7</sub>Cl<sub>0.3</sub>, another member of the LGPS family.[19] The thio-LISICONs are a group of materials found in the ternary Li<sub>2</sub>S–GeS<sub>2</sub>–P<sub>2</sub>S<sub>5</sub>, Li<sub>2</sub>S–SiS<sub>2</sub>–Al<sub>2</sub>S<sub>2</sub>, and Li<sub>2</sub>S–SiS<sub>2</sub>–P<sub>2</sub>S<sub>5</sub> systems. Their crystal structure is, depending on the composition, either orthorhombic in the *Pnma* space group or monoclinic, *P2<sub>1</sub>/m* space group. And also exhibit 1D conduction along the a-axis. Conductivities are in the order of 10<sup>-5</sup> - 10<sup>-3</sup> S/cm.[32] Lithium argyrodites describe the three compositions; Li<sub>6</sub>PS<sub>5</sub>Cl, Li<sub>6</sub>PS<sub>5</sub>Br, and Li<sub>6</sub>PS<sub>5</sub>I. They crystallise in the *F3 m* space group and have ion conductivities of 1.9 × 10<sup>-3</sup>, 6.8 × 10<sup>-4</sup>, and 4.6 × 10<sup>-7</sup> S cm<sup>-1</sup>, respectively. The Li ions in the argyrodite structure are confined in cage-like structures around the halogen atoms. These cages can be opened up and connected to a 3D network when S<sup>2-</sup>/X<sup>-</sup> site disorder is introduced. Because of similarities in the atomic radii of S and Cl, this disorder is most prominent in the Li<sub>6</sub>PS<sub>5</sub>Cl compound, hence

the high ionic conductivity.[33] At last, the LPS system contains a wide range of structures in the  $\text{Li}_2\text{S} - \text{P}_2\text{S}_5$  binary system. Different materials with varying structures are obtained by variations of the  $\text{Li}_2\text{S}/\text{P}_2\text{S}_5$  ratio. Depending on the synthesis method and heat treatment, crystalline or amorphous materials can be synthesised.[34] The highest conductivity value with  $17 \text{ mS cm}^{-1}$  was reported for the crystalline  $\text{Li}_7\text{P}_3\text{S}_{11}$  compound with a 70/30 ratio.[35] Other reported compounds are the 80/20,[36] 75/25,[37] 67/33,[38] 50/50[39] glasses and glass-ceramics. Like the previously discussed material classes, the crystalline structures of these LPS materials are mainly built up of a network of  $[\text{PS}_4]^{3-}$  tetrahedra, with the exception of the 67/33 compound. These tetrahedra can be edge-sharing (50/50), corner-sharing (70/30), or isolated (75/25, 80/20).[40] Considering the glass compositions, the highest conductivity was found for the 75/25 glass with reported conductivity values ranging from  $1$  to  $7 \times 10^{-4} \text{ S cm}^{-1}$  (Figure 3).[27, 34, 41–49] The widespread conductivity values lead to disagreement within the community about the relative performance of amorphous versus crystalline and pristine versus oxygen-substituted  $\text{Li}_3\text{PS}_4$ .



3: Overview of reported conductivity values for LPS and LPSO from ball milling synthesis. Black squares: amorphous LPS, red circles: amorphous LPSO, blue triangles: glass-ceramic LPS with a small amount of crystallites, green triangle: mainly  $\beta$ -LPS phase.

Due to the comparatively simple composition,  $\text{Li}_3\text{PS}_4$  is a suitable material to investigate Li-ion conduction in thiophosphates. However, the spread of reported conductivity values hinders meaningful comparisons. Hence, a deeper understanding of the underlying structure-property

relationships is needed to understand the discrepancies in the literature and enable further development of materials and understanding of relevant parameters, which influence the ionic conduction.

## 1.2 Mechanochemical Synthesis

Three main synthesis routes are commonly proposed for the preparation of solid electrolyte materials; high-temperature solid-state synthesis, solvent-mediated wet chemical synthesis, and mechanochemical synthesis.[40, 50] All three of those have different advantages and disadvantages. High-temperature solid-state reactions typically yield highly crystalline material with good purity. The disadvantages are high energy demand and, concerning commercialisation, low scalability potential.[51] The wet chemical route offers control over particle size and morphology by appropriate choice of solvent, temperature, and drying techniques as well as good scalability.[52] However, the use of toxic solvents, which often cannot be completely removed from the product, limits the achieved conductivity values and the commercialisation potential.[40, 53, 54] The mechanochemical approach, on the other hand, offers low-energy, low-cost synthesis with good scalability. The main drawbacks are the long synthesis time and lack of control over impurity phases.[34] Considering all of the above, the mechanochemical synthesis method has emerged as the most used method for the preparation of sulfide solid electrolytes.

Mechanochemical synthesis is a method of creating new materials through mechanical energy. It involves the use of mechanical force, such as grinding or milling, to provoke chemical reactions that form new compounds. The process typically occurs in a high-energy ball mill, where the grinding balls and the educts of the material to be synthesised are placed together. As the mill operates, kinetic energy is transferred to the reactants by collision or friction between the milling media. If the energy transfer is low compared to the activation energy of the reaction, the transferred energy is converted into plastic deformation, leading to amorphisation or particle cracking. These phenomena are observed in a classical comminution experiment. However, if the transferred energy is high enough, these collisions can break chemical bonds in the reactants and facilitate the formation of new bonds, leading to the creation of new materials. There are several different kinds of ball mills, which differ in the way, the milling media is brought to collision. Examples are tumbling ball mill[55], vibrating ball mill[56], agitator ball mill[57] and planetary ball mill[58]. The most commonly used ball

mill for laboratory synthesis of SEs is the planetary ball mill due to its high stressing energy, whereas for upscaling of the process, the agitator ball mill is the most promising setup.[59]

The governing parameters, which can be adjusted to tune the process, are the rotational speed, the milling media size, as well as the milling-media filling-ratio, and the sample filling-ratio. Most studies on the mechanochemical synthesis of solid electrolytes use similar parameters, but without elucidating the tangible influence of each one. The reason for that is partly a lack of understanding of the process inside the ball mill and at the same time difficulties in measuring the specific influence of each parameter on the process. More recently, theoretical calculations, using the Discrete Element Method (DEM), were employed to study the effects of the above-mentioned parameters on the stressing energy, the collision frequency, and the power input during milling.[60, 61] Moreover, experimental setups have been developed at DESY (Hamburg, Germany) for in situ synchrotron x-ray diffraction measurement during milling to investigate reaction mechanisms. [62–64] The stressing energy ( $E_s$ ) is the energy dissipated at a given collision between either two grinding balls or a grinding ball with the wall of the jar. This energy depends mainly on the relative velocity ( $v_r$ ) and masses ( $m_1, m_2$ ) of the two colliding objects, as demonstrated in equation (1).

$$E_s = \frac{m_1 \cdot m_2}{2 \cdot (m_1 + m_2)} v_r^2 \cdot (1 - COR^2) \quad (1)$$

$COR$  is the coefficient of restitution and describes the elasticity of the collision. Increasing either the relative velocity ( $v_r$ ) and/or the mass of the grinding media ( $m_1$ ) will increase the stressing energy.

The collision frequency ( $f_c$ ) is the number of collisions within a given time interval. The number of grinding balls and the rotational speed are the determining factors for the collision frequency. The product of stressing energy and collision frequency then equates to the total power  $P$  (equation (2)).[60]

$$P = E_s \cdot f_c \quad (2)$$

Many of these values, like the velocity of the grinding media or the collision frequency, are impossible to determine experimentally, thus, simulations can yield important insights into the effects of milling parameters, which cannot be accessed otherwise. The concurring results of the simulation studies reveal that the rotational speed has a large influence on the total



power, as both the collision frequency and the stressing energy increase with increasing rotational speed. Both effects can be attributed to an increased velocity of the milling media.

Contrary, the grinding media size has almost no effect on the total power input. The reason for this is the opposing effects of the media size on the stressing energy and the collision frequency. On the one hand, the stressing energy increases with increasing milling media size because the media mass increases. On the other hand, the collision frequency decreases because the number of grinding balls decreases, given that the media filling ratio is held constant.[60, 61] The influences of media and sample filling-ratios can be discussed on the basis of the above-mentioned relations. Increasing the milling-media filling-ratio, as defined in equation (3), increases the number of balls and thus the collision frequency.

$$\delta_m = \frac{V_{media}}{V_{jar}} \quad (3)$$

As a result, the total power will also increase at first. However, above a threshold of approximately 0.5 - 0.6, the effect is reversed because the movement of the milling media is increasingly restricted, resulting in lower velocities and hence lower stressing energies.[59]

The sample filling-ratio, defined as the ratio of sample volume to milling media volume (equation (4)), is less impactful than the parameters mentioned before.

$$\delta_m = \frac{V_{sample}}{V_{media}} \quad (4)$$

An excessive sample filling-ratio may again lead to hindrance in the movement of the milling media. In addition, the sample film around the milling media and the jar walls adds a dampening effect to the collisions, which is dependent on the film thickness. Low sample filling-ratios reduce the effectiveness of the process, as less material is processed at a time. Further, the risk of abrasion increases because the collisions are less damped.[59]

### 1.3 Structure Analysis

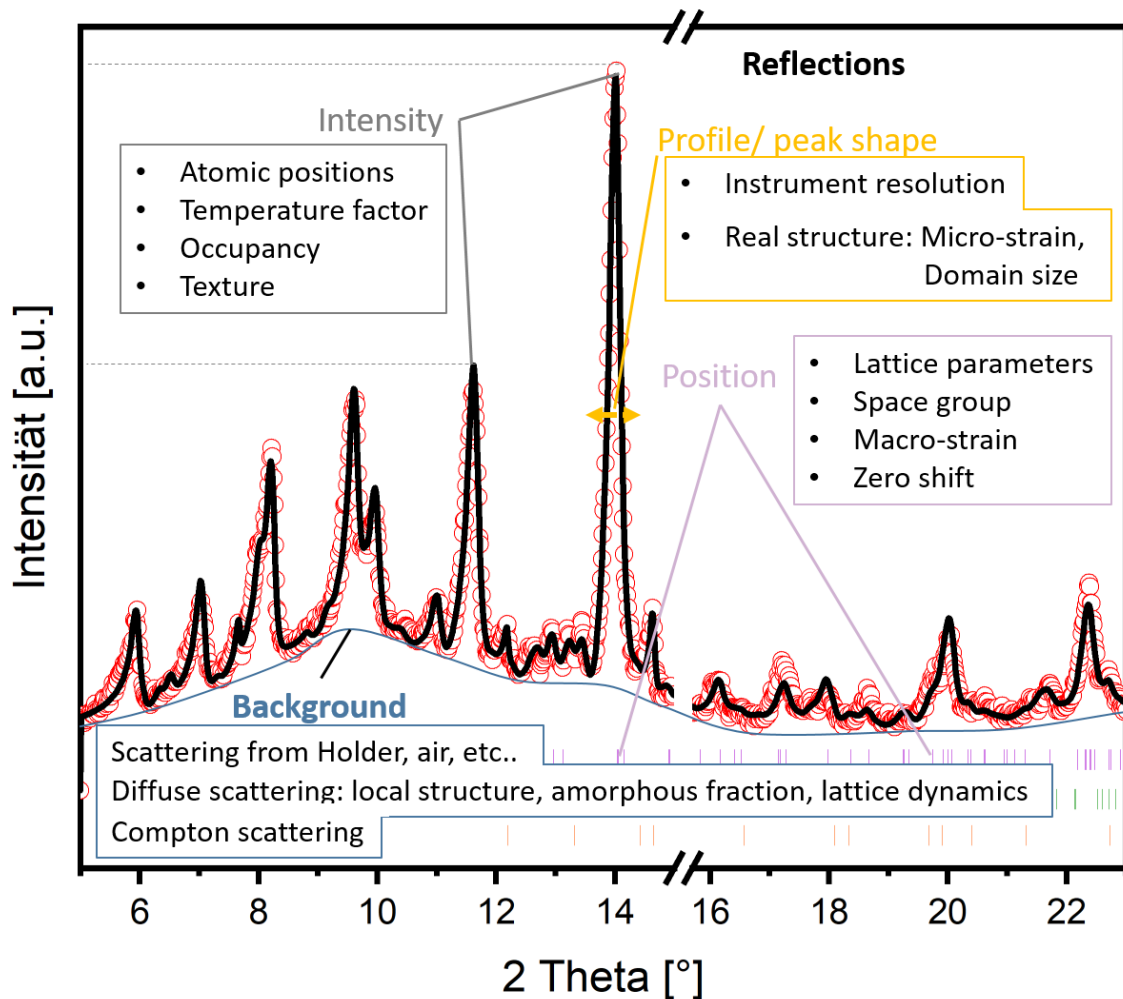
There are a number of different tools available for the characterisation of the atomic structure of condensed matter. Each technique can reveal information on different length scales, thus the combination of multiple methods is often advisable as they can yield complementary results.

### 1.3.1 Diffraction

Diffraction techniques are the most commonly used techniques for the study of crystalline materials. These techniques provide information about the crystal structure, including atomic positions and occupancies, as well as the microstructure (size and strain). In a typical diffraction experiment, the sample is placed in a probe beam, and the probe is scattered at the lattice planes of the crystallites according to Bragg's law (equation (5) with  $d$ : distance between lattice planes,  $\lambda$ : wavelength of the probe beam,  $\theta$ : scattering angle,  $n$ : diffraction order) and the angle between incoming and outgoing probe is recorded. The result is a diffractogram of intensity versus diffraction angles. This diffractogram can be used to identify the crystal symmetry (spacegroup) of the compound, e.g. by comparison with a database.

$$n \lambda = 2d \sin(\theta) \quad (5)$$

However, in most cases, the basic structure is already known. In that case, the Rietveld refinement method can be used to extract additional structural information from the diffractogram.[65] When employing the Rietveld method, a diffraction pattern is calculated from a selected structure model, and the calculation is then iteratively fitted to the experimental data by least-square refinement. During these iterations, structural parameters of the model are adjusted to improve the fit. The position of the reflection peaks is determined by the lattice parameters, the space group and the position of the sample in the beam. The peak Intensities are mainly dependent on the atom type and the occupancy of the correlating atom position. Other factors that affect the intensities are preferred orientations of crystallites or thermal vibrations of the atoms can affect the relative intensities. Finally, the peak shape decodes all kinds of distortions and imperfections compared to an ideal infinite crystal. Mainly size and strain effects lead to a broadening of the peaks but also the instrument resolution needs to be considered. By analysing the whole diffraction pattern with the Rietveld method, all of these parameters can be calculated and quantified. Figure 4 depicts the factors and how each contributes to the diffractogram.



4: Explanation of parameters affecting different aspects of the diffractogram. Adapted from Dinnebier 2008.[66]

Diffraction experiments are not exclusively done with x-rays. The probe for the diffraction experiment can be any particle that can be accelerated to a wavelength in the Å regime. The wavelength needs to fit the atomic distances of lattice planes in a crystal and the probe needs to interact with matter in a way that allows for diffraction and later detection of the particle-wave. Three different probes are commonly used; x-ray photons, neutrons, and electrons. X-rays are the most widely used probe due to the availability of laboratory x-ray diffractometers. The wavelength in these laboratory machines can be tuned by the choice of cathode material. Standard cathodes are Cu ( $\text{Cu}_{K\alpha}$ : 1.54 Å) and Mo ( $\text{Mo}_{K\alpha}$ : 0.71 Å). Other available cathodes are for instance Ag ( $\text{Ag}_{K\alpha}$ : 0.56 Å) or Co ( $\text{Co}_{K\alpha}$ : 1.79 Å). A wider range of x-ray energies is available with synchrotron radiation at large-scale facilities. Neutrons are only available at large-scale facilities with either a neutron reactor or a spallation source. The wavelength of neutrons can be tuned by adjusting their energy through moderators at different temperatures. The range of achievable wavelengths stretches from several hundred to a hundredth of an Å. Electron

diffraction is usually done in combination with electron microscopy. At typical transmission electron microscope (TEM) operation voltages of 80 – 300 kV electrons are accelerated to wavelength between 0.04 and 0.02 Å. Choosing the right probe is important to get the desired information, because different atom types may interact more strongly with one or the other probe. X-rays and electrons interact almost exclusively with the electron cloud. Therefore, atoms with more electrons (a larger electron cloud) interact more strongly. Thus, the scattering intensity increases linearly with the atomic number. Neutrons on the other hand interact with the atom core. The mechanism of this interaction is not yet fully understood and there is no clear trend within the periodic table to predict which atoms are good neutron scatterers. In some cases, even two isotopes of the same atom have widely different neutron scattering lengths. Neutron and x-ray diffraction experiments can often yield complementary results, as x-rays are sensitive to heavy elements and neutrons have comparatively large scattering crosssections with several light elements, such as hydrogen, carbon, lithium, oxygen and others.

The combination of microscopy and diffraction is a unique feature of electron diffraction. In x-ray diffraction (XRD) and neutron diffraction (ND) experiments typically a large part of the sample is illuminated, hence the result corresponds to an average over the whole sample. In contrast, in electron diffraction (ED) experiments in a transmission electron microscope (TEM) a small area of several nanometers can be selected, which may be interesting for inhomogeneous samples. However, electrons have a low mean free path inside condensed matter, as compared to x-rays and neutrons, of only a few nanometers. Hence, the investigated samples need to be thin. In addition, high-energy electron beams can be destructive to soft matter and metastable structures.

### 1.3.2 Local environment analysis techniques

There are a variety of additional techniques for the local structure analysis on a Å scale. The above-mentioned TEM for instance is capable of atomic resolution. With the right setup and careful sample preparation, these microscopes can image lattice planes and even molecular structures[67, 68]. TEM images, however, mainly yield information on the symmetry and spatial arrangement of atoms. For chemical information, other methods are more useful. Raman and magic-angle-spinning nuclear magnetic resonance (MAS-NMR) spectroscopy are powerful tools for investigating the local chemical environments, including coordination and bonding situations.

In Raman spectroscopy, the sample is excited with laser light and the inelastically scattered photons are detected. The method works due to the interaction of light with the Raman active vibrational modes of molecules, leading to a shift in the energy of the scattered light, which is characteristic of the molecular structure. Consequently, Raman spectroscopy primarily provides information on the bonding situation in molecular solids.

MAS-NMR is an advancement of classical solution NMR to be able to measure solid material. As in solution NMR, the sample is placed in a magnetic field to align the nuclear spins of all the atoms in the sample. Next, a radio frequency (RF) pulse is applied to “flip” the spin states of the observed nuclei. After the pulse, the spin states relax back to the original state to align with the magnetic field, emitting the energy difference between the two states as radio signals. The frequency of these radio signals is dependent on the local magnetic field at every nucleus, which is highly sensitive to the surrounding electronic, ergo chemical, environment. The frequencies of the radio signals are also dependent on the orientation of the nucleus and its environment relative to the external magnetic field following a  $[3\cos^2(\Theta)-1]$  dependency. The angle dependency does not affect the NMR result if the orientation of the structure changes on a time scale faster than the NMR experiment because only an average orientation is recorded. This case applies to small molecules in solution. For solids or large molecules, however, the orientation of each nucleus towards the magnetic field does not change during the experiment. Therefore, each nucleus emits a signal with a different frequency based on its orientation, even though the chemical environment might be identical. The result is an extensive peak broadening and the loss of structural information. For powder samples, the characteristic line shape retrieved from a solid-state NMR experiment is called a Pake pattern. The problem can be solved by spinning the sample at high frequency at a relative angle of  $54.736^\circ$ , which is therefore called the magic angle. At this angle, the  $[3\cos^2(\Theta)-1]$  term becomes zero and any angle-dependent contribution to the radio signal vanishes, resulting in narrow line widths and high-frequency resolution. To conclude, MAS-NMR spectroscopy can reveal local chemical environments around a target nucleus.

Similar information can be gained by x-ray absorption spectroscopy (XAS). As the name suggests, the sample is placed in an x-ray beam and the absorption of x-ray photons is measured either by comparison of incoming and outgoing beam intensity or by measurement of fluorescence. The energy of the x-ray beam has to be adjusted depending on

the observed atom type. The absorbed energy then depends strongly on its oxidation state, but also on the surrounding atoms. The absorption spectrum can be divided into two parts, the x-ray absorption near edge structure (XANES) and extended x-ray absorption fine structure (EXAFS). Each of these spectral regions contains different information about the sample. The XANES region is defined by electronic transitions of the target atom type and thus decodes oxidation numbers. The EXAFS region appears due to interference and multiple scattering with the neighbouring atoms, hence yielding information on the bonding situation of the target atom. XAS experiments are typically done at synchrotron facilities because x-ray energies can be tuned more easily. However, lab XAS machines are becoming available for some energy ranges.

All of these techniques probe the local atomic environment of a target atom type and can therefore be generally used on crystalline as well as amorphous samples, although a broader distribution, of bond lengths for instance, often leads to peak broadening and reduced resolution. On the other hand, the degree of broadening can then be analysed to estimate the degree of disorder in the material.

### 1.3.3 Pair Distribution Function Analysis

In order to bridge the gap between local and average structure, another way for the analysis of diffraction data has regained attraction in recent years. The so-called pair distribution function (PDF) analysis is a method to analyse the full diffraction data (total scattering) and convert it into real space to directly display atom-pair distances within the material of interest. In contrast to classical diffraction analysis, like the Rietveld method described earlier, PDF analysis considers both Bragg scattering (from ordered structures) and diffuse scattering (from disordered regions), thus providing comprehensive structural information.

In order to get to the pair distribution function, a series of mathematical transformations and corrections have to be applied to the data. As described earlier, the experiment yields a diffractogram of intensity vs diffraction angle. The diffraction angle can be converted into the scattering vector, or, to be more precise, its magnitude  $Q$ , resulting in an  $I(Q)$  function. At this point, a number of corrections need to be applied to account for contributions from the instrument, the sample container, and everything in the pathway of the beam that is not the sample itself. For this reason, measurements of the empty instrument and the sample holder are important to be able to subtract any intensity, which does not originate from the sample.

The corrected  $I(Q)$  function describes the  $Q$ -dependent intensity for the whole illuminated sample area. At first, this function is converted into the total scattering structure function,  $S(Q)$ , which equals the average  $Q$ -dependent intensity per atom (see equation (6)).

$$S(Q) = \frac{I(Q)}{N\langle b_{coh} \rangle^2} - \frac{\langle b_{tot}^2 \rangle - \langle b_{coh} \rangle^2}{\langle b_{coh} \rangle^2} \quad (6)$$

Where  $N$  is the number of atoms in the illuminated area,  $\langle b_{coh} \rangle^2$  and  $\langle b_{tot}^2 \rangle$  are the average coherent and total scattering power of all atoms in the sample. Another commonly used reciprocal space function is the  $F(Q)$ . Depending on the community the term  $F(Q)$  can refer to either of the two functions below (equation (7) or (8)).

$$F(Q) = Q[S(Q) - 1] \quad (7)$$

$$F_K(Q) = \langle b_{coh} \rangle^2 [S(Q) - 1] \quad (8)$$

Multiplying  $S(Q)$  by  $Q$  emphasises the noise at high  $Q$ , which helps to determine the  $Q_{max}$  value for the conversion to the real space PDF where the noise can have a large impact on the quality of the function. In some cases, structure models are fitted directly to either the  $S(Q)$  or one of the  $F(Q)$  functions. However, in most cases, further mathematical conversions are done to get a real space function. Often fitting to both functions is advised, as, although both describe the same data and thus contain the same information, the emphasis lies on different aspects. The reciprocal space function naturally represents long-range periodic structures with high definition, whereas the PDF highlights short-range interatomic distances. This phenomenon is a common rule for all Fourier pairs, where a broad signal in one converts to a sharp signal in the other and vice versa.

As indicated, the PDF, which, in the disordered crystalline community, commonly refers to the  $G(r)$  function, can be calculated from the  $F(Q)$  by Fourier transformation according to equation (9).

$$G(r) = \frac{2}{\pi} \int_0^{\infty} F(Q) \sin(Qr) dQ \quad (9)$$

The  $G(r)$  function describes the density of atoms, weighted by their scattering length, and reduced by the average number density of the sample and is therefore also called the reduced distribution function. Accordingly,  $G(r)$  can also be written as equation (10).

$$G(r) = 4\pi r [\rho(r) - \rho_0 \gamma_0(r)] \quad (10)$$

Where  $\rho(r)$  is the atom density, weighted by their scattering lengths,  $\rho_0$  is the average atom number density of the material, and  $\gamma_0(r)$  is a function describing nanoparticle shapes. The  $\gamma_0(r)$  function can be added if applicable, otherwise it is set to one. Two other functions are also commonly named PDFs by other scientific communities. The liquid and amorphous community, for instance, commonly labels the  $g(r)$  function (equation (11)) as PDF, which is otherwise known as the pair density function.

$$g(r) = \frac{\rho(r)}{\rho_0} \quad (11)$$

In addition to that, there is yet another function, called the total pair distribution function  $G_K(r)$  as presented in equation (12). The  $G_K(r)$  function is also occasionally referred to as PDF or simply  $G(r)$ .

$$G_K(r) = \langle b_{coh} \rangle^2 \frac{\rho(r) - \rho_0 \gamma_0(r)}{\rho_0} \quad (12)$$

Two more variations of the  $G(r)$  function exist, which can be found in the literature; the differential correlation function  $D(r)$  and the total correlation function  $T(r)$  which can be derived from the  $G(r)$  function according to equation (13) and (14) respectively.

$$D(r) = \langle b_{coh} \rangle^2 G(r) \quad (13)$$

$$T(r) = \langle b_{coh} \rangle^2 [G(r) + 4\pi r^2 \rho_0] \quad (14)$$

To avoid confusion, a practical way to identify which function is presented, the low and high  $Q$  limits may help. These limits together with a mathematical derivation and additional information on the presented functions can be found in the reviews of Keen[69] and Petersen et al.[70, 71] In this thesis, PDF refers to the  $G(r)$  unless otherwise stated.

As explained earlier, the  $G(r)$  is a real space function, which describes the number of atoms found at a distance  $r$  from any specific atom in the system. Consequently, the peak positions correspond to bond lengths and other distances of atom pairs found in the structure. Whether the atoms are chemically bonded does not change the signal. The peak intensity is dependent on the number of atoms found at the specific distance  $r$  and their scattering length, hence the type of the atom pair. A high degree of disorder leads to a broader distribution of distances for a specific atom pair, thus resulting in a broader peak width. The  $Q_{max}$  value has to be chosen individually for every experiment by the scientist and is determined on the one hand by the maximum  $Q$  space the instrument is able to scan (wavelength, maximum angle ( $Q =$



$4\pi \sin(\theta) / \lambda$ ) and the level of noise in the data. The maximum real space resolution is given as:

$$\Delta r = 2\pi / Q_{max} \quad (15)$$

Thus, for a good resolution, a high  $Q_{max}$  value is required. Hence, an instrument with a short wavelength and large angular range is ideal for total scattering experiments. For x-ray total scattering that typically means, synchrotron radiation is necessary for high-resolution PDFs. The  $Q_{max}$  values typically achievable at these facilities are in the range of 25 – 30  $\text{\AA}^{-1}$ .<sup>[72]</sup> However, for crystalline materials, laboratory x-ray machines with Mo or Ag cathodes and a high angular detection range may be sufficient. The  $Q_{max}$  values are in the range of 17  $\text{\AA}^{-1}$  for Mo cathodes and approximately 22  $\text{\AA}^{-1}$  for Ag cathodes respectively. Note, that the time taken for a total scattering experiment at a laboratory x-ray source is significantly longer than the same experiment at a synchrotron source due to the lower scattering intensity. Neutrons have some intrinsic advantages as a probe for total scattering experiments. The scattering intensity of x-rays is Q-dependent, whereas that of neutrons is not. Therefore, a higher range of measurable scattering angles at comparable wavelengths allows data acquisition with  $Q_{max}$  values up to 50  $\text{\AA}^{-1}$ .<sup>[73]</sup> However, for both x-ray and neutron PDFs, the instrument  $Q_{max}$  is not necessarily the  $Q_{max}$  value applied to the data. The signal-to-noise ratio usually decreases with increasing Q. Therefore, converting reciprocal space data with a high  $Q_{max}$  value often means incorporating a lot of noise, which can have large effects on the real space function. On the other hand, a low  $Q_{max}$  value creates so-called termination ripples, which appear because the Fourier transformation is not performed over the whole Q space. In practice, the result is a convolution of the  $G(r)$  with a sinc function, creating a small oscillation that overlays with the data. Especially for amorphous and highly disordered material, with low-intensity signals, the differentiation between ripples and data can become non-trivial.

#### 1.3.4 Reverse Monte Carlo

The analysis of the real space data can be done by fingerprinting, i.e. comparing the data to a database to identify compounds in the sample. Depending on the sample and data quality, single peak analysis of the first few peaks might be possible as well to extract coordination numbers and geometries by integration. Rietveld-like refinement of the whole function or an extended region of it is also possible. The most commonly used software for this purpose is

PDFgui.[74] As in classical Rietveld refinement, lattice parameters, atomic positions, and thermal displacement factors can be retrieved from the analysis.

Another approach is the analysis by reverse Monte Carlo (RMC) simulation. While traditional Monte Carlo simulations start with a model and predict various properties of a material based on that, the RMC method takes the opposite approach; experimental data, often structural data obtained from techniques like x-ray or neutron diffraction, are used to construct a model, which can reproduce these data. The first step is to create a starting model, which can be refined in the later steps. The starting model should already be as close as possible to the real structure and ideally include all relevant features that characterize the material structure (molecular moieties, density, etc.). From this starting model, a data set, e.g. a diffractogram, is calculated and compared to the experimental data. Next, the atom positions within the model are modified and the diffraction pattern is calculated again. The new pattern is compared to the data and the fit is evaluated. If the modification improves the fit, the move is accepted, if it reduces the fit there is a high chance that the move is rejected. The simulation has to be able to allow some “bad” moves, otherwise it cannot escape local minima. This process is repeated iteratively over many cycles until the structure model can accurately reproduce all data. The method is particularly useful for amorphous and other disordered systems where traditional crystallographic methods cannot provide a complete picture due to the lack of long-range order. The basic principle is not too dissimilar to the Rietveld method, however, instead of using a single unit cell as a representation for the whole structure, the RMC method can handle larger configurations with several thousand atoms. The direct refinement of each atom position gives insights into the local arrangement of these disordered materials. Another advantage is the simultaneous refinement of multiple different data sets. Within this thesis, RMCprofile[75] was used as the software for all RMC simulations. The program allows simultaneous refinement of synchrotron, neutron diffraction as well as EXSAFS data both in reciprocal and real space.

The main challenge of RMC is the large number of refined variables. As mentioned before, the structure models often contain a few thousand up to tens of thousands of atoms with three special coordinates each to be refined. Therefore, even including multiple data sets, the risk of overfitting needs to be reduced as much as possible. For this purpose, the introduction of

meaningful constraints is crucial to avoid unphysical results. The introduction of constraints also allows the inclusion of additional knowledge about the investigated material.

## 1.4 Chemical Analysis

The analysis of the chemical composition is important to confirm the success of the synthesis procedure and allow accurate conclusions from further analysis of the investigated materials. Several techniques are available for this task. For the current work, the relevant techniques are X-ray Photoelectron Spectroscopy (XPS) and Energy Dispersive X-ray spectroscopy (EDX). Other commonly used methods include optical emission spectroscopy or mass spectroscopy.

### 1.4.1 X-ray Photoelectron Spectroscopy

The X-ray Photoelectron Spectroscopy (XPS) analysis is based on the photoelectric effect. When photons hit a substrate, the photon can be absorbed by transferring its energy to an electron in an atomic orbital of an element in the substrate material. If the energy exceeds the binding energy of the electron, this electron is emitted from the surface of the substrate and can be detected. By measuring the kinetic energy of these photoelectrons, the binding energy can be determined, according to equation 16, allowing for the identification of the emitting elements, their chemical environment and oxidation states.

$$E_b = h\nu - (E_k + W) \quad (16)$$

Following the basic principle of energy conservation, the kinetic energy of the electron after ejection from the material surface ( $E_k$ ) equals the photon energy ( $h\nu$ ) minus the binding energy of the electron ( $E_b$ ) and the work function ( $W$ ). The work function describes the energy loss at the surface of the material and corrects for other instrument-related errors. Therefore, the obtained spectra have to be normalised to a reference peak with known binding energy. The method is mainly used for surface analysis as it is surface sensitive because the mean free path of electrons in condensed matter is limited. The mean free path describes the average distance a particle (in this case an electron) can move inside a medium without being scattered or reabsorbed by the medium. Further, some XPS instruments are equipped with an ion gun, which is used for depth profiling by ion polishing of the sample. XPS yields quantitative information on the chemical composition as well as electronic states of the emitting elements. Its applications span across various fields, including nanotechnology, material science, and catalysis, enabling precise and quantitative characterization of surfaces.

## 1.4.2 Scanning Electron Microscopy & Energy Dispersive X-ray Spectroscopy

A somewhat reverse principle is applied when using EDX spectroscopy. In this case, the sample is irradiated by an electron beam, thereby exciting core electrons onto higher energy levels. When the electron relaxes back to the core level, the excess energy is dissipated in form of x-ray photons. The energy of these photons is characteristic for each element as it correlates to their specific energy level dispersion. The same limitations for electron penetration as for XPS also apply to the EDX method, thus EDX is also a surface sensitive method. In addition, the intensity of the signal scales with the number of electrons of the analysed atoms. Therefore, light elements are more difficult to detect.

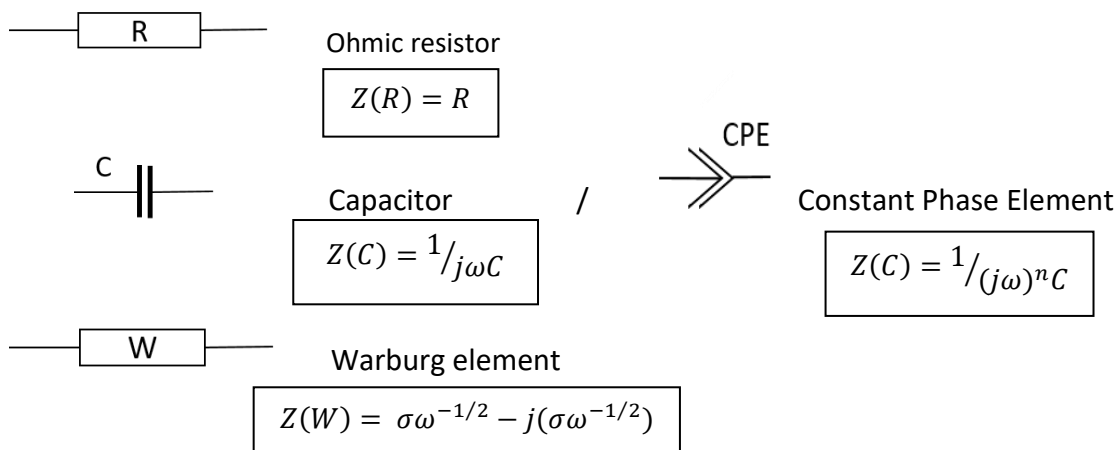
EDX is mostly applied in combination with scanning electron microscopy (SEM) as the electron beam can be used for imaging as well as EDX measurements. The contrast for the imaging is generated either by the detection of secondary electrons or backscattered electrons. Secondary electrons are electrons which are ejected from the material by the primary electron beam. This contrast mode is suitable for studying the morphology of a sample. Backscattered electrons are primary electrons which are backscattered at the sample surface. The intensity of the backscattered electrons scales with the atomic number of the scattering atom, heavy elements scatter more electrons. Therefore, this contrast mode yields information on the chemical composition as heavy elements appear brighter. The combination of the two techniques allows to investigate correlations of chemical composition and morphology and gives insights into the homogeneity of the sample.

## 1.5 Analysis of ion dynamics

### 1.5.1 Impedance spectroscopy

For the electrochemical analysis of a solid electrolyte, the main figure of interest is the ionic conductivity. The most commonly used method to measure conductivity is electrochemical impedance spectroscopy (EIS). The impedance of a material is the vector sum of its complex alternating current (AC) resistance and reactance. The resistance measures the energy loss in the system and contributes the real part of the impedance (mechanical analogue of a damper), whereas the reactance is a measure of the energy stored and released within the system and makes up the imaginary part of the impedance (mechanical analogue of a spring). The reactance is frequency-dependent, whereas the resistance is not. For the measurement, an AC signal is applied to the sample and varied over a set range of frequencies. Two

measurement modes are possible, either a small AC voltage is applied and the current is measured (potentiostatic mode) or a small AC current is applied and the voltage is measured (galvanostatic mode). In most cases both measurement modes yield the same result, only if the material changes due to the applied signal, the results may be different. The output of either periodic, sinusoidal input signal is again a periodic sinusoidal output signal, which may differ in amplitude and phase. The data obtained from these measurements is typically represented in a Nyquist plot, which is a graphical representation of the complex impedance. The imaginary part of the impedance is plotted against its real part (Figure 5 A, D). Another common representation is the Bode plot, which shows the impedance (magnitude, real part,...) and phase angle against the frequency (Figure 5 C, F). For the interpretation of the data, an equivalent circuit model is proposed that is a representation of electrochemical features expressed as electronic components. The most used representations for the testing of battery components are:



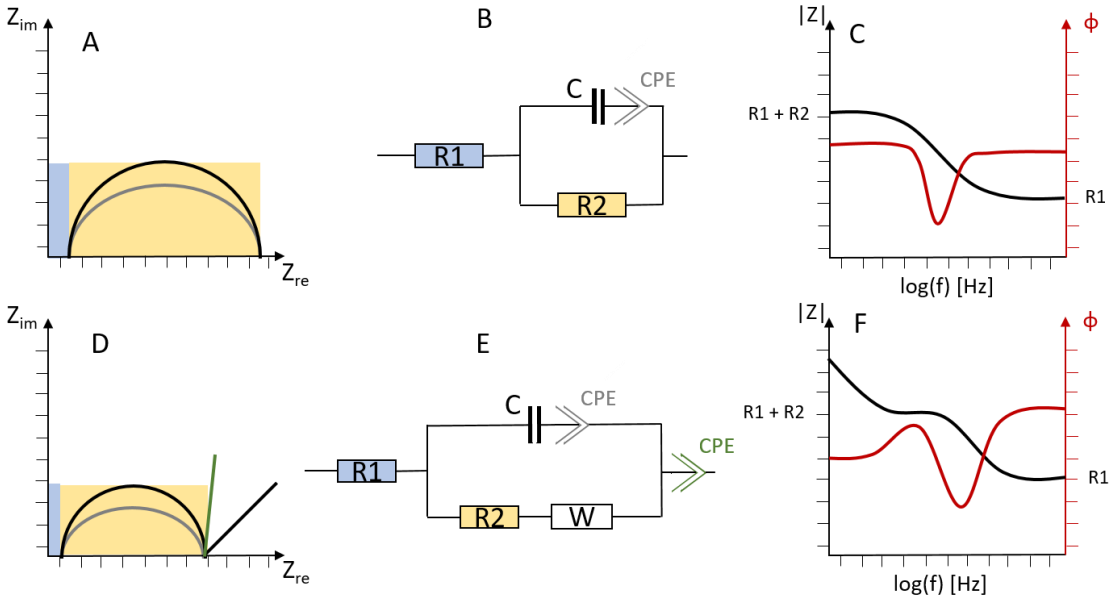
The Ohmic resistor describes the resistance of a material to conduct a current. An Ohmic resistor inside an equivalent circuit only contributes to the real part of the impedance as no energy is stored. The capacitor on the other hand can store and release energy and therefore only contributes to the imaginary part of the impedance. It has a frequency-dependent resistance that increases with decreasing frequency. The constant phase element (CPE) describes an imperfect capacitor and is often used instead as it more accurately describes real systems. The imperfection manifests in a constant shift ( $n$ ) of the phase angle. An ideal capacitor creates a phase shift of  $90^\circ$  whereas the CPE element describes a phase shift of  $90 \pm n$ . The Warburg element describes a diffusion-limited contribution to the impedance. Like

the capacitor, it is also frequency dependent and the impedance increases linearly with decreasing frequencies. However, unlike the capacitor, the Warburg impedance contributes equally to the real and imaginary part of the impedance.

The complexity of the investigated system determines the complexity of the equivalent circuit. A most simple design, which is regularly used for the analysis of solid electrolyte materials, is the Randles circuit as pictured in Figures 5 B and E. In the most simple case, a resistor ( $R_1$ ) is connected to a parallel configuration of another resistor ( $R_2$ ) with a capacitor ( $C$ ) or a CPE. The first resistor ( $R_1$ ) represents all ohmic resistances in the experimental setup except the investigated material, e.g. electrodes sample holder, etc.). This resistor is typically orders of magnitude smaller than the impedance of the solid electrolyte and shifts values on the  $Z'$  (real) axis of the Nyquist plot away from the origin. Starting from this point, the parallel connection of the capacitor with the second resistor creates a semi-circle with the resistance value of the second resistor as the circle diameter. In the case of a non-ideal capacitive behaviour (CPE), the semicircle shape is attenuated (or depressed) (grey lines in Figure 5 A and D). In that case, the impedance response is best fitted with a CPE element. The semicircle in the Nyquist plot appears due to the frequency-dependent impedance of the capacitor. At high frequencies, the capacitor has a low Impedance, consequently, the current in the equivalent circuit would pass the capacitor. As the frequency decreases, the capacitor impedance increases and so does the imaginary part of the impedance in the Nyquist plot. At the same time, an increasing amount of current can pass the resistor as the capacitors impedance approaches the resistors resistance. Hence, also the real part of the impedance increases. At the top of the semicircle, the two impedances are equal. This point is called the relaxation frequency. At low frequencies, the capacitor impedance is far greater than the resistor resistance, thus, all current passes the resistor. The end of the semicircle therefore corresponds to the combined resistances of both resistors ( $R_1 + R_2$ ). In the Bode plot, the combined resistor resistances  $R_1 + R_2$  can be read off the Y-axis at low frequencies and  $R_1$  at the plateau at high frequencies. The inflexion point, which is also marked by the peak in the phase angle curve (red curve in Figures 5 C and F), corresponds to the relaxation frequency. Because this point is dependent on the ohmic resistance of the resistor as well as the capacitance of the capacitor, a change in either or both values will shift the two curves in the Bode plot to different frequency values.

A commonly used extension of the Randles cell includes a Warburg element (Figure 5 E) to account for any diffusion-related processes. This element is more often found in

representations of cells with liquid electrolytes. In the Nyquist plot, the Warburg element manifests as a straight line angled at 45° to the real axis. Similarly, the behaviour at low frequencies changes in the Bode plot. For testing of solid electrolytes under blocking conditions (ions cannot diffuse into the electrode) the low-frequency behaviour is also a straight line with a larger angle to the x-axis, which is usually modelled by another CPE and explained by the capacitive behaviour due to electrode polarization.[76]



5: Examples for two simple equivalent circuits used in battery analysis (Randles cell (B), diffusion extended Randles cell (E)) and their representation as Nyquist (A, D) and Bode (C, F) plots.

In real systems, the situation is usually more complicated. Often a stack of different material layers or a material mix is analysed. In theory, a strength of EIS is the possibility to analyse multiple conduction processes in one measurement because every part of the sample contributes a semicircle in the Nyquist plot with a size according to the resistance of the specific process. The equivalent circuit in that case would be a series of simple Randles cells. In practice, however, these semicircles are not always resolved nicely. If the time constant,  $\tau$  is too similar for each Randles cell, the superposition of multiple semicircles might result in one larger semicircle, allowing only the analysis of the combined resistance. The time constant  $\tau$  is defined as the product of the resistance and the capacitance of the circuit (equation 17). Phenomenologically,  $\tau$  is a measure for the time it takes to charge and discharge the capacitor in the Randles cell model, ergo the time scale on which the conduction process takes place.

$$\tau = R \cdot C \quad (17)$$

For crystalline SEs for instance, a frequently discussed issue is the differentiation of bulk conductivity and grain boundary conductivity. Although grain boundaries are known to affect the total conductivity of the sample, the impedance measurement may not be able to differentiate between the two. In some instances, temperature-dependent measurement can be a way to overcome this problem. Especially at low temperatures different activation energies lead to increasingly different kinetics, revealing additional features in some systems.

After fitting the data, the conductivity of the sample can be calculated from the acquired resistances according to equation 18.

$$\sigma = \frac{1}{R} \cdot \frac{d}{A} \quad (18)$$

Where  $\sigma$  is the conductivity,  $R$  is the resistance,  $d$  is the thickness, and  $A$  the area of the sample.

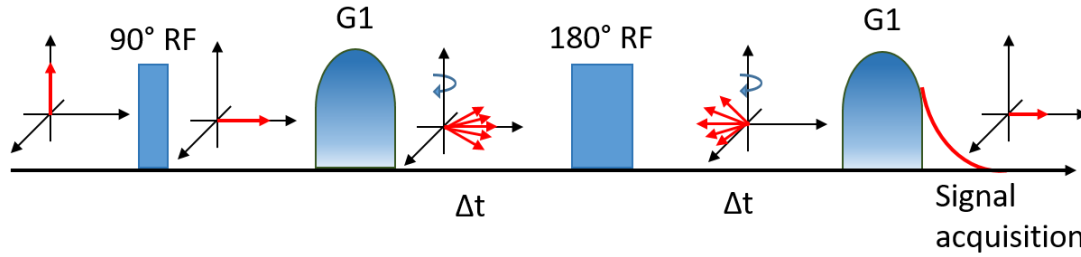
### 1.5.2 Nuclear Magnetic Resonance Spectroscopy

NMR spectroscopy can also be utilised to probe ion dynamics. In contrast to EIS, which analyses the dynamics across the whole sample, the length scales observed by NMR can vary from a few Angstrom to several hundred nanometers. Several different NMR techniques are available, for the current work, two techniques have been utilised to analyse the samples.

Pulsed field-gradient (PFG) NMR is used to investigate dynamics on a scale of typically a few hundred nanometers. The basic principle is the same as for classical NMR explained on pages 21/22. However, as the name suggests, a small gradient magnetic field is applied additionally to the homogenous field. The gradient essentially marks the position of each investigated atom in the sample because the local magnetic field around the atom depends on its position within the gradient. The pulse sequence for a PFG-NMR experiment starts with a 90° RF pulse. Next, a pulsed gradient magnetic field is applied, which dephases the nuclear spins depending on their position in the sample. After a certain time ( $2 \times \Delta t$ ), another gradient field is pulsed with the same strength and duration as the first. In between the two gradient pulses, a 180° pulse can be applied to reduce the intensity loss due to  $T_2$  relaxation, which is the normal dephasing of spins in the x-y plane over time without a gradient. This second gradient realigns the spins if the atoms have remained at the same position. If the atoms have moved during the time between the two gradient pulses, the full magnetisation cannot be restored because



the local field at the moving atoms changed between the first and the second pulse. From the decreasing signal intensity with increasing gradient strength, the diffusion coefficient can be calculated. A schematic representation of this pulse sequence is drawn in Figure 6.

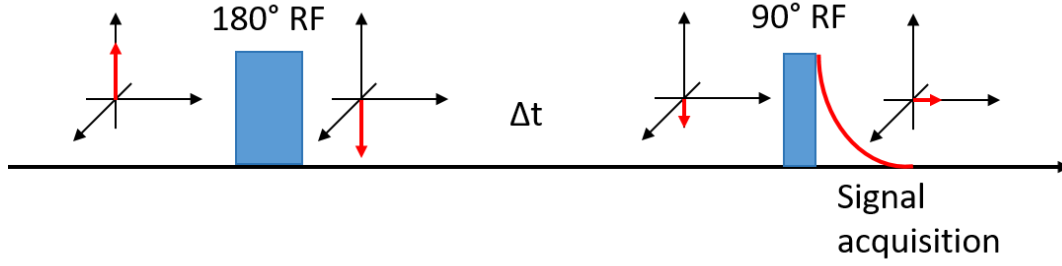


6: Example of a simple pulse sequence for PFG-NMR experiments. Red arrows represent the magnetisation vectors.

Spin-lattice, or  $T_1$  relaxometry is another NMR technique, which is used to investigate dynamics. Contrary to the PFG-NMR, the  $T_1$  relaxometry probes the local hopping of ions or molecules on an Å length scale. The  $T_1$  relaxation describes the time needed for the magnetic moment of the nuclear spins to realign with the external field after perturbation by an RF pulse. The realignment requires the dissipation of the energy correlated with the spin “flip”. This energy dissipation mostly happens due to interaction with the lattice, hence, the  $T_1$  relaxation is also called spin-lattice relaxation. These spin-lattice interactions are proportional to the hopping rate of the investigated atoms if  $\tau^{-1}$  is of the order of  $\omega_L$  as described by Bloembergen, Purcell, and Pound[77] (see equation (19)).

$$T_1^{-1} \sim \left( \frac{\tau}{1 + \omega_L^2 \cdot \tau^2} + \frac{4\tau}{1 + 4\omega_L^2 \cdot \tau^2} \right) \quad (19)$$

Where  $\omega_L$  is the Larmor frequency and  $\tau$  is the correlation time, ergo the inverse of the hopping rate. In order to measure the  $T_1$  relaxation, a 180° RF pulse is applied first to achieve an inversion of the spin states. After a certain time  $\Delta t$ , a 90° pulse is applied and the NMR signal is detected. During the time  $\Delta t$ , the spins start to relax, thus the magnitude of the magnetisation after the 90° pulse is reduced and the detected magnetisation depends on the time given between the two pulses  $\Delta t$  and the relaxation time  $T_1$ . A scheme of the pulse sequence with the according change of the macroscopic magnetisation vector (red arrow) is displayed in Figure 7.



7: Example of a simple pulse sequence for  $T_1$  relaxometry experiments. Red arrows represent the magnetisation vectors.

From the hopping rate, the diffusion coefficient can be estimated using the distance between neighbouring atom sites  $l$  in the crystal lattice retrieved from a structure model according to equation (20).

$$D = \frac{l^2}{6\tau} \quad (20)$$

Both NMR techniques yield a diffusion coefficient  $D$ , which can then be converted into a conductivity by applying the Nernst-Einstein equation (equation (21)).

$$\sigma = \frac{D \cdot N \cdot q^2}{k_B T} \quad (21)$$

Where  $\sigma$  is the conductivity,  $N$  is the concentration of moving atoms and  $q$  is their charge. Similar to the EIS experiments, the NMR techniques are theoretically able to differentiate between different conduction processes given that these processes have sufficiently different activation energies and/or dynamics.

The combination of experiments probing long and short-range dynamics can help to interpret data and understand transport mechanisms. All of the above-mentioned experiments (EIS, PFG-NMR,  $T_1$  relaxometry) can be conducted at a series of different temperatures to extract activation energies  $E_A$ . The relationship between the activation energy of a thermally activated process and its rate constant (the conductivity in this case) is described by the Arrhenius equation (equation (22)).

$$\sigma = \frac{\sigma_0}{T} \cdot e^{-\frac{E_A}{k_B T}} \quad (22)$$

Where  $E_A$  is the activation energy and  $\sigma_0$  is a constant. By bringing this equation into its logarithmic form (equation (23)), it is easy to see that the logarithm of the conductivity is

linearly related to the inverse temperature. When plotted, the activation energy can be read off the slope of the resulting plot.

$$\ln(\sigma T) = \ln(\sigma_0) - \frac{E_A}{k_B} \cdot T^{-1} \quad (23)$$

## 2 Motivation

Despite extensive research in recent years, the conduction mechanism in SEs is not yet fully understood, posing a significant challenge in the development of ASSBs. Ongoing research in material design, interface engineering, and synthesis methods is critical to harness the full potential of these materials in practical battery applications. Especially the connection between crystal structure and ionic conductivity needs to be further examined to enable purposeful material development.

Due to the comparatively simple composition,  $\text{Li}_3\text{PS}_4$  is a suitable model system to investigate Li-ion conduction in thiophosphates. However, the spread of reported conductivity values hinders meaningful comparisons and leads to contradicting claims. Hence, a deeper understanding of the underlying structure-property relationships is needed to understand the discrepancies in the literature and enable further development of materials and understanding of conduction mechanisms.

This thesis aims to provide new insights into structure-property relationships in Li thiophosphate glasses and glass ceramics, with a focus on the oxygen-substituted 75/25 LPS systems to understand the tangible influence of oxygen substitution on the material structure and link structural evolution to the ionic conductivity. Different synthesis routes and parameters will be evaluated. The product materials will be examined carefully with a variety of analytical methods to obtain full structural information. State-of-the-art x-ray diffraction techniques like PDF analysis are useful tools to investigate amorphous and disordered structures. Spectroscopy techniques like MAS-NMR and Raman add information on the chemical environment. All this information is used to find a suitable structure model, which is further refined using computational techniques like RMC modelling, resulting in a better understanding of the materials composition and structure. Further, the ionic conductivity is studied by EIS and PFG-NMR to obtain information on the ion mobility on different length scales. In the second chapter, the crystallisation behaviour of the oxy-sulfide glasses and the effects on their ionic conductivity are studied to help answer the question of whether, and how temperature treatment steps should improve the SEs properties. Finally, the mechanochemical synthesis process is optimised, reducing time and energy costs whilst improving the performance and widening the range of available products.

## 3 Results and Discussion

### 3.1 The influence of oxygen substitution on the atomic structure and ionic conductivity of Li oxy-sulfide glasses

Although oxygen substitution is a known strategy to improve the chemical stability of Li thiophosphates the tangible effect of oxygen on the material structure remains unknown. Previous reports agree on the beneficial impact of oxygen substitution on the chemical stability. However, the influence on the conductivity is still under debate with contradicting results being published.

Various studies have documented the successful creation of oxy-sulfide glasses and glass ceramics under diverse reaction conditions and with different precursors.  $\text{Li}_3\text{PO}_4$  and  $\text{Li}_2\text{O}$  are two common precursors for introducing oxygen, differing primarily in the oxygen incorporation mechanism.  $\text{Li}_3\text{PO}_4$  already consists of tetrahedral units similar to the thiophosphate structure, while in the case of  $\text{Li}_2\text{O}$ , these tetrahedra are generated during the synthesis process. The synthesis of Li-oxysulfide glasses encompasses a broad range of methods, including solvent-assisted wet chemical synthesis, high-temperature solid-state synthesis, and mechanochemical synthesis using a ball mill, each offering adjustable parameters. The vast variety of available synthesis routes (including different methods, adjustable parameters, and precursors) has led to unclear correlations in research findings, revealing varying effects of oxygen substitution on conductivity. Some studies indicate a small enhancement of conductivity at minimal oxygen levels, while others note a consistent decline. Additionally, the reported conductivity figures and ideal compositions vary widely. For instance, Takada et al. achieved enhanced conductivity in  $(1-x)\text{Li}_3\text{PS}_4-x\text{Li}_3\text{PO}_4$  for up to 20 %  $\text{Li}_3\text{PO}_4$  using a quenching method.[50] Huang et al. found the highest room-temperature conductivity in amorphous powders of  $0.7\text{Li}_2\text{S} (0.3 x)\text{P}_2\text{S}_5-x\text{Li}_3\text{PO}_4$  prepared via high-energy ball milling at only  $x = 1$  mol %.[78] Similarly, Mo et al. also observed improvements in ionic conductivity, electrochemical stability, and cyclability in a  $0.95(0.7\text{Li}_2\text{S}-0.3\text{P}_2\text{S}_5)-0.05\text{Li}_3\text{PO}_4$  glass electrolyte by doping with  $\text{Li}_3\text{PO}_4$ .[79] Phuc et al. reported enhanced conductivity in  $\text{Li}_3\text{PS}_4-x\text{Li}_3\text{PO}_4$  prepared by liquid-phase synthesis over pure  $\text{Li}_3\text{PS}_4$ , again with the best performance at  $x = 1$  mol %.[80] Conversely, Trevey et al. and Tsukasaki et al. noted a decrease

in conductivity with partial substitution of  $\text{Li}_2\text{S}$  by  $\text{Li}_2\text{O}$  in their studies using mechanochemical syntheses.[27, 45]

Despite these advancements, there's a noted absence of in-depth structural analysis on how oxygen substitution alters the thiophosphate structure, even though existing research on pure  $\text{Li}_3\text{PS}_4$  suggests a significant influence of atomic structure on ion conductivity.[81, 82] The divergent outcomes underline the necessity of understanding structure-property relationships for a targeted material design. This chapter describes the systematic investigation of O-substituted Li-thiophosphate compounds prepared by mechanical milling, to elucidate the tangible influence of Oxygen on the atomic structure.

### 3.1.1 Experimental

$(3-x)\text{Li}_2\text{S} + x\text{Li}_2\text{O} + \text{P}_2\text{S}_5$  ( $0.8 \leq x \leq 2.4$ ) oxy-sulfide glasses (LIO series) were prepared by high energy ball milling in a planetary micro mill Pulverisette 7 Premium line (Fritsch, Germany). Appropriate amounts of  $\text{Li}_2\text{S}$  (Sigma-Aldrich, 99.98 %),  $\text{Li}_2\text{O}$  (Alfa Aesar, 99.5 %), and  $\text{P}_2\text{S}_5$  (Sigma-Aldrich, 99.9 %) powders with a total mass of 2 g were weight and filled in a 45 mL  $\text{ZrO}_2$  milling jar together with 75 g of 3 mm  $\text{ZrO}_2$  grinding balls. All steps up to this point were done in an Ar-filled glovebox to prevent oxidation of the materials. The milling protocol for samples was 540 cycles of 5 min milling + 15 min cooling break (7.5 d total time sped in the ball mill) after every 72 cycles (24 h) the jars were removed from the mill and opened inside the glovebox to scrape of baked powder from the side of the walls of the jar. The chunks were ground in the mortar and then returned to the jar.

LPS/LPO mixed powders (MM series) were prepared by mixing  $\text{Li}_3\text{PS}_4$  from the ball milling procedure explained above with  $\text{Li}_3\text{PO}_4$  (Sigma-Aldrich, 99.98 %) in an agate mortar for 15 min.

Scanning electron microscopy (SEM) images were captured using a Zeiss Merlin microscope (ZEISS SMT AG, Germany) operating at an acceleration voltage of 5 kV. Accompanying energy-dispersive X-ray spectroscopy (EDX) analyses were conducted with a 60 mm<sup>2</sup> XFlash detector (Bruker, Germany) integrated into the SEM system. Samples were transferred with an airtight transfer shuttle to prevent oxidation.

X-ray photoelectron spectroscopy (XPS) analyses were conducted using a K-Alpha spectrometer (ThermoFisher Scientific, UK), which features a micro-focused, monochromatic Al  $K_\alpha$  x-ray source ( $\lambda=1486.6$  eV) with a spot size of 400  $\mu\text{m}$ . To mitigate localised charge build-

up during these analyses, a charge neutralization system utilizing 8 eV electrons and low-energy argon ions was implemented. The Thermo Advantage software facilitated both data collection and analysis, adhering to methodologies outlined by Parry et al. (2006).[83] Quantitative assessments incorporated the analyzer's transmission function, Scofield sensitivity factors, and calculations of effective attenuation lengths for photoelectrons, following the approach by Scofield (1976).[84] The TPP-2M formalism was used to calculate effective attenuation lengths.[85] Calibration of all spectra was performed against the carbonaceous C 1s peak at a binding energy of 285.0 eV.

X-ray diffraction (XRD) patterns were gathered using an STOE Stadi P powder diffractometer (STOE & Cie GmbH, Germany) which was equipped with a Mythen1K detector and utilised Mo  $K_{\alpha 1}$  radiation ( $\lambda = 0.70932 \text{ \AA}$ ). The measurements were performed in Debye-Scherrer geometry and the samples were filled in 0.5 mm glass capillaries.

Total scattering experiments were carried out at the high-resolution powder diffraction beamline (P02.1) at PETRA III (DESY), utilizing synchrotron radiation at a photon energy of 60 keV ( $\lambda = 0.2073 \text{ \AA}$ ). 1 mm capillaries were used for the measurements. A Varex area detector, positioned 300 mm from the sample, was used to record the diffraction patterns. An empty capillary underwent measurement in identical conditions to allow for the removal of background contribution. In order to calibrate the instrument resolution, LaB<sub>6</sub> (NIST660c) was also measured. The pair distribution function (PDF) was then derived using PDFgetX3, with a maximum Q value of  $27 \text{ \AA}^{-1}$ . The dampening factor  $Q_{\text{damp}}$  was set at  $0.028 \text{ \AA}^{-1}$ , ascertained by fitting the LaB<sub>6</sub> PDF with PDFgui. The fitted parameters were: scale factor, lattice parameters, isotropic atomic displacement parameters, and particle diameter.

Raman spectra were obtained using a LabRAM HR Evolution spectrometer (HORIBA Scientific, Japan), employing a 50x magnification lens, an excitation wavelength of 632.8 nm, and a grating of 600 g/mm. Measurements were conducted on samples enclosed in sealed glass capillaries with a 0.7 mm diameter. Baseline correction and normalization were done through the Horiba LabSpec 6 software.

<sup>31</sup>P magic-angle spinning (MAS) nuclear magnetic resonance (NMR) spectra were acquired using an Avance 500 MHz spectrometer (Bruker, Germany) at an 11.7 T magnetic field, corresponding to a 202.5 MHz resonance frequency. The powder samples were loaded into a 2.5 mm ZrO<sub>2</sub> MAS rotor within an argon-filled glovebox, with subsequent measurements

conducted at a 30 kHz spinning speed. Data collection was facilitated through a rotor-synchronised Hahn-echo pulse sequence. The  $^{31}\text{P}$  chemical shift was calibrated against  $\text{H}_3\text{PO}_4$  (85%, 0 ppm).

The temperature-dependent  $^7\text{Li}$  pulsed-field gradient (PFG) NMR measurements were performed on a Bruker Avance spectrometer at a magnetic field of 7.05 T. The maximal gradient strength of the diffusion probe head is 30 T/m. A stimulated-echo pulse sequence was used for the detection.[86] The gradient duration and the diffusion time were set to 2 ms and 400 ms. The recycle delay was always well above five times the spin-lattice relaxation time. All samples were measured in 5 mm evacuated borosilicate glass tubes.

Temperature-dependent  $^7\text{Li}$   $T_1$ -relaxation time measurements were performed on a Bruker Avance 200 MHz spectrometer at a magnetic field strength of 4.7 T. The samples were sealed in evacuated borosilicate glass tubes. The data was acquired with an inversion recovery and solid echo pulse sequence. The recycle delays were always well above  $5 \cdot T_1$ .

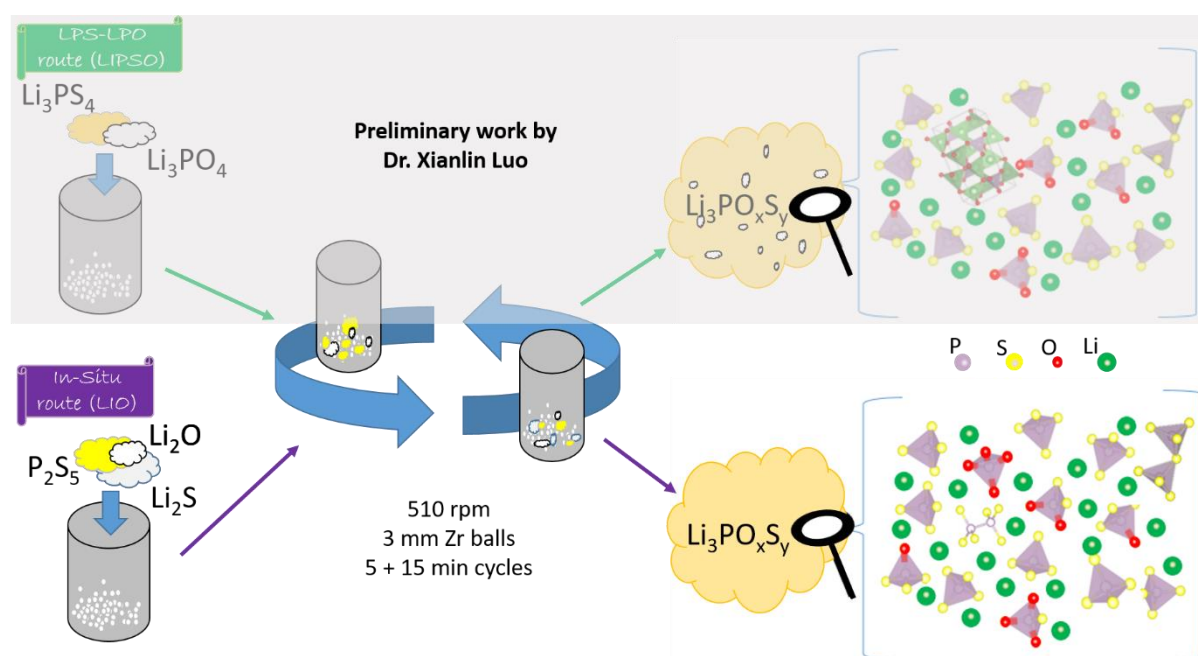
EIS measurements were conducted in a CompreDrive (Rhd instruments GmbH & Co. KG, Germany), using a 6 mm CompreCell with an  $\text{Al}_2\text{O}_3$  core. The sample powder was filled into the cell in an argon-filled glovebox. The powder was pressed inside the CompreDrive with a pressure of 400 MPa for 130 s. If not stated otherwise, the measurements were done under blocking conditions (WC electrodes) under 100 MPa of pressure.

### 3.1.2 Synthesis

Li oxysulfide glasses were synthesised as described in the experimental section above using  $\text{Li}_2\text{S}$ ,  $\text{Li}_2\text{O}$ , and  $\text{P}_2\text{S}_5$  as precursor materials. The products were thoroughly analysed regarding chemical composition, atomic structure, and ionic conductivity. In order to investigate the influence of precursor materials on all of these properties, the results were compared to previous experiments by Dr. Xianlin Lou, where  $\text{Li}_3\text{PS}_4$  and  $\text{Li}_3\text{PO}_4$  were used as precursors.[44] To ensure comparability between the two experiment sequences, all experimental procedures and synthesis parameters were chosen according to the experiment sequence done by Dr. Lou. A critical distinction between the previous experiments, termed LIPSO series, and the current sequence, termed LIO series, is that in LIPSO, the end structural units such as  $[\text{PS}_4]^{3-}$  or  $[\text{PO}_4]^{3-}$  tetrahedra are pre-existing in the reactants. In contrast, these tetrahedra must form during the synthesis process in the LIO approach, as mentioned in the introduction. A



schematic representation of these two approaches is provided in Figure 8. Given the higher bond energy of P–O compared to P–S, the  $[\text{PO}_4]^{3-}$  unit is predicted to be the most thermodynamically stable tetrahedron within the  $\text{PS}_x\text{O}_{4-x}$  series, suggesting a lower tendency for O to S substitution in the LIPSO sequence. On the other hand, in the LIO sequence, as all phosphorus atoms are initially linked to sulfur, this might facilitate a simpler substitution of S with O, potentially resulting in more varied  $\text{PS}_x\text{O}_{4-x}$  tetrahedral structures at lower oxygen concentrations. In the following, the analysis results for the LIPSO series as published by Lou 2022[44] will be compared to the analysis results for the LIO series acquired in this work. For the readers convenience, both datasets will be presented here. To avoid confusion all results, that were not acquired within this thesis are marked by grey boxes.



8: Schematic overview of the two compared synthesis routes.

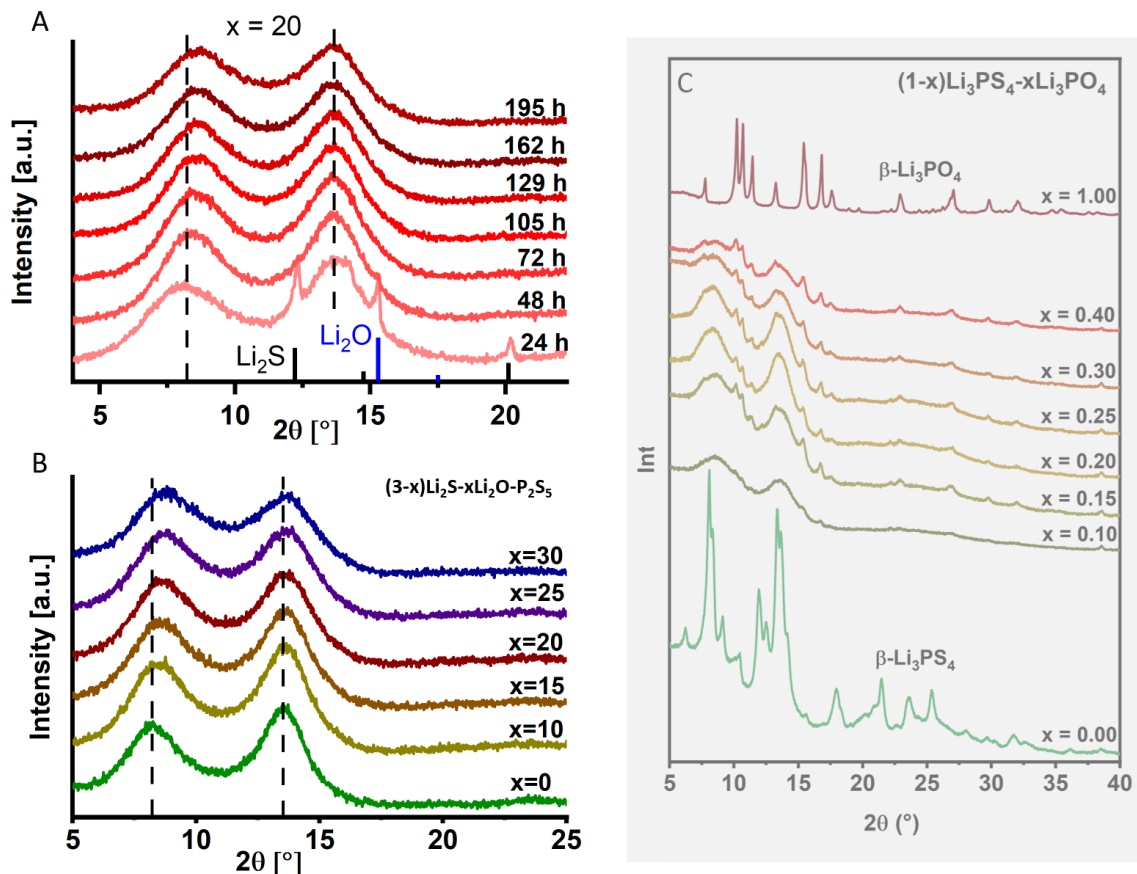
Within the composition range;  $(3-x)\text{Li}_2\text{S} + x\text{Li}_2\text{O} + \text{P}_2\text{S}_5$  ( $0.8 \leq x \leq 2.4$ ), six different samples with varying oxygen concentrations were synthesised, as summarised in Table 1. Five samples with oxygen concentrations of 10–30 %, corresponding to the LIPSO samples, and one sample with lower oxygen substitution of 3.75 % which is equal to the substitution level for which Machida et al. found an increased conductivity compared to the pristine LPS.[46] The stoichiometry containing 40 % oxygen substitution is not accessible using  $\text{Li}_2\text{S}$ ,  $\text{Li}_2\text{O}$  and  $\text{P}_2\text{S}_5$ . Additionally, one reference sample of pure LPS without any oxygen substitution was synthesised under the same conditions.

Table 1: Overview over LIO samples.

Sample ID	Stoichiometry	Oxygen substitution level [%]
LIOref	$\text{Li}_3\text{PS}_4$	0
LIO0	$\text{Li}_3\text{PO}_{0.15}\text{S}_{3.85}$	3.75
LIO1	$\text{Li}_3\text{PO}_{0.4}\text{S}_{3.6}$	10
LIO2	$\text{Li}_3\text{PO}_{0.6}\text{S}_{3.4}$	15
LIO3	$\text{Li}_3\text{PO}_{0.8}\text{S}_{3.2}$	20
LIO4	$\text{Li}_3\text{POS}_3$	35
LIO5	$\text{Li}_3\text{PO}_{1.2}\text{S}_{2.8}$	30

The synthesis progression was monitored by XRD measurements. The measurements were conducted each time the jars were opened to loosen baked powder (every 24 or 33 h). The diffractograms exhibit two broad humps around 6.5 to 10 and 11.5 to 15 two theta, which correspond to the positions of the main reflexes of  $\text{Li}_3\text{PS}_4$  (see Figure 9 C). The humps thus indicate an amorphous phase with structural similarities to  $\text{Li}_3\text{PS}_4$ . Similarities to one of the three polymorphs cannot be deduced from the XRD, because their respective diffractograms have their main peaks in the same region. On top of these humps, sharp reflections are visible for short milling times, which can be assigned to the precursor materials  $\text{Li}_2\text{S}$  and  $\text{Li}_2\text{O}$ . After 24 h these sharp reflections of the precursor materials were visible in all samples. However, with increasing milling time, the reflections gradually disappear. Most reflections vanish after about 72 h of total milling time, after approximately 129 h no evidence of starting material can be found by XRD in any of the samples. As XRD is only capable of detecting crystalline compounds of a certain minimum size, the milling continued up to 195 h of total time spent in the ball mill to ensure a complete reaction of all precursor material and keep synthesis procedures close to the LIPSO series. An example of this structural evolution with milling time, monitored by XRD, is presented for the sample LIO3 ( $x = 1.6$ ) in Figure 9 A. The data on all other samples can be found in the Appendix Figure 42.

The amorphous fraction underwent some evolution. The first hump shifts slightly to higher angles with increasing milling time as indicated by the dashed lines in Figure 9 A. The shift indicates a compression in the structure, which can be attributed to the incorporation of



9: X-ray diffractograms of LIO3 ( $x = 20$ ) at progressing time steps during ball milling synthesis (A) and all LIO samples after 195 h total milling time (B). Diffraction patterns of the LIPSO series for comparison (C) reprinted with permission from [44].

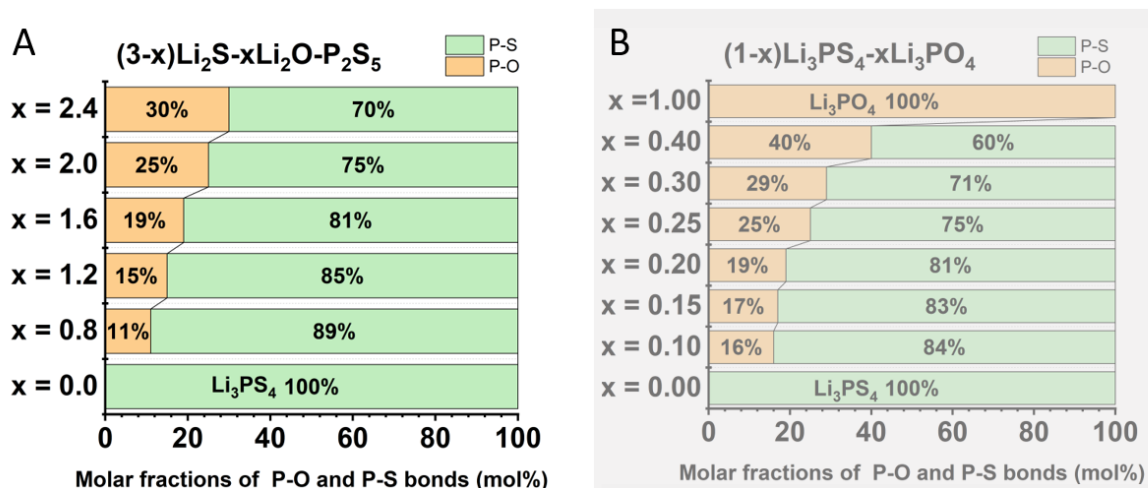
oxygen into the amorphous matrix. The P – O bond is shorter than the P – S bond (2.05 Å and 1.54 Å respectively), therefore, the structure contracts as more and more oxygen is incorporated. Consequently, the finding suggests that the thiophosphate phase is created first and then reacts with the  $\text{Li}_2\text{O}$ . If  $\text{Li}_2\text{O}$  was the first to react, an oxygen-rich phase should appear at short milling times, which would then be diluted by reaction with  $\text{Li}_2\text{S}$ . The consequence of this scenario, however, would be a shift of the humps in the opposite direction as an increasing amount of P – S bonds would inflate the structure.

A similar evolution of the diffractograms can be observed when comparing the different samples after 195 h of total milling time. With increasing oxygen concentration, the amorphous signal shifts to higher angles. Moreover, the width of the humps increases with increasing oxygen content, indicating a higher degree of disorder for highly substituted compounds. The added uncertainty on the bond lengths due to oxygen substitution is the most likely explanation for the increasing disorder. For the LIPSO series, similar patterns have been reported. [44] The main difference is the persistence of crystalline  $\text{Li}_3\text{PO}_4$  even after a total milling time of 180 hours when  $\text{Li}_3\text{PS}_4$  and  $\text{Li}_3\text{PO}_4$  are used as precursor materials. For the

sake of comparison, the diffractograms of the LIPSO series together with diffractograms of crystalline LPS and LPO are reprinted in Figure 9 C. Besides the LPO reflections, the amorphous signal is almost identical. Broadening is noticeable in both the LIPSO and LIO series, but the shift towards higher angles is more marked in the LIO series. The more noticeable contraction could signify a more effective mixing of different  $PS_xO_{4-x}$  tetrahedral forms in the LIO series as compared to the LIPSO experiments.

The LIPSO diffraction data was analysed again using Rietveld refinement to extract the crystallite size of the remaining LPO crystals. The amorphous LPS phase was excluded from the refinement and instead treated as part of the background. The analysis revealed that the crystallite size experiences a minor increase from 10 to 15% LPO content, moving from 23 to 49 nm, and then gradually declines to 17 nm for the sample with 40% LPO. All refinement plots can be viewed in the appendix (Figure 45).

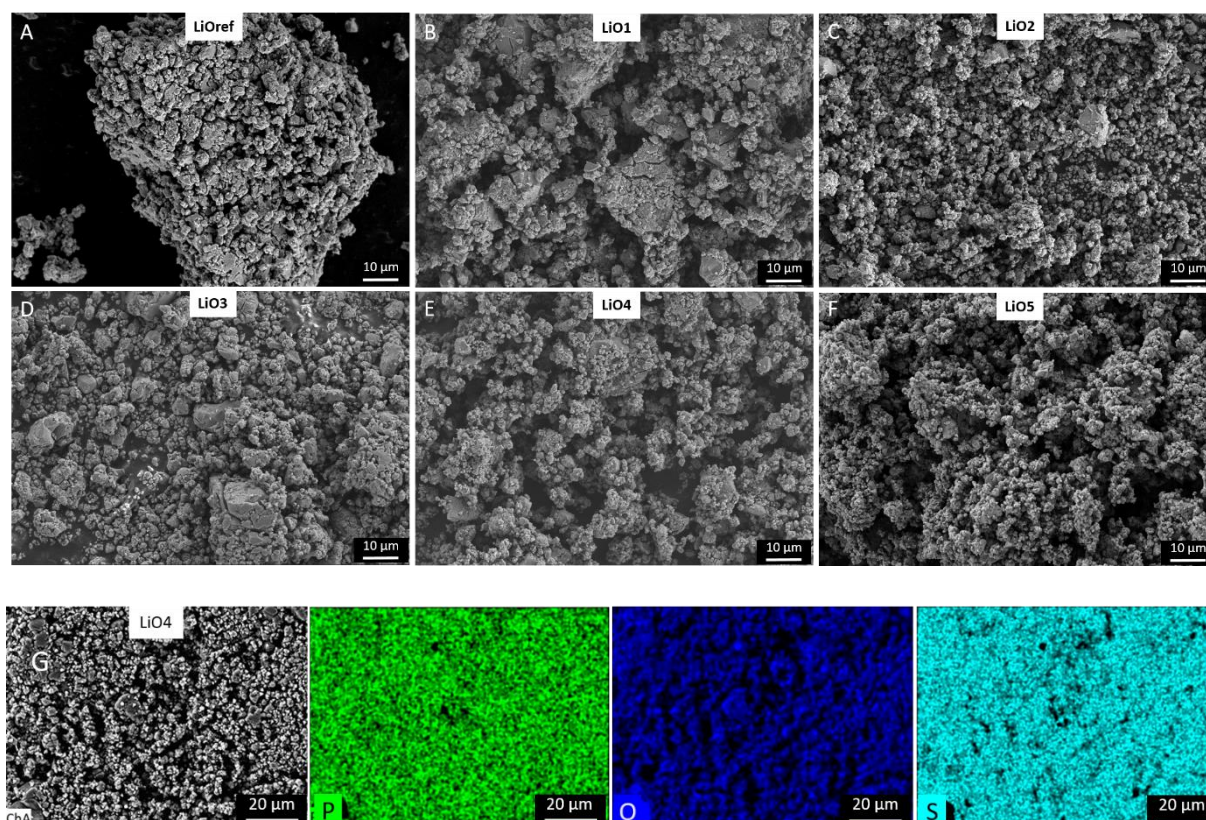
XPS analysis was performed on all samples to confirm the chemical composition. To accurately measure oxygen levels, high-resolution P 2p spectra were acquired from both the starting materials and oxy-sulfide mixtures. The stoichiometry matches the desired compositions, as depicted in Figure 10 A, ensuring that the synthesis was successful and the LIO samples are indeed comparable to the LPSO samples (Figure 10 B) in terms of total oxygen concentration.



10: fraction of P - S and P - O bonds calculated from XPS analysis for LIO samples (A) and LIPSO samples (B). B is reprinted with permission from [44].

Next, SEM was applied to study the morphology and particle size of the materials. All samples exhibit broad particle size distributions with sizes ranging from a tenth of a micrometre down into the sub-micrometre range, as seen in Figure 11 A-F. With increasing oxygen content, there is a tendency towards smaller particle sizes, most likely due to the hard Li<sub>2</sub>O crystals

adding to the comminution process. However, overall, the chemical composition does not seem to significantly influence the particle size or morphology. EDX measurements further confirm the homogenous distribution of all elements in the samples, proving an intimate mixing of reactants. Figure 11 G displays EDX mapping of phosphorous (green), oxygen (blue), and sulphur(cyan) on the sample with 25 % oxygen substitution. EDX maps of all samples can be viewed in the appendix Figure 44.

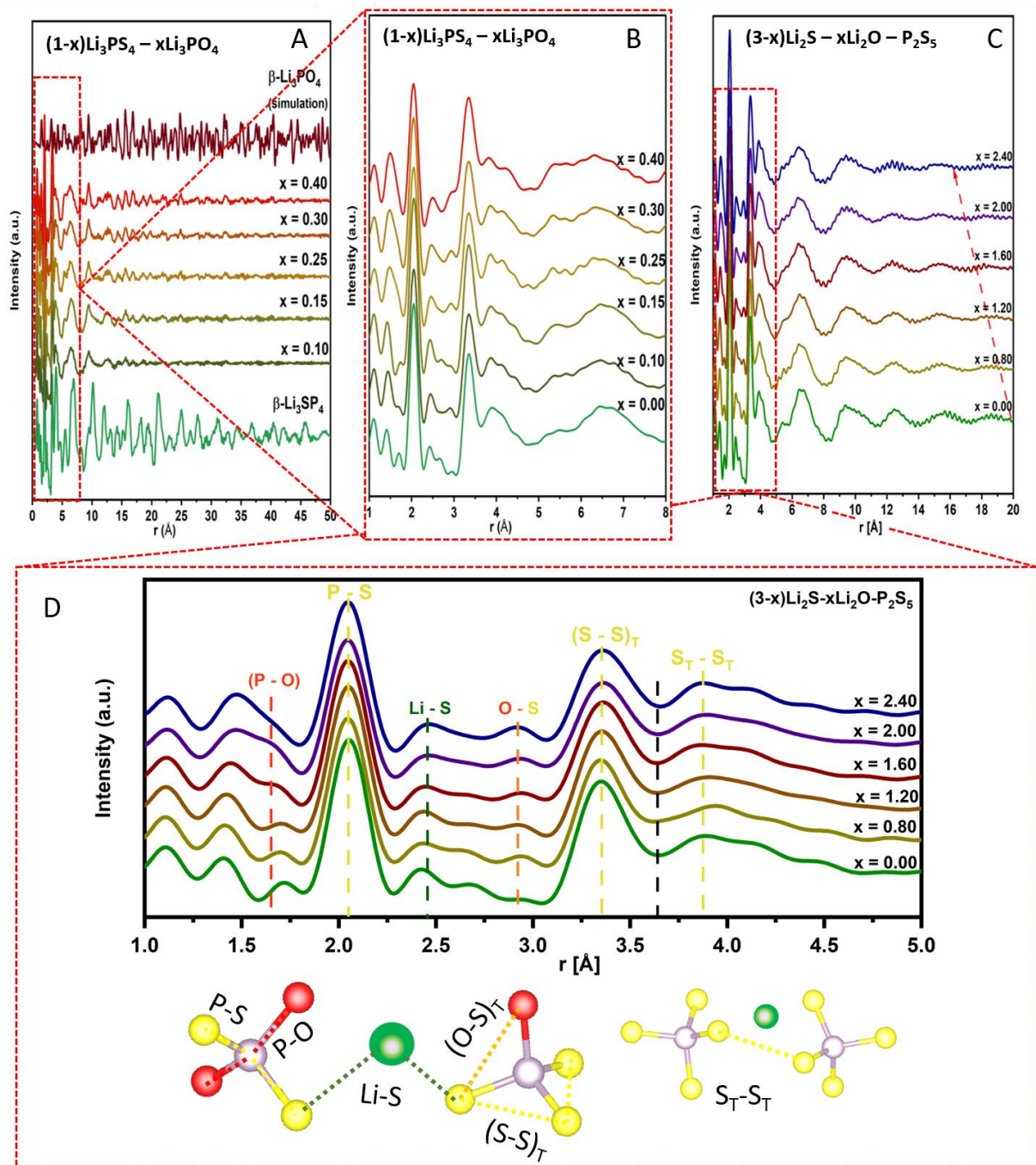


*11: SEM of all LIO samples (A-F) and EDX maps of P(green), O(blue) and S(cyan) for LIO4 (G).*

### 3.1.3 Structure Analysis

Up to this point, the chemical composition and average structure were investigated, giving some idea about the reaction mechanism and already showing discrepancies between LIO and LIPSO series. However, to understand how oxygen is incorporated, the focus of the analysis needs to be on the local structure of these materials.

Various analytical techniques were utilised for a comprehensive understanding of the structure on the atomic scale. Pair distribution function (PDF) analysis stands out as a powerful method for analysing the local structure of both crystalline and amorphous substances. Total scattering data for all samples from the LIO, as well as LIPSO series (except LIPSO  $x = 20$ , due to material shortage), were collected at the high-resolution powder diffraction beamline (P02.1) at PETRA III (DESY). The resulting PDFs, depicted in Figures 12 A and C, reveal deviations in the mid to high  $r$  region. The LIO PDFs only exhibit sharp peaks up to about 5 Å,



12: Synchrotron PDF of LIPSO (A), with zoom-in on the low  $r$  region (B) and LIO (C) with zoom-in to low  $r$  and detailed peak assignment (D).

followed by some broader oscillations, whereas the LIPSO samples contain defined correlations up to 50 Å. These peaks starting from  $r > 8$  Å can be attributed to the crystalline LPO phase, which was already detected by the XRD analysis (Figure 12 A).

As oxygen content increases, peak intensities for  $r > 8$  Å rise, hinting at an extended correlation length for the phosphate phase, though this effect is compounded by the increase of total crystalline LPO fraction, which amplifies overall peak intensity.

The low  $r$  region is almost identical in both experimental series (Figure 12 B and D). This region is dominated by the thiophosphate phase for all samples. The main peaks were attributed to the intra-tetrahedral  $[\text{PS}_4]^{3-}$  distances. The initial peak at 2.05 Å is identified with the P-S bond, while the subsequent peak at 3.35 Å aligns with the intra-tetrahedral S-S distance. Two small peaks appear in between the P – S and S – S peaks. These two correlate with the theoretical distances for Li – S and S – O respectively. However, the convolution of the PDF with termination ripples prevents a peak assignment with absolute certainty. Further, the second peak, correlating with the S – O distance was also observed in the LPS sample, which confirms that it is most likely a ripple rather than a real peak. The same problem arises for the P – O pair. The bond length should be approximately 1.55 Å.[87] However, all PDFs exhibit large termination ripples in this area, preventing a clear peak assignment. The last attributable peak is found at 3.85 Å. The peak is considerably broader compared to the P – S and S – S peaks. Hence it was assigned to the inter-tetrahedral S – S distances, or the S – S distances within a Li polyhedra. A detailed peak assignment is presented in Figure 12 D, the change from intra to inter-tetrahedral signals is marked by the dashed line. The whole region experiences little to no change upon oxygen substitution in both experimental series, proving that the integrity of the tetrahedra is not affected by the introduction of oxygen. Calculations based on the P – S and S – S distances, with the assumption of a tetrahedral configuration, yield an S-P-S bond angle of  $109.56^\circ$ , closely mirroring the ideal tetrahedral angle of  $109.57^\circ$ . This similarity confirms that the glasses predominantly consist of uniform  $[\text{PS}_4]^{3-}$  tetrahedra, aligning with findings from previous research.[34, 40, 42, 88] However, the exact connectivity of these tetrahedra, whether isolated or corner- or edge-shared, remains unclear from the PDF alone. Similar distributions could arise from either arrangement without changes in bond lengths and angles. Insights into the tetrahedra connectivity are inferred from the ratio of peak integrals between the P – S and S – S peaks. The coordination number for P – S is expected to match

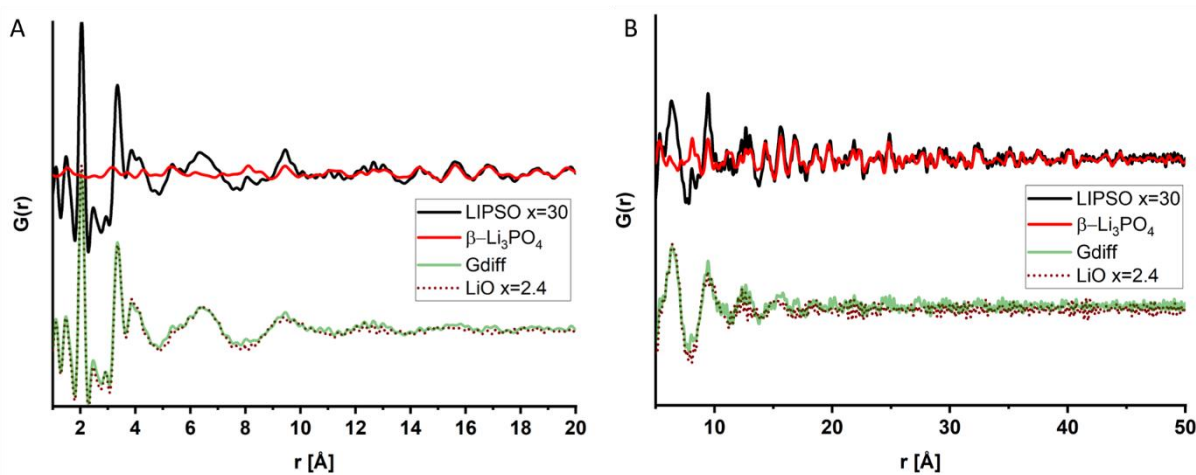
the number of sulfur atoms in the formula unit, which varies from 4 to 2.8 as oxygen substitution increases. The coordination number for S–S ranges between 3 and 1.8 in structures with exclusively isolated tetrahedra, and between 6 and 3.6 in structures with solely corner-sharing tetrahedra. Two different S–S distances are observable in the material's structure as explained above; intra-tetrahedral S–S pairs produce a distinct peak at 3.35 Å, while inter-tetrahedral S–S pairs result in a wider peak around 3.85 Å in the PDF. The extensive overlap of these peaks complicates their separation and accurate integration, reducing the precision of the analysis. Moreover, the presence of any contaminants that introduce alternate coordination environments would further alter the peak integrals, thus hindering a reliable assessment of the coordination numbers based on the available data.

The mid-range region of the LIO PDFs ( $5 < r < 20$ ) is characterised by broad oscillations stemming from the amorphous matrix. These oscillations align closely with the peaks found in crystalline  $\beta$ -Li<sub>3</sub>PS<sub>4</sub>, indicating that the spatial arrangement of tetrahedra is not entirely random. If it were, the PDFs should level off around 3.8 Å. Oscillations beyond this point suggest some degree of order in the spacing between neighbouring [PO<sub>x</sub>S<sub>4-x</sub>]<sup>3-</sup> tetrahedra, likely mediated by the presence of Li. The physical constraints imposed by Li–S and Li–O bond lengths necessitate a certain spacing between tetrahedra. However, as mentioned before, these Li polyhedra are less defined, which is also indicated by the quick falloff in oscillation intensity. The orientation of the phosphorous tetrahedra towards one another is suggested to be random by the absence of clear features atop the oscillations. The correlation length, indicating the extent of observable order, decreases with an increase in oxygen content from approximately 20 Å for pure thiophosphate to about 17 Å for samples with a 30% oxygen concentration. This reduction in correlation length with higher oxygen substitution is likely due to the varying bond lengths introduced by the presence of oxygen, with P–O and Li–O bonds being shorter than their sulfur counterparts. The relatively short correlation lengths across all samples highlight the glassy nature of the materials, devoid of long-range order.

The mid and high  $r$  regions of the LIPSO PDFs show more and sharper peaks, extending further (Figure 12 A). All of these peaks, starting around 8 Å, are attributable not to the thiophosphate phase but to  $\beta$ -Li<sub>3</sub>PO<sub>4</sub>. The correlation length in the thiophosphate phase is presumed similar to that in the LIO series. By individually fitting the nanocrystalline  $\beta$ -Li<sub>3</sub>PO<sub>4</sub> phase,



contributions from the LPO phase to the total PDF can be isolated, and the resulting difference curve represents the purely amorphous thiophosphate phase. Comparing the residuals to LIO series samples reveals no significant differences in the amorphous phase between synthesis routes, even in samples with 30% oxygen content, as illustrated in Figure 13. The same is true for all other samples, fits and comparisons of all other samples can be found in the appendix, Figure 46. All peaks and oscillations are identical concerning position with only miniscule variations in intensities for individual peaks. Fitting the LPO phase with PDFgui showed a trend consistent with the XRD Rietveld refinements, where crystallite size decreases with increasing



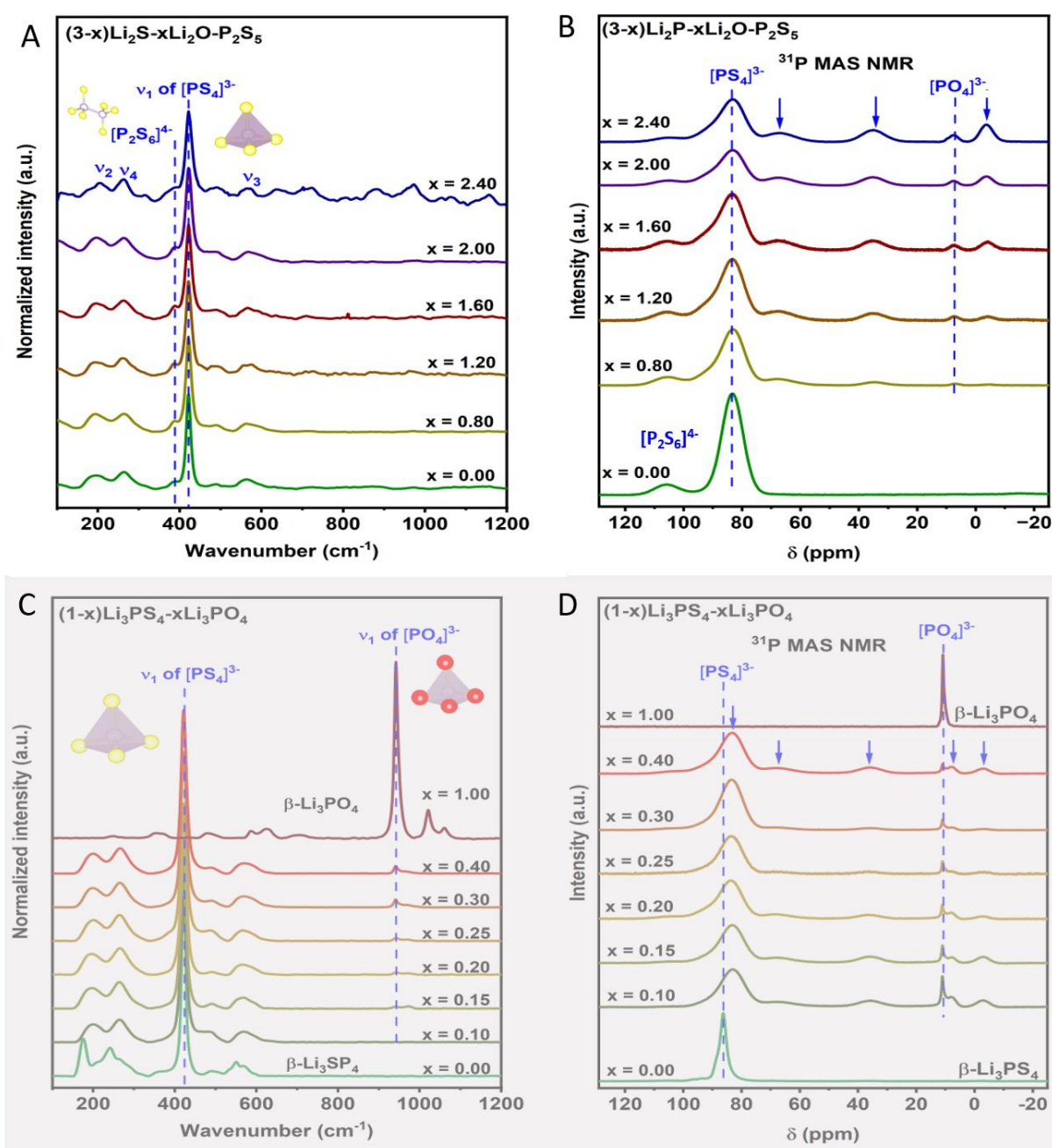
13: PDF of LIPSO sample with 30 % LPO (black) with PDFgui fit of the  $\beta$ -LPO phase (red) and the difference curve (green) compared to the LIO sample with the same oxygen content (brown, dotted) A: low and mid r region, B: mid and high r region.

oxygen content. In summary, LIPSO samples are characterised by  $\beta$ -Li<sub>3</sub>PO<sub>4</sub> nanocrystals embedded within an amorphous matrix predominantly composed of [PS<sub>4</sub>]<sup>3-</sup> tetrahedral, whereas LIO samples seem to be a homogenous material with exclusively amorphous character.

In order to detect the individual building blocks of the material, especially in the amorphous phase, spectroscopic techniques were employed. Synchrotron PDF analysis provided initial insights into the glass structure but fell short of identifying oxygen correlations. The absence of oxygen-related signals can be explained by the low scattering crosssection of the light oxygen atom with synchrotron radiation. Therefore further analysis methods with higher sensitivity to light elements are needed, to overcome these limitations and gain a deeper understanding of the structural units responsible for glass formation.

First Raman spectroscopy was chosen as a quick and readily available method. The resulting spectra feature the [PS<sub>4</sub>]<sup>3-</sup> internal P – S symmetric stretching vibration  $\nu_1$  as the main peak at

421  $\text{cm}^{-1}$ . As predicted by selection rules for the  $T_d$  symmetry,[89] the peaks for the antisymmetric P–S stretching  $\nu_3$  as well as the two S–P–S bending vibrations  $\nu_2$  and  $\nu_4$  are also visible (Figure 14 A). The bending vibrations are detected at 190 and 265  $\text{cm}^{-1}$  and the antisymmetric stretching mode at 562  $\text{cm}^{-1}$ . Furthermore, the  $\nu_1$  peak at 421  $\text{cm}^{-1}$  features a shoulder peak to lower wavenumbers. This signal indicates the presence of  $[\text{P}_2\text{S}_6]^{4-}$  units, which is a common impurity phase. Impurities containing  $[\text{P}_2\text{S}_6]^{4-}$  units are reported in most studies investigating ball-milled LPS and are explained by incomplete reaction during the



14: Raman and  $^{31}\text{P}$  MAS-NMR spectra of LIO (A, B) and LIPSO (C, D), with the assignment of the main bands and sketches of  $\text{PS}_4^{3-}$ ,  $\text{PO}_4^{3-}$ , and  $\text{P}_2\text{S}_6^{4-}$  structural units. Blue arrows in the NMR plots point to the peaks of mixed  $\text{PO}_x\text{S}_y^{3-}$  units. C and D are reprinted with permission from [44]

milling process.[34, 42, 81] All Raman spectra are depicted in Figure 14 A. Notably, none of the spectra show any oxygen-related signals, even at 30 % oxygen concentration. In contrast, symmetric stretching vibrations of  $[\text{PO}_4]^{3-}$  tetrahedra were reported for the LIPSO series (Figure 14 C).[44]

However, the relative peak intensities of the LIO Raman spectra are reduced at high oxygen concentrations as signified by the reduced signal-to-noise ratio.

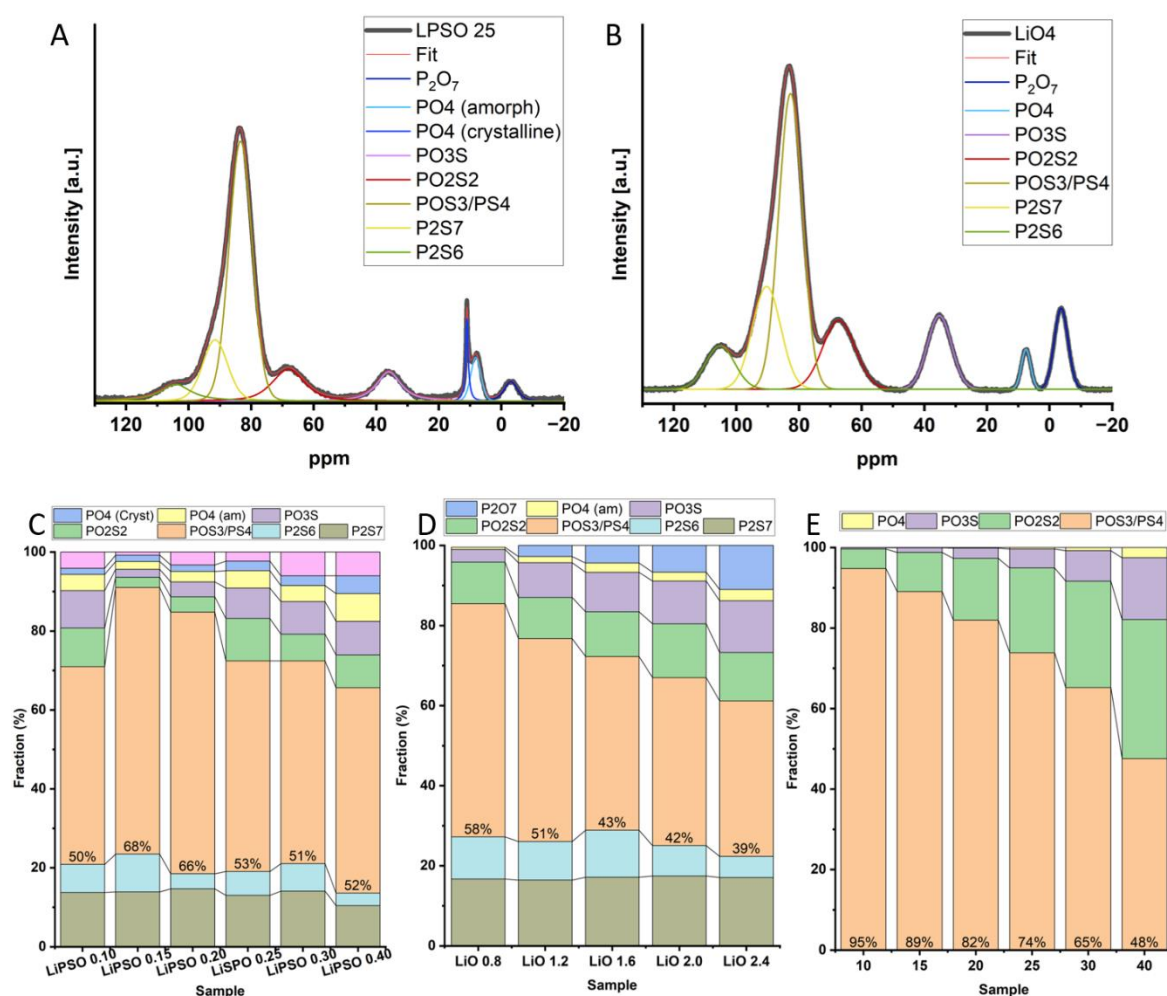
This intensity loss for the thiophosphate signals may be explained by the decreasing amount of sulphur due to the substitution with oxygen. The absence of phosphate signals suggests a more intimate dispersion of oxygen into the thiophosphate matrix. When sulphur atoms in a  $[\text{PS}_4]^{3-}$  tetrahedra are only partially replaced by oxygen, the tetrahedral symmetry is broken and the vibration modes might not be Raman active anymore, due to the selection rules of the relevant energy transitions. Another possible explanation would be that oxygen is not actually replacing sulphur but is bound in another way that does not produce a Raman signal.

$^{31}\text{P}$  MAS-NMR was employed to probe the local chemical environment of the phosphorous atoms and unravel if, and how oxygen is replacing sulfur in the thiophosphate matrix. In agreement with the Raman spectra, the NMR spectra, presented in Figure 14 B, are all dominated by the  $[\text{PS}_4]^{3-}$  signal found at 83.1 ppm. Compared to the same peak in the pure thiophosphate glass (green graph), the signals for the oxy-sulfides are broadened and slightly asymmetric, with a tail towards higher ppm. The broadening becomes more pronounced with higher oxygen concentration. The peak is connected to the oxygen content because of  $[\text{POS}_3]^{3-}$  units, which are commonly attributed to the same peak.[90] The  $[\text{P}_2\text{S}_6]^{4-}$  units, which were already detected by Raman spectroscopy, can also be found in the NMR spectra as a broad peak at around 105 ppm.[91] The intensity of this peak is decreasing with increasing oxygen content. At lower ppm, there are a number of additional peaks, which are not observed in the pure thiophosphate sample. The intensity of these peaks increases with increasing oxygen content, suggesting them to be oxygen-related. Amorphous  $[\text{PO}_4]^{3-}$  units are detected at 8.8 ppm. The two peaks in between the  $[\text{PS}_4]^{3-}/[\text{POS}_3]^{3-}$  and the  $[\text{PO}_4]^{3-}$  signal are consequently assigned to the mixed tetrahedral species,  $[\text{PO}_2\text{S}_2]^{3-}$  and  $[\text{PO}_3\text{S}]^{3-}$ , at 69.5 and 36.3 ppm respectively. The resonance at -2.8 ppm was assigned to corner-sharing  $[\text{P}_2\text{O}_7]^{4-}$  units.[92–94] The NMR spectra reveal, that oxygen is indeed replacing sulphur within the phosphorous tetrahedra, resulting in mixed  $[\text{PO}_x\text{S}_{4-x}]^{3-}$  units. The intensity of all oxygen-containing

tetrahedra correlates with the total oxygen content. Signals representing all possible  $\text{PO}_x\text{S}_{4-x}$  substitutions, with  $0 \leq x \leq 4$ , are present in all samples, indicating that the ball milling process provides limited control over the oxygen distribution within the final product.

Compared to the report for the LIPSO experiments, the MAS-NMR spectra are qualitatively similar, the only difference being an additional sharp peak at 10.9 ppm in the LIPSO spectra, which was again attributed to the presence of crystalline LPO (Figure 14 D).[44]

In order to quantify the results, the NMR spectra of both LIO and LIPSO series were deconvoluted and integrated. The deconvolution was done by fitting Gaussian/Lorentzian peaks to the MAS-NMR spectra using the software dmfit.[95] The main peak at around 83 ppm was fitted with two curves to account for the asymmetry. A larger peak centred around 82.9 ppm was assigned to the contribution of  $[\text{PS}_4]^{3-}$  and  $[\text{POS}_3]^{3-}$  units. A second peak at 91



15: MAS-NMR fits for LIPSO (A) and LIO (B) samples with 25 % oxygen substitution. As well as bar diagrams representation of the relative quantities of structural units in the LIPSO sample (C), LIO sample (D), and a calculated statistical distribution of oxygen (E)

ppm was attributed to the presence of corner-sharing  $[P_2S_7]^{4-}$  units.[34, 91] All other peaks were fitted as single peaks, as demonstrated in Figures 15 A and B on the example of the LIO sample (A) and the LIPSO sample (B) with 25 % oxygen substitution each. The deconvolution of all other samples from LIO and LIPSO are found in the appendix Figures 47, 48. The integration of the fitted lines yields relative quantities of the structural units in the samples. The quantitative analysis of both experimental series revealed clear discrepancies in the composition of samples from different series with equal oxygen concentrations.

In the LIO series, the quantity of oxygen-containing tetrahedra rises nearly linearly with an increase in oxygen content, whereas no clear correlation can be observed within the LIPSO series. Generally, the LIPSO samples contain more amorphous  $[PO_4]^{3-}$  but less  $[PO_2S_2]^{3-}$  units. The result hints at a better dispersion of oxygen in the LIO series as predicted by the reactivity of the precursor materials. For comparison, the same results for a purely statistical distribution of  $[PO_xS_y]^{3-}$  units are depicted in Figure 15 E. Contrary to the random distribution, the actual distribution within the samples shows anomalies. Specifically, the concentration of  $[PO_4]^{3-}$  units is elevated across all samples. The concentration of  $[PO_3S]^{3-}$  and  $[PO_2S_2]^{3-}$  are higher than expected at lower oxygen levels and lower than expected at higher oxygen levels. This pattern indicates a tendency for oxygen atoms to aggregate, forming species with high oxygen substitution. The observation makes sense considering that sulphur to oxygen substitution requires significantly less energy than oxygen to sulphur substitution. Consequently, low-substituted tetrahedra are likely to incorporate more oxygen during the synthesis, whereas highly substituted tetrahedra are unlikely to lose oxygen. Qualitatively, the trend for the LIO series vaguely follows the statistic distribution, meaning a steady increase of all oxygen-containing species. The unusual trend found for the LIPSO series, on the other hand, cannot be easily explained by a semi-random process. The conditions during the ball milling seem to be insufficient to effectively react the highly thermodynamically stable  $Li_3PO_4$ . Hence, collisions only trigger a reaction if ideal conditions are met. For that reason, less controllable parameters, like the initial mixing state of powders/ powder and grinding balls, may have a larger influence on the product composition. In the LIO series, the precursor materials are more reactive, therefore, most collisions trigger a reaction. Consequently, the process becomes more homogenous and mainly depends on the collision frequency, which is well described by a statistical process.

The quantities of other impurity units like  $[P_2S_7]^{4-}$  and  $[P_2S_6]^{4-}$  are less affected by the oxygen substitution. The  $[P_2S_7]^{4-}$  quantity remains almost unchanged across the entire range of oxygen concentrations in both series. The amount of  $[P_2S_6]^{4-}$  appears to diminish with higher oxygen levels. Overall both impurities are quantitatively more common in the LIO compared to the LIPSO series. This is likely due to the pre-calcination of amorphous  $Li_3PS_4$  to form  $\beta$ -LPS before its incorporation with  $\beta$ - $Li_3PO_4$  in LIPSO, as opposed to the in-situ formation of  $Li_3PS_4$  glass in the LIO synthesis. This heat treatment is known to reduce the discussed impurity phases.[42, 44] The results are summarised in Table 2 and illustrated in Figures 15 C and D. The absolute numbers of the unit quantities might not accurately represent the true composition, because the intensity of NMR peaks may be selectively reduced when the relaxation time of the nuclei is long in comparison to the time between pulses. However, as all samples are made up of the same building blocks, any selective intensity suppression, if present, will occur for all samples in the same way. Thus, the relative quantities are well-comparable between the samples, and the derived trends are still accurate.

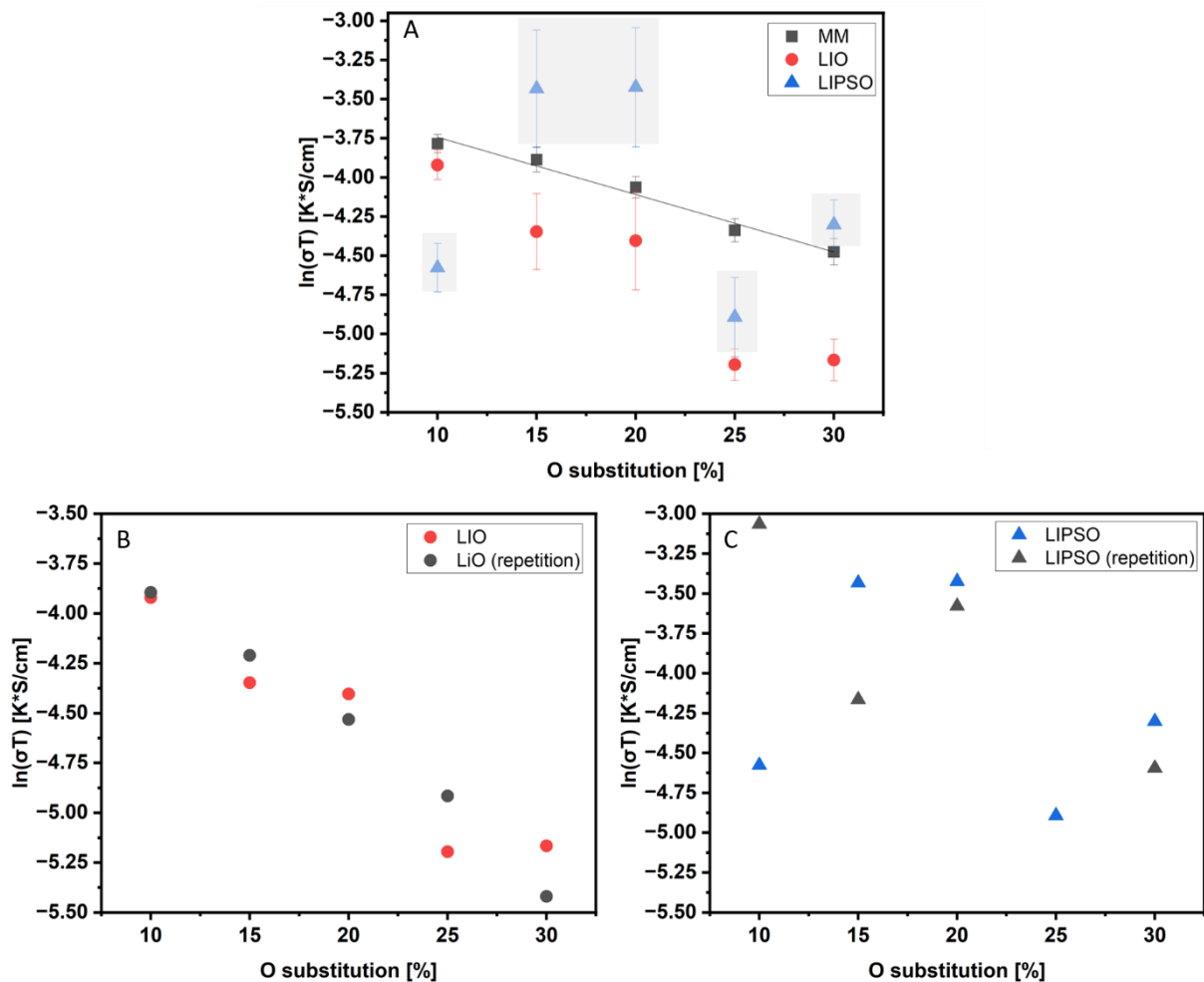
Through structural analysis of oxy-sulfide glasses, the specific structural units present in each glass and their degree of order were identified. The LIPSO and LIO series exhibit notable structural differences. In contrast to the LISPO samples, LIO samples are identified as “true” glasses due to their homogeneous amorphous structure, whereas LIPSO samples are defined as glass ceramics due to the combination of crystalline particles inside the amorphous matrix.[44] This dissimilarity is attributable to the greater chemical and mechanical resilience of the respective precursor materials. The robustness of  $Li_3PO_4$  prevents its complete transformation under the applied ball milling conditions. Despite identical stoichiometry between the two material types, their differing structures suggest variations in physical and chemical properties. The amorphous matrix, predominant in all samples, is mainly composed of  $[PS_4]^{3-}$  tetrahedra with assorted  $[PO_xS_{4-x}]^{3-}$  mixed species. In essence, both synthesis routes produce materials with identical stoichiometry and structural units, but they differ significantly in the distribution and quantity of the oxygen-containing units.

Table 2: Fractions of different structural units found in oxy-sulfide glasses based on NMR analysis and calculated statistical distribution.

Structure unit/ Sample	P <sub>2</sub> S <sub>7</sub>	P <sub>2</sub> S <sub>6</sub>	POS <sub>3</sub> /PS <sub>4</sub>	PO <sub>2</sub> S <sub>2</sub>	PO <sub>3</sub> S	PO <sub>4</sub> (cryst)	PO <sub>4</sub> (am)	P <sub>2</sub> O <sub>7</sub>
LIPSO 0.10	13.74	7.10	50.14	9.76	9.5	1.59	4.06	4.11
LIPSO 0.15	13.92	9.53	67.59	2.56	2.04	1.61	1.96	0.8
LIPSO 0.20	14.66	3.83	66.28	3.89	3.78	1.65	2.65	3.27
LIPSO 0.25	13.02	6.05	53.34	10.76	7.7	2.47	4.39	2.27
LIPSO 0.3	14.14	6.97	51.54	6.78	8.31	2.5	4.03	6.06
LIPSO 0.4	10.42	3.17	52.02	8.27	8.54	4.53	7.02	6.01
LIO 0.8	16.71	10.51	58.22	10.41	3.15	-	0.58	0.43
LIO 1.2	16.43	9.64	50.65	10.31	8.65	-	1.53	2.79
LIO 1.6	17.14	11.73	43.37	11.18	9.84	-	2.33	4.40
LIO 2.0	17.45	7.58	41.96	13.46	10.65	-	2.21	6.68
LIO 2.4	17.08	5.25	38.84	12.08	12.92	-	2.84	10.98
Stat. 10 % P-O	-	-	94.77 (65.61/29.16)	4.86	0.36	-	0.01	-
Stat. 15 % P-O	-	-	89.05 (52.2/36.85)	9.75	1.15	-	0.05	-
Stat. 20 % P-O	-	-	81.92 (40.96/40.96)	15.36	2.56	-	0.16	-
Stat. 25 % P-O	-	-	73.83 (31.64/42.19)	21.09	4.69	-	0.39	-
Stat. 30 % P-O	-	-	65.17 (24.01/41.16)	26.46	7.56	-	0.8	-
Stat. 40 % P-O	-	-	47.52 (12.96/34.56)	34.56	15.36	-	2.56	-
LIPSO 0.10 (repetition)	9.595	9.41	63.42	6.65	6.61	2.16	0.81	1.34
LIPSO 0.15 (repetition)	12.47	8.55	59.07	7.91	5.79	2.325	2.13	1.76
LIPSO 0.20 (repetition)	11.13	5.41	64.67	4.63	6.63	3.31	2	2.22
LIPSO 0.3 (repetition)	13.57	6.12	48.92	7.34	6.96	6.58	4.68	5.83

### 3.1.4 Electrochemical analysis

For an SE material, one key figure of merit is its ion conductivity. Consequently, in the next step, oxy-sulfide glasses were further analyzed with regard to their Li-ion conductivity. EIS measurements revealed a distinctly different conductivity trend for the LIO series compared to the one published for the LIPSO series. For the LIPSO series an unexpected conductivity pattern was reported[44]: starting with low conductivity at 10% oxygen substitution, peaking between 15–20%, then reducing again at 25%, and experiencing a minor resurgence at 30% oxygen substitution. Contrarily, the LIO series shows a trend where lithium-ion conductivity continuously diminishes as the oxygen content increases, yet this decline exhibits steps indicating non-linear behaviour (Figure 16 A). The discrepancy between the two conductivity trends is most likely related to the structural differences between the LIO glasses and LIPSO glass ceramics. As previously discussed, the primary distinction between the LIPSO and LIO series lies in the presence of  $\beta$ - $\text{Li}_3\text{PO}_4$  nanocrystals within the LIPSO samples and the variation



16: EIS measurements of LIO, LIPSO and mixed LPS/LPO samples (A), LIPSO and a repetition series (B) and LIO and a repetition series (C).



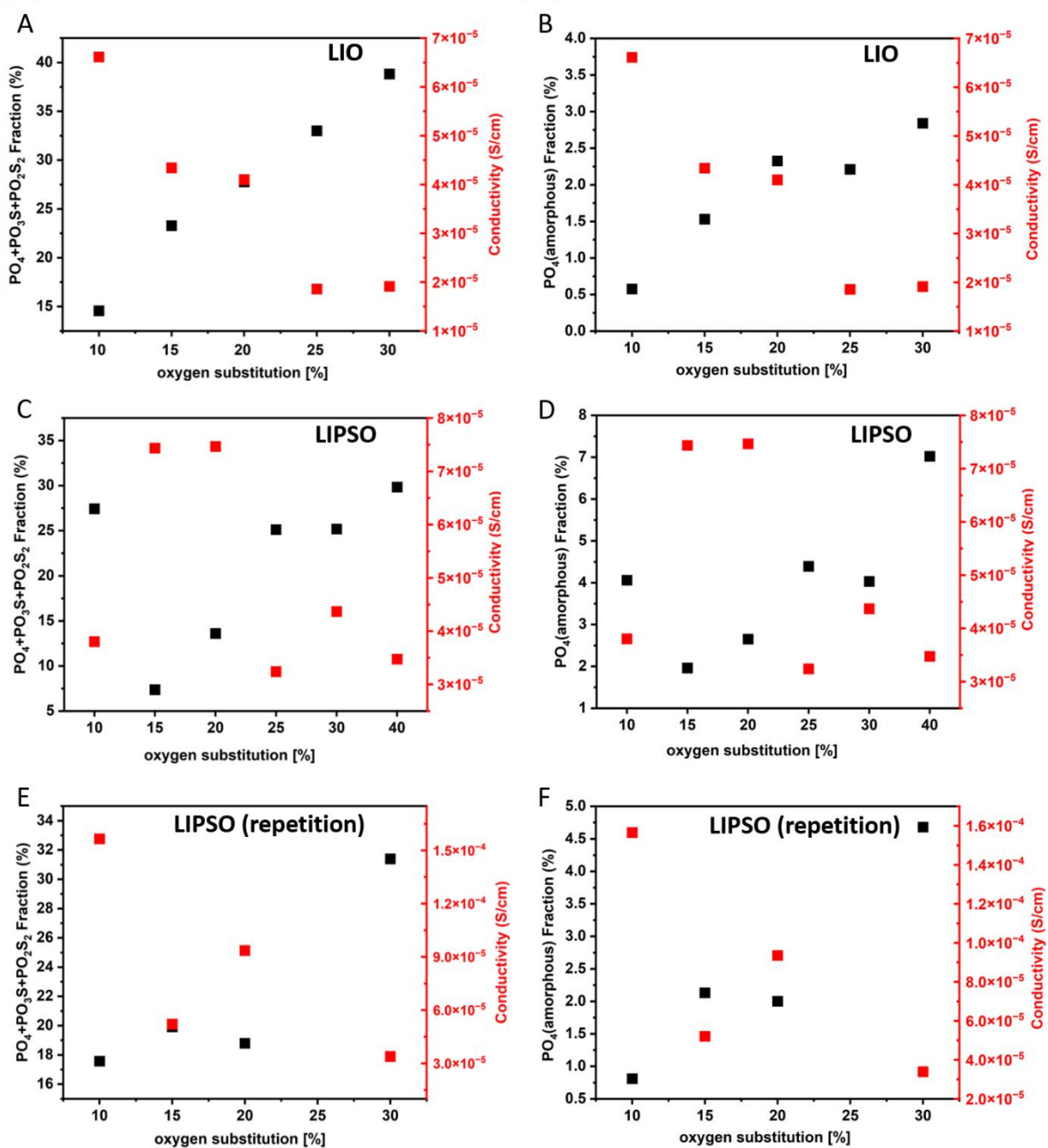
in oxygen distribution, which influences the proportion of different structural units. In order to quantify the influence of  $\beta$ - $\text{Li}_3\text{PO}_4$  nanocrystals within the thiophosphate matrix, a third experimental series was prepared by manually mixing amorphous LPS with crystalline LPO for 15 min in a mortar, subsequently, their Li-ion conductivity was measured using EIS. As a result, this manually mixed series (termed MM), exhibits a linear response between the logarithmic conductivity and the percentage of  $\beta$ - $\text{Li}_3\text{PO}_4$ , which aligns with expectations for a mixture combining materials of high and low conductivity.

Therefore, the presence of  $\beta$ - $\text{Li}_3\text{PO}_4$  nanocrystals cannot explain the conductivity trend of the LIPSO series, as an increasing amount of LPO phase should uniformly decrease ion conductivity.

In order to investigate the reproducibility of the results, both experimental series were repeated under the same conditions. The repetition of the LIO series yielded similar results with an almost linear conductivity decrease with increasing oxygen substitution (Figure 16 B). The LIPSO repetition series on the other hand not reproduce the results reported by Lou. However, the repetition of LIPSO also exhibits a nonlinear, zigzag-like trend, which is unexplainable by just taking into account the total oxygen content (Figure 16 C).

This insight demands further investigation of the role of the specific  $[\text{PO}_x\text{S}_{4-x}]^{3-}$  tetrahedra formed during the synthesis. The analysis of peak integrals from NMR data reveals a definitive correlation between the presence of highly substituted tetrahedra (with two or more oxygen atoms per tetrahedron) and the ionic conductivity of the materials. Comparing the total quantity of oxygen-containing species with  $n_o > 2$  (illustrated by the black dots in Figure 17) against the ion conductivity (represented by the red dots in Figure 17) revealed an inverse relationship in all samples, indicating that an increased concentration of oxygen clusters correlates with diminished conductivity, and vice versa (Figures 17 A, C and E). This correlation is further supported by examining the relationship between the concentration of  $[\text{PO}_4]^{3-}$  units present in the amorphous phase and the conductivity, as shown in Figures 17 B, D, and F. Although the correlation is evident, the inverse mirroring effect between the structural unit content and conductivity trends is not uniformly precise across all graphs. The disparity when focusing on the  $[\text{PO}_4]^{3-}$  content may be attributed to the relatively low abundance of  $[\text{PO}_4]^{3-}$  units compared to other structural units that also influence ion conductivity. The collective impact of various oxygen-containing structural units, as well as the level of impurity phases,

and their distribution within the material plays a crucial role in determining the overall ion conductivity. This complexity might explain why certain aspects of the conductivity trends are not perfectly mirrored in the structural unit fraction curves. The detrimental impact of oxygen clustering on ion conductivity in oxy-sulfide materials aligns with theoretical predictions for crystalline  $\beta$ -LPS made by Banerjee et al.[96] Their theoretical analysis suggested that ion conductivity is higher when oxygen atoms are evenly dispersed rather than clustered, with predictions indicating an increase in ion conductivity with minor amounts of dispersed oxygen.



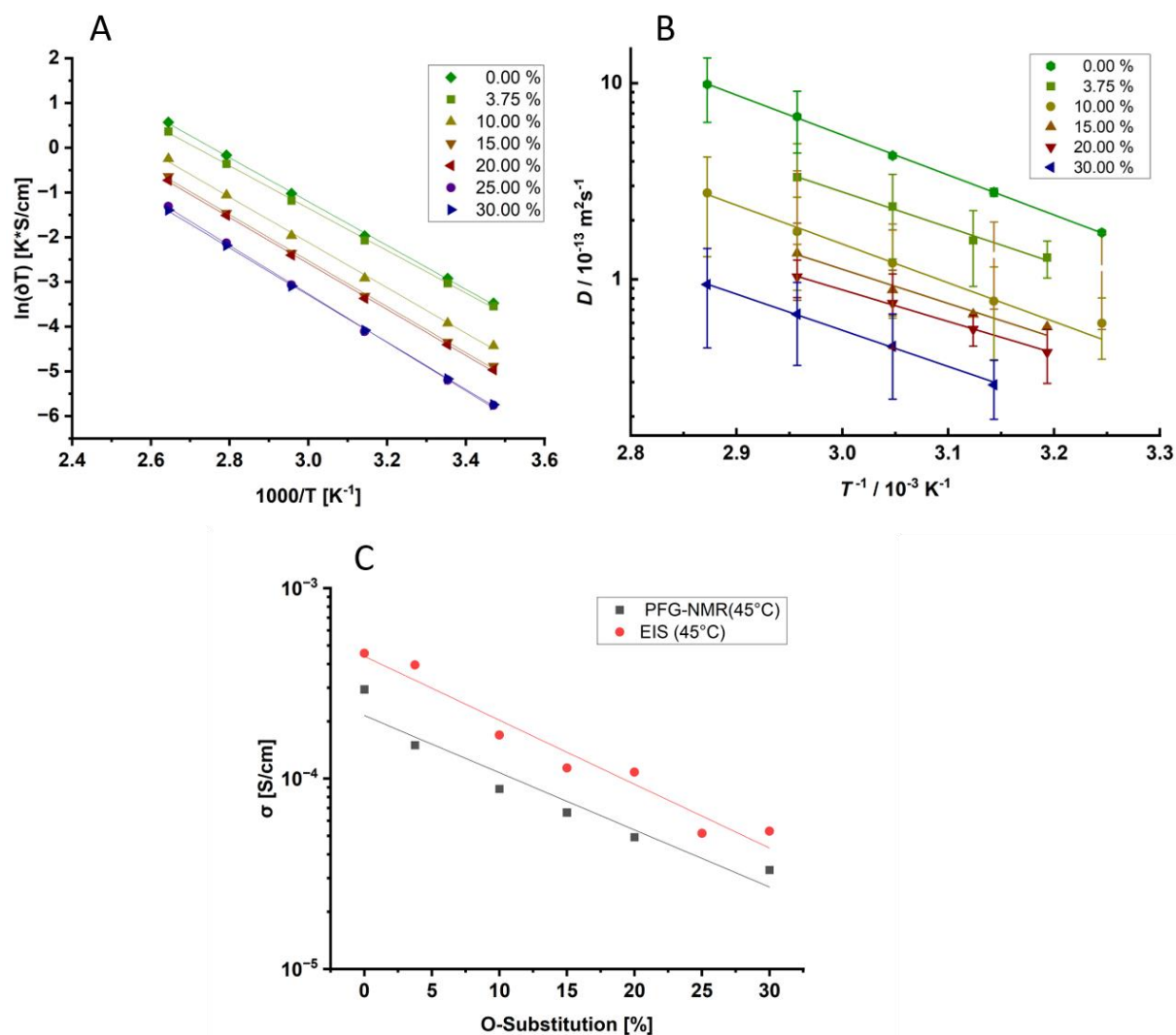
17: Left: Comparison of conductivity trends and fraction of high oxygen substituted tetrahedral of the LiO samples (A), LIPSO samples (C), and the repetition LIPSO series (E). Right: Comparison of conductivity trends and fraction of amorphous  $[\text{PO}_4]^{3-}$  units of the LiO samples (B), LIPSO samples (D), and the repetition LIPSO series (F).

Given that  $[\text{PO}_4]^{3-}$  units contain the highest concentration of oxygen atoms, they are identified as having the most significant negative impact on Li-ion conductivity. Our experimental observations corroborate these theoretical insights, illustrating the complex relationship between structural composition and ion transport properties in these materials. As part of a collaboration with the working group of Karsten Albe (TU Darmstadt), the experimental results could qualitatively be confirmed in theoretical calculation on oxy-sulfide glasses by Dr. Marcel Sadowsky, using atomistic simulations. The simulations were built up of tetrahedral units with systematically substituting oxygen in the form of only  $[\text{PO}_4]^{3-}$ ,  $[\text{PO}_3\text{S}]^{3-}$ ,  $[\text{PO}_2\text{S}_2]^{3-}$ , or  $[\text{POS}_3]^{3-}$ . In accordance with the experiments, lower conductivity values were calculated for the structures containing higher substituted tetrahedra.[97]

Various ion conductivity values have been reported for oxy-sulfide glasses and glass ceramics, as documented in several studies.[26, 27, 45, 90] As mentioned in the introduction, the reported values do not always confirm each other. The current study has shown that an in-depth investigation of the structural units may explain some of the discrepancies. Variations in the synthesis procedure, e.g. milling parameters or heating steps, and the choice of precursor materials lead to materials with identical stoichiometry but different atomic configurations and varying amounts of impurities. The combined structural and electrochemical analysis has yielded strong indications, that all the different structural units contribute to the total ionic conductivity, but not in equal amounts. Another source of error may be the conductivity measurement itself. EIS is a powerful technique to determine the effective conductivity of the whole sample and even identify different dynamic processes within a sample, but only if these processes happen on separate time scales. However, the comparison of EIS measurement results with other techniques capable of investigating ion dynamics, like PFG-NMR and  $T_1$  relaxometry improves the reliability of the data and may lead to further insights on the conduction mechanism, as each method probes a different length scale.

PFG-NMR studies on the LIO samples revealed a similar trend as found in the EIS measurements. The diffusion coefficient decreases with increasing oxygen substitution (Figure 18 A, B). From the diffusion coefficient, a conductivity value can be estimated using the Nernst-Einstein equation (equation 21). The number density of Li ions,  $N_{\text{Li}}$ , was estimated to  $1.9 \times 10^{28} \text{ m}^{-3}$  based on density measurements using a He-gas pycnometer. The conductivity

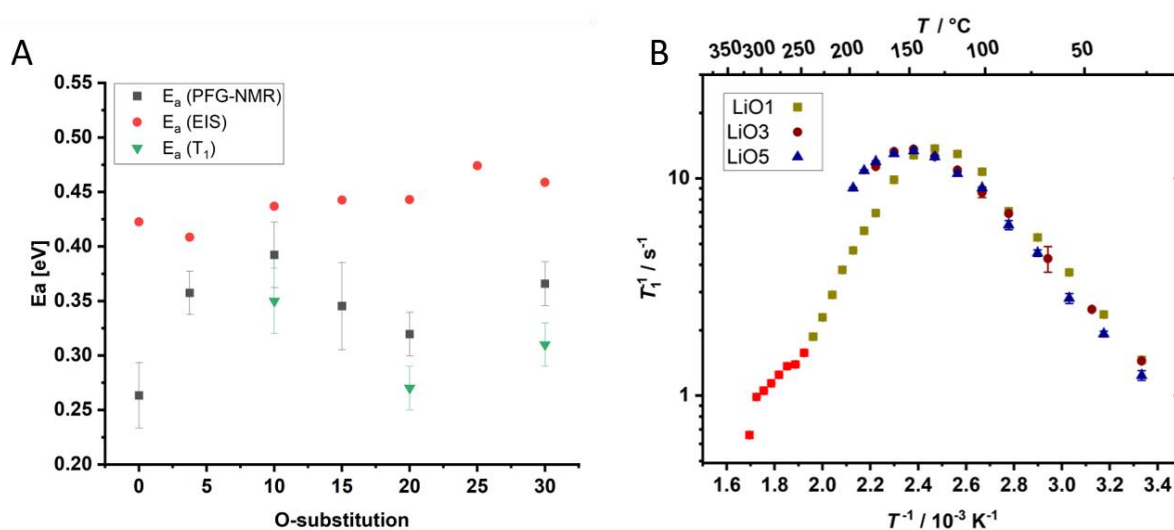
values are slightly lower, but overall in good agreement with the EIS data (Figure 18 C). The conductivities retrieved from PFG-NMR are expected to be lower than corresponding EIS values, because the PFG-NMR can only measure the diffusion in the direction of the magnetic gradient and, in contrast to the EIS measurements, no electric field is applied leading to a non-directed diffusion process. Furthermore, the conversion of diffusion coefficients into conductivity values is not precise as the number density of charge carriers, in this case Li ions, can only be estimated. Both datasets display an almost linear trend, however, the slope of the linear regression is slightly lower for the PFG-NMR results. A possible reason for this could be trapped Li ions. The conductivity is dependent on the mobility and the number density of charge carriers. The diffusion coefficient, however, only depends on the ion mobility, and the conductivity values were calculated assuming a constant number density of Li-ions.



18: Results for temperature-dependent ion dynamic measurements with EIS (A), PFG-NMR (B) and comparison of the derived room temperature conductivities (D)

If the number density is reduced because Li ions are trapped by surrounding oxygen and no longer contribute to the ion conduction, the conductivity may drop faster than the diffusion coefficient.

Activation energies were calculated from temperature-dependent measurements by fitting a linear regression to the plot of logarithmic conductivity versus inverse temperature according to Arrhenius law (equation (22), (23)). The data from the PFG-NMR measurements were fitted with a Gaussian distribution of diffusion coefficients, owing to the disordered character of the materials. The Li environments are not well defined, as seen from the PDF analysis earlier; therefore, dynamics are better represented by a distribution than a single diffusion coefficient. The error bars in Figure 18 B correspond to the width of this distribution (standard deviation of a Gaussian distribution). The activation energies exhibit a dissimilar trend comparing EIS and PFG-NMR. The EIS data indicate a slight increase in the activation energies from 0.41 to 0.46 eV as oxygen substitution increases, whereas the PFG-NMR studies reveal an increase from 0 to 10 % oxygen substitution followed by a parabolic behaviour between 10 and 30 % oxygen substitution (see Figure 19 A). Generally, all activation energies are in a



19: Activation energies for the LiO series determined by different analytical methods (A) and  $T_1$  relaxometry of three representative samples (B).

similar range for all oxygen-containing samples between 0.32 and 0.39 eV. The activation energies calculated from NMR are generally lower than the ones calculated from the EIS data, which is attributed to the higher influence of inter-particle ion transfer in the EIS data, as the range of the PFG-NMR measurement does not include hops over multiple particles.

In order to get insights into the local hopping processes,  $T_1$  relaxometry was performed for LIO1, LIO3, and LIO5 to represent a low, medium, and highly substituted material. The hopping rates clearly shift towards slower dynamics from LIO1 to LIO3 and 5, as signified by the shift of the maxima to lower temperatures as shown in Figure 19 B. Samples LIO3 and LIO5 exhibit similar  $T_1$  relaxation times, suggesting similar average local-hopping dynamics. The data points are fitted with the BPP model as described in Chapter 1.3.2 to extract the exact hopping rates and activation energies. The fitting with one average relaxation rate only yields satisfying results for LIO3 and LIO5, for the LIO1 sample, a fit with two dynamical components was suggested. This approach yields a slow and a fast component, which could be explained by oxygen-rich and oxygen-poor Li environments. In theory, the different possibilities of arranging oxygen and sulphur around a Li-ion would allow for multiple components. However, fitting too many parameters reduces the reliability of the results, as the best mathematical model is not necessarily the most physically accurate. LIO3 and 5 were also fitted with two components to compare with the LIO1 fit. However, the missing high-temperature region again reduces the reliability and increases the error of the fitted data to unjustifiable values. Physically, a change from two to one relaxation time is also reasonable as higher oxygen levels reduce the amount of oxygen-poor Li environments. Assuming one average component, the activation energies closely mirror the activation energies found in the PFG-NMR experiment but are offset by circa -0.04 eV. All energies are in a similar range, between 0.27 and 0.35 eV, and deviate from the almost linear trend retrieved from the EIS measurements between LIO1 and LIO5.

The decrease of the activation energies from EIS to PFG-NMR to  $T_1$  relaxometry is caused by the stepwise decrease of observed diffusion lengths. Thus, contributions from particle boundaries and other inhomogeneities, only affecting the long-range transport but not the local dynamics, reduce the activation energies derived from EIS measurements. The discrepancy between the trends of conductivity and activation energies calculated from the two NMR experiments hints at more complex correlations between oxygen substitution, local Li environment, and ion mobility. The undefined nature and variety of these Li environments in all materials complicate the interpretation of the data. However, the oscillation found for the NMR experiments, indicates that there are at least two opposing trends affecting the ion mobility. On the one hand, the increase in bond energy of Li – O compared to Li – S should lead to an increase in the activation energy, as observed for low oxygen contents. On the other

hand, several theoretical studies on  $\beta$ -LPS have shown that oxygen doping may in some instances reduce the activation energy for Li diffusion due to flattening of the energy landscape or altering of the Li distribution.[96, 98] As these effects are sensitive to the precise composition of structural units as well as their orientation towards each other, the error in the activation energy in correlation with the total oxygen substitution can be assumed to be large due to the undefined nature of the glasses. Furthermore, oxygen substitution leads to a change in the material density, caused by a contraction of the network due to the shortened bond lengths of phosphorus and lithium to oxygen.

### 3.1.5 Neutron total scattering

To gain a better understanding of the Li environment inside the Li oxy-sulfide glasses, neutron PDF data were acquired at NOMAD (Oak Ridge National Laboratory Spallation Neutron Source). Neutron and synchrotron PDF datasets were then thoroughly analyzed and a DFT-calculated structure model was fitted to the data using the RMC method. As mentioned in the introduction, neutrons and x-rays have fundamentally different interactions with matter; when passing through matter, x-rays interact with the electron cloud, while neutrons only interact with the core of the atoms in their path. Despite these differences, neutrons, and x-rays can often be used in similar experiments and therefore yield complementary data. In the following discussion on neutron PDFs and RMC modelling, PDF will be used synonymously for the  $G_k(r)$  function.

Li oxy-sulfide glasses have proven to be a challenging material to study with diffraction experiments as all the elements, of which the materials are made, are weak scatterers for both x-rays and neutrons. As an example, Table 3 lists the neutron and x-ray scattering coefficients [<https://addie.ornl.gov/helpsheet>] for the compound  $\text{Li}_3\text{PO}_3$ . The coefficients are dependent on the scattering length, and element abundance within the material. The intensity of the peaks in the PDF scales with the corresponding coefficients, but mainly depends on the coordination numbers, hence the atomic structure. The green-coloured numbers are the highest coefficients for the respective probe, therefore the total PDF will be dominated by the respective partial PDFs. The yellow-coloured numbers are less than half as large as the highest one. These partials may still be visible in the total PDF but with lower intensity. The red-coloured numbers have a magnitude of about 1/10 or less compared to the highest one. These partials may only be visible in the total PDF if the peaks are isolated and there are no noise or

termination ripples in the same area. Accordingly, the x-ray PDF should be heavily dominated by the sulfur-sulfur and sulfur-phosphorous interactions because sulfur and phosphorous are the heaviest atoms, and sulfur is also the most abundant element in the material. Sulfur-oxygen and sulfur-lithium may also be visible. All other pairs have significantly lower coefficients and will be challenging to detect. In conclusion, x-rays are a good probe to analyze the anion Network of the  $[\text{PS}_4]^{3-}$  tetrahedra, however, x-rays are not suitable to get Information about the Li environment or the oxygen correlations. The analysis of the synchrotron PDF in Chapter 2.1 confirms this conclusion; P – S and S – S peaks could be easily identified, Li – S and O – S peaks were most likely there but not useful for any analysis because of their low intensity and possible overlap with termination ripples.

*Table 3: Neutron and x-ray scattering coefficients for  $\text{Li}_3\text{PO}_3$ . Green values are the pairs with the strongest coefficients, yellow values are about one third of the strongest one and red values are less than one tenth of the strongest coefficient.*

**Partial scattering factors for neutron (in barn)**

	Li	O	P	S
Li	0.005076563	-0.010336594	-0.00913781	-0.01521366
O		0.005261689	0.00930293	0.01548857
P			0.00411202	0.01369229
S				0.01139823

**Partial scattering factors for x-ray**

	Li	O	P	S
Li	0.012657236	0.022500700	0.04218760	0.13500599
O		0.009999844	0.03749833	0.11999971
P			0.03515368	0.22499299
S				0.36000392

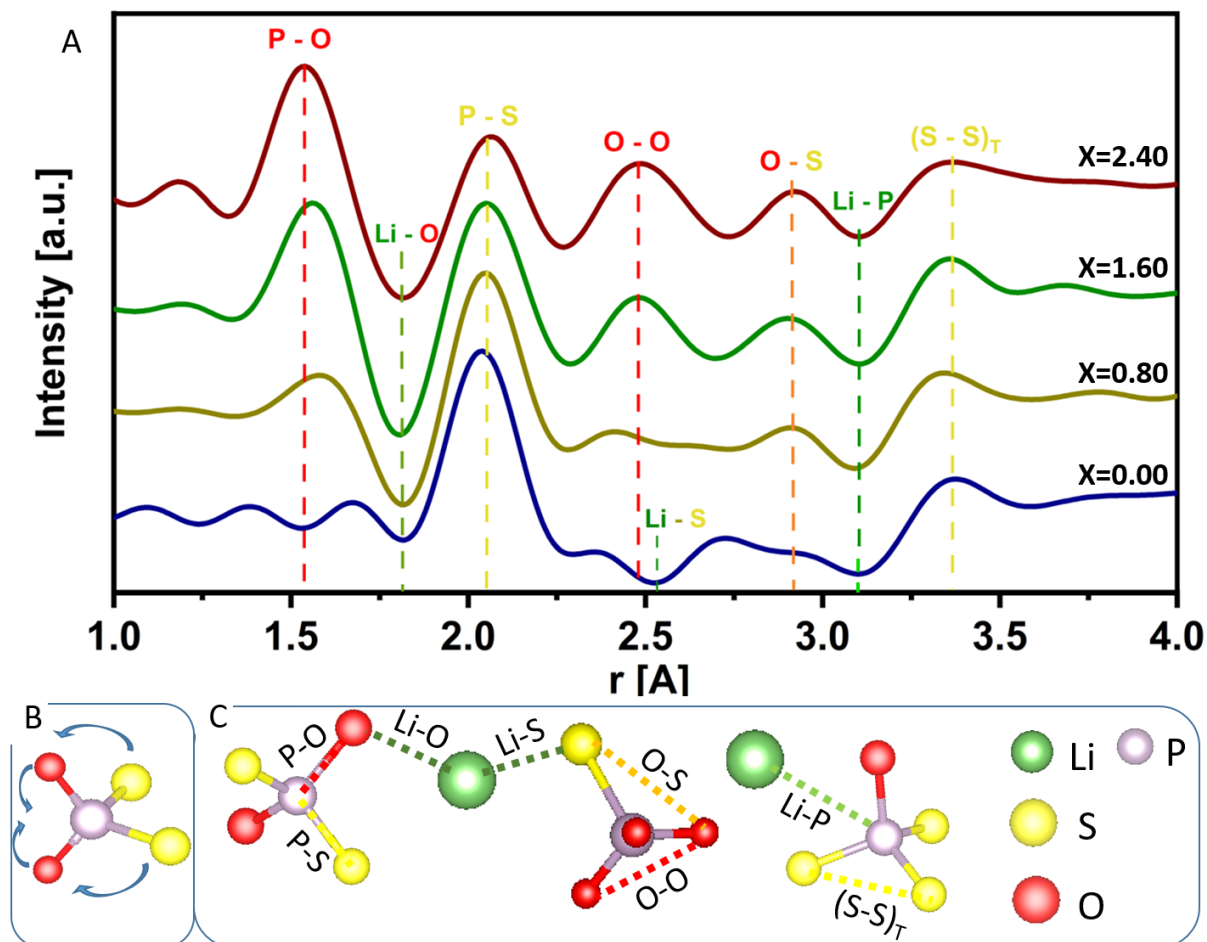
The neutron PDF on the other hand should contain more information as all the coefficients are on a similar scale. The PDF should still have the highest intensities for the sulfur



interactions but, contrary to the x-ray experiment, in the neutron PDF, the lithium-sulfur and sulfur-oxygen partials should be the most dominant. Additionally, Li has a negative scattering length with neutrons, therefore all peaks corresponding to lithium correlations, except lithium-lithium, are negative, which should make it easy to identify lithium-X peaks. Ultimately, neutron PDF experiments in this case are useful to complement the x-ray data with information on Li and O correlations.

As predicted, the neutron PDFs contain more assignable peaks than the synchrotron PDFs (see Figures 21 A-C), thereby offering more detailed information about the atomic structure of the oxy-sulfide glasses up to about 4 Å. The first peak can be attributed to the P – O bond. The peak moves from 1.58 Å for the sample with 10 % oxygen to 1.54 Å for the sample with 30 % oxygen. The bond length for  $\beta$ -Li<sub>3</sub>PO<sub>4</sub> was calculated to be around 1.545 Å.[87] Therefore we can assume that adjacent S atoms, bound to the same phosphorous, slightly increase the P – O bond. The second peak at 1.82 Å was assigned to Li – O. As mentioned earlier, lithium has a negative scattering length with neutrons, hence all Li – X peaks are negative. In this case, the bond length is slightly smaller than that calculated for  $\beta$ -Li<sub>3</sub>PO<sub>4</sub>. [87] The peak position does not change with increasing oxygen content, however, the peak appears to broaden, indicating a more disordered Li environment for higher oxygen concentrations. The P – S peak at 2.05 Å is already known from the synchrotron PDF (see Chapter 3.1.3, Figure 12). The peak position agrees well between the two PDFs but the neutron PDFs detect a slight shift to larger distances with increasing oxygen content, which was not observed in the synchrotron PDFs. The origin of this peak shift is not clear, one possible explanation would be an increasing overlap with the negative Li – O peak, which is broadening for the higher oxygen concentrations and would not affect the synchrotron PDFs. At around 2.5 Å there are two overlapping peaks. The PDF of the reference sample without any oxygen substitution exhibits a negative peak with a minimum at 2.53 Å, corresponding to Li – S. The PDFs of the samples with higher oxygen substitution feature positive peaks in the same area with a maximum at 2.49 Å, matching the O – O distance within one tetrahedra containing at least two oxygen. The PDF of the sample containing 10 % oxygen is almost flat as both peaks cancel each other out. The next peak at 2.91 Å was attributed to O – S pairs within one tetrahedron. Next to the O – S peak, the negative Li – P peak can be identified at 3.1 Å. The intensity of the Li – P peak seems to decrease with increasing oxygen substitution, which fits the assumption of increasing disorder already suggested earlier. At the same time, the overlap with the neighbouring O – S peak

might add to the effect. The last identifiable feature is the S – S peak at 3.36 Å, already known from the synchrotron PDF analysis (Figure 12). The peak assignment for the neutron PDFs is



presented in Figure 20 A.

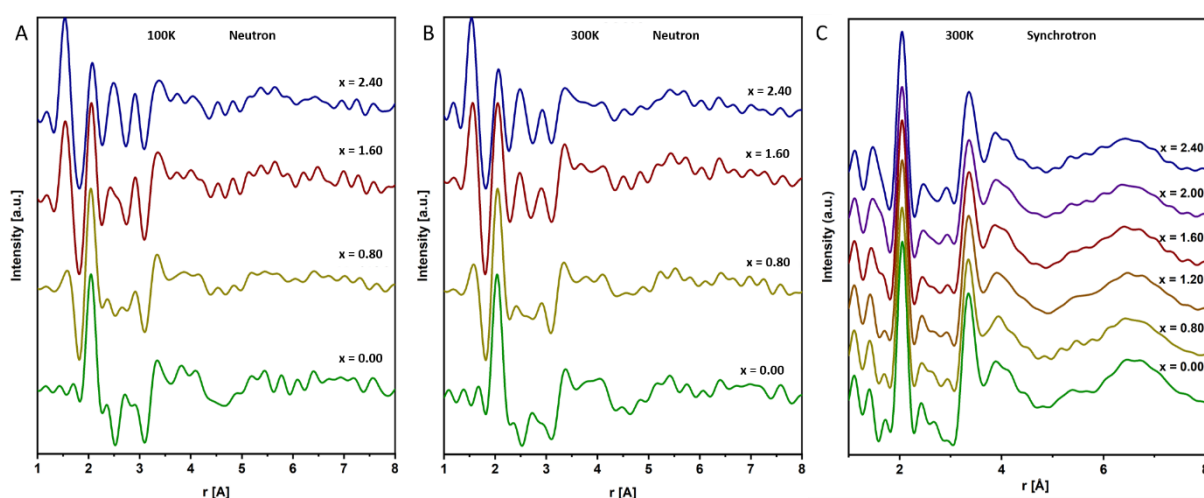
20: Peak assignment for the neutron PDFs (A) with schematic illustration of the distortions for mixed tetrahedral (B) and corresponding distances in the glasses (C).

With the information on the distances for P–O, P–S, O–O, and O–S, and assuming a tetrahedral symmetry, the O–P–S and O–P–O bond angles were calculated to 117.7° and 105.9° respectively. The two angles both deviate from the ideal tetrahedral angle of 109.5°. The angle deviations can be understood when considering the size difference between O<sup>2-</sup> and S<sup>2-</sup> ions. Most oxygen atoms are bound in mixed tetrahedra with two or three O atoms ([PO<sub>2</sub>S<sub>2</sub>]<sup>3-</sup> or [PO<sub>3</sub>S]<sup>3-</sup>). In that case, the bulkier S<sup>2-</sup> ion occupies more space and pushes the O<sup>2-</sup> ions away, as illustrated in Figure 20 B, decreasing the angle between the O atoms and increasing the angle between S and O atoms.

The Li ions appear to be in a less ordered coordination environment than the phosphorous atoms. Although the Li–O and Li–S bond lengths are well defined, the absence of a second

O – O or O – S peak for the  $[\text{LiO}_x\text{S}_{4-x}]^{3-}$  polyhedra indicates that the bond angles and thus coordination polyhedra are not well defined. A second S – S peak is visible at around 3.88 Å, but the peak shape is broad and the intensity is low compared to the  $[\text{PO}_x\text{S}_{4-x}]^{3-}$  S – S peak even though there are more Li-polyhedra than P-polyhedra in the material. The S – Li – S bond angle was calculated to be 100.1°. The crystal structure of  $\beta\text{-Li}_3\text{PS}_4$  contains tetrahedral and octahedral sites for the Li ions. The S – Li – S bond angle in an ideal tetrahedron is 109.5°, while it is 90° in an ideal octahedron. Therefore the calculated bond angle of 100.1° could be interpreted as a mix of tetrahedral and octahedral coordinated Li ions. However, for the above-mentioned reasons, other distorted geometries are also expected, leading to the glassy character of the material proven by the fast intensity decrease of the PDFs at high r values.

Neutron PDFs were collected at 300 and 100 K. At low temperatures, the resolution can get better due to the suppression of thermal motion. Additionally, thermally-activated rotations or vibrations of structural moieties, in this case, for example, the  $[\text{PO}_x\text{S}_{4-x}]^{3-}$  tetrahedra, that could have an averaging effect can be “frozen out”. A frequently discussed topic for the understanding of fast ion conduction in Li thiophosphates is the so-called “paddle wheel effect”, which describes a correlation between cation and anion motion.[99–101]. According to this theory, the tetrahedral species can rotate, thereby pushing the Li-ions through like a paddle wheel. Being able to turn this rotating motion of the tetrahedral units on and off by measuring the PDF at different temperatures could help to answer the question if the paddle wheel effect exists in oxy-sulfide glasses. Comparing the two datasets (Figure 21 A, B), however, the PDFs show few obvious deviations. Three peaks get notably sharper and more intense; Li – S at 2.53 Å, S – O at 2.91 Å, and Li – P at 3.1 Å.

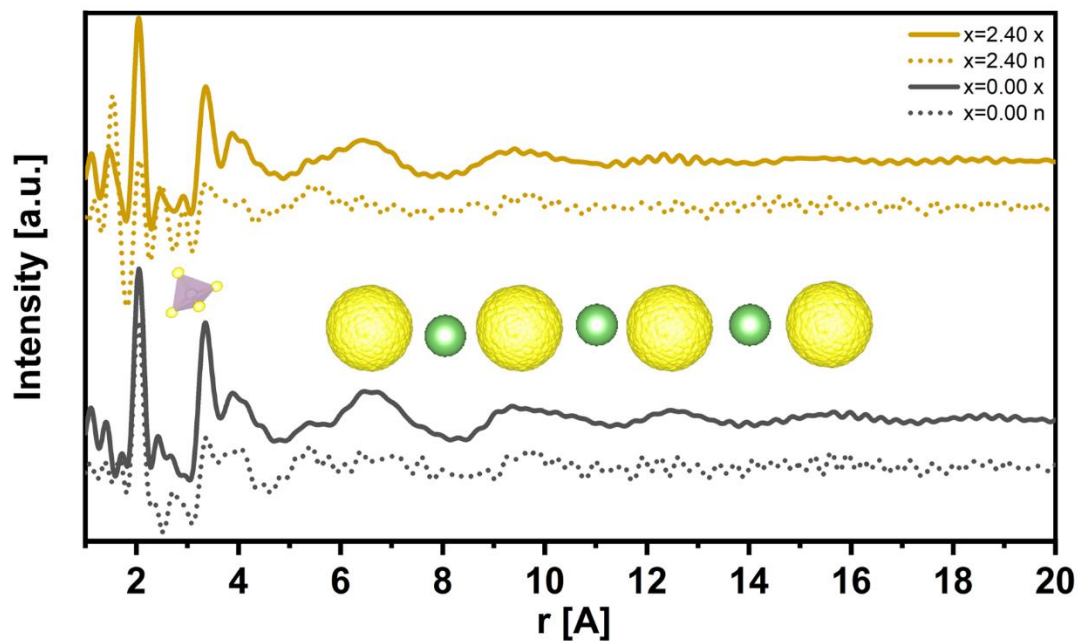


21: Comparison of neutron PDF at 100K (A), neutron PDF at 300K (B), and synchrotron PDF at RT (C).

The Li – S bond should naturally become more defined as the Li-ion mobility is reduced because Li is more likely to be found in its thermodynamically ideal position at low temperatures when there is not enough thermal energy to move to a less ideal configuration. The sharpening of the Li – P peak is most likely a direct consequence of the more defined Li – S bond because the sulfur is connecting Li and P. The sharpening of the S – O peak implies, that the mixed  $[\text{PO}_x\text{S}_{4-x}]^{3-}$  tetrahedra are more flexible than the pure  $[\text{PS}_4]^{3-}$ , which is in line with the observation of distortion for the  $[\text{PO}_x\text{S}_{4-x}]^{3-}$  tetrahedra. No additional features in the mid and long-range correlations can be found. The large termination ripples make a reliable interpretation of small features in this region impossible. Concerning the paddle wheel effect, there is therefore no direct hint neither for, nor against it. The absence of additional features in the high  $r$  region of the low-temperature PDF could be used as an argument against the effect because turning off a possible rotating motion of the tetrahedra should reveal new features. However, if the orientation of the tetrahedra towards each other is truly random even without any rotating motion, the PDF cannot distinguish between rotating and randomly orientated static tetrahedra.

While the short-range order is more detailed in the neutron PDFs, the information on the mid-range order, 5 - 20 Å can be better analyzed from the synchrotron PDFs because there is less peak overlap at higher  $r$ . The oscillations in the PDFs between 5 and 20 Å describe the ordering of the  $[\text{PO}_x\text{S}_{4-x}]^{3-}$  tetrahedra. Since the Li ions separate the tetrahedra, they have to keep a certain distance from each other, which is defined by the Li coordination environment, as mentioned in the synchrotron PDF discussion. The oscillations only describe the distance between the  $[\text{PO}_x\text{S}_{4-x}]^{3-}$  tetrahedra, with no information about the orientation of these tetrahedra towards each other, essentially describing the packing of large spheres (randomly orientated tetrahedral stacked on top of each other) as pictured in Figure 22. Any defined orientation of neighbouring tetrahedra towards each other would be decoded in features on top of the oscillations. In the discussion of the synchrotron PDFs, a faster depletion of these oscillations for the samples with higher oxygen content was found. Introducing oxygen adds

uncertainty to the bond length because P – O and Li – O are significantly shorter than P – S and Li – S, causing the loss of long-range correlation between the  $[\text{PO}_x\text{S}_{4-x}]^{3-}$  tetrahedra.



22: Schematic illustration of angle deformation in mixed tetrahedra.

### 3.1.6 Structure model refinement with RMC

Amorphous materials per definition do not have a long-range ordered structure, hence they cannot be reduced to a small unit cell, with 3D periodicity, which is the basis for so-called small-box modelling approaches like (real-space) Rietveld refinement. Therefore, large box modelling, using the RMC method, is necessary to obtain a better understanding of the real structure and help to interpret more subtle features found in the PDFs. In this work, the program RMCprofile was used for RMC modelling.[75] First, a starting model is needed which can be subsequently refined to fit the observed PDF data. Because there is no unit cell data for the oxy-sulfide glasses, a molecular dynamics (MD) simulated model was created by Dr. Marcel Sadowsky (University of Darmstadt).  $\beta$ - $\text{Li}_3\text{PS}_4$  was taken as the initial structure because it is the first crystal phase that appears when crystallizing amorphous  $\text{Li}_3\text{PS}_4$ . The  $\beta$ - $\text{Li}_3\text{PS}_4$  structure model was amorphised by density functional theory (DFT) calculation, heating to high temperatures while expanding the box followed by instantaneous cooling and equilibration of the box size. The DFT calculated amorphous structures were then used to train a machine learning (ML) potential. The ML potential allows for an accurate calculation of larger structures with more atoms using molecular dynamics (MD), which would take immense computational power and time to simulate using DFT. Since RMCprofile can handle

up to several thousand atoms, a large structure model is beneficial to have good statistics for the refinement.

Constraints are a useful tool in RMC fitting; they allow for some control over the process and prevent unphysical results. All information gathered about the material before the fitting should be used to set meaningful constraints and guide the program. In the case of Li-oxy-sulfide glasses, the main concern is the integrity of  $[\text{PO}_x\text{S}_{4-x}]^{3-}$  tetrahedra. All previous structure analysis tools have unanimously shown these structural units make up most of the material. Consequently, constraints need to be set that force the program to keep the tetrahedral symmetry of the  $[\text{PO}_x\text{S}_{4-x}]^{3-}$  units. There are multiple options on how to achieve this goal: The easiest option is the distance window constraints. As the name suggests, a minimum and a maximum distance is set for each pair of atoms, creating a distance window which restricts the movement of the atom pairs. Reasonable distance windows can be found by looking at the PDF and choosing the edges of the corresponding atom pair peak. Distance window constraints work well for isolated and uncorrelated peaks, where the distance windows function as peak assignments, and the program can easily model each peak by only moving atoms of the corresponding atom pair. For more complex structures, the distance window constraints often create box-like partial PDFs because intensity piles up at the edges of the distance windows as atoms get stopped there when the algorithm tries to move them further away to fit another feature. Besides, the distance window constraint only constraints distances, or bond length, not bond angles. As a result, this constraint is in this case not sufficient to keep the integrity of molecular structures or coordination polyhedra.

Another approach is to set up a molecular potential, meaning a P – S and a P – O bond, and the three bond angles; O – P – O, O – P – S, and S – P – S are defined and given a potential energy. Here the constraint is purely used to prevent the disassembly of tetrahedral units, thus the potential energy is arbitrarily chosen to be strong enough to keep the tetrahedra intact but still allow for some distortion, especially for the mixed tetrahedra. A potential can also be given to other bonded atoms, like Li – S and Li – O. RMCprofile will then try to model these bonds to create a Gaussian-shaped peak around the ideal bond length that has to be set. The width of the Gaussian peak is determined by the bond energy and experiment temperature given to the program. Given that the temperature is usually known, the bond energy should be chosen so that the peak width created through the potential constraint matches the actual peak width of the PDF.

A third option that is available to constrain the fitting in RMCprofile, is to give it an ML potential. Having a trained ML potential to guide the fitting is arguably the most sophisticated method, considering that the ML potential contains information on all distances and angles in the model. Nonetheless, the success of the fitting will strongly depend on the accuracy of the ML potential.

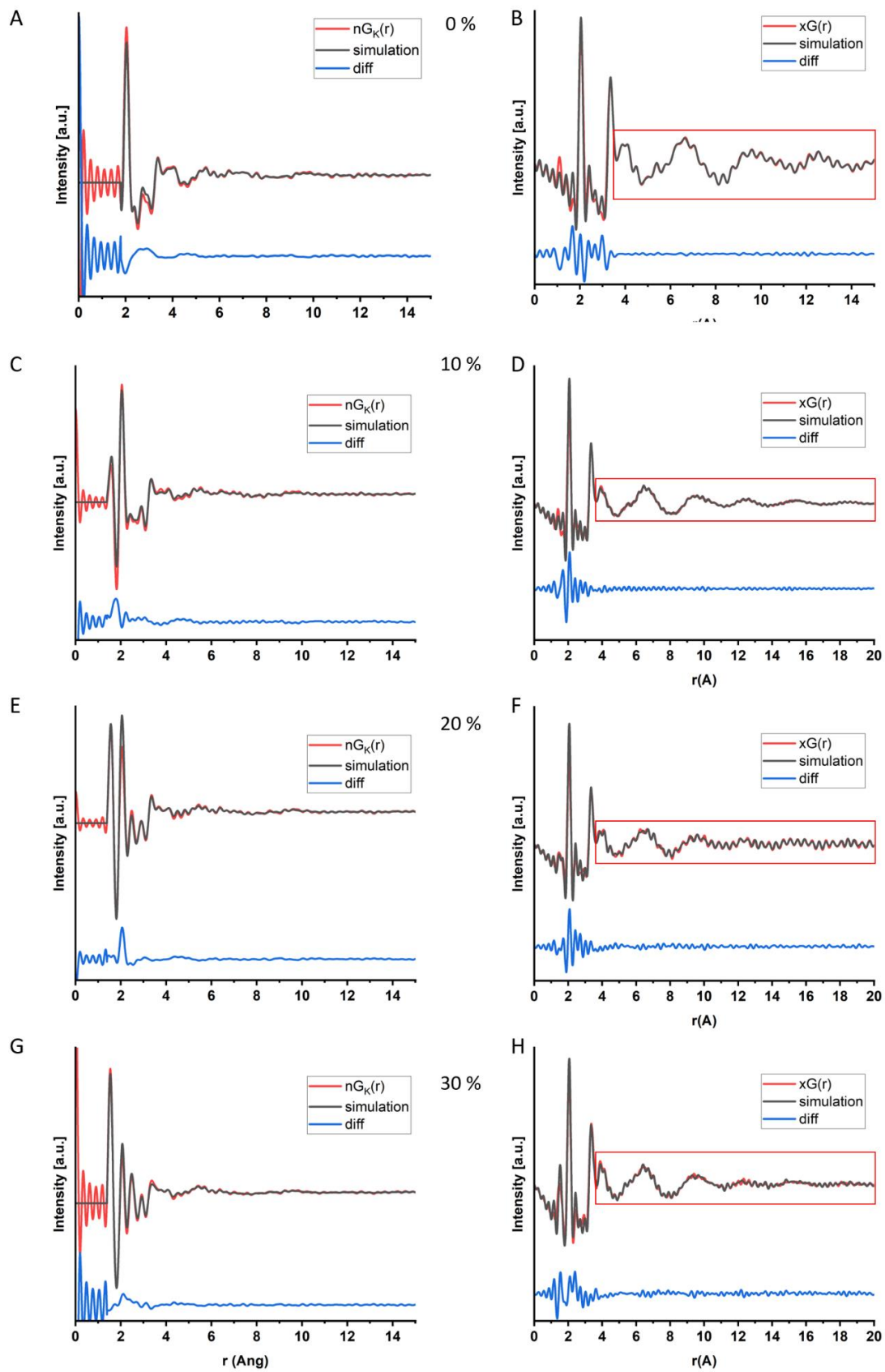
All three approaches were used for the refinement of Li-oxy-sulfide glass structures. The best results could be achieved with the use of molecular potential constraints. The sample with an intermediate oxygen concentration of 20 % was used to essay and evaluate the different strategies to find the most suitable approach. RMCprofile allows the simultaneous fitting of different data sets, e.g. synchrotron and neutron total scattering as well as EXAFS. Nevertheless, simultaneous fitting of synchrotron and neutron data initially resulted in unsatisfactory and often physically unsensible partial PDFs and/or structure models. It should be noted that both datasets were measured on samples from two different batches of the same material, which may explain some of the mismatch. Variations in the amount of impurities like  $[P_2S_6]^{4-}$  and  $[P_2S_7]^{4-}$  units found in the MAS-NMR and Raman data (see Chapter 3.1.3.) can alter the scale of certain peaks. Both impurity phases were not integrated into the model, instead, the model was chosen to only contain  $[PO_xS_{4-x}]^{3-}$  tetrahedra with the correct distribution that was taken from the NMR results. The reasoning behind this approach was that the PDFs do not show any distinct features that can be assigned to the impurity phases. Such weakly constrained units might increase the risk of overfitting. In addition, the simulation of the starting model becomes much easier. However, these impurity phases can change the intensity ratio of the peaks, which led to difficulties for the scaling of the data, especially for simultaneous fitting. To overcome this challenge and still use all of the available data for the refinement, only the high  $r$  region ( $r \geq 3.7 \text{ \AA}$ ) of the synchrotron  $G(r)$  was included, as this region of the synchrotron data adds additional information for the orientation of the  $[PO_xS_{4-x}]^{3-}$  tetrahedra (red boxes in Figure 23).

The simultaneously refined datasets were; neutron  $G_K(r)$ ,  $F(Q)$  and Synchrotron  $G(r \geq 3.7 \text{ \AA})$ ,  $F(Q)$ . Although  $F(Q)$  and  $G(r)$  or  $G_K(r)$  contain the same data, each emphasises different aspects. While most intense features in the  $G(r)$  mainly describe the local structure, the  $F(Q)$  highlights the mid and long-range order. Consequently, the simultaneous refinement of the model to both functions is often advisable.

When comparing the simulated PDF of the starting model to the data, all features are represented, and the fit is good enough for further refinements (see Appendix Figure 49). The main discrepancy between the initial simulation and the data lies in the Li environment; the Li – O partial PDF is broader in the simulation, whereas the Li – S partial is too narrow. From a chemical point of view, a narrow Li – O bond distribution is sensible since oxygen has a higher bonding energy with lithium than sulfur. Consequently, the Li ions get “pulled” toward the oxygen atoms. The sulfur atoms cannot always follow, as they are bound by the well-defined  $[\text{PO}_x\text{S}_{4-x}]^{3-}$  tetrahedra, creating a broader distribution of Li – S bonds

The molecular potential has proven to be a suitable constraint after careful adjustment of the bond and angle potential energies. By constraining the P – S and P – O bond lengths as well as the O – P – O, O – P – S, and S – P – S bond angles, O – O, O – S, and S – S are ultimately controlled as well. The Li – S, and Li – O bonds were also constrained with a potential energy, but the angles were not as all evidence points to an undefined Li environment. With the described strategy, the RMC simulations successfully refined the structure model to accurately reproduce both neutron and synchrotron total scattering data for all samples with oxygen substitution levels of 0, 10, 20 and 30 % whilst remaining physically sensible. Figure 23 presents the fitted  $G(r)$ s of all samples. The  $F(Q)$ s, as well as the simulated partial PDFs, can be found in the appendix Figure 50.

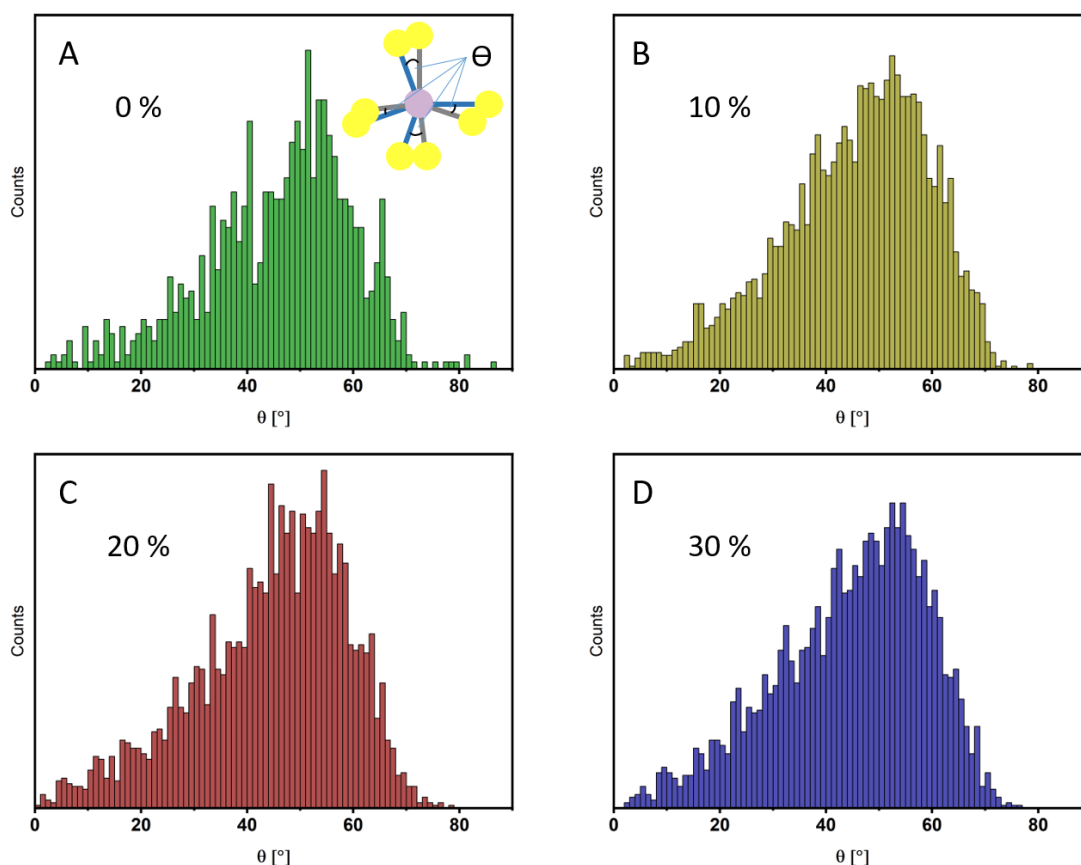




23: Neutron (left) and synchrotron (right) data and simulations from RMC refined structures for oxy-sulfide glasses with 0 (A, B), 10 (C,D), 20 (E, F) and 30 % (G, H) oxygen substitution. Red boxes mark the region that was used in the RMC simulation.

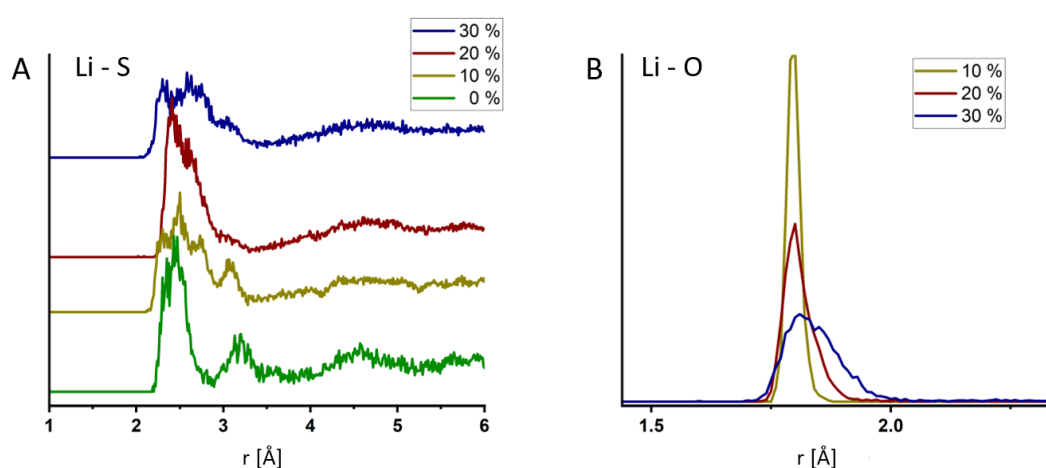
The main discrepancies between data and simulations can be found in the intensity ratio of the first three peaks. As explained above, the disregarded impurity phases are most likely the reason for this error.

For further analysis of the structure, the orientation of  $[\text{PO}_x\text{S}_{4-x}]^{3-}$  tetrahedra towards each other was examined by calculating the angles between the P – O/S bonds of each tetrahedron with its nearest neighbour. From the resulting histograms of angles, displayed in Figure 24, a nearly random configuration can be assumed for all examined structure models. The model that was refined to the LPS data with 0 % oxygen substitution had fewer atoms than the models for the other three samples, thus, the statistics for the angles are slightly worse. In conclusion, no evidence for any ordering of  $[\text{PO}_x\text{S}_{4-x}]^{3-}$  tetrahedra was found. Moreover, the substitution of oxygen does not seem to affect the orientation of the tetrahedra towards each other.



24: Histograms of calculated angles between nearest  $\text{PO}_x\text{S}_{4-x}$  tetrahedra for structures with 0 (A), 10 (B), 20 (C) and 30% (D) oxygen substitution. Two nearest tetrahedra are placed on top of each other and the smallest angle between each pair of bonds is calculated (A inset).

Additionally, the influence of oxygen substitution on the Li environment was studied by examining the Li – S and Li – O partial  $G(r)$ s. The first Li – S peak is notably broadened in the samples containing oxygen compared to the pure LPS, especially towards higher  $r$  (Figure 25 A). This broadening was hypothesised earlier as a result of the short Li – O bonds. The Li is orientated closer to adjacent oxygen atoms. Hence, the distances to adjacent sulphur atoms are increased. The features, that appear at 10 % oxygen substitution on top of the peak are most likely results of overfitting. Because the Li – S and O – O peaks cancel each other out in intensity, both are only weakly defined by the data. The Li – O peak exhibits a similar behaviour, the peak also broadens with increasing oxygen substitution. The broadening could be explained by the increasing possibility of multiple oxygen atoms surrounding one Li atom. If the structure does not allow the Li to be positioned close to all adjacent oxygen atoms, some Li – O bonds will increase, causing a broader Li – O peak.



25: Li - S (A) and Li - O (B) partial  $G(r)$ s calculated from the refined structure models.

### 3.1.7 Summary and conclusion

In this chapter, the tangible influence of oxygen substitution on the atomic structure of Li oxy-sulfide glasses is examined by careful structure analysis, combining several analytical techniques. As a result, all oxygen-containing structural moieties were identified and quantitatively analysed. Further, the comparison to previous experiments established a link between precursor materials and product structure, which led to a better understanding of the synthesis procedure and improved the control over the product structure and properties. The following electrochemical analysis revealed that each of the oxygen-containing structural units contributes differently to the total ionic conductivity of the material; highly oxygenated

tetrahedra are more detrimental to the Li-ion conductivity than those containing less oxygen. Thus, the total oxygen content, as well as the distribution of oxygen within the material, needs to be controlled to achieve the best compromise of stability and conductivity. In an effort to understand the precise influence of oxygen on the Li environment and glass network, the materials were studied by neutron total scattering in combination with RMC modelling. The investigation revealed short P – O and Li – O bonds, leading to a contraction of the network, and an increasing bond length disorder with increasing oxygen substitution, whereas the orientation of tetrahedral units seems to be unaffected. The results strongly suggest that the stronger Li – O bond is mainly responsible for the negative effect of oxygen on the conductivity. However, the multitude of possible Li coordination arrangements and the non-linear relationship of activation energies for local hopping processes and ion conductivity hint at more complex correlations. Unravelling these correlations will remain the task for future investigations.

## 3.2 Influence of oxygen substitution on the crystallisation behaviour of Li oxy-sulfide glasses

### 3.2.1 Experimental

The glass-ceramics were synthesised by calcination of the oxy-sulfide glasses at 250 °C under vacuum in a glass oven (Büchi, Germany) for 12 h.

High-temperature impedance spectroscopy measurements were performed inside a custom cell designed for temperatures up to 600 °C (a description of the components and construction of the cell can be found in the following chapter). The samples were pressed into a pellet at 400 MPa for one minute. The pellet was loaded into the cell and covered by Ti-sputtered aluminium disks to prevent reactions between the sample and the electrodes. The cell was sealed inside an Ar-filled glovebox. The sealed measurement cell was placed inside a tube furnace and contacted by an Al<sub>2</sub>O<sub>3</sub>-shielded KANTHAL® wire. Two parts of a glass tube were placed around the cell, and the gap was filled with glass wool. The experiment was carried out under a steady Ar flow. The furnace temperature was ramped up to 150 °C within 10 min, and then increased further in steps of 50 °C, within 5 min, up to a maximum temperature of 500 °C. At every step, the temperature was held for 90 min and an EIS experiment was performed every 5 min.

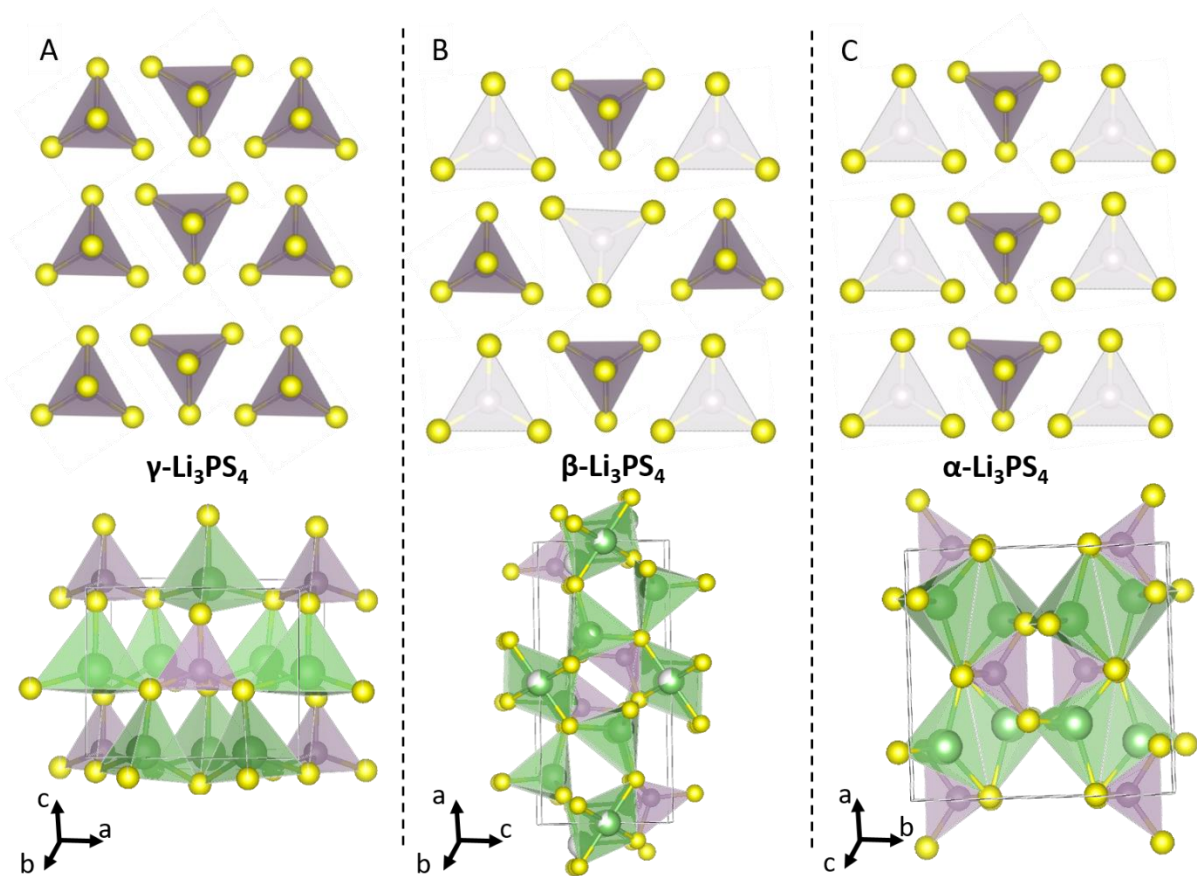
### 3.2.2 Introduction Crystal Phases of LPS

Another important aspect, still under debate, concerns the crystallinity of the electrolyte. Can a crystallisation step enhance the Li-ion conductivity of thiophosphate or oxy-sulfide electrolytes? In theory, a perfectly crystalline material should be ideal for ion conduction, because a perfectly ordered crystal provides straight channels for the ions to move through, whereas in glass, the tortuosity is inherently much higher. However, the described scenario is idealised and almost impossible to achieve in a real system. Achieving straight ion channels through the whole electrolyte layer is practically impossible, as it would necessitate the entire electrolyte layer to be composed of a single crystal with a precise orientation. In practice, pressed polycrystalline powders are commonly used. Therefore, the electrolyte layer contains a lot of crystallites with random orientation and the ion channels do not necessarily line up. The result of this mismatch is a grain boundary resistance. For a crystal structure where ions can move in all three dimensions, the transition between two grains with different orientations should be easier than for a crystal structure with only one-dimensional

conduction channels. For glassy materials, these grain boundaries are arguably less impactful, because there are no clear channels that can align or misalign as the ion transport properties are approximately isotropical in all directions. Moreover, the structure of the anion network determines the available atom positions that Li can occupy and their coordination environment. Hence, there is no definite answer to the question if crystalline or glassy materials are better ion conductors, it depends on the exact material that is being used. For LPS, the consensus in the literature seems to be, that glassy LPS is a slightly better Li-ion conductor than the crystalline  $\beta$ -LPS. However, the conductivity values for both materials are in the range of  $10^{-4}$  S cm<sup>-1</sup> and there is still some controversy over which material performs best in a battery. Recent studies by Lu et al.[47] and Tsukasaki et al.[48] suggests that the highest conductivity may be achieved with an intermediate composition of an amorphous material containing a small fraction of crystallites. Consequently, after studying the influence of oxygen substitution on the LPS glasses, the crystallization behaviour of the oxy-sulfide glasses was investigated to understand the influence of oxygen on the crystallization behaviour, crystalline phases, and Li-ion conduction of these crystalline phases.

Li<sub>3</sub>PS<sub>4</sub> (LPS) has three known crystalline phases, which are stable at progressively higher temperatures;  $\gamma$ -LPS,  $\beta$ -LPS, and  $\alpha$ -LPS.  $\gamma$ -LPS is the room temperature phase, it has an orthorhombic symmetry (space group  $Pmn2_1$ ) as illustrated in Figure 26 A, and its ion conductivity is the lowest of the three phases with  $3.0 \times 10^{-7}$  S cm<sup>-1</sup>. [102] The phase transition to  $\beta$ -LPS occurs at around 300 °C. [103]  $\beta$ -LPS crystallizes in another orthorhombic space group  $Pnma$ , seen in Figure 26 B, and has a significantly higher Li-ion conductivity in the order of  $2 \times 10^{-4}$  S cm<sup>-1</sup>. [47, 48] At 500 °C a second phase transition to the  $\alpha$ -LPS phase can be observed. [103]  $\alpha$ -LPS also has an orthorhombic crystal structure (space group  $Pbcn$ ) that is depicted in Figure 26 C. Because the  $\alpha$  phase is only stable at elevated temperatures and transforms back to the  $\gamma$  phase upon cooling, the RT conductivity of  $\alpha$ -LPS is unknown. From ab initio molecular dynamics (AIMD) calculations, an RT conductivity of about  $8 \times 10^{-2}$  S cm<sup>-1</sup> was predicted. [104] For practical application,  $\beta$ -LPS is thus the preferred crystal phase, as it has high RT conductivity and does not transform back to  $\gamma$ -LPS. As Figure 26 illustrates, the main difference between all three phases is the orientation of the [PS<sub>4</sub>]<sup>3-</sup> tetrahedra, which ultimately changes the Li coordination. In  $\gamma$ -LPS, all Li-ions are coordinated in corner-sharing tetrahedral sites, while in the  $\beta$ -LPS phase, the coordination alternates between tetrahedral and octahedral coordination symmetries. In the high-temperature  $\alpha$ -LPS phase, the

coordination returns to purely tetrahedral, but in contrast to the  $\gamma$  phase, the tetrahedra in the  $\alpha$ -LPS phase are edge-sharing instead of corner-sharing, bringing the Li positions closer together.

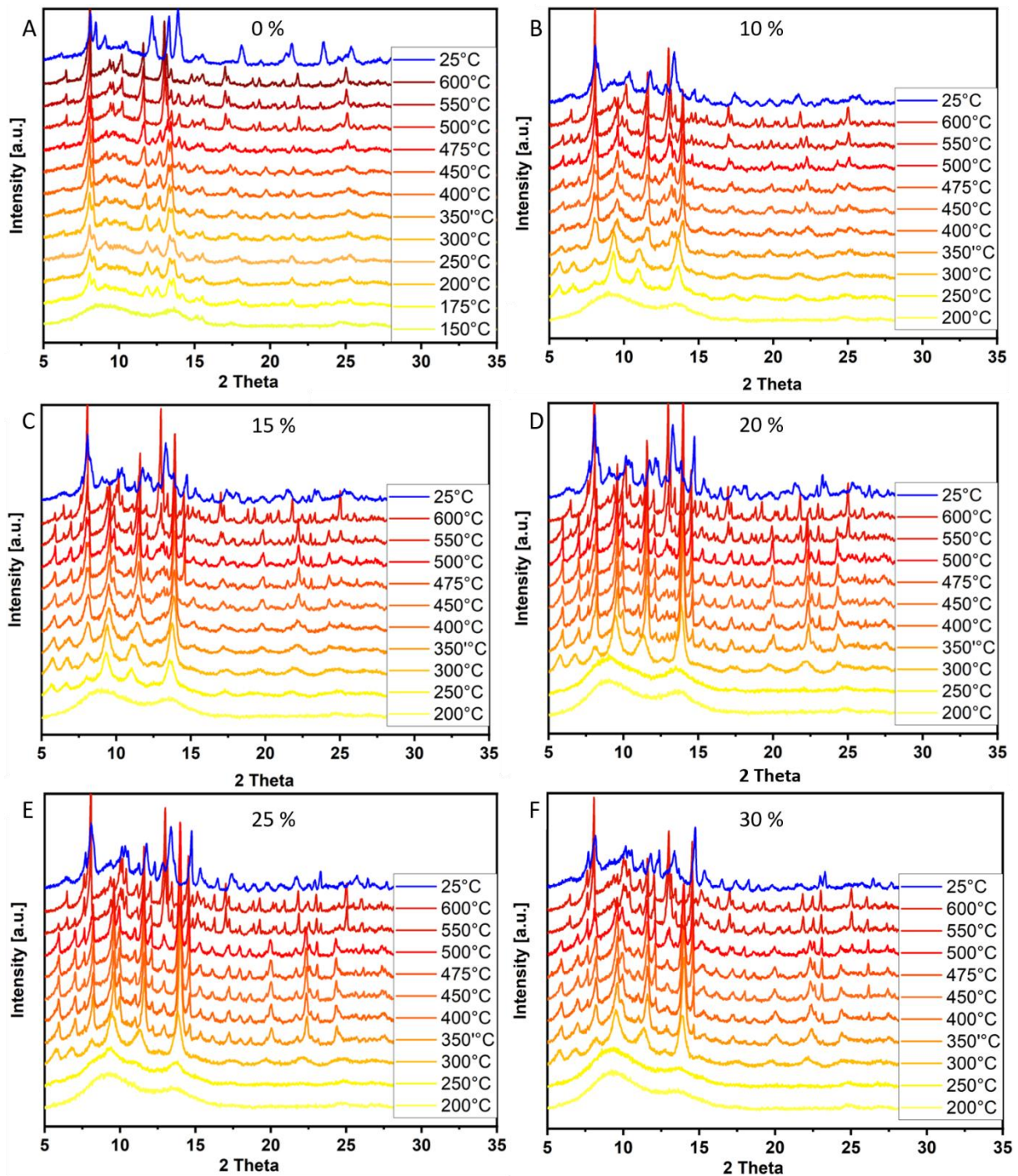


26:  $[PS_4]_3$ -tetrahedra orientation and crystal structure of  $\gamma$ -LPS (A),  $\beta$ -LPS (B) and  $\alpha$ -LPS (C).

### 3.2.3 Temperature-dependent structure analysis

To investigate the crystallisation behaviour of the oxy-sulfide glasses, first, a series of temperature-dependent XRD experiments were performed. The samples were heated from RT to 150 °C and then stepwise further up to 600 °C in increments of 50 °C. An XRD pattern was recorded at every temperature step, while the temperature was held constant. Afterwards, the sample was naturally cooled down to RT, and another XRD experiment was performed. All oxy-sulfide samples exhibit similar behaviour, which differs from the crystallisation behaviour of the reference LPS sample without oxygen substitution. The LPS sample behaves as expected; the onset of crystallisation was found between 150 and 175 °C, and the crystallinity then increases with increasing temperature, indicated by the narrowing of the reflections. A phase transition can be observed between 475 and 500 °C. A third phase appears upon cooling back to RT (Figure 27 A).

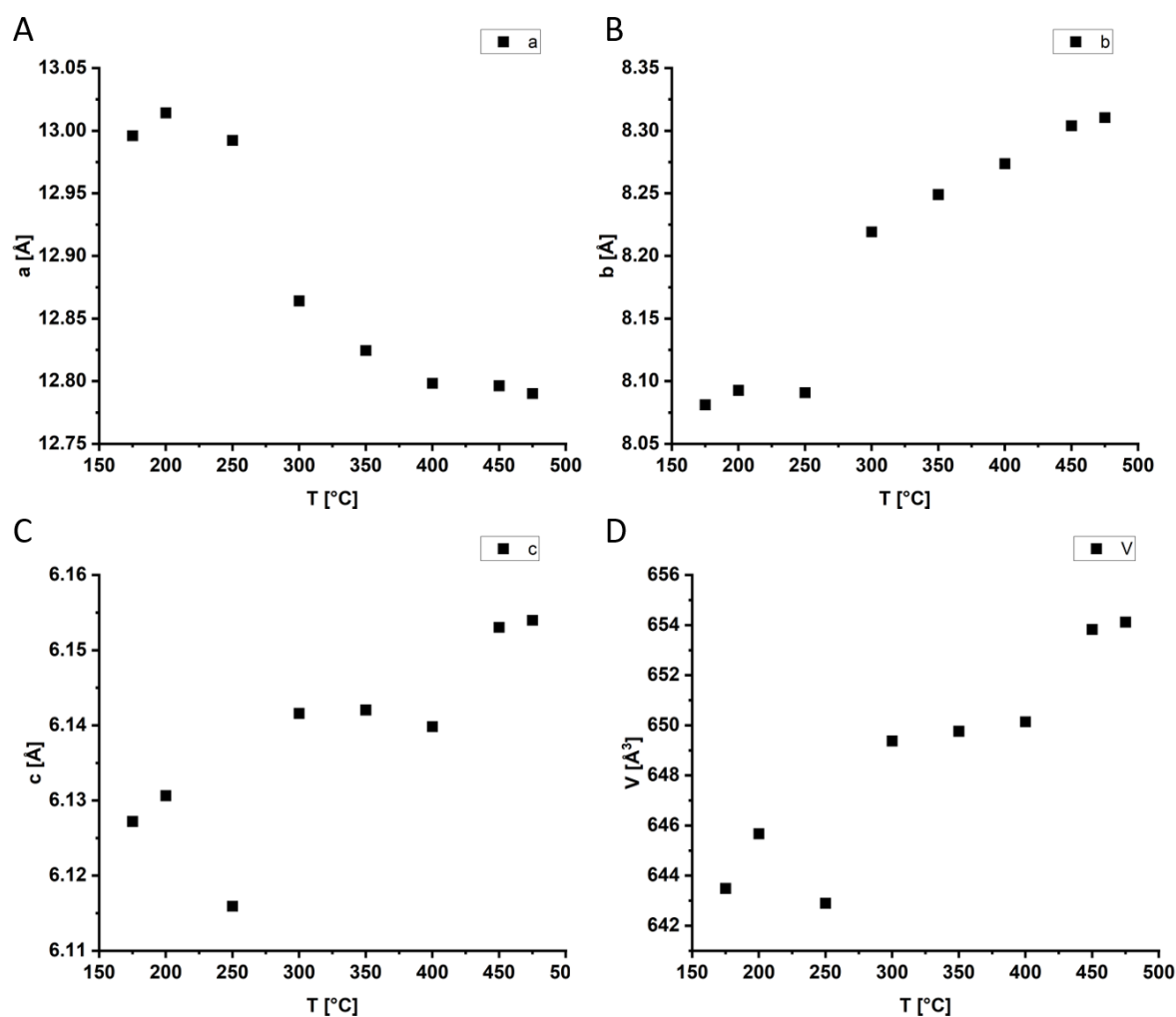
For the oxy-sulfide glasses, the crystallisation temperature gradually increases with increasing oxygen content. Even with an oxygen content of only 10 %, the sample remains amorphous up to temperatures above 200 °C and finally crystallises at 250 °C. At 20 % oxygen, the crystallisation temperature further increases to 300 °C. With increasing temperature, the crystallinity increases. Additionally, other crystalline phases can be identified. The crystallisation temperature, type and phase fraction of these additional phases change depending on the oxygen concentration (Figure 27 B - F).



27: Temperature-dependent XRD of LIO samples. Percentages denote the level of oxygen substitution.



All appearing crystal phases were identified by comparison with reference data from the ICSD database. Subsequent quantitative phase analysis was performed during Rietveld refinement. For the LPS sample, the initial crystalline phase, appearing at 175 °C, was refined with the  $\beta$ -LPS structure, in line with literature reports on the crystallization of LPS.[42] The temperature is below the reported transition temperature for the  $\gamma$  to  $\beta$  phase transition, thus, the crystallisation of  $\beta$ -LPS from the glassy state must have a lower activation energy than the transition from  $\gamma$ -LPS. The clear identification of the crystal phase is not trivial, due to the similarity of both structures ( $\beta$  and  $\gamma$ -LPS) and the extensive peak broadening due to the low crystallinity. A mix of both  $\gamma$  and  $\beta$ -LPS or another intermediate structure are also likely scenarios. One argument against a pure  $\beta$ -LPS is another notable transition between 250 and 300 °C, signalled by a sudden change in the lattice parameters (Figure 28). The temperature range fits the phase transition temperature published for the  $\gamma$  to  $\beta$ -LPS transition.[103] An additional reflection appears at  $13.9\ 2\theta$  in the diffractograms between 400 and 550 °C.



28: Cell parameter (A-C) and unit cell volume (D) versus Temperature for  $\beta$ -LPS.

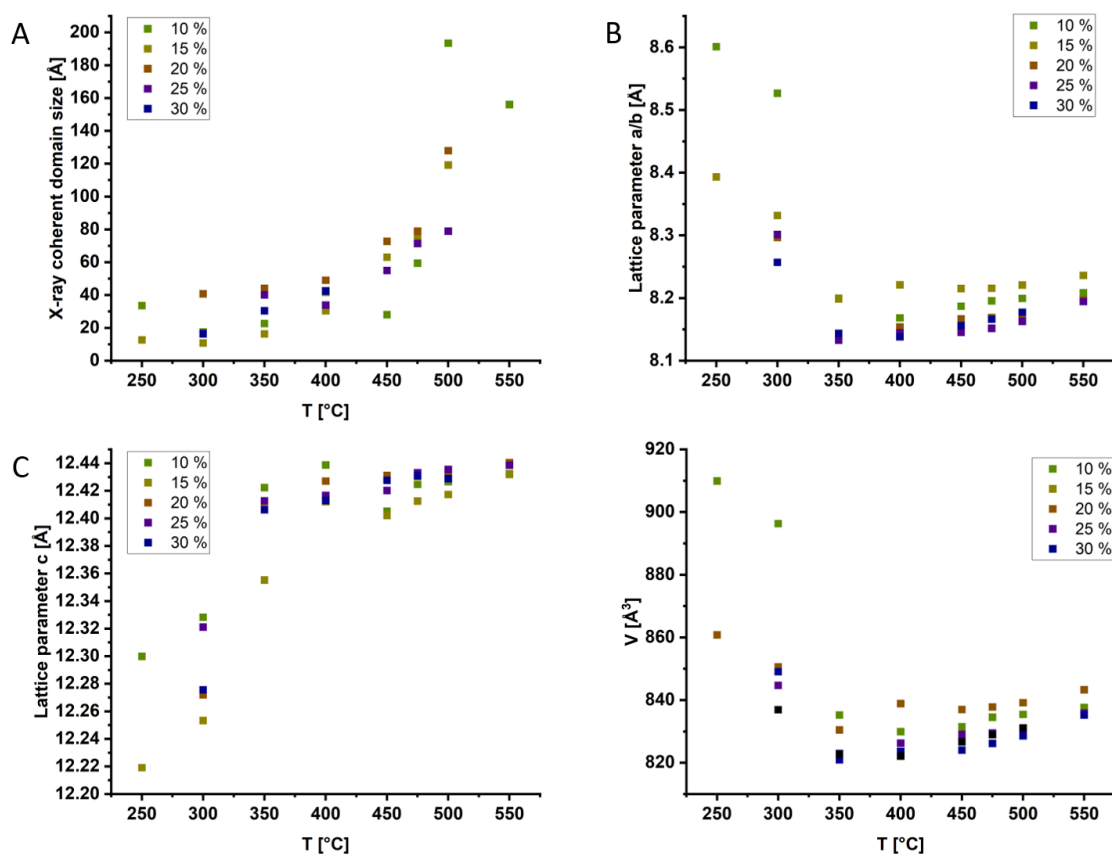
This additional reflection can be modelled by an LGPS-like phase in the  $P4_2/nmc$  space group. Kato et al. described the formation of an LGPS-like LPS structure, which forms when an excess of Li is used in the synthesis.[19] Small weighing errors or a non-homogenous distribution of Li within the sample could trigger the formation of such a Li-rich LGPS-like phase. It has to be noted, however, that a single reflection is not a clear proof, but rather an indication.

Features of  $\alpha$ -LPS can be identified, starting at 475 °C and the diffractograms at 500, 550, and 600 °C can be modelled almost exclusively with the  $\alpha$ -LPS phase. The additional reflection assigned to the LGPS-like phase disappears at 600 °C. The third phase appearing when the sample is cooled back down to RT could be identified as 100 %  $\gamma$ -LPS. All Rietveld refinements can be found in the Appendix (Figure 51 - 56).

In contrast to the pure LPS sample, the oxy-sulfide glasses do not initially crystallize in neither  $\gamma$  nor  $\beta$ -LPS phase. In all cases, the first crystalline phase is a nanocrystalline phase, that can be refined in the LGPS-type structure ( $P4_2/nmc$  space group), which is the same structure type as the fast-conducting  $\text{Li}_{10}\text{GeP}_2\text{S}_{12}$  (LGPS).[29] The crystallite sizes were calculated from Rietveld refinement to values between ca. 10 and 40 nm at the respective crystallisation temperature. No clear correlation between oxygen substitution level and crystallite size was found. In all samples, the crystalline domain size grows exponentially with increasing temperature (Figure 29 A). Further, the Rietveld analysis of the diffractograms revealed a sudden change in the lattice parameters between 300 and 350 °C (Figure 29 B, C).

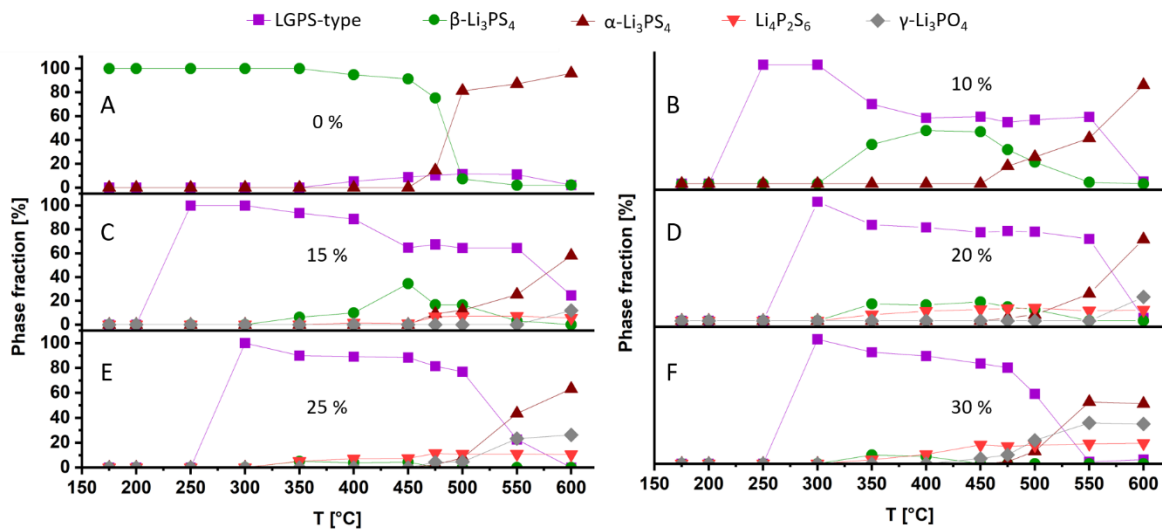
The discontinuity of the lattice parameters is most severe in the sample with 10 % oxygen substitution and becomes less prominent as oxygen substitution increases. Lattice parameters  $a$  and  $b$  are decreasing overall with increasing oxygen substitution (Figure 29 B), whereas the  $c$  parameter does not show a clear trend at low temperatures and increases with increasing oxygen substitution at high temperatures over 450 °C (Figure 29 C).

$\beta$ -LPS also appears as a secondary phase in the samples with low oxygen content, between 350 and 500 °C. Further, all samples contain crystalline  $\text{Li}_4\text{P}_2\text{S}_6$ , which forms at different temperatures depending on the oxygen content. For 10 % oxygen substitution, crystalline



29: Evolution of Crystalline domain size (A) cell parameters (B, C) and unit cell volume (D) for the LGPS-type phase in all oxysulfide samples with 0 to 30 % oxygen substitution. The results were retrieved from Rietveld refinement of the x-ray diffractograms.

$\text{Li}_4\text{P}_2\text{S}_6$  appears at 475 °C, for 15 % at 450 °C, and in samples with oxygen substitution of 20 % and more, at 350 °C already. The transition to  $\alpha$ -LPS can be observed in all samples; however, the transition temperature is dependent on the oxygen concentration. The  $\beta$ -LPS phase, which appears in the samples with up to 20 % oxygen substitution (LIO1, 2, 3), transforms to  $\alpha$ -LPS between 500 and 550 °C. The LGPS-type phase also transforms to  $\alpha$ -LPS. The transition happens between 550 and 600 °C for the samples with oxygen levels up to 20 % and shifts to lower temperatures with increasing oxygen concentration. At 600 °C, the appearance of crystalline  $\gamma$ -LPO indicates a phase separation between an oxygen-rich and an oxygen-poor phase. The refined phase fractions of  $\gamma$ -LPO agree well with the stoichiometric oxygen content. The evolution of the different phase fractions with increasing temperature can be viewed in Figure 30.

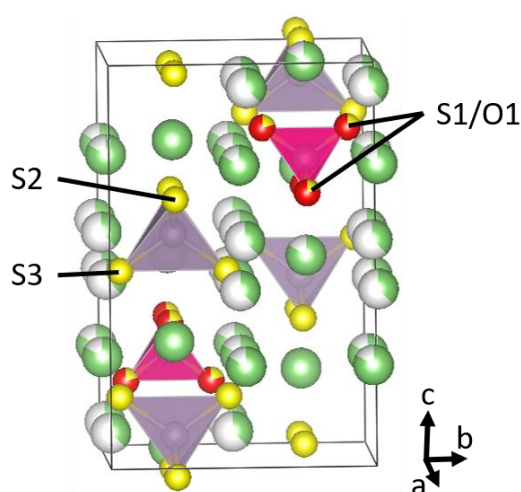


30: Evolution of phase fractions with temperature for oxysulfides with 0 to 30 % oxygen substitution. The values were retrieved from Rietveld refinement of the x-ray diffractograms.

Comparing the evolution of phase fractions with the evolution of the lattice parameters, the discontinuity in the lattice parameters between 300 and 350 °C correlates well with the appearance of secondary phases. This is most obvious for the sample with 10 % oxygen substitution as there is a high amount of  $\beta$ -LPS forming in the mentioned temperature range. Accordingly, the change in the lattice parameters is most prominent. In the samples with 25 and 30 % oxygen substitution, almost no  $\beta$ -LPS phase was found, however, other secondary phases like  $\text{Li}_4\text{P}_2\text{S}_6$  and  $\gamma$ -LPO also start to form between 300 and 350 °C. Hence, the analysis suggests that a phase separation is taking place, causing the disruption in the lattice parameters.

Oxygen substitution clearly has a large influence on crystallisation behaviour. The significant difference in P – O to P – S and Li – O to Li – S bond lengths creates micro-strain in the material and prevents the formation of  $\beta$ -LPS. Instead, an LGPS-type structure is stabilised and appears as the dominant crystalline phase. The LGPS-type structure seems to be more resistant to defects and variations of structural parameters. Literature reports on the materials in the LGPS-type structure suggest that whenever a perturbation is introduced into the 75/25  $\text{Li}_2\text{S}/\text{P}_2\text{S}_5$  system, the response is the LGPS-type structure. Famously, the aliovalent substitution of P with Ge led to the discovery of LGPS.[29] The discovery was followed by combinations with other metal ions (Si, Sn), all with the same crystal structure and high ionic conductivities in the  $10^{-3}$  S/cm range.[31, 105] The excellent conductivities render the LGPS-type structure particularly interesting for solid-state electrolyte research. The structure of the

LGPS-type can accommodate at least two different types of  $MX_4$  ( $M = P, Ge, Si, \dots / X = S, O$ ) tetrahedra,  $[PS_4]^{3-}$  and  $GeS_4$  in the case of LGPS and  $[PS_4]^{3-}$  and  $[PO_xS_{4-x}]^{3-}$  in case of the oxy-sulfides. In agreement with other literature reports, Rietveld refinement revealed that the oxygen substitution only seems to affect the S1 position (see Figure 31).[28, 106] As illustrated in Figure 31, the structure keeps an ordered arrangement of unsubstituted  $PS_4$  (purple) and substituted  $[PO_xS_{4-x}]^{3-}$  tetrahedra (pink) by restricting all oxygen substitution to the S1 position. All LGPS-type analogues have in common, that the Li content is slightly higher than that of  $Li_3PS_4$ . An LGPS-type structure can be created within the  $Li_2S / P_2S_5$  system by substituting some of the P for more Li as mentioned earlier.[19] Consequently, the same can be assumed for the observed LGPS-type structure. Suzuki et al. and Neveu et al. suggested a stoichiometry of  $Li_{3.35}P_{0.93}S_{3.5}O_{0.5}$  and  $Li_{3.2}PS_{3.7}O_{0.3}$  respectively, both containing additional Li.[26, 107] The different stoichiometry might then explain the formation of the  $Li_4P_2S_6$  phase, which contains less Li and more P than  $Li_3PS_4$  and could therefore counterbalance the formation of a Li-rich (and P-poor) LGPS-type structure. The phase fraction of both the LGPS-type and  $Li_4P_2S_6$  increase with increasing oxygen content.



31: Structure of LGPS-type  $Li_3PO_xS_{4-x}$ . Oxygen-containing tetrahedra are coloured pink.

The thermodynamically most stable compounds are  $Li_3PO_4$  and  $Li_3PS_4$ , thus, given enough time and thermal energy, a phase separation will occur as observed by the experiments. For most samples, a full phase separation requires heating to 600 °C. However, in the sample with 30 % oxygen content,  $\gamma$ -LPO already starts to appear at around 450 °C, suggesting that the reaction starts at lower temperatures. If this phase separation already starts at 350 °C, it could explain the formation of  $\beta$ -LPS in the samples with low oxygen substitution and the impact on the

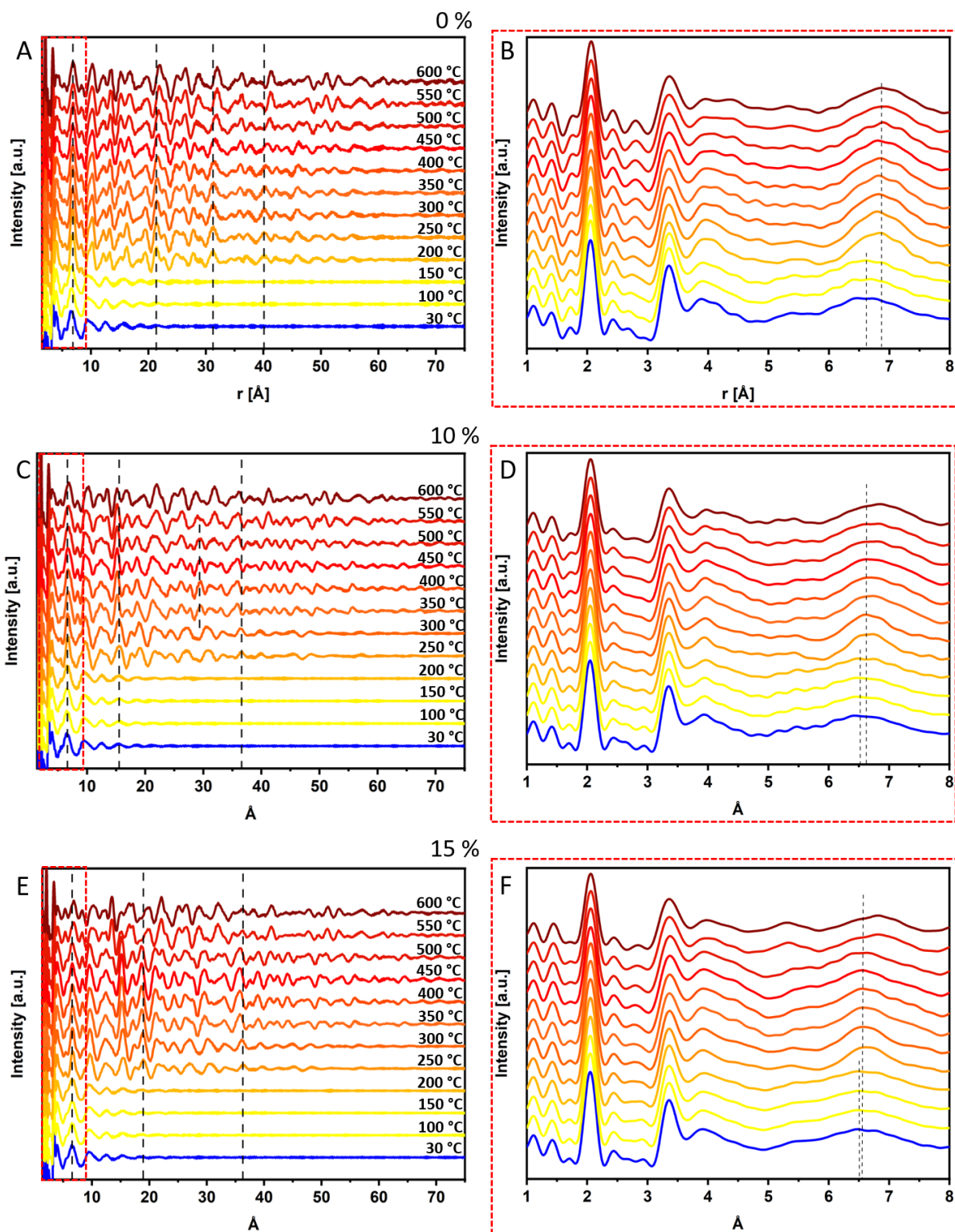
lattice parameters. When most oxygen is bound to  $[\text{PO}_4]^{3-}$  tetrahedra, the overall number of oxygen-containing tetrahedra is reduced. As a result, larger areas of unsubstituted material form, which naturally crystallise as  $\beta$ -LPS instead of the LGPS-type phase. At the same time, the effective oxygen concentration within the LGPS-like phase is increased, resulting in the observed change in the lattice parameters. Xu et al. and Suzuki et al. have demonstrated that the LGPS-type structure can also be synthesised by melt quenching which requires heating to over 700 °C followed by rapid cooling.[28, 107] Considering the observed phase separation at high temperatures, the conclusion is that these melt-quenched materials must consist mainly of  $[\text{PS}_4]^{3-}$  and  $[\text{PO}_4]^{3-}$  units with little to no intermediate  $[\text{PO}_x\text{S}_{4-x}]^{3-}$  species.

In order to investigate the evolution of structural units during the crystallisation process, synchrotron PDF measurements were conducted on the samples with 10 and 15 % oxygen substitution as well as the reference sample with 0 % substitution. The experiments were conducted at Petra III at DESY. The samples were heated from 30 °C to 600 °C in steps of 50 °C and a total scattering experiment was performed at every temperature step. The obtained  $G(r)$  functions allow investigation of possible local structure changes during the crystallisation process.

For the reference LPS sample, crystallisation is observed between 150 and 200 °C in accordance with the xrd data (Figure 32 A). The PDFs do not change significantly with higher temperatures. Even at temperatures above 500 °C, where the transition to the  $\alpha$ -phase was observed in the xrd experiments, the PDFs only exhibit slight deviations at  $r \geq 20$  Å. The low  $r$  region, depicted in Figure 32 B, stays nearly unchanged over the whole temperature range. Some peak broadening due to thermal vibrations can be observed for the P – S and S – S peaks at 2.05 and 3.35 Å respectively, but their positions stay unchanged. The second S – S peak, which is connected to the Li polyhedral, appears to sharpen upon crystallisation and then split into two overlapping peaks at higher temperatures. The next observable oscillation at around 6.6 Å notably shifts to higher  $r$  upon crystallisation, suggesting that the density of the material is higher in the glassy state.

Substituting 10 % oxygen increases the crystallisation temperature to 250 °C as discussed before. Further the high  $r$  region ( $r \geq 20$  Å) of the PDFs change between 300 and 350°C, which is attributed to the crystallisation of  $\beta$ -LPS, which appears in the xrd from this temperature on. The changes in the PDF are accompanied by an apparent shift to lower  $r$  in the region between

$r = 15$  and  $r = 20$  Å. This shift reflects the change in the lattice parameters. The low  $r$  region, presented in Figure 32 D, shows no changes with temperature other than a slight thermal broadening and the sharpening of the second S-S peak. The peaks at higher  $r$  shift less upon



32: Temperature-dependent synchrotron PDF measurements on samples with 0 (A, B), 10 (C, D), and 15% oxygen substitution (E, F). The extended  $G(r)$ s up to 75 Å are displayed on the left. The low  $r$  region up to 8 Å is presented on the right.

crystallisation compared to the reference sample, indicating that the density of the LGPS-type phase is closer to that of the glass. A shift to higher  $r$  can be detected above 550 °C as  $\alpha$ -LPS is formed.

The sample with 15 % oxygen substitution behaves similarly to the 10 % sample. The crystallisation is observed at 250 °C, followed by the appearance of  $\beta$ -LPS and shift to lower  $r$  at 350 °C and finally the phase transition to  $\alpha$ -LPS at 550 °C (Figure 32 E). The low  $r$  region (Figure 32 F) exhibits the same behaviour as discussed above

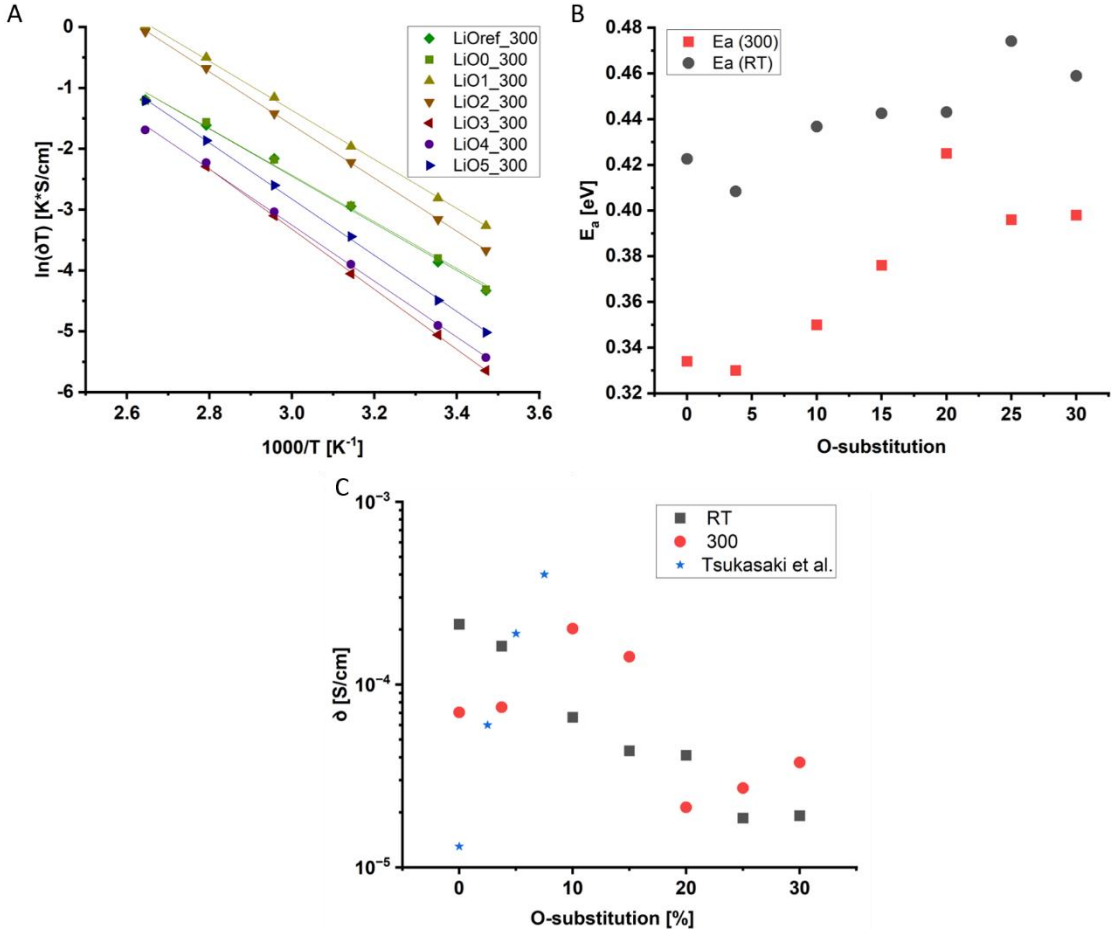
The PDF measurements indicate that the local structure of the investigated materials up to approximately 10 Å is nearly unaffected by the crystallisation process. The integrity of the tetrahedral building blocks of the anion network is kept in all appearing phases. The Li environment becomes more defined upon crystallisation as indicated by the sharpening of the second S-S peak. However, the peak shape overall stays broadened with low intensity, suggesting a high degree of disorder for the Li polyhedra in the crystalline state, or extensive movement of the  $[\text{PO}_x\text{S}_{4-x}]^{3-}$  tetrahedral at high temperatures in both  $\beta$ -LPS and the LGPS-type structure. The low scattering power of oxygen atoms with x-rays prohibits a detailed analysis of the evolution of oxygen-containing units. In order to test the proposed theory of oxygen clustering inside the LGPS-type phase at elevated temperatures, temperature-dependent neutron scattering, or MAS-NMR experiments would be needed.

#### 3.2.4 Electrochemical analysis

Impedance spectroscopy was used to investigate the electrochemical properties of the crystallised samples. The focus of the analysis was the low crystallinity phase at 300 °C. At this temperature, the LGPS-type structure forms in every sample with oxygen substitution but no crystalline impurity phases can be detected yet. Furthermore, Tsukasaki et al. published a study in 2020 where they investigated the same material class but with lower oxygen contents (2.5, 5, and 7.5 % oxygen).[45] They compared oxy-sulfide glasses and glass-ceramics which were synthesised by heating the glasses to 300 °C. When the oxygen substitution reached 5 %, the glass-ceramics crystallised in the LGPS-type structure. While the Li-ion conductivity of the oxy-sulfide glasses steadily decreased with increasing oxygen substitution, the conductivity of the glass-ceramics continuously increased with increasing oxygen content, surpassing the glass conductivity at 7.5 % oxygen substitution. A further improvement of the conductivity with more oxygen substitution was predicted but not investigated. The current work takes



over with the examination of higher substituted oxy-sulfides (10 – 30 % oxygen). The structure model and the increase of the crystallisation temperature for higher substituted oxy-sulfides are in good agreement with the observations made by Tsukasaki et al. The room temperature conductivity of the oxy-sulfide glass-ceramics does indeed increase for lower oxygen substitution levels up to 10 %. With further oxygen substitution, however, the conductivity rapidly decreases again (Figure 33 C). Temperature-dependent EIS measurements were performed on the heat-treated samples, as presented in Figure 33 A, to extract activation energies. The activation energies do not follow the conductivity trend. Low values of around 0.33 eV were found for the unsubstituted sample and the sample with 3.75 % oxygen substitution, followed by a steady increase with a spike at 20 % oxygen substitution and an activation energy of 0.43 eV. For higher oxygen levels, the activation energies drop back to 0.4 eV (Figure 33 B). Generally, the heat-treated samples all have lower activation energies than the glasses.



33: T-dependent Impedance measurements of LIO samples heated to 300 °C (A), activation energies of heat-treated samples (B), and comparison of Li-ion conductivities of oxy-sulfide glasses and glass-ceramics with reference data from [45] (C).

In comparison to the glasses, the glass-ceramics that form the LGPS-type structure, mostly exhibit a higher Li-ion conductivity, whereas the pure LPS sample has a lower conductivity after the heat treatment (Figure 33 C). Consequently, the LGPS-type structure seems to be more advantageous for Li-ion conduction as compared to  $\beta$ -LPS. The conductivity values reported by Tsukasaki et al. are also included in the Figure as blue stars. The data fit reasonably well except for the unsubstituted sample, which has a much higher conductivity in the current experimental series. The predicted increase in conductivity for higher oxygen substitution levels could not be confirmed. Instead, the conductivity exhibits a maximum at around 10 % (or 7.5 % including the reference data) and then decreases for higher oxygen substitution levels. The reason for this might be the increasing activation energies.

Nevertheless, heat treatment could be a promising method to maintain high conductivity values at comparably high oxygen substitution levels.

The wavy shape of the conductivity trend hints at multiple different factors with opposite effects on the ionic conductivity. On the one hand, the formation of the LGPS-type structure has a positive effect on the conductivity. As other materials with the same structure (LGPS, LiSiPS, etc.) have demonstrated, the LGPS-type structure facilitates Li-ion transport due to the formation of fast-conducting 1D channels along the c-axis with partial occupancies for all Li sites along the conduction pathway.[29] A higher oxygen substitution leads to a larger phase fraction of LGPS-type structure and therefore should be beneficial for the ionic conductivity. On the other hand, oxygen binds more strongly to Li than sulphur. The strong coordination reduces Li-ion mobility, as indicated by the increasing activation energies. The study of the oxy-sulfide glasses had already shown that the Li-ion conductivity generally decreases with increasing oxygen substitution (see Chapter 3.1.4). The observed conductivity trend indicates that for low oxygen concentrations, the benefits of the superior crystal structure outweigh the negative consequences of the oxygen atoms in the structure. However, once the oxygen concentration increases, more and more Li ions get “trapped” by oxygen, and for oxygen substitution levels above approximately 10 %, the increase in LGPS-type phase fraction cannot compensate for the slower kinetics of Li ions connected to oxygen. The increase of the activation energy with increasing oxygen concentrations supports this assumption. While the LGPS-type structure provides faster conduction pathways, Li ions need a higher activation energy to jump past the oxygen atoms. In addition to the optimum at 10 % oxygen substitution, the conductivity trend also features a minimum at 20 % oxygen substitution. The

minimum for the conductivity correlates with a spike in the activation energy, indicating an unfavourable oxygen constellation being the most likely cause for the low conductivity.

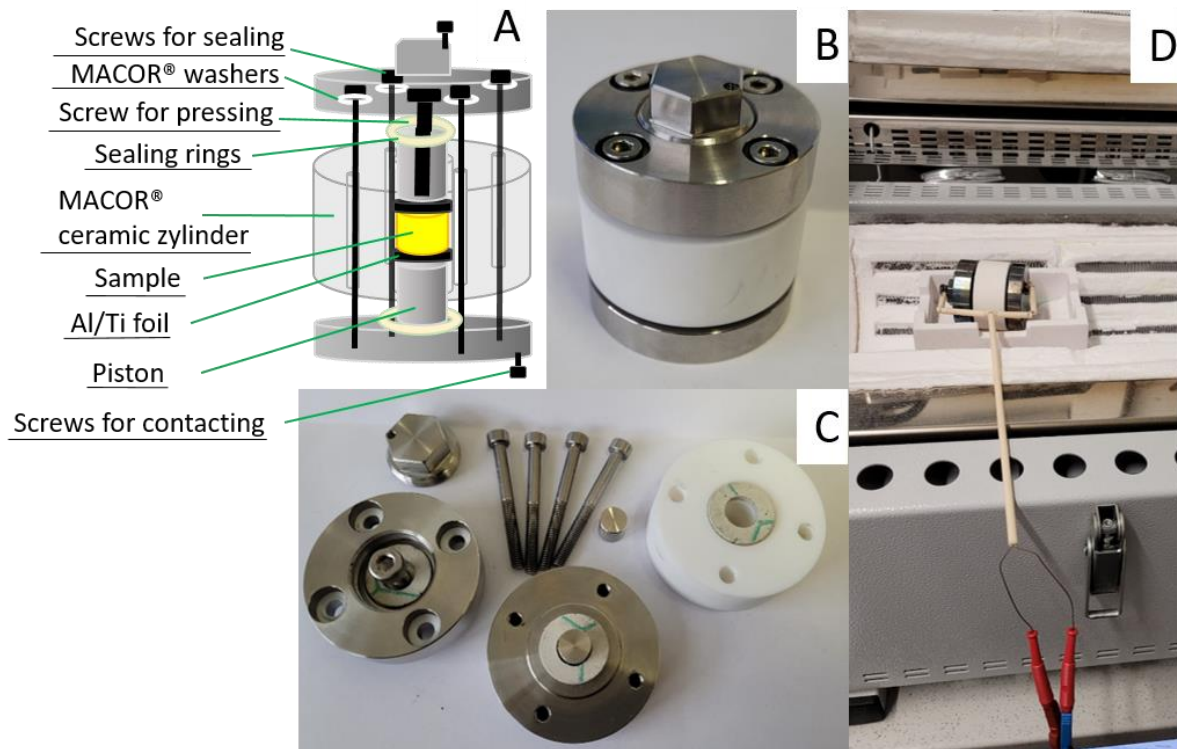
### 3.2.5 High-temperature Impedance spectroscopy

To further investigate the influence of the crystallisation process and possibly evaluate the Li-ion conductivity of high-temperature phases, a new measurement cell was developed to perform EIS measurements at elevated temperatures. Some crystal phases are only stable at elevated temperatures and thus cannot be analysed by room temperature measurements. Nevertheless, the study of different polymorphs can be useful for understanding structure-property relationships, which is essential for targeted material design. The previously discussed LGPS-type structure is a good example of how the discovery of a beneficial crystal structure led to the development of promising solid electrolytes. In the case of LPS, the high-temperature  $\alpha$ -Phase was predicted by theoretical calculations to have a high ionic conductivity.[104] Recently, Kimura et al. stabilised  $\alpha$ -LPS at room temperature, by rapid heating and cooling, and confirmed an improved conductivity as well as cycling performance compared to  $\beta$ -LPS and LPS glass.[108] The high-temperature (HT) Impedance cell should enable the convenient electrochemical analysis of high-temperature phases. Once a promising crystal phase or phase mix is identified, by comparison of the results with Temperature-dependent XRD, efforts can be made to stabilize the desired crystal phase or to find native materials with similar structures. Furthermore, the effect of crystallization temperature and time on the ion conductivity can be directly examined to improve crystallisation protocols. For the currently studied system, there are three points of interest: First, crystallisation of the materials from the glass at approximately 175 °C for LPS and between 200 and 300 °C for the oxy-sulfides. Then the sudden change of the cell parameters, accompanied by the appearance of secondary phases between 200 and 250 °C for LPS and 300 and 350 °C for the oxy-sulfides. Finally the phase transition to  $\alpha$ -LPS at 500 °C for LPS and between 550 and 600 °C for the oxy-sulfides.

The design for the measurement cell was inspired by the room temperature impedance measurement cells for air-sensitive samples, which were developed in the group. [109] The corpus of the cell is a cylinder made from Macor<sup>®</sup>, a glass-ceramic consistent of mainly silicate mixed with other metal oxides. The material is stable up to 1000 °C and is an electrical insulator.[[https://www.schroederglas.com/macor.php?gad\\_source=1&gclid=EAIaIQobChMI](https://www.schroederglas.com/macor.php?gad_source=1&gclid=EAIaIQobChMI)

[waqtmJHVgwMVVmVBAh36XAkmeAAYAyAAEgKUUfD\\_BwE](#)] The centre of the cylinder is hollow. Additionally, four smaller holes are drilled through the outside of the cylinder to accommodate the screws to tighten the cell. The sample is placed in the centre hole and held in place by two steel pistons. The top and bottom of the cell are also made of steel. Isoplan® 750 GREENLINE rings (Frenzelit, Germany) are used as sealing between the steel caps and the Macor® cylinder. After the assembly, the cell can be tightened with 4 screws, which are placed at equal distances around the outer circumference of the cylinder. The threads for the screws are placed in the bottom steel part. Hence, Macor® washers are used to prevent short circuits. In this way, the screws are only in contact with the bottom steel part but not with the top. The top accommodates another screw in a hole in the middle, which can be used to push down the piston, thereby applying pressure on the sample. Finally, the pressing screw is covered by a steel cap. The cap as well as the bottom steel part have smaller threads for contacting screws. A schematic overview of the cell along with photos of the cell parts and the fully assembled cell is presented in Figures 34 A - C.

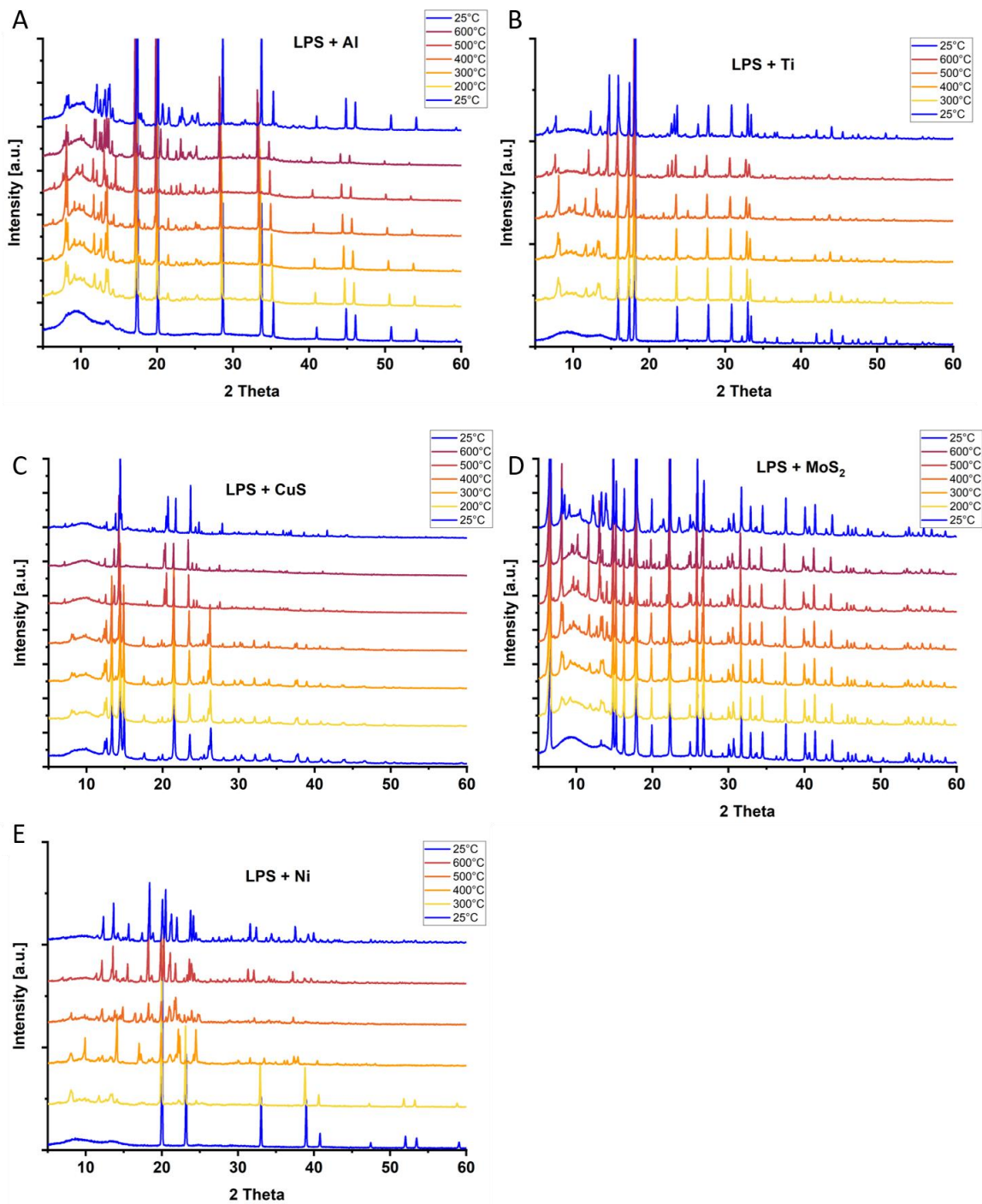
To perform the measurement, the fully assembled cell was placed into a tube furnace and covered with two parts of a glass tube. The glass tube can then be flooded with inert gas to prevent oxidation of the sample as the sealing is not perfect at high temperatures. The contacting wires were shielded with Al<sub>2</sub>O<sub>3</sub> channels to reduce the effect of temperature on the electric conductivity of the wire. Outside the furnace, the contacting wires can then be connected to a potentiostat to perform electrochemical experiments. A picture of the experiment setup is shown in Figure 34 D.



34: Schematic illustration of the high-temperature impedance spectroscopy measurement cell (A) and pictures of the c parts (B), the fully assembled cell (C), and the contacted cell in the furnace (D).

During test runs a few challenges occurred. The main problem is the high reactivity of the thiophosphate samples. Especially at temperatures above 300 °C the steel pistons will react with the LPS sample, which is visible as a black layer on either side of the pallet. Analysis of the interlayer by SEM and EDX revealed a two-phase interlayer, which consists of a thick iron-containing interlayer and a thin but dense cobalt-containing layer on top (Appendix Figure 62). To get meaningful data, any kind of reaction of the sample with the cell has to be avoided because the reaction products will alter the impedance of the cell in an unknown way, which would be a challenge for the data analysis. Therefore a suitable “barrier” material needs to be found, that is unreactive with LPS over a wide temperature range, ideally up to 600 °C, and has a good electronic conductivity. Different metals were tested with regard to their reactivity with LPS by mixing the material in powder form with LPS powder and performing temperature-dependent XRD. If the materials react, reflections of the reaction products should appear in the diffractogram. The tested materials were Ni, Al, Ti, CuS, and MoS<sub>2</sub>. The condition of good electric conductivity mainly restricts the choice of material to metals. Noble metals like Au and Ag are reactive with sulphur and can not be used. Additionally, a low-cost material would be desirable. Al and Ti are both reactive metals but build a dense passivation

layer of  $\text{Al}_2\text{O}_3$  and  $\text{TiO}_2$  respectively. Ni is generally less reactive and often used for high-temperature applications, the reaction temperature to form NiS from the elements is 900 °C. However, judging from the x-ray diffractograms presented in Figure 35, Ni is not suitable as the reflections disappear already at 400 °C (Figure 35 E). Al and Ti look more promising, both seem to be stable up to at least 500 °C (Figure 35 A, B) which would be sufficient to cover the transition from glassy LPS to  $\beta$  and finally  $\alpha$ -LPS. The diffractograms show the crystallisation and phase transition of LPS while the reflections from the metals stay unchanged, suggesting that no reaction is taking place. Rietveld refinements on the diffractograms at 500 °C confirm this observation (see Appendix Figure 63). However, the refinement for the test with Al revealed an unreasonably high amount of  $\text{Li}_4\text{P}_2\text{S}_6$ , which indicates a reaction between LPS and Al. At 600 °C new peaks appear in both diffractograms, which cannot be explained by the  $\alpha$ -LPS phase, thus the experiment temperature should be limited to 500 °C. As an alternative, CuS and  $\text{MoS}_2$  were also tested. Both materials have decent electronic conductivities.[110] Moreover, since the materials are metal sulfides, further reaction with sulfur should be limited. As evident from the diffractograms in Figures 35 C and D, this is only true for  $\text{MoS}_2$ . CuS (Figure 35 C) is stable up to 400 °C before the reflections start to disappear.  $\text{MoS}_2$  (Figure 35 D) appears to be stable over the whole temperature range, even after heating to 600 °C all reflections remain unchanged. The main issue with using  $\text{MoS}_2$  however, is the reaction with Li to  $\text{Li}_2\text{S}$  and Mo when a current is applied.[111] The conversion is theoretically reversible, but at lower frequencies some of the Mo might react with sulfur from the thiophosphate, effectively creating a  $\text{Li}_2\text{S}$  layer.

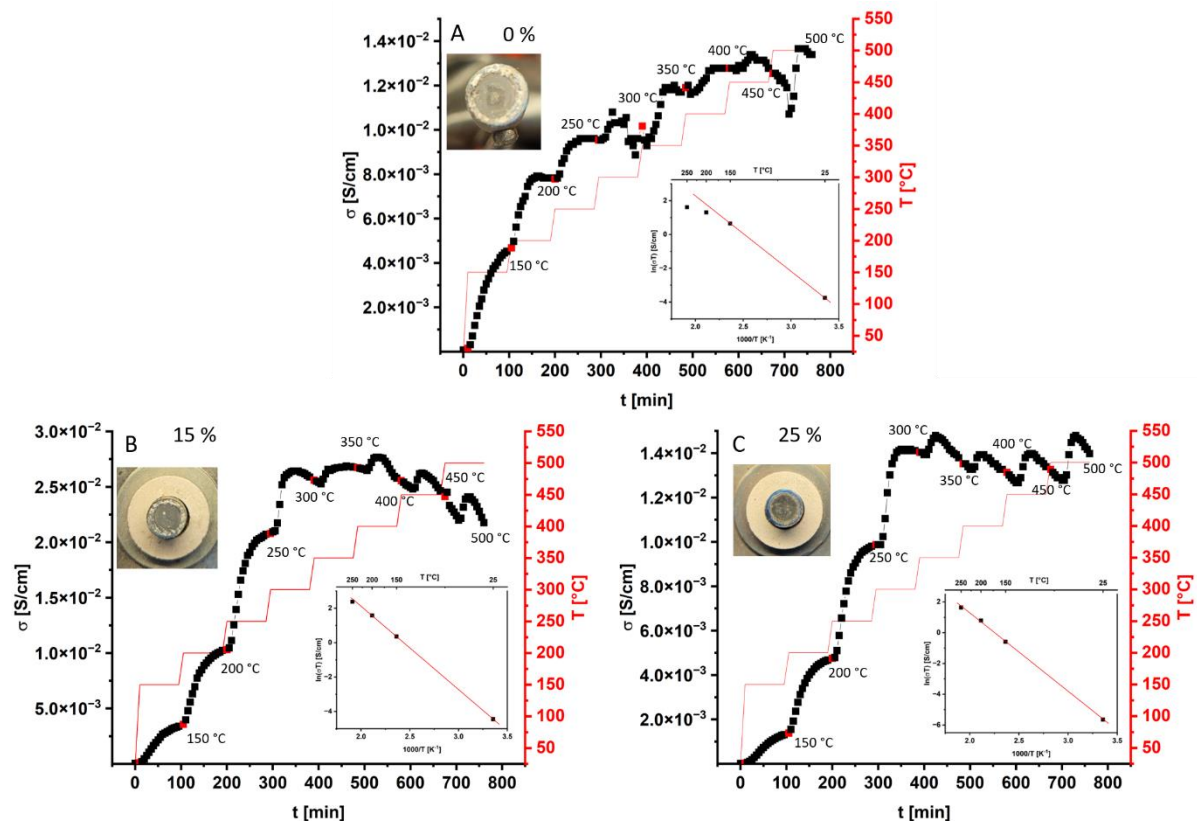


35: Temperature-dependent x-ray diffractograms of LPS mixed with Al (A), Ti (B), CuS (C), MoS<sub>2</sub> (D) and Ni (E).

After the evaluation of the reactivity tests, Ti was chosen as the barrier material. A sheet of Al foil was coated with Ti. Then 8 mm  $\varnothing$  platelets were cut out and placed between the steel pistons and the sample. Three experiments were conducted, on LPS, LIO2 and LIO4 (0, 15 and 25 % oxygen substitution) as a proof of concept. For the measurement, an initial EIS measurement was performed at room temperature, then the furnace was ramped to 150 °C

and stepwise further up to 500 °C. The temperature was held at every 50 °C step for 90 min and a series of EIS measurements was performed during the holding times.

In the low-temperature regime, up to 250 °C, the conductivity for all samples increases exponentially during each holding time with a  $e^{-a/t}$  dependency. At higher temperatures, the behaviour changes to a more chaotic trend, as presented in Figure 36. For the reference LPS sample with 0 % oxygen substitution, the conductivity increased exponentially after the furnace was set to 150 °C, but without plateauing. When the temperature is set to 200 °C, the conductivity again follows an exponential trend. After the first 5 data points, a small kink can be observed after which the conductivity goes through a maximum and plateaus before the temperature is raised again (the first measurement at each temperature is marked by red data points). Between 200 and 250 °C, the conductivity rises exponentially and goes into a plateau. The overall conductivity change is smaller than the change between 150 and 200 °C. Between 250 and 300 °C, the conductivity increases initially and then suddenly drops and plateaus.



36: Li-ion conductivity development for samples with 0 (A), 15 (B) and 25 % (C) oxygen substitution during heating up to 500 °C in the HT-impedance cell. Red data points indicate the first measurement after the furnace has been heated to the next higher temperature.

The next two temperature steps are again described by an exponential increase of the conductivity, with a large increase from 300 to 350 °C and a smaller one from 350 to 400 °C.



Between 400 and 450 °C, the conductivity goes through a maximum before it decreases again. The steady decrease continues even after the furnace temperature has been set to 500 °C. After approximately 45 min at 500 °C, the conductivity exhibits a steep increase before it starts to slightly decrease again (Figure 36 A).

For the sample with 15 % oxygen substitution, the first three temperature steps (25 - 150 °C, 150 - 200 °C, 200 – 250 °C) are all characterised by the same exponential increase, all without reaching a plateau. After the furnace is set to 300 °C, the conductivity trend starts similarly as for the previous step, with a sharp increase. However, after approximately 25 min, the steep increase is damped out and the conductivity goes through a maximum before starting to decrease. Between 300 and 350 °C, the conductivity slightly increases again. For the remaining temperature steps to 400, 450 and 500 °C, the conductivity trend exhibits a saw-tooth-like behaviour, where it increases with some delay after the temperature rise and then steadily decreases until after the next temperature step (Figure 36 B).

The conductivity of the sample with 25 % oxygen substitution displays similar behaviour to the one with 15 % oxygen substitution; exponential increase for each temperature step up to 250 °C, then a damped increase between 250 and 300 °C, followed by the saw-tooth-like behaviour for the remaining temperature steps to 350, 400, 450 and 500 °C. The main differences are the delayed dampening of the conductivity between 250 and 300 °C as compared to the 15 % sample, and the fact that the average conductivity stays almost constant between 350 and 500 °C. In contrast, the average conductivity decreases in the same range for the 15 % sample (Figure 36 C). It should be noted that the scale on the y-axis is larger for the 15 % sample as compared to the other two. This observation is in agreement with the results of the previously discussed experiments where the samples were heated to 300 °C. The conductivities of the samples with 10 and 15 % oxygen substitution were found to be increased in comparison to the unsubstituted LPS as well as the higher substituted samples.

The unstable nature of the conductivity trends at high temperatures suggests that the Al/Ti disks could not prevent the reaction of the sample with the electrodes. A black covering of the electrodes further proved the reaction after the samples were removed (see pictures in Figure 36). Under these circumstances, a clear interpretation of the data is challenging as the precise time and influence of the reaction on the total conductivity is unknown. The applied pressure and electric fields during the experiment might explain the enhanced reactivity

compared to the stability measurements done by XRD discussed earlier. Moreover, the exact temperature of the sample at each data point is not defined. Only the furnace temperature can be controlled. However, the measurement cell, especially because of the thick Marcor® cylinder acts as a thermal shielding. Thus, the temperature inside the cell is lagging behind the temperature of the furnace. The  $e^{-a/t}$  dependent conductivity trends for the low temperatures are a result of the internal temperature of the cell approaching the furnace temperature. Consequently, the temperature evolution inside the cell needs to be calibrated to obtain accurate temperature-dependent conductivity data.

Nevertheless, the data can be used to evaluate the potential of the method. The cell seems to be stable up to 250 °C. Furthermore, the temperature region where the conductivity trend behaves “normal” appears to increase with increasing oxygen substitution of the sample. This observation can most likely be attributed to the increasing chemical stability of the samples with higher oxygen substitution. As a result, the cell should be usable up to higher temperatures, when the reaction between sample and electrodes can be effectively prevented. Within the stable temperature range falls the crystallisation temperature for the samples with up to 15 % oxygen substitution. The crystallisation events are visible as small kinks in the data. However, to better visualize the effect, the data should be plotted in an Arrhenius plot where any deviation from the linear regression signals a change in the activation energy. When plotting the last data point of every temperature step between 25 and 250 °C for the LPS sample in an Arrhenius plot, a change in the activation energy is visible between 150 and 200 °C where the sample should crystallise according to the temperature-dependent XRD experiments (inset Figure 36 A). The same plot for the samples with 15 and 25 % oxygen substitution shows a linear dependency for the whole temperature range up to 250 °C (inset Figure 36 B and C). The sample with 15 % oxygen substitution should also display a change in the activation energy between 200 and 250 °C as the crystallisation was observed within this temperature range. However, more data points would be needed to observe this change. With a correct temperature calibration, all data points could be used in the Arrhenius plot, increasing the accuracy and reliability of the analysis. The reproducibility also needs to be further investigated once a suitable set-up is found, however, various test runs have indicated that the trends are at least qualitatively reproducible

Some features in the high-temperature region do correlate with the XRD experiments. For the LPS sample, the drop in the conductivity between 250 and 300 °C falls into the same region

where the sudden change of the lattice parameters was observed from the XRDs. Additionally, the steep increase between 450 and 500 °C could be attributed to the formation of  $\alpha$ -LPS which was predicted to have a high Li-ion conductivity, as discussed before. However, considering the unknown reactions between the samples and the measurement cell, further experiments need to be done to improve this method and enable reliable conclusions. The most important issues to be solved are the prevention of reactions and the establishment of an accurate temperature calibration inside the cell.

### 3.2.6 Summary and conclusion

In this Chapter, the influence of oxygen substitution on the crystallisation behaviour of Li oxy-sulfide glasses was investigated. In agreement with the Literature, the substitution of oxygen was found to change the crystallisation products. Instead of the known LPS polymorphs, an LGPS-like phase formed. Investigations of all appearing phases clarified the formation mechanism involving an enrichment of Li and oxygen within the LGPS-like structure compared to the LPS glass. The evaluation of the Li-ion conductivity revealed that oxygen substitution in combination with temperature treatment can be a viable strategy to produce materials with high oxygen concentration and good ionic conductivity as the maximum conductivity is reached at 10 % oxygen substitution and a conductivity comparable to that of the unsubstituted glass. Furthermore, a new measurement cell was developed to enable the electrochemical characterisation of high-temperature phases and evaluate crystallisation protocols with minimal experimental effort. The potential of the cell has been demonstrated, although challenges remain due to sample reactivity and temperature calibration.

### 3.3 Optimisation of the Mechanochemical Synthesis Procedure

The results from the analysis of oxy-sulfide glasses (see Chapter 3) indicated that the used synthesis parameters were not ideal, judging from the high amount of impurity phases ( $[\text{P}_2\text{S}_6]^{4-}$ ,  $[\text{P}_2\text{S}_7]^{4-}$ ) and limited reproducibility. Similar issues arise when comparing the reported conductivity values for  $\text{Li}_3\text{PS}_4$  found in literature, which spread over almost one order of magnitude (Figure 3). In order to reduce the spread of conductivity values and thereby the risk of false conclusions when comparing different samples, an improved synthesis protocol that reduces impurity phases and enhances reproducibility seems desirable.

Ball milling is a commonly used synthesis method but most studies do not explain why a certain set of parameters is used. Commonly, moderate rotational speeds (350 - 600 rpm) are used with varying ball sizes between 3 and 10 mm.[34, 36, 41, 42, 46] The synthesis conditions chosen for the LIO series described earlier fit into this range and the analysis revealed high amounts of impurity phases and insufficient reproducibility of the process. A more recent study by Hofer et al. demonstrated in a high-energy ball mill how optimised milling parameters can effectively increase the ionic conductivity of LPS, by increasing the phase fraction of  $[\text{PS}_4]^{3-}$  units and reducing impurities like  $[\text{P}_2\text{S}_6]^{4-}$  and  $[\text{P}_2\text{S}_7]^{4-}$ , while saving time and energy during the process.[112] The results presented in this chapter were acquired by Daniel Hilscher as part of his Master thesis, which I had the pleasure to supervise.

#### 3.3.1 Experimental

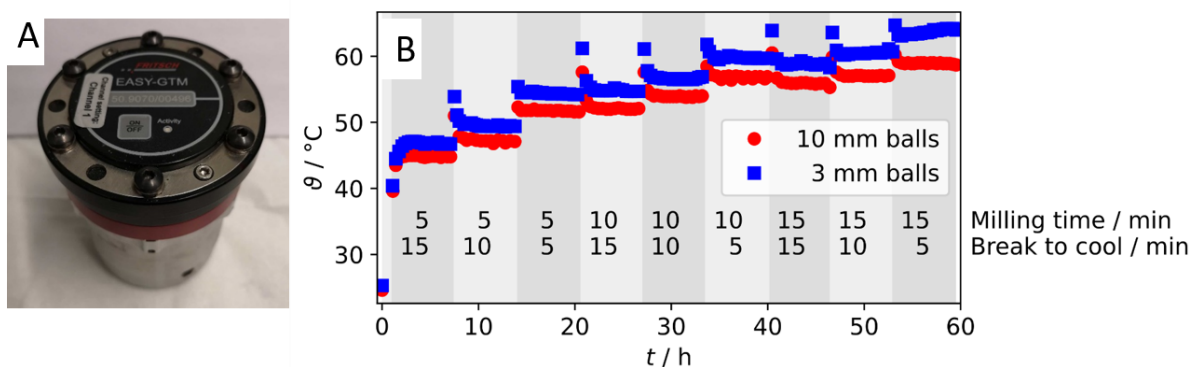
$\text{Li}_3\text{PS}_4$  glasses and glass ceramics were prepared by high-energy ball milling in a planetary micro mill Pulverisette 7 Premium line (Fritsch, Germany). Appropriate amounts of  $\text{Li}_2\text{S}$  (Sigma-Aldrich, 99.98) and  $\text{P}_2\text{S}_5$  (Sigma-Aldrich, 99.9 %) powders with a total mass of 1 g were weighed and filled in an 80 mL  $\text{ZrO}_2$  milling jar together with 75 g of 3 or 10 mm  $\text{ZrO}_2$  grinding balls. All steps up to this point were done in an Ar-filled glovebox to prevent oxidation of the materials. The EASY-GTM system together with the MillControl software (Fritsch, Germany) was used to record temperature and pressure inside the milling jars during the milling process.

XRD and EIS measurements were done as described on pages 309-40

#### 3.3.2 Synthesis Parameter Optimisation

To establish an improved synthesis protocol, a similar analysis was done for the planetary ball mill Fritsch Pulverisette 7. The results from Hofer et al. suggest using high rotational speed and large grinding balls. Keeping in mind, that temperature treatment is known to reduce

impurities, a large energy input seems sensible. Under these conditions, temperature control is important to avoid damage to the equipment. Cooling breaks prevent temperature build-up but can extend the total synthesis time significantly. Therefore, the optimization of cooling and milling times was done first. The EASY-GTM system from Fritsch was used to monitor the temperature development inside the milling jar, a photo of the closed jar can be seen in Figure 37 A. The test runs contained 1 g of 75/25  $\text{Li}_2\text{S}/\text{P}_2\text{S}_5$  mix and 75 g of grinding balls. Two ball sizes of 3 and 10 mm were tested and the rotational speed was set to 700 rpm, which is close to the recommended maximum speed as described in the user manual of the ball mill. The milling and cooling times were varied between 5 and 15 min, starting with 5 min of milling followed by 15 min of cooling. Then the cooling time was reduced to 10 and finally 5 min. Next, the milling time was increased to 10 min and the cooling time was again varied from 15 to 5 min. The same procedure was repeated once more with a milling time of 15 min per cycle. All combinations were run for a total of 6:40 h back-to-back without stopping the mill. As presented in Figure 37 B, the temperature inside the milling jar only slightly increases between different sets of milling/cooling times but stays almost constant between cycles of each set. Only for 15 min milling/ 5 min cooling and 3 mm grinding balls, a slow rise in temperature could be detected. Nevertheless, the 15/5 set was evaluated as a suitable condition because the overall temperature of the jar was in a moderate range and the temperature rise was judged to be too insignificant to pose a risk or influence the reaction in any way. Generally, the jar with smaller grinding balls developed more heat, which can be explained by a higher amount of friction as well as higher collision frequency due to the high number of balls in the jar. The temperature spikes at the first cycle of every new set can be explained by a missing cooling break.



37: Investigation of temperature development during ball milling synthesis. A: Photo of the closed ball-milling jar. B: plot of temperature development over time for different sets of milling and cooling times with 10 mm balls (red) and 3 mm balls (blue).

The last milling step of the previous set was followed immediately by the first milling step of the next set. The steep increase in temperature at these points highlights the general need for cooling steps during the synthesis.

In the next step, the influence of three ball milling parameters; total milling time, rotational speed, and grinding ball diameter, on the ionic conductivity of the product were investigated. The total milling time only counts the milling step but does not include the cooling breaks, 5 h of total milling time is equal to 20 cycles of 15/5 milling/cooling. The ball-to-powder ratio was fixed at 75 g balls/ 1 g sample powder. The so-called Design of Experiment (DoE) approach was utilised to scan the parameter space and find the governing correlations with minimal experimental effort.[113] The most simple version for a DoE with three parameters (factors) is the 2<sup>3</sup> factorial design, meaning that two values, minimum and maximum, are tested for all three factors. The resulting combinations yield a total of eight experiments. For the current study, the milling time was varied between 5 and 15 h, the rotational speed between 300 and 700 rpm, and the grinding ball size between 3 and 10 mm. The samples were premixed in the ball mill at 100 rpm for 10 min. All experiments and the corresponding values for the three factors are collected in Table 4, blue fields contain minimum values and red fields contain maximum values. To avoid systematic errors, the experiments were performed in random order.

*Table 4: overview of DoE experiments with values for investigated factors*

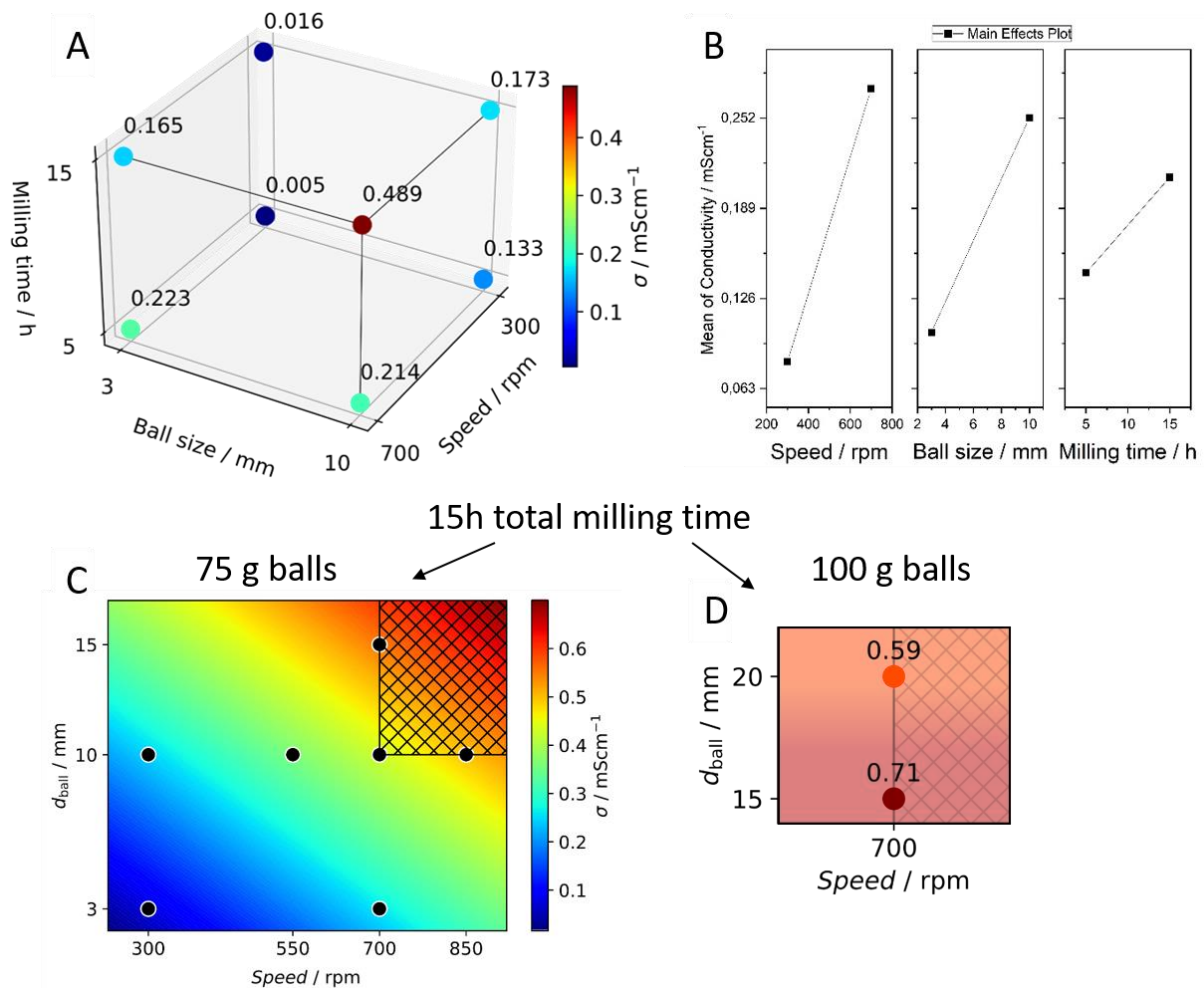
<b>Experiment</b>	<b>total milling time [h]</b>	<b>rotational speed [rpm]</b>	<b>grinding ball size [mm]</b>
S3	15	700	10
S4	15	700	3
S5	15	300	10
S6	5	700	10
S7	5	700	3
S8	5	300	10
S9	5	300	3
S10	15	300	3

All samples were analysed by XRD and EIS. The results of the EIS measurements are presented in Figure 38 A. The experiments exhibit clear trends for the three factors, which are in good

agreement with the study from Hofer et al. All factors have a positive correlation with the ionic conductivity of the product, meaning that the experiments with parameters set to their maximum yielded materials with higher conductivity. The  $2^3$  factorial design, as it is used here, assumes a linear correlation between factors and the response value, in this case, the Li-ion conductivity. Following this linear model, the DoE results suggest setting all parameters to the maximum value and predicting even higher conductivity values if the factors can be pushed past the limits set in the first set of experiments. The impact of each individual parameter can be determined by analysing the changes in conductivity values along each axis of the DoE. In the current study, the rotational speed appears to be the most impactful factor, closely followed by the ball size, as illustrated in Figure 38 B. The milling time seems to have less impact. Essentially, the factors increasing the energy input per collision are the most impactful. When the ball size is small, the rotational speed drastically influences the conductivity, when the rotational speed is set to the minimum value; the ball size is the crucial parameter. However, at high speed or using large grinding balls, when the energy input is already at a moderate level, the change in conductivity by varying the other factors is noticeably less drastic. Because the collision energy is not a fixed value but has a distribution, the total milling time can compensate for lower average energy input to some extent as the number of high energy impacts builds up over time.

Following the predictions of the DoE, two additional experiments were conducted, pushing the upper limits for rotational speed and ball size to 850 rpm and 15 mm balls respectively. Both values represent the limits for the safe operation of the ball mill and cannot be applied at the same time without damaging the ball mill. Therefore, 10 mm balls were used at 850 rpm and the rotational speed was set back to 700 rpm to test the 15 mm grinding balls. The full parameter space is presented in Figure 38 C. The grid marks the inaccessible region. The two experiments could indeed verify the predictions from the first DoE. Both experiments yielded LPS materials with exceptionally high conductivity values of 0.7 and 0.6 mS/cm respectively. To further increase the ball size to 20 mm, the total ball mass needs to be increased to 100 g instead of 75 g used for all previous experiments to ensure the safe operation of the mill. The speed limit remains at 700 rpm. Therefore, two more experiments were conducted; one with 100 g of 20 mm balls to investigate the effect of further increased ball size, and one with 100 g of 15 mm balls to get an idea of the influence of the increased ball mass. The results are presented in Figure 38 D. Increasing the ball size to 20 mm did not improve the conductivity,

the value stayed at around 0.6 mS/cm which is the same as for the experiment with 75 g of 15 mm balls. The addition of more 15 mm balls to get to the total mass of 100 g instead of 75 g, however, did increase the conductivity to about 0.7 mS/cm, which is the highest measured conductivity together with the experiment with 10 mm balls but 850 rpm. The powder-to-sample ratio thus, seems to have a measurable impact on the conductivity of the product.



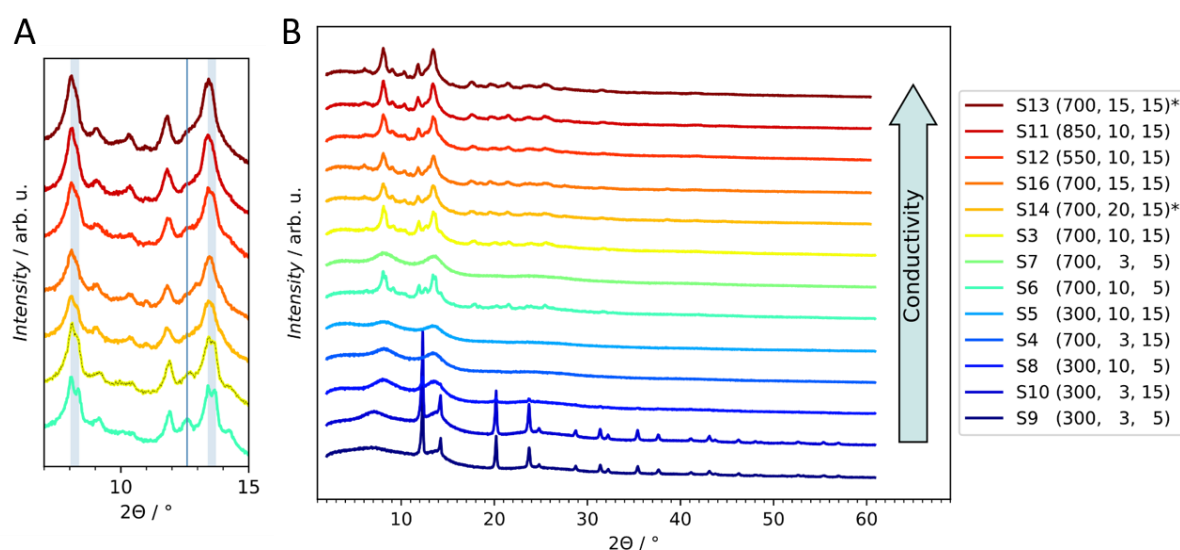
38: Conductivity response for all DoE experiments (A), correlation of the three investigated factors (B), and 2D response surface for 15 h of milling time with 75 g milling media (C) and 100 g milling media (D).

### 3.3.3 Fabrication of metastable Phases

The XRD analysis revealed a clear correlation between the diffractograms and the Li-ion conductivity of the materials. Figure 39 shows the diffractograms of all samples sorted by their ionic conductivity. The samples with the lowest conductivity exhibit reflections originating from the starting materials Li<sub>2</sub>S and P<sub>2</sub>S<sub>5</sub>. These two samples were both milled at low rotational speed and with small grinding balls. Under these conditions, the milling time was not enough



to react all of the samples. While the rotational speed was higher for the synthesis used in the previous chapters, similar observations were made. Hence, extensively long milling times were necessary to obtain the final product. Upon increasing either the ball size or the rotational speed, the reaction is finished much faster. After 5 h total milling time, the samples are mostly amorphised. Only the S8 sample, synthesised at low speed and short time, exhibits small reflections of starting materials. Consequently, the S8 sample has the lowest conductivity of the group. The conductivity value of these samples ranges from  $1.33$  to  $2.23 \times 10^{-4}$  S/cm, which is comparable to the conductivity values of the reference samples synthesised for the LIO series and also other conductivity values found in the literature (see Figure 41). However, the synthesis time is drastically reduced from several days down to 15 or even 5 hours. When both speed and ball size is set to the maximum value, or beyond, the diffractogram changes from broad humps of amorphous LPS to broadened reflections of a semicrystalline phase. These samples with at least two parameters set to maximum, have the highest conductivities. The sample milled for 5 h (sample S6) was identified as mainly  $\beta$ -LPS, it has the lowest conductivity of the group with  $2.14 \times 10^{-4}$  S/cm, which is in the same range as the amorphous samples. After 15 h (sample S3) total milling time, the conductivity doubles to  $4.89 \times 10^{-4}$  S/cm. At the same time, changes in the diffractogram can be observed, as highlighted in Figure 39 A. The two doublet peaks at around  $8.2^\circ$  and  $13.5^\circ$   $2\theta$  are merged into one peak while the intensity for the peak at  $12.6^\circ$   $2\theta$  decreases. The same trend can be observed when comparing the rest of the semicrystalline samples. The conductivity of the materials increases as the doublet peaks merge into single peaks, the intensity of the  $12.6^\circ$   $2\theta$

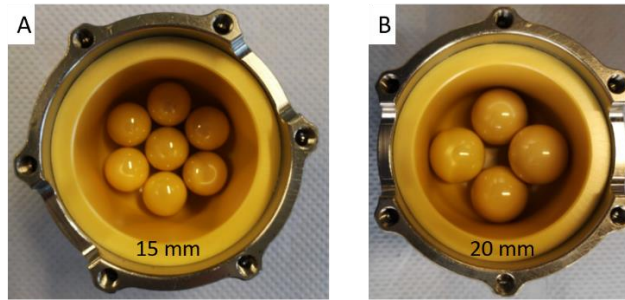


39: X-ray diffractograms of all DoE samples sorted by their ion conductivity with zoom in the low angle region (A).

reflections decreases and a new reflection at  $10.4^\circ 2\theta$  appears. The single peaks at  $8.2^\circ$  and  $13.5^\circ 2\theta$  (samples S16, S12, S11, and S13) are characteristic of  $\alpha$ -LPS, which is the high-temperature phase of LPS. This  $\alpha$ -LPS phase is thought to have the highest conductivity of the three LPS polymorphs.

The results suggest that, as the impact energy increases with the use of large grinding balls  $\geq 10$  mm combined with high rotational speed  $\geq 700$  rpm, conditions are met to form  $\alpha$ -LPS in the ball mill at room temperature without the need for additional heat treatment. This would be the first report of a room temperature synthesis of  $\alpha$ -LPS. Because impacts are short, hence the energy is transferred in short pulses, the formed  $\alpha$ -LPS is instantly quenched and therefore cannot transform back to a low-temperature polymorph like  $\beta$  or  $\gamma$ -LPS. The conditions are similar to a crystallisation experiment with large heating and cooling rates, which Kimura et al. used in their work to stabilize  $\alpha$ -LPS at room temperature.[108]

Summarising all this, the Li-ion conductivity of LPS can be increased by increasing the phase fraction of its highest conducting polymorph,  $\alpha$ -LPS. Because  $\alpha$ -LPS is the high-temperature phase, large energy transfer in a short time scale is necessary to synthesise and stabilise  $\alpha$ -LPS at room temperature. For the mechanochemical synthesis, these large energy transfers can be achieved by using large grinding balls and high rotational speed. However, for the used setup, a ball size larger than 15 mm was not beneficial. The powder-to-sample ratio was only tested in one experiment, where a larger total ball mass was proven to have a positive impact. Different theories may explain this observation; more balls in the jar increase impact frequency. At the same time, a larger amount of grinding balls may result in a thinner powder film on the grinding media surface, because there is more surface area to be covered. The thinner powder film is more likely to transform impact energy into a chemical reaction or crystallization and less into deformation of the film. Another reason for this specific experimental setup might be the position of the grinding balls in the jar. The amount of 15 mm balls needed for a total of 75 g fits into a closed packing at the bottom of the jar, as depicted in Figure 40 A. During the milling process, the balls might occasionally get stuck into this position, which results in fewer collisions because the balls are restricting each others movement. A similar constellation is reached with 100 g of 20 mm ball (see Figure 40 B), which might explain the similar performance for these two experiments.

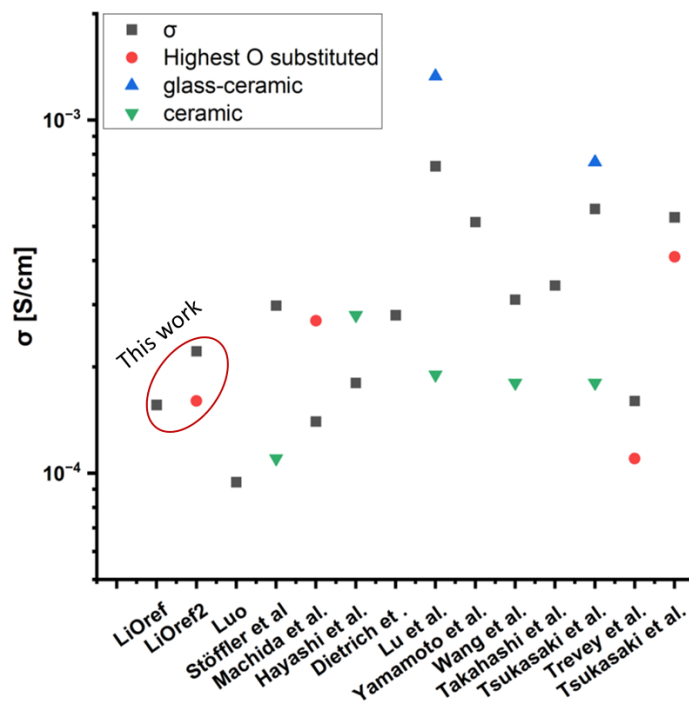


40: Photos of milling jars with 75 g of 15 mm balls (a), and 100 of 20 mm balls (b).

To further improve the conductivity of the product, the phase fraction of  $\alpha$ -LPS needs to be further increased. The model derived from the DoE suggests using even higher rotational speeds, or larger ball sizes. For practical reasons, both are not possible with the Pulverisette 7 and therefore need to be tested elsewhere. The increase of  $\alpha$ -LPS phase fraction from experiment S6 (700, 10, 5) to S3 (700, 10, 15) indicates that longer milling times could also be a strategy to increase the  $\alpha$ -LPS fraction.

## 4 Conclusion & Outlook

The reported Li-ion conductivity values for LPS and LPSO spread over a wide range. A comparison of conductivity values found in literature reports and samples measured within this work is presented in Figure 41.



41: Overview over reported conductivity values for LPS and LPSO from ball milling synthesis. Black squares: amorphous LPS, red circles: amorphous LPSO, blue triangles: glass-ceramic LPS with small amount of crystallites, green triangle: mainly  $\beta$ -LPS phase.

Most conductivity values for amorphous LPS lie in the range between 0.1 to 0.3 mScm<sup>-1</sup>. The data on  $\beta$ -LPS are slightly below the amorphous samples on average, but overall in a similar range. The spread of conductivity values may explain why there seems to be no clear consensus in the field, as to which one of the two is the better Li-ion conductor. A batch of pure  $\beta$ -LPS might outperform an LPS glass sample containing a high amount of impurities or precursor material and vice versa. Moreover,  $\beta$ -LPS samples are almost always labeled as glass-ceramics owing to the fact, that the samples usually contain some amorphous fraction that can be challenging to quantify. The influence of different phase fractions of amorphous and crystalline LPS was demonstrated by Lu et al.[47] Their optimised heat treatment conditions yielded the highest conductivity value reported for LPS so far. Consequently, conductivity values should not only be compared to own experiments but also to the literature average to prevent false conclusions due to “unfair” comparisons. The same can be said about

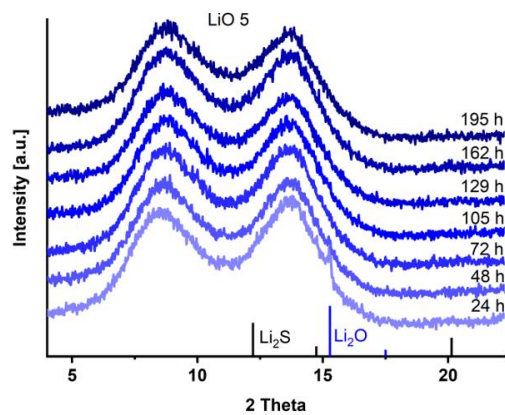
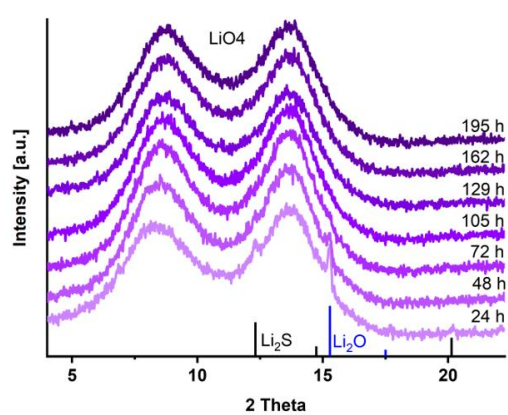
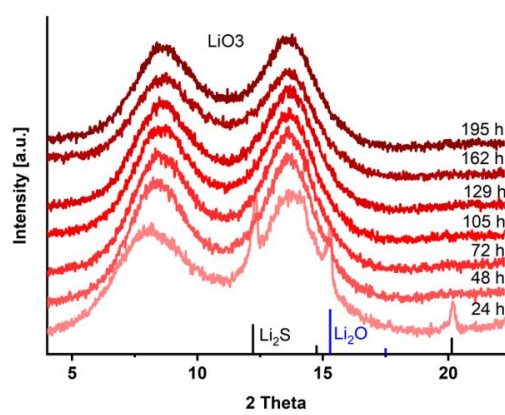
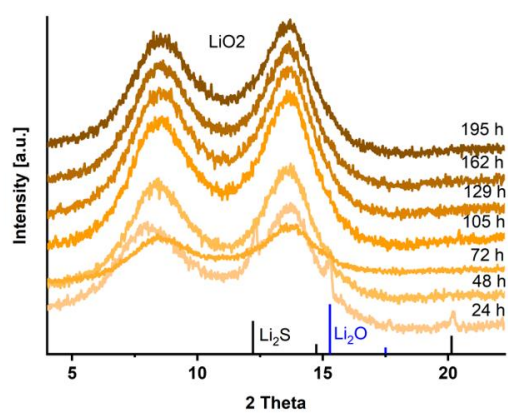
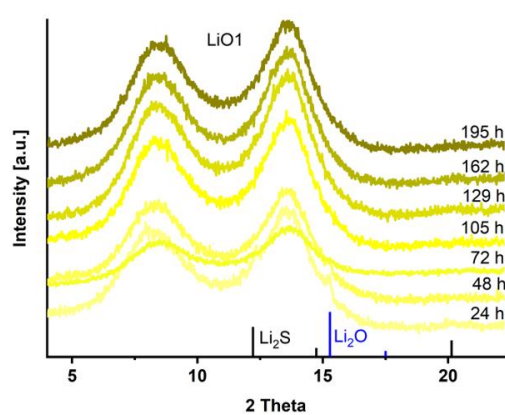
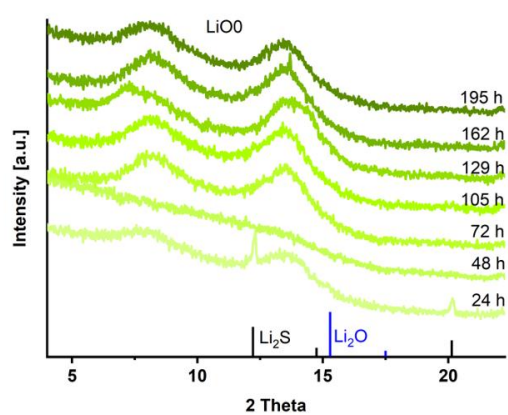
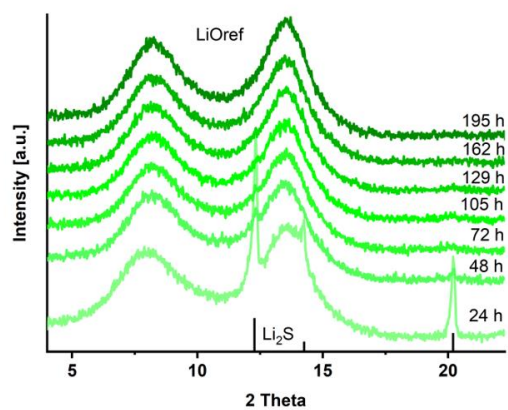
the influence of oxygen substitution. Studies that claim to observe a positive effect of small amounts of oxygen substitution on the ionic conductivity of LPS either compare their values to a comparatively low conducting LPS samples[46] or investigate crystallised samples,[45] where oxygen doping can introduce a change in the crystal structure as demonstrated in this thesis. Comparing the conductivity data of multiple studies in combination with the results from the current work does not allow the conclusion that oxygen substitution inherently improves the Li-ion conductivity of LPS. Rather, a small amount of oxygen doping (< 5 %) does not significantly decrease the conductivity. Further, a higher amount of oxygen substitution can be used to stabilise the high-conducting LGPS-like structure, which has comparable and in some cases improved Li-ion conductivity compared to amorphous and  $\beta$ -LPS.

Oxygen substitution has proven to be impactful to the structure and properties of Li oxy-sulfide glasses and glass ceramics. The correlations are more complex than what is often recognised in the Literature. The unveiled importance of oxygen distribution to the ionic conductivity highlights the need for in-depth structural analysis to discover and understand the factors governing ion conductivity.

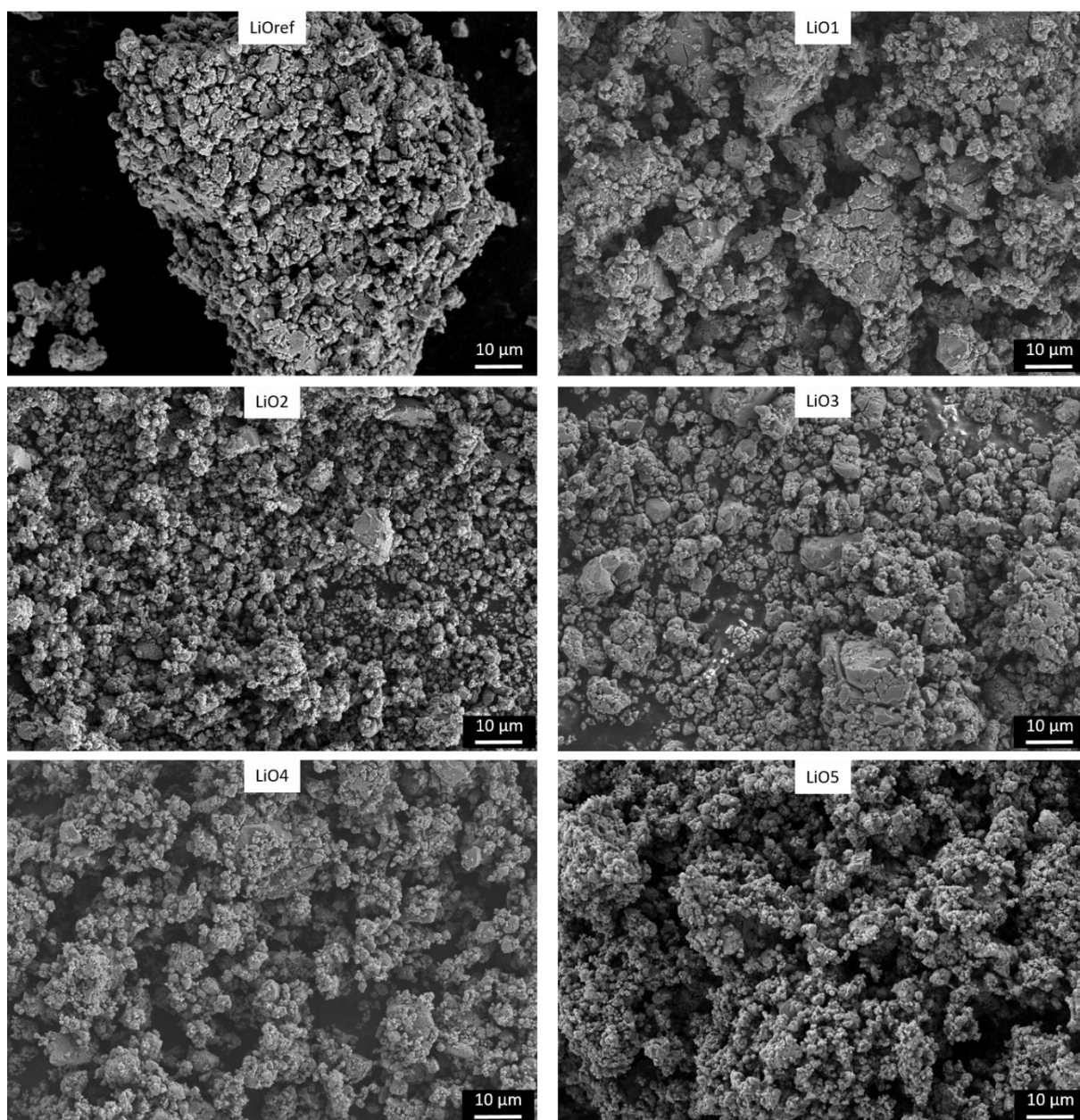
Evaluating different polymorphs is another option to access a material with desired properties. Besides temperature treatments, mechanochemical synthesis offers the potential to synthesise metastable products at room temperature, as demonstrated with the stabilisation of  $\alpha$ -LPS. To harvest the full potential of this method, parameter studies are important for the understanding of the precise impact of each synthesis parameter on the product structure.

The results of this work have implications beyond the scope of Li oxy-sulfides. The procedure may offer guidelines for the characterisation of other amorphous molecular solids or the effects of ion substitution. Additionally, the developed high temperature impedance cell shows potential for the in situ characterisation of high temperature phases and the evaluation of temperature treatment protocols. Furthermore, the potential and limitations of mechanochemical synthesis have been investigated. Reproducibility can be an issue if the synthesis parameters and precursor materials are not carefully chosen. However, understanding the available synthesis parameters allows fast and energy-saving synthesis of different stable and metastable structures.

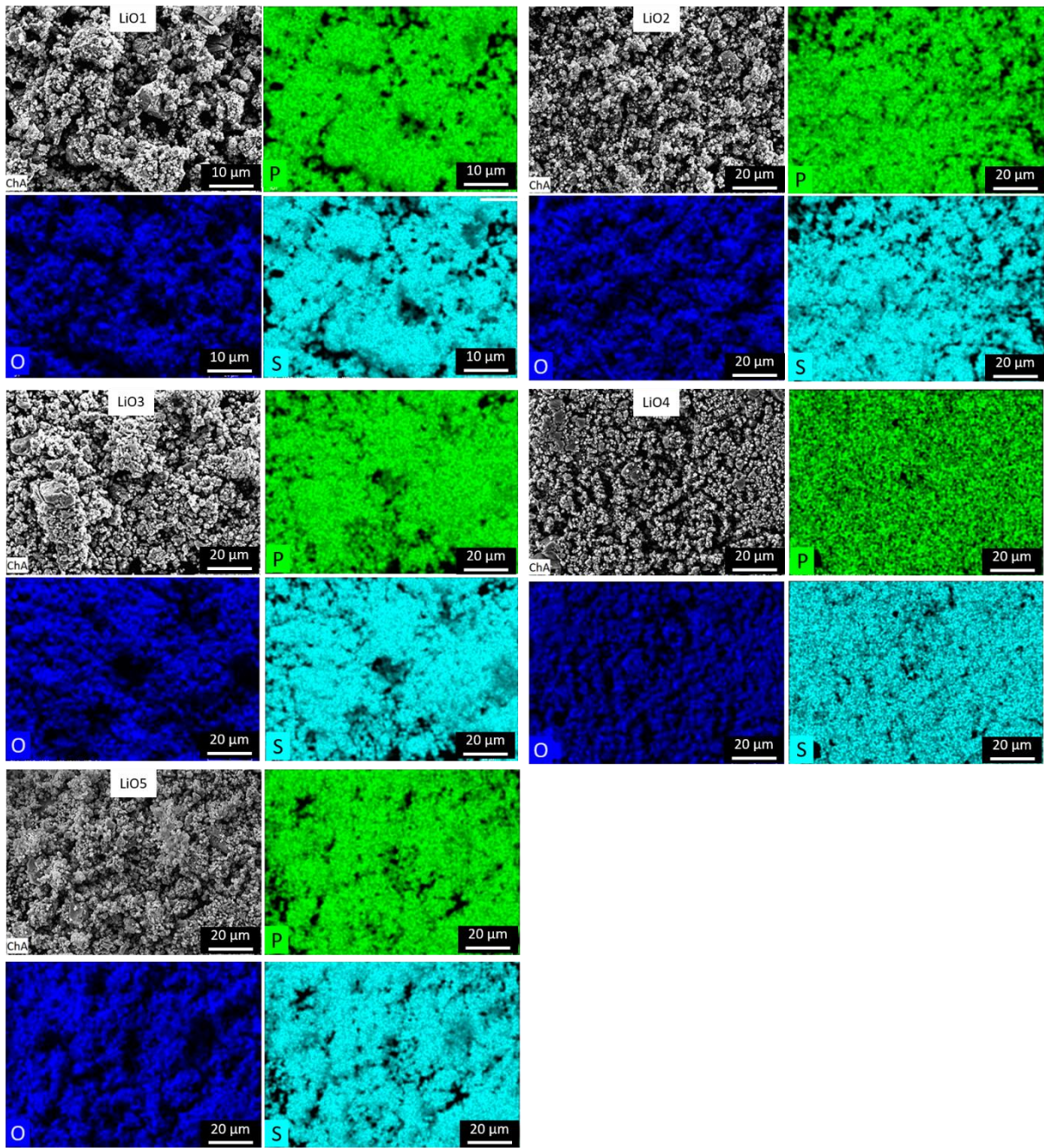
## 5 Appendix



42: X-ray diffractograms of each sample from the LIO series in between milling cycles.

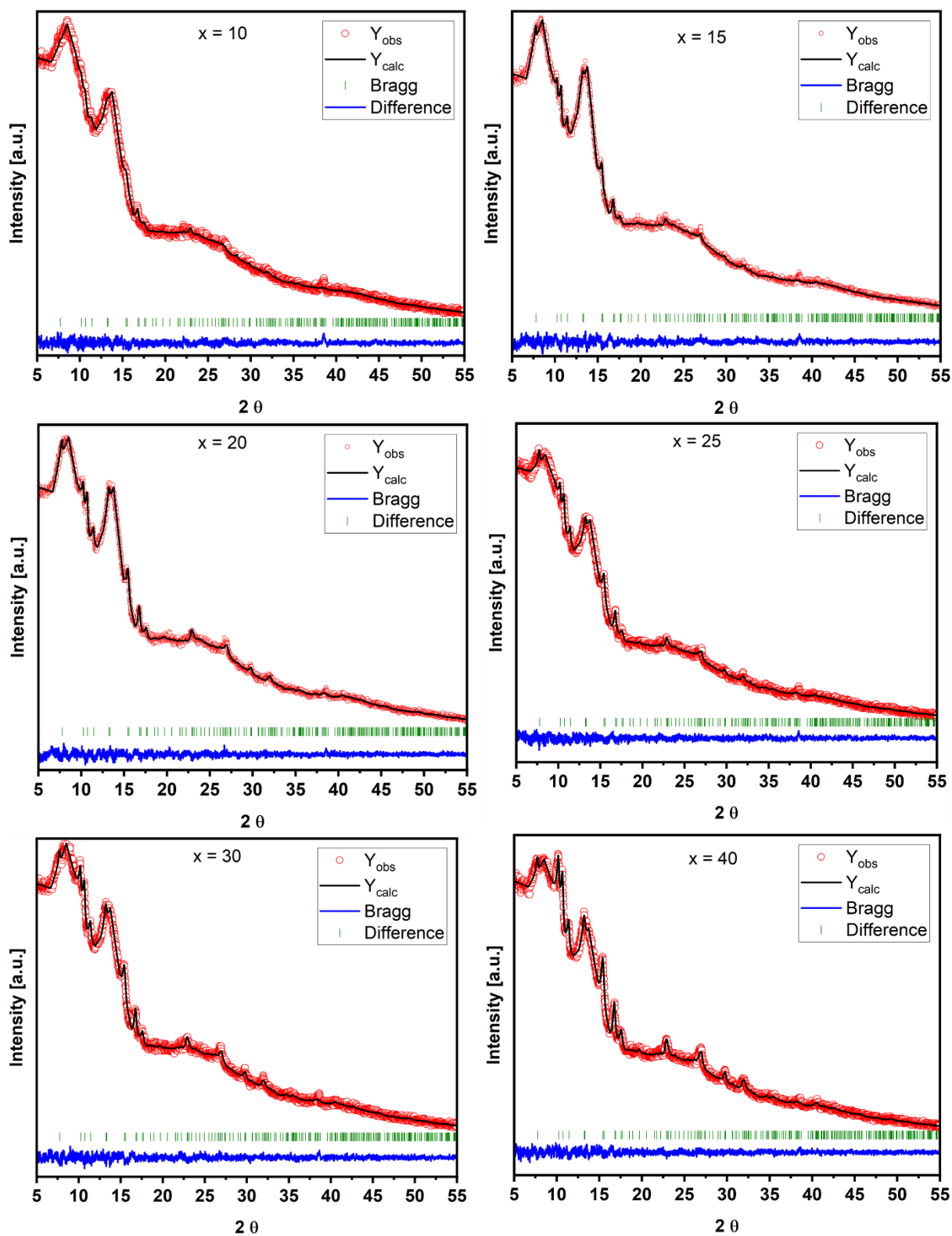


43: SEM images of all samples.

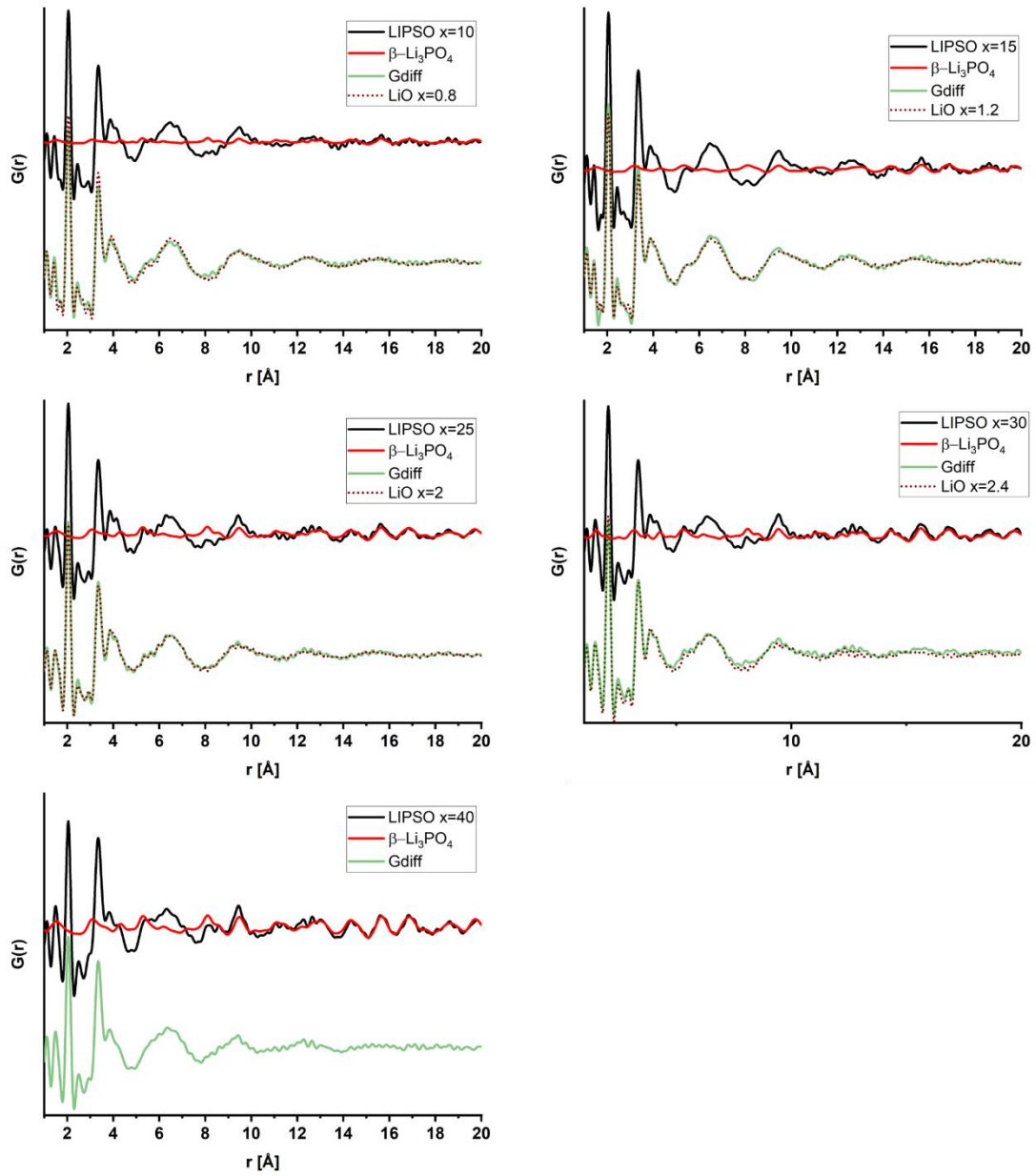


44: EDX maps for P(green), O(blue) and S(cyan) of all LIO samples.

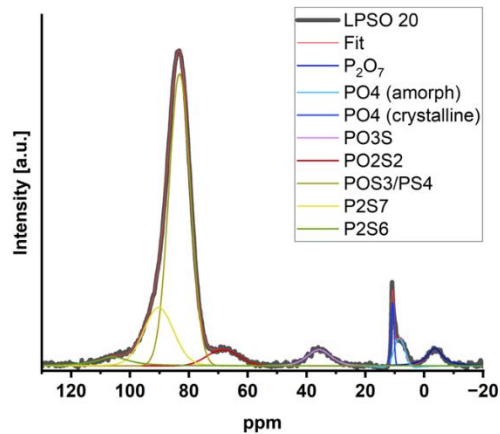
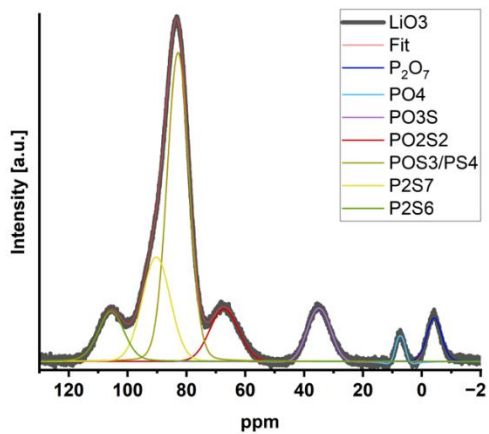
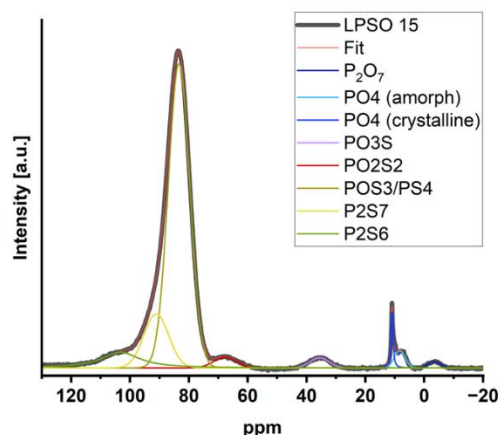
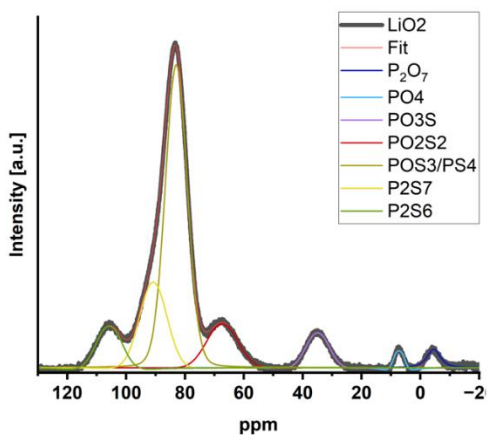
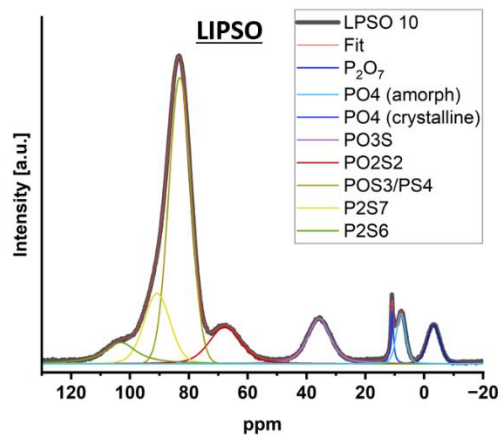
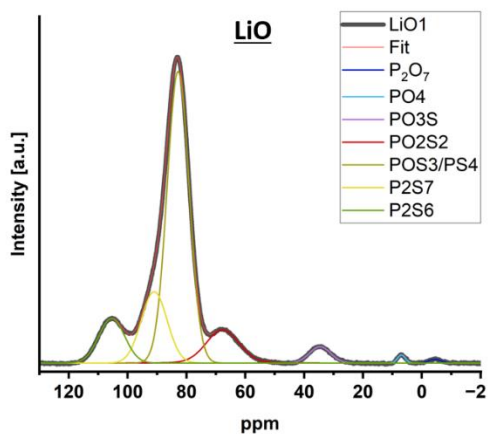




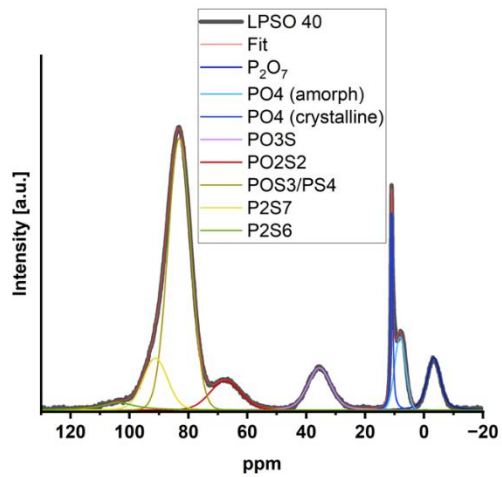
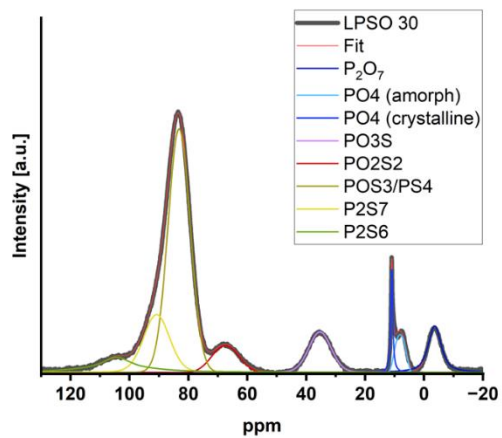
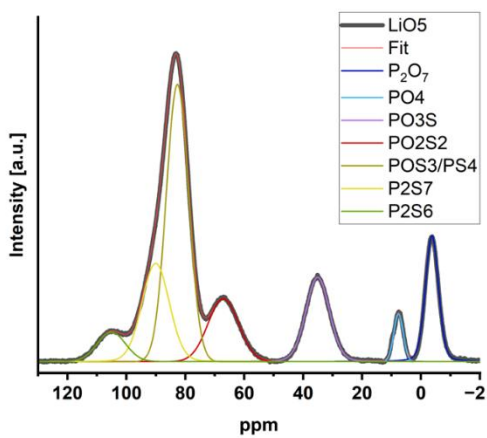
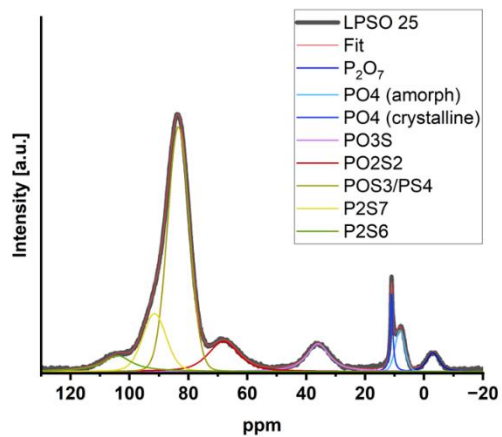
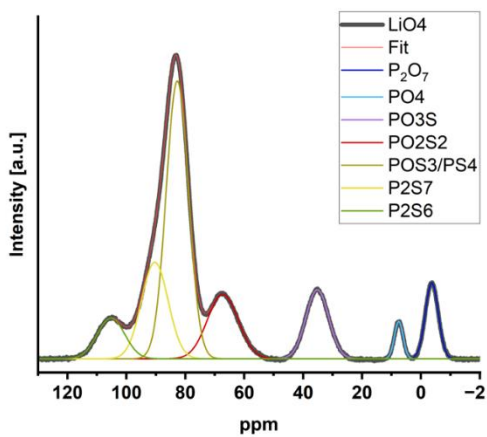
45: Rietveld refinements of the LIPSO samples. Only  $\beta$ - $\text{Li}_3\text{PO}_4$  phase was refined.



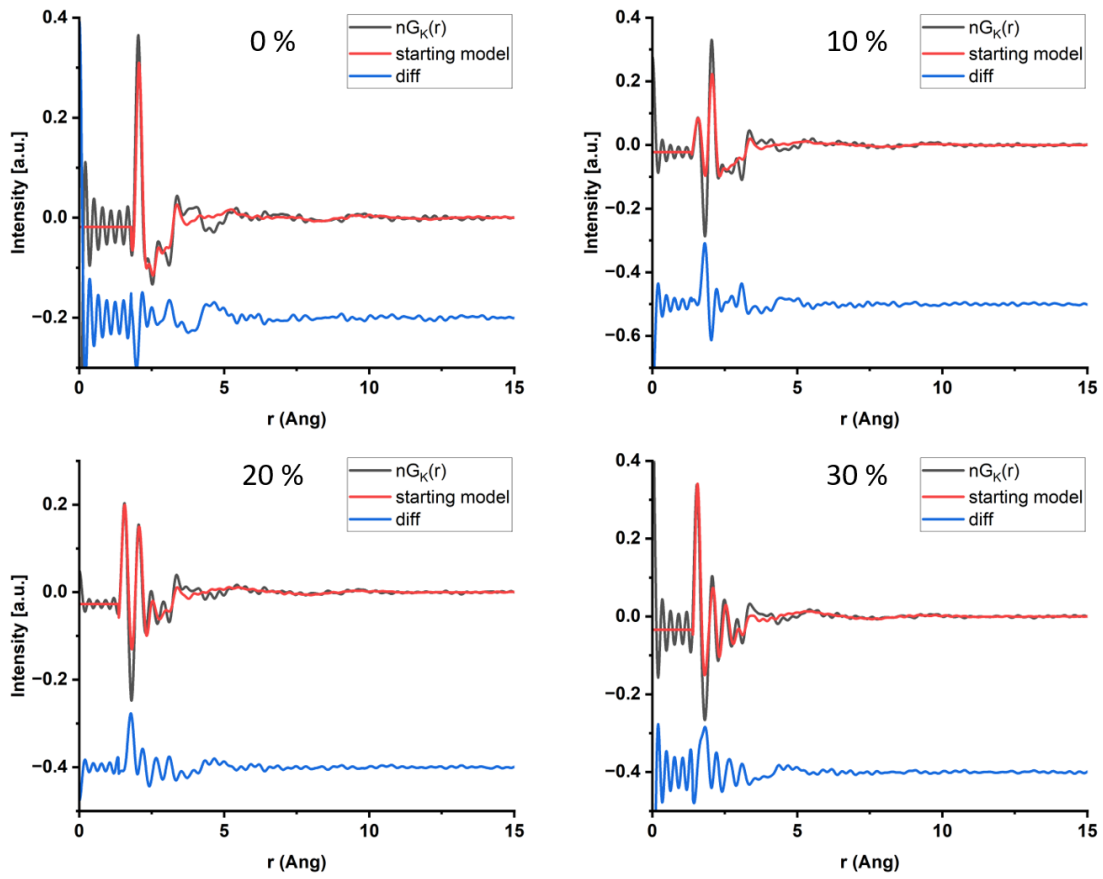
46: PDF of LIPSO samples (black) with PDFgui fit of the  $\beta$ -LPO phase (red) and the difference curve (green) compared to the LIO sample with the same oxygen content (brown, dotted).



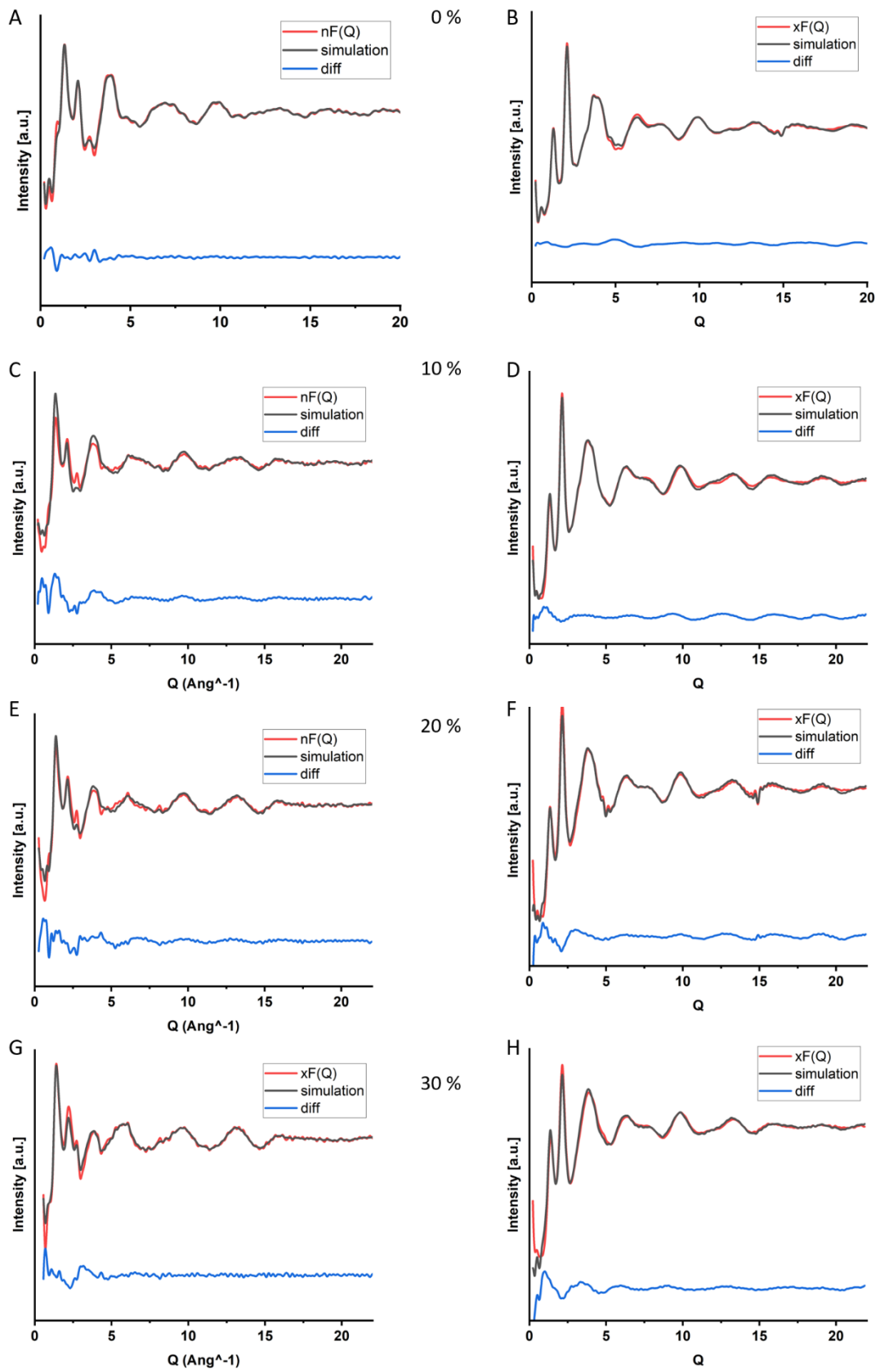
47: MAS-NMR fits of LIO (left) and LIPSO (right) samples with 10, 15 and 20 % oxygen.



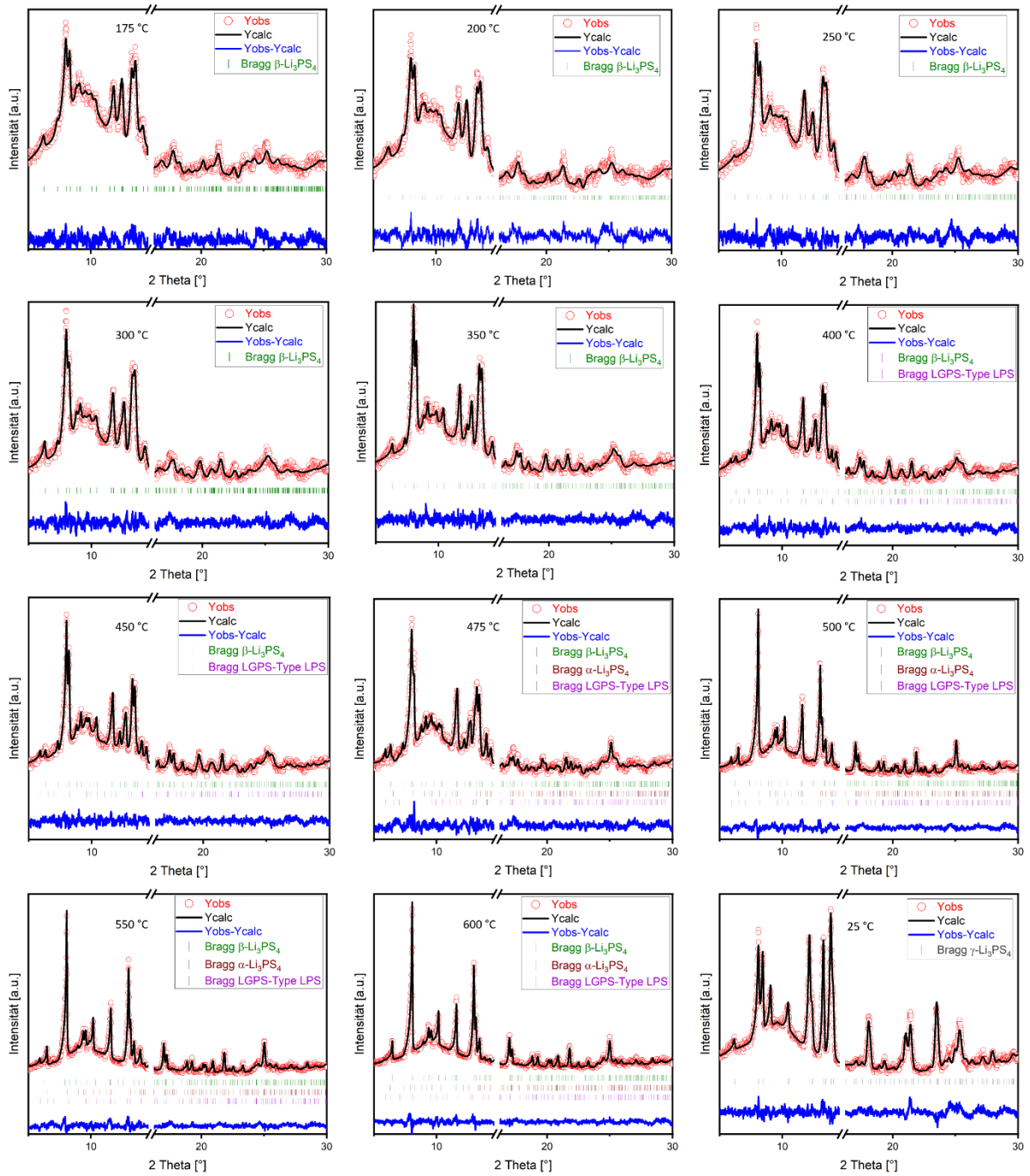
48:MAS-NMR fits of LIO (left) and LPSO (right) samples with 25, 30 and 40 % oxygen.



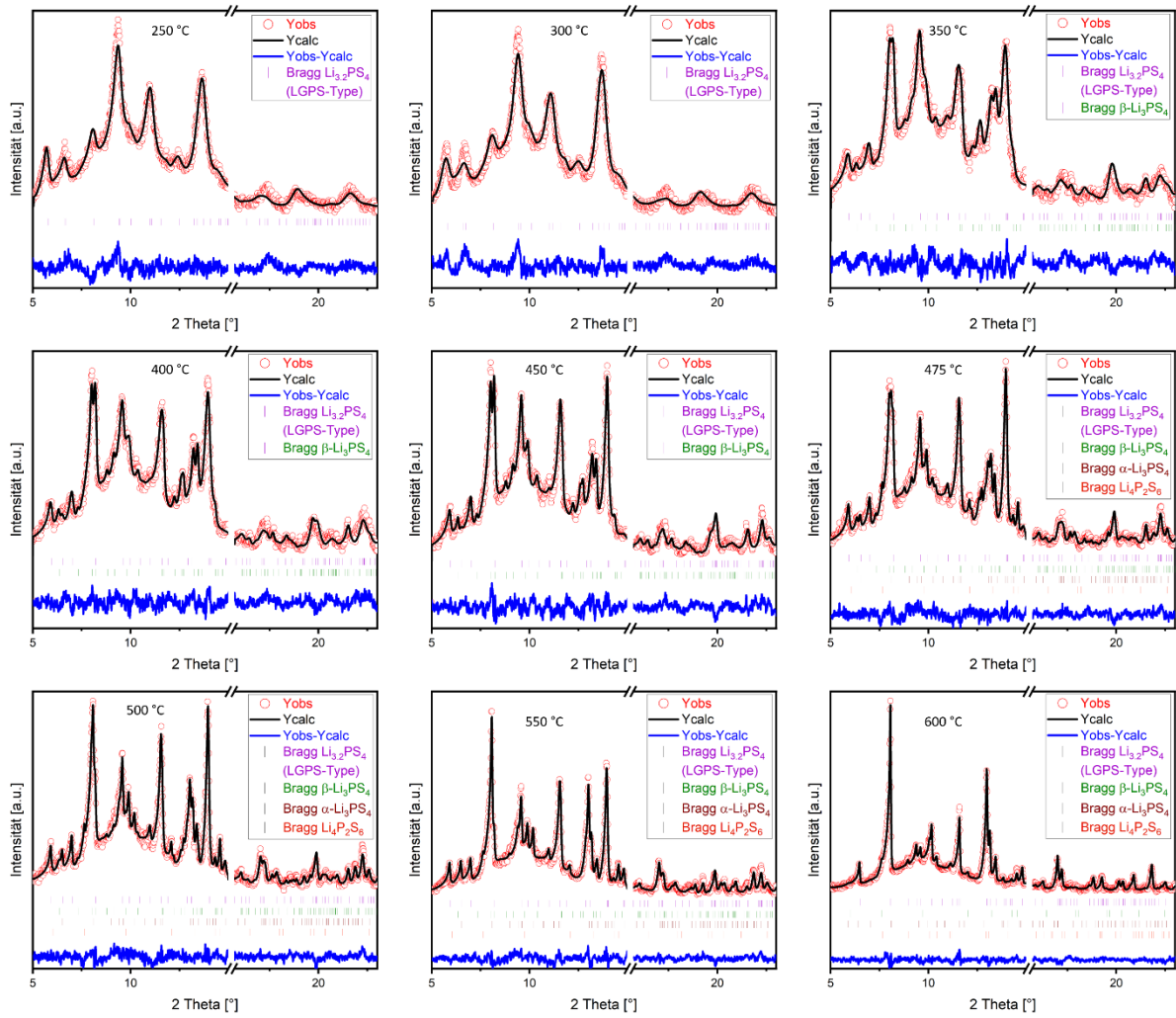
49: Simulated neutron PDFs for the starting models compared the the data.



50: Neutron and synchrotron  $F(Q)$  data and simulated  $F(Q)$ s from RMC refined structure models for 0 (A, B), 10 (C, D), 20 (E, F) and 30% (G, H) oxygen substitution.

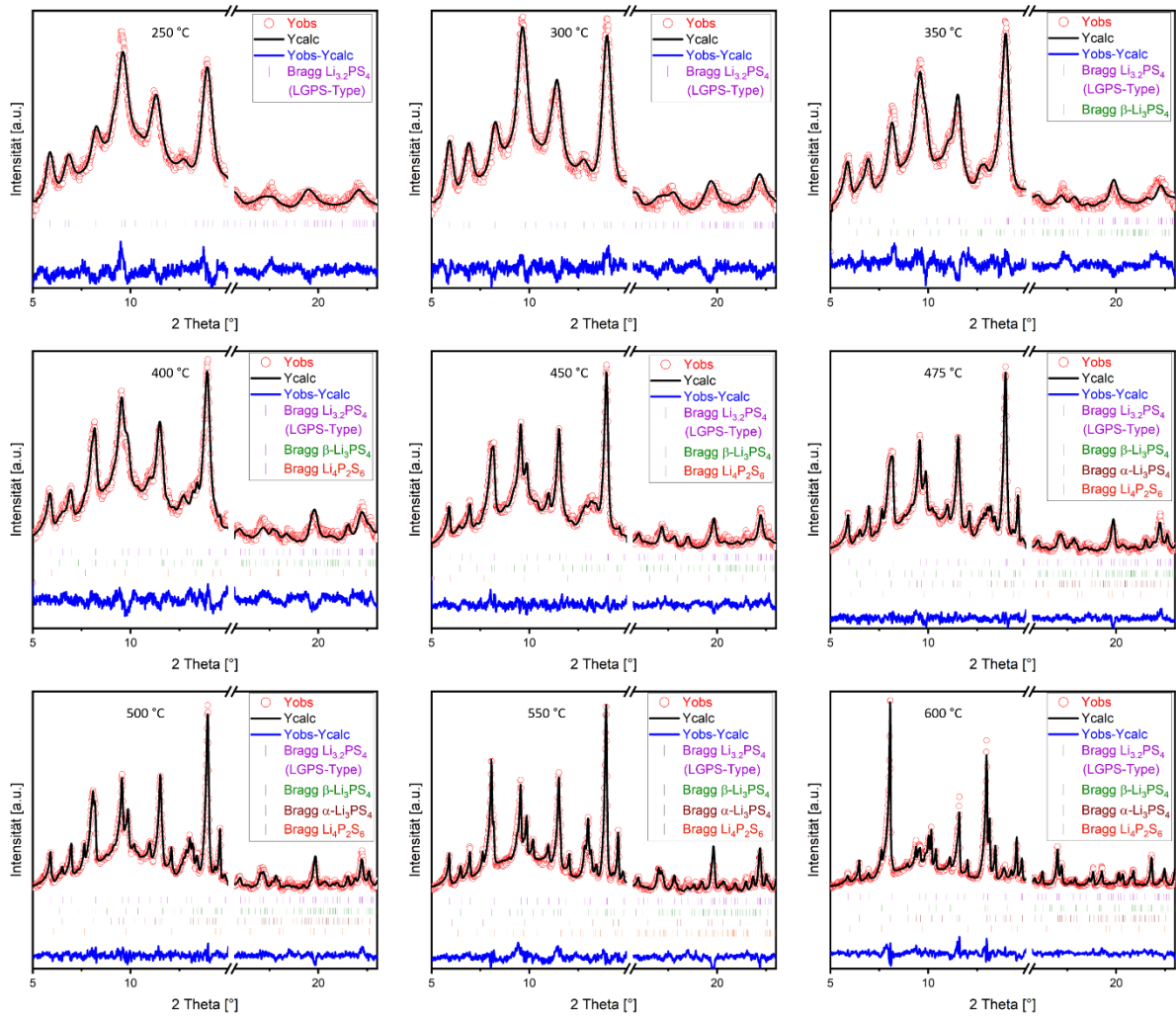


51: Rietveld refinement of Temperature-dependent x-ray diffractograms from the sample with 0 % oxygen substitution.

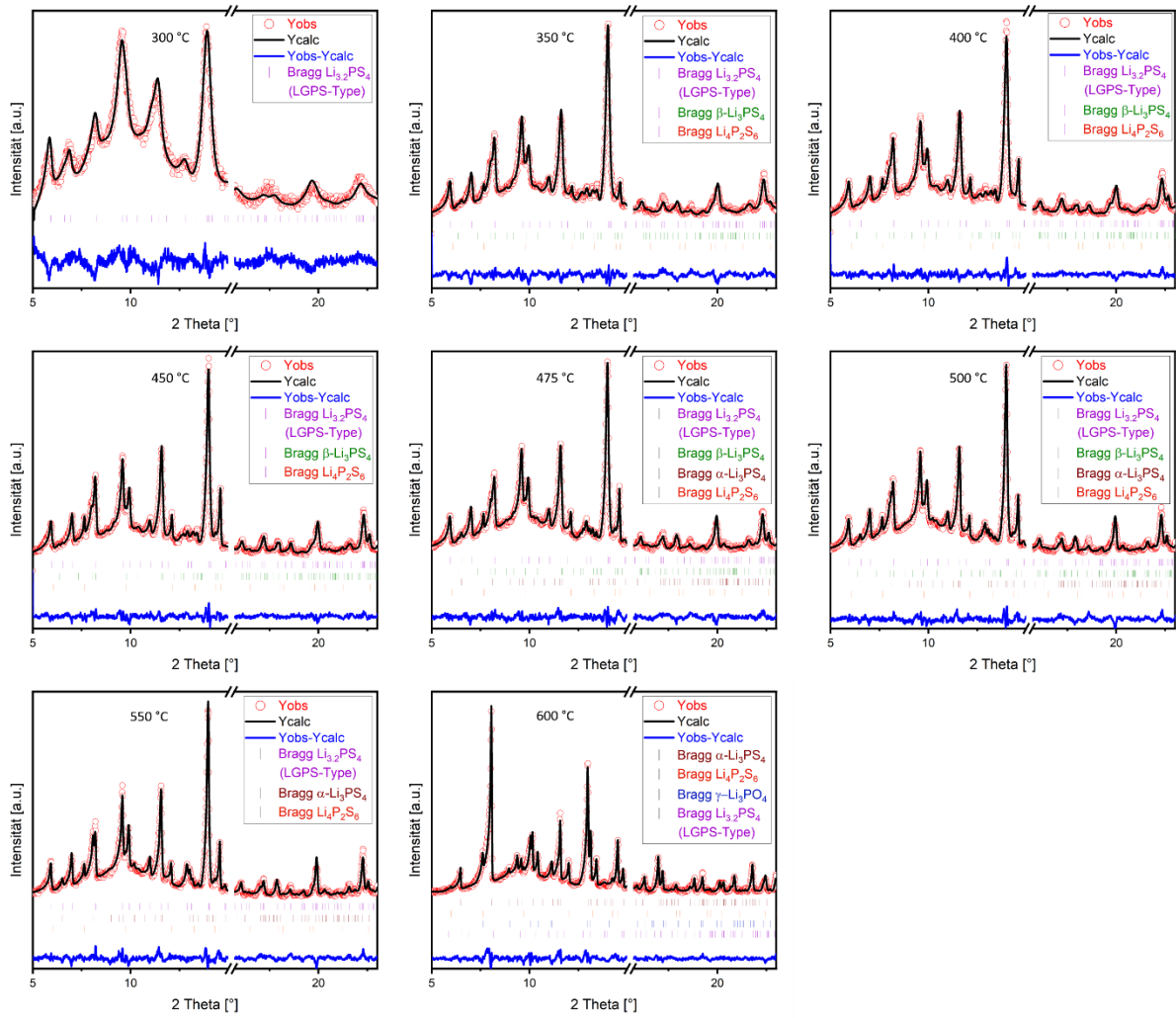


52: Rietveld refinement of Temperature-dependent x-ray diffractograms from the sample with 10 % oxygen substitution.

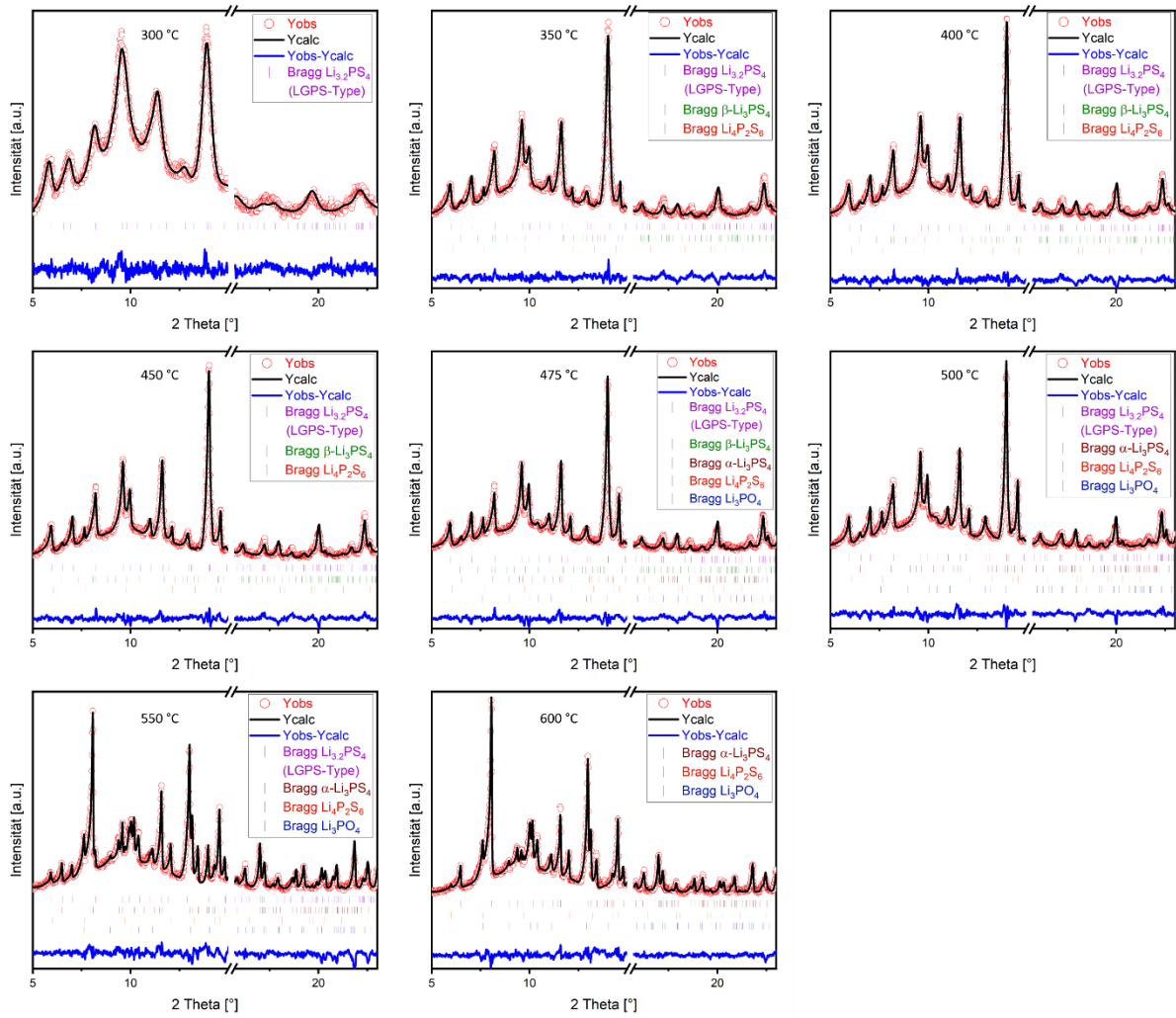




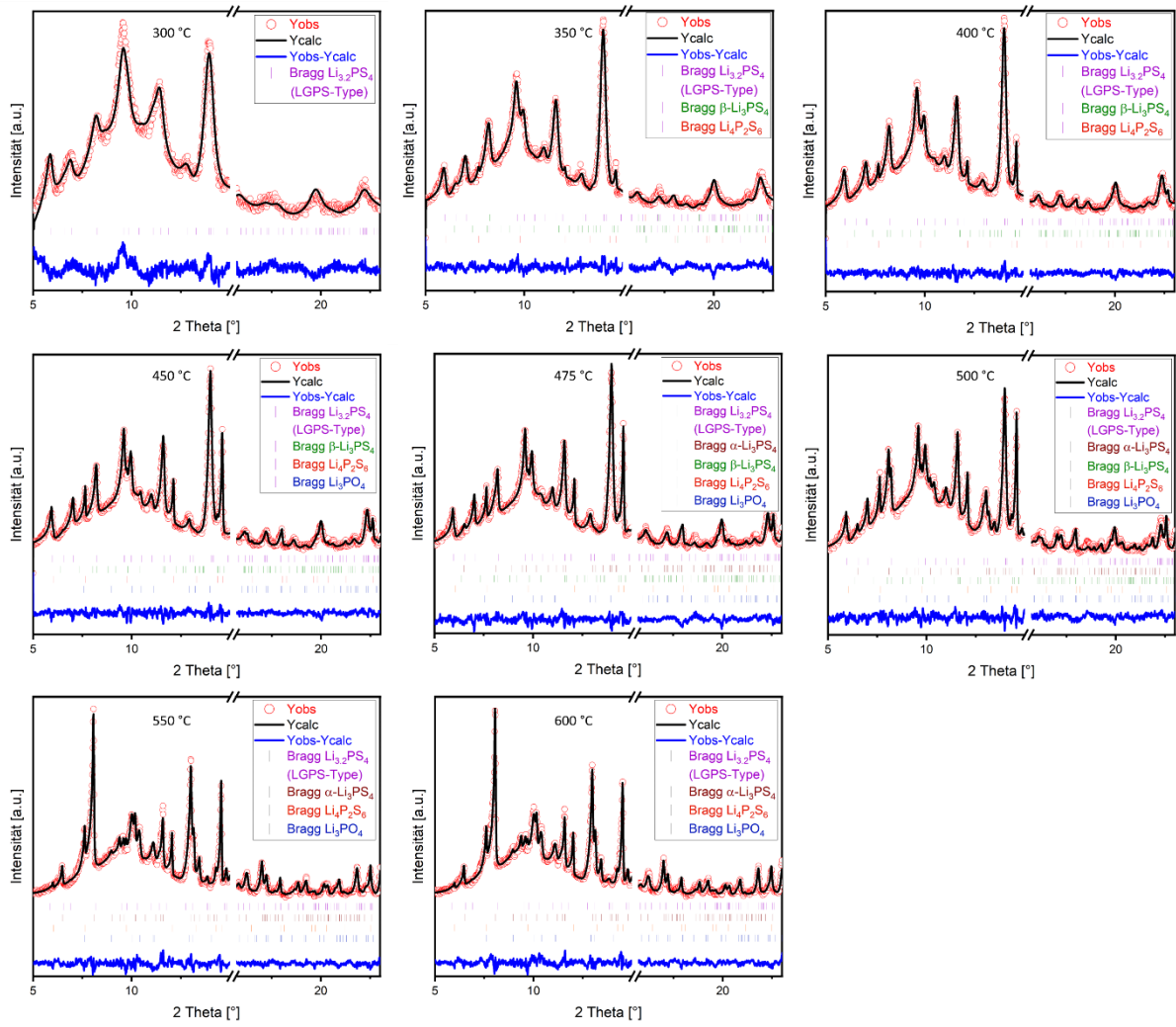
53: Rietveld refinement of Temperature-dependent x-ray diffractograms from the sample with 15 % oxygen substitution.



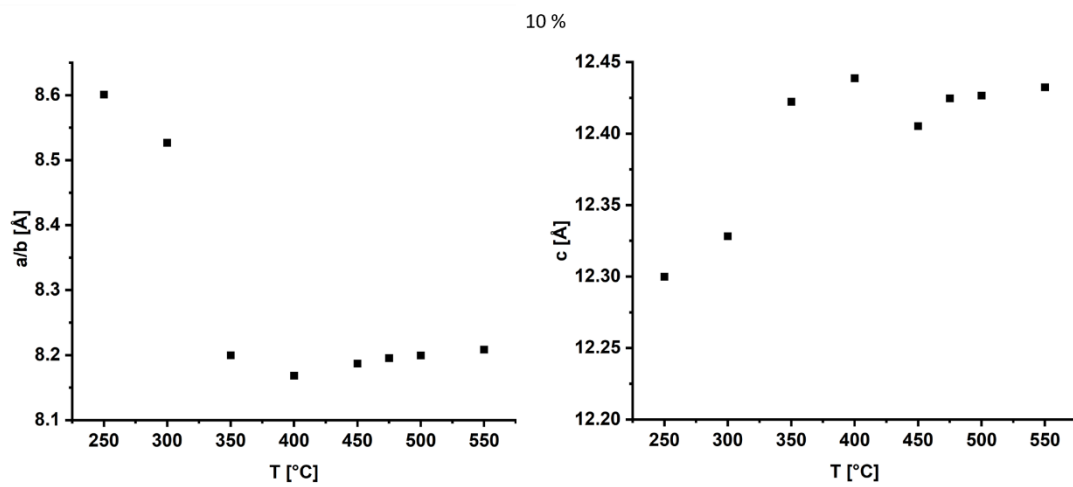
54: Rietveld refinement of Temperature-dependent x-ray diffractograms from the sample with 20 % oxygen substitution.



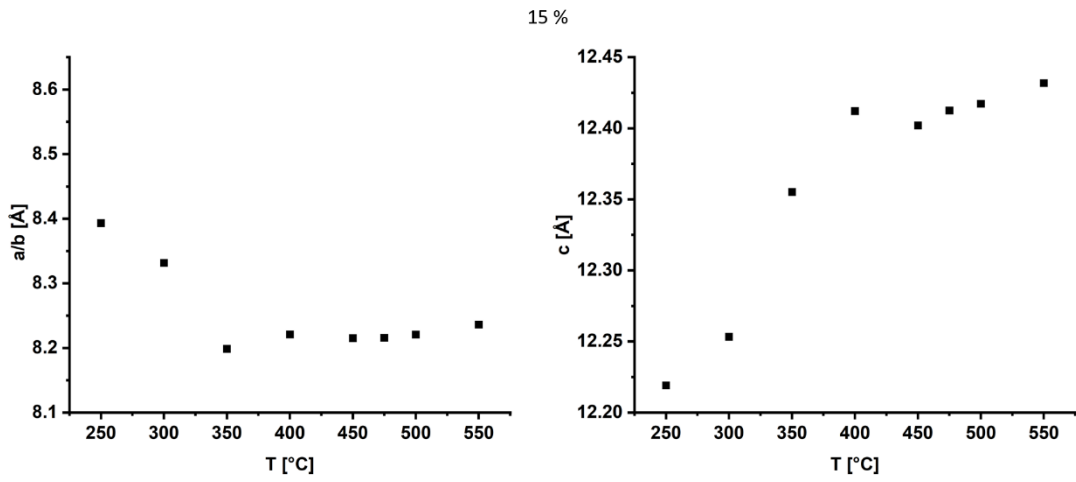
55: Rietveld refinement of Temperature-dependent x-ray diffractograms from the sample with 25 % oxygen substitution.



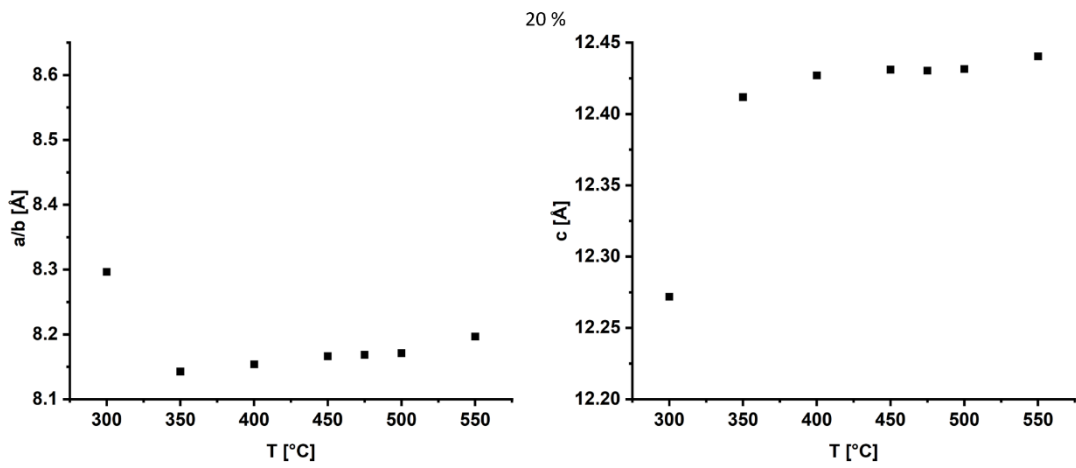
56: Rietveld refinement of Temperature-dependent x-ray diffractograms from the sample with 30 % oxygen substitution.



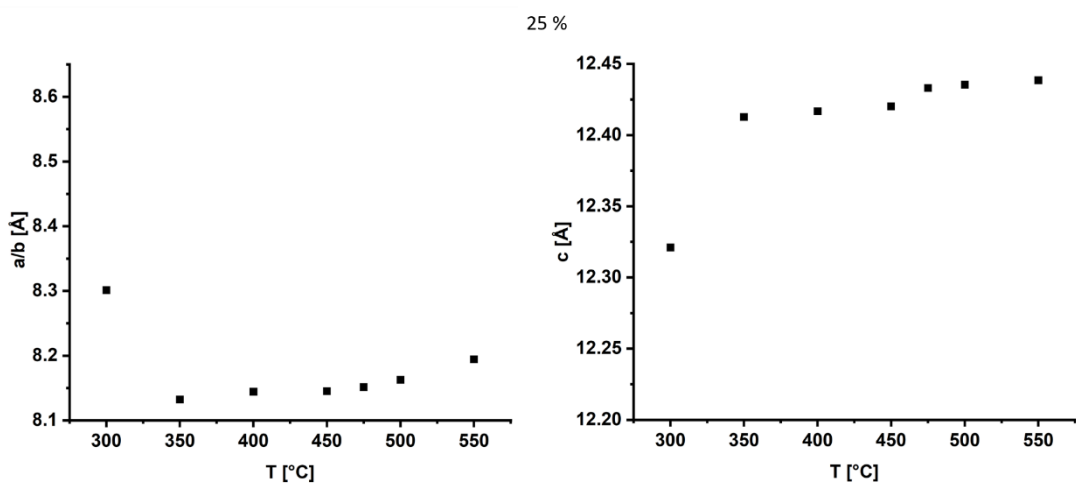
57: Evolution of lattice parameters with temperature for the sample with 10 % oxygen substitution.



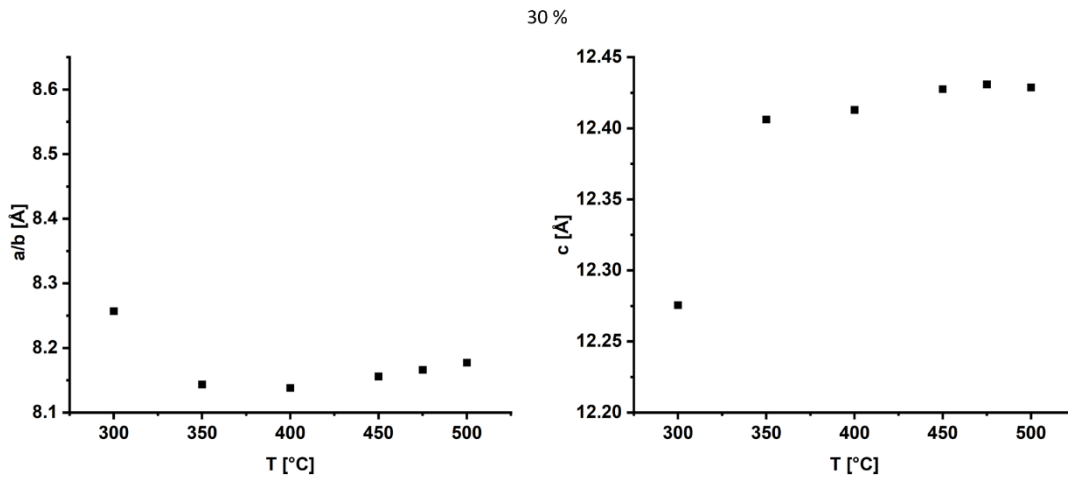
58: Evolution of lattice parameters with temperature for the sample with 15 % oxygen substitution.



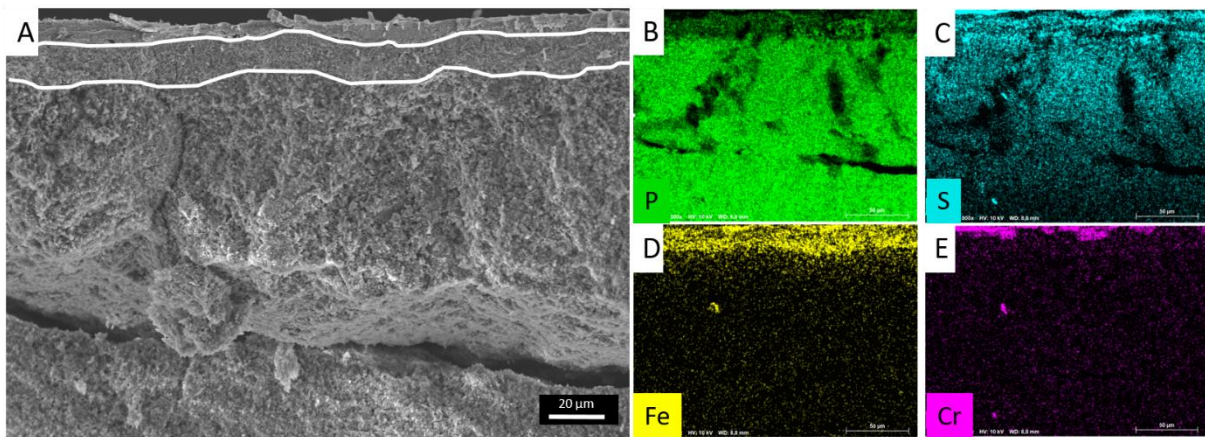
59: Evolution of lattice parameters with temperature for the sample with 20 % oxygen substitution.



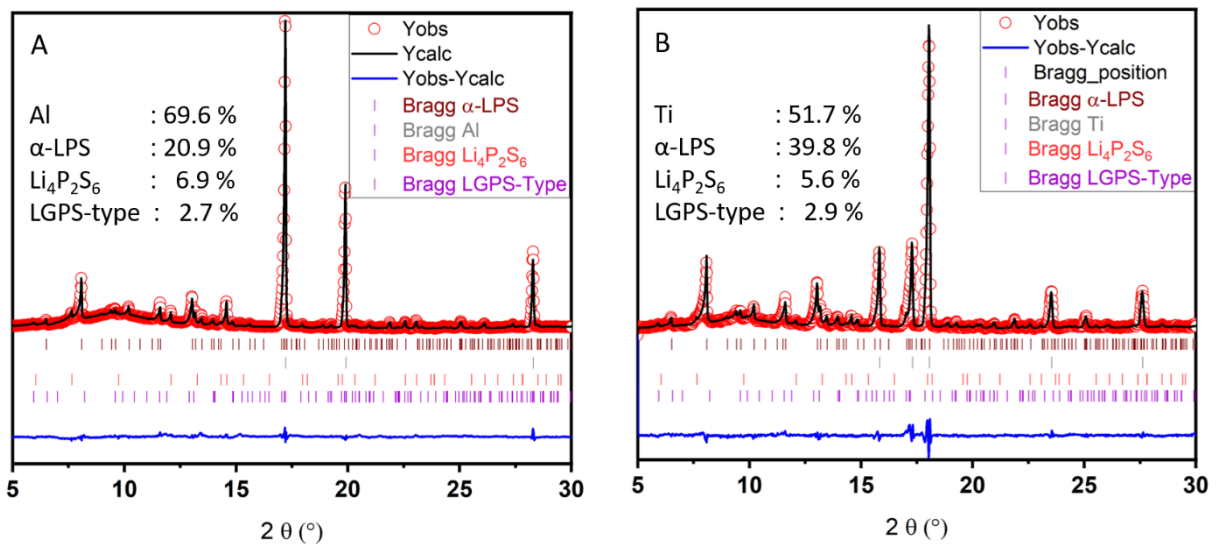
60: Evolution of lattice parameters with temperature for the sample with 25 % oxygen substitution.



61: Evolution of lattice parameters with temperature for the sample with 30 % oxygen substitution.



62: SEM image of the LPS pellet after test run in the HT-impedance cell (A) and EDX mapping for phosphorous (B), sulfur (C), iron (D) and chrome (E).



63: Rietveld refinement of LPS mixed with Al (A) and Ti (B) at 500 °C.

Table 5 Neutron and x-ray scattering coefficients for  $\text{Li}_3\text{PS}_4$

Partials for neutron (in barn)				Partials for x-ray		
	Li	P	S	Li	P	S
Li	0.00507656	-0.00913781	-0.02028488	0.01046049	0.03486567	0.14876643
P		0.00411202	0.01825639		0.02905253	0.24792532
S			0.02026352			0.52892958

Table 6 Neutron and X-ray scattering coefficients for  $\text{Li}_3\text{PO}_{0.4}\text{S}_{3.6}$

Partials for neutron (in barn)					
	Li	O	P	S	
Li		0.005076563	-0.004134638	-0.00913781	-0.01825639
O			0.00084187	0.00372117	0.00743451
P				0.00411202	0.01643075
S					0.01641345
Partials for x-ray					
	Li	O	P	S	
Li		0.011264871	0.0080102	0.0375467	0.14418552
O			0.001423969	0.01334933	0.05126356
P				0.03128658	0.24029104
S					0.4613782

Table 7 Neutron and X-ray scattering coefficients for  $\text{Li}_3\text{PO}_{0.6}\text{S}_{3.4}$

Partials for neutron (in barn)				
	Li	O	P	S
Li	0.005076563	-0.006201956	-0.00913781	-0.01724214
O		0.001894208	0.00558176	0.01053223
P			0.00411202	0.01551793
S				0.0146404

---

Partials for x-ray				
	Li	O	P	S
Li	0.011702309	0.012481879	0.03900475	0.14146317
O		0.003328346	0.02080156	0.0754435
P			0.0325015	0.23575415
S				0.42751883

Table 8 Neutron and X-ray scattering coefficients for  $\text{Li}_3\text{PO}_{0.8}\text{S}_{3.2}$

Partials for neutron (in barn)				
	Li	O	P	S
Li	0.005076563	-0.008269275	-0.00913781	-0.0162279
O		0.003367481	0.00744235	0.01321691
P			0.00411202	0.01460511
S				0.01296865

---

Partials for x-ray				
	Li	O	P	S
Li	0.012165731	0.017301564	0.04054937	0.13841435



O	0.00615138	0.02883376	0.09842338
P		0.03378859	0.23067315
S			0.39369873

Table 9 Neutron and X-ray scattering coefficients for  $Li_3PO_3$

Partials for neutron (in barn)				
	Li	O	P	S
Li	0.005076563	-0.010336594	-0.00913781	-0.01521366
O		0.005261689	0.00930293	0.01548857
P			0.00411202	0.01369229
S				0.01139823

---

Partials for x-ray				
	Li	O	P	S
Li	0.012657236	0.0225007	0.0421876	0.13500599
O		0.009999844	0.03749833	0.11999971
P			0.03515368	0.22499299
S				0.36000392

Table 10 Neutron and X-ray scattering coefficients for  $Li_3PO_{1.2}S_{2.8}$

Partials for neutron (in barn)				
	Li	O	P	S
Li	0.005076563	-0.012403913	-0.00913781	-0.01419941
O		0.007576832	0.01116352	0.0173472

P		0.00411202	0.01277947
S			0.00992913

---



---

**Partials for x-ray**

---

	Li	O	P	S
Li	0.013179139	0.028114183	0.04392715	0.13120126
O		0.01499353	0.04685343	0.13994147
P			0.03660319	0.21865225
S				0.32653441

## References

- [1] Manthiram A, Yu X, Wang S. Lithium battery chemistries enabled by solid-state electrolytes. *Nat Rev Mater* 2017; 2(4)  
[<https://doi.org/10.1038/natrevmats.2016.103>]
- [2] Pereirinha PG, González M, Carrilero I, Anseán D, Alonso J, Viera JC. Main Trends and Challenges in Road Transportation Electrification. *Transportation Research Procedia* 2018; 33(3): 235–42  
[<https://doi.org/10.1016/j.trpro.2018.10.096>]
- [3] Heubner C, Nikolowski K, Reuber S, Schneider M, Wolter M, Michaelis A. Recent Insights into Rate Performance Limitations of Li-ion Batteries. *Batteries & Supercaps* 2021; 4(2): 268–85  
[<https://doi.org/10.1002/batt.202000227>]
- [4] Goodenough JB, Park K-S. The Li-ion rechargeable battery: a perspective. *J Am Chem Soc* 2013; 135(4): 1167–76  
[<https://doi.org/10.1021/ja3091438>][PMID: 23294028]
- [5] Janek J, Zeier WG. A solid future for battery development. *Nat Energy* 2016; 1(9)  
[<https://doi.org/10.1038/nenergy.2016.141>]
- [6] Durmus YE, Zhang H, Baakes F, *et al.* Side by Side Battery Technologies with Lithium-Ion Based Batteries. *Adv. Energy Mater.* 2020; 10(24)  
[<https://doi.org/10.1002/aenm.202000089>]
- [7] Janek J, Zeier WG. Challenges in speeding up solid-state battery development. *Nat Energy* 2023; 8(3): 230–40  
[<https://doi.org/10.1038/s41560-023-01208-9>]

- [8] Xu B, Lee J, Kwon D, Kong L, Pecht M. Mitigation strategies for Li-ion battery thermal runaway: A review. *Renewable and Sustainable Energy Reviews* 2021; 150: 111437  
[<https://doi.org/10.1016/j.rser.2021.111437>]
- [9] Betz J, Bieker G, Meister P, Placke T, Winter M, Schmich R. Theoretical versus Practical Energy: A Plea for More Transparency in the Energy Calculation of Different Rechargeable Battery Systems. *Adv. Energy Mater.* 2019; 9(6)  
[<https://doi.org/10.1002/aenm.201803170>]
- [10] Yang Y, Yang S, Xue X, *et al.* Inorganic All-Solid-State Sodium Batteries: Electrolyte Designing and Interface Engineering. *Adv Mater* 2024; 36(1): e2308332  
[<https://doi.org/10.1002/adma.202308332>][PMID: 37730213]
- [11] Hamada M, Tatara R, Kubota K, Kumakura S, Komaba S. All-Solid-State Potassium Polymer Batteries Enabled by the Effective Pretreatment of Potassium Metal. *ACS Energy Lett.* 2022; 7(7): 2244–6  
[<https://doi.org/10.1021/acsenergylett.2c01096>]
- [12] Lou S, Zhang F, Fu C, *et al.* Interface Issues and Challenges in All-Solid-State Batteries: Lithium, Sodium, and Beyond. *Adv Mater* 2021; 33(6): e2000721  
[<https://doi.org/10.1002/adma.202000721>][PMID: 32705725]
- [13] Bachman JC, Muy S, Grimaud A, *et al.* Inorganic Solid-State Electrolytes for Lithium Batteries: Mechanisms and Properties Governing Ion Conduction. *Chem Rev* 2016; 116(1): 140–62  
[<https://doi.org/10.1021/acs.chemrev.5b00563>][PMID: 26713396]
- [14] Han L, Lehmann ML, Zhu J, *et al.* Recent Developments and Challenges in Hybrid Solid Electrolytes for Lithium-Ion Batteries. *Front. Energy Res.* 2020; 8  
[<https://doi.org/10.3389/fenrg.2020.00202>]
- [15] Hu Y, Li W, Zhu J, *et al.* Multi-layered electrolytes for solid-state lithium batteries. *Next Energy* 2023; 1(3): 100042  
[<https://doi.org/10.1016/j.nxener.2023.100042>]
- [16] Li C, Wang Z-y, He Z-j, *et al.* An advance review of solid-state battery: Challenges, progress and prospects. *Sustainable Materials and Technologies* 2021; 29(9): e00297  
[<https://doi.org/10.1016/j.susmat.2021.e00297>]
- [17] Liang J, Luo J, Sun Q, Yang X, Li R, Sun X. Recent progress on solid-state hybrid electrolytes for solid-state lithium batteries. *Energy Storage Materials* 2019; 21: 308–34  
[<https://doi.org/10.1016/j.ensm.2019.06.021>]
- [18] Woolley HM, Vargas-Barbosa NM. Hybrid solid electrolyte-liquid electrolyte systems for (almost) solid-state batteries: Why, how, and where to? *J. Mater. Chem. A* 2023; 11(3): 1083–97  
[<https://doi.org/10.1039/D2TA02179J>]
- [19] Kato Y, Hori S, Saito T, *et al.* High-power all-solid-state batteries using sulfide superionic conductors. *Nat Energy* 2016; 1(4): 652  
[<https://doi.org/10.1038/NENERGY.2016.30>]
- [20] Kwon O, Hirayama M, Suzuki K, *et al.* Synthesis, structure, and conduction mechanism of the lithium superionic conductor  $\text{Li}_{10+\delta}\text{Ge}_{1+\delta}\text{P}_{2-\delta}\text{S}_{12}$ . *J. Mater. Chem. A* 2015; 3(1): 438–46  
[<https://doi.org/10.1039/C4TA05231E>]

- [21] Zhang Q, Cao D, Ma Y, Natan A, Aurora P, Zhu H. Sulfide-Based Solid-State Electrolytes: Synthesis, Stability, and Potential for All-Solid-State Batteries. *Adv Mater* 2019; 31(44): e1901131 [https://doi.org/10.1002/adma.201901131][PMID: 31441140]
- [22] Zhu Y, Mo Y. Materials Design Principles for Air-Stable Lithium/Sodium Solid Electrolytes. *Angew Chem Int Ed Engl* 2020; 59(40): 17472–6 [https://doi.org/10.1002/anie.202007621][PMID: 32597549]
- [23] Chen S, Xie D, Liu G, *et al.* Sulfide solid electrolytes for all-solid-state lithium batteries: Structure, conductivity, stability and application. *Energy Storage Materials* 2018; 14: 58–74 [https://doi.org/10.1016/j.ensm.2018.02.020]
- [24] Wu J, Liu S, Han F, Yao X, Wang C. Lithium/Sulfide All-Solid-State Batteries using Sulfide Electrolytes. *Adv Mater* 2021; 33(6): e2000751 [https://doi.org/10.1002/adma.202000751][PMID: 32812301]
- [25] Ohtomo T, Hayashi A, Tatsumisago M, Kawamoto K. Characteristics of the Li<sub>2</sub>O–Li<sub>2</sub>S–P<sub>2</sub>S<sub>5</sub> glasses synthesized by the two-step mechanical milling. *Journal of Non-Crystalline Solids* 2013; 364(3): 57–61 [https://doi.org/10.1016/j.jnoncrysol.2012.12.044]
- [26] Neveu A, Pelé V, Jordy C, Pralong V. Exploration of Li–P–S–O composition for solid-state electrolyte materials discovery. *Journal of Power Sources* 2020; 467: 228250 [https://doi.org/10.1016/j.jpowsour.2020.228250]
- [27] Trevey JE, Gilsdorf JR, Miller SW, Lee S-H. Li<sub>2</sub>S–Li<sub>2</sub>O–P<sub>2</sub>S<sub>5</sub> solid electrolyte for all-solid-state lithium batteries. *Solid State Ionics* 2012; 214: 25–30 [https://doi.org/10.1016/j.ssi.2012.02.034]
- [28] Xu M, Song S, Daikuhara S, *et al.* Li<sub>10</sub>GeP<sub>2</sub>S<sub>12</sub>-Type Structured Solid Solution Phases in the Li<sub>9+δ</sub>P<sub>3+δ</sub>S<sub>12</sub>-kOk System: Controlling Crystallinity by Synthesis to Improve the Air Stability. *Inorganic chemistry* 2022; 61(1): 52–61 [https://doi.org/10.1021/acs.inorgchem.1c01748]
- [29] Kamaya N, Homma K, Yamakawa Y, *et al.* A lithium superionic conductor. *Nat Mater* 2011; 10(9): 682–6 [https://doi.org/10.1038/nmat3066][PMID: 21804556]
- [30] Bron P, Johansson S, Zick K, Schmedt auf der Günne J, Dehnen S, Røling B. Li<sub>10</sub>SnP<sub>2</sub>S<sub>12</sub>: an affordable lithium superionic conductor. *J Am Chem Soc* 2013; 135(42): 15694–7 [https://doi.org/10.1021/ja407393y][PMID: 24079534]
- [31] Harm S, Hatz A-K, Moudrakovski I, *et al.* Lesson Learned from NMR: Characterization and Ionic Conductivity of LGPS-like Li<sub>7</sub>SiPS<sub>8</sub>. *Chem. Mater.* 2019; 31(4): 1280–8 [https://doi.org/10.1021/acs.chemmater.8b04051]
- [32] Tao B, Ren C, Li H, *et al.* Thio-/LISICON and LGPS-Type Solid Electrolytes for All-Solid-State Lithium-Ion Batteries. *Adv Funct Materials* 2022; 32(34) [https://doi.org/10.1002/adfm.202203551]
- [33] Yu C, Zhao F, Luo J, Zhang L, Sun X. Recent development of lithium argyrodite solid-state electrolytes for solid-state batteries: Synthesis, structure, stability and dynamics. *Nano Energy* 2021; 83: 105858 [https://doi.org/10.1016/j.nanoen.2021.105858]

- [34] Dietrich C, Weber DA, Sedlmaier SJ, *et al.* Lithium ion conductivity in Li<sub>2</sub>S–P<sub>2</sub>S<sub>5</sub> glasses – building units and local structure evolution during the crystallization of superionic conductors Li<sub>3</sub>PS<sub>4</sub>Li<sub>7</sub>P<sub>3</sub>S<sub>11</sub> and Li<sub>4</sub>P<sub>2</sub>S<sub>7</sub>. *J. Mater. Chem. A* 2017; 5(34): 18111–9  
[<https://doi.org/10.1039/c7ta06067j>]
- [35] Seino Y, Ota T, Takada K, Hayashi A, Tatsumisago M. A sulphide lithium super ion conductor is superior to liquid ion conductors for use in rechargeable batteries. *Energy Environ. Sci.* 2014; 7(2): 627–31  
[<https://doi.org/10.1039/c3ee41655k>]
- [36] Hayashi A, Hama S, Minami T, Tatsumisago M. Formation of superionic crystals from mechanically milled Li<sub>2</sub>S–P<sub>2</sub>S<sub>5</sub> glasses. *Electrochemistry Communications* 2003; 5(2): 111–4  
[[https://doi.org/10.1016/S1388-2481\(02\)00555-6](https://doi.org/10.1016/S1388-2481(02)00555-6)]
- [37] Garcia-Mendez R, Smith JG, Neufeind JC, Siegel DJ, Sakamoto J. Correlating Macro and Atomic Structure with Elastic Properties and Ionic Transport of Glassy Li<sub>2</sub>S–P<sub>2</sub>S<sub>5</sub> (LPS) Solid Electrolyte for Solid-State Li Metal Batteries. *Adv. Energy Mater.* 2020; 10(19): 2000335  
[<https://doi.org/10.1002/aenm.202000335>]
- [38] CHIKU M, TSUJIWAKI W, HIGUCHI E, INOUE H. Microelectrode Studies on Kinetics of Charge Transfer at an Interface of Li Metal and Li<sub>2</sub>S–P<sub>2</sub>S<sub>5</sub> Solid Electrolytes. *Electrochemistry* 2012; 80(10): 740–2  
[<https://doi.org/10.5796/electrochemistry.80.740>]
- [39] Dietrich C, Weber DA, Culver S, *et al.* Synthesis, Structural Characterization, and Lithium Ion Conductivity of the Lithium Thiophosphate Li<sub>2</sub>P<sub>2</sub>S<sub>6</sub>. *Inorganic chemistry* 2017; 56(11): 6681–7  
[<https://doi.org/10.1021/acs.inorgchem.7b00751>][PMID: 28485931]
- [40] Kudu ÖÜ, Famprakis T, Fleutot B, *et al.* A review of structural properties and synthesis methods of solid electrolyte materials in the Li<sub>2</sub>S – P<sub>2</sub>S<sub>5</sub> binary system. *Journal of Power Sources* 2018; 407(4): 31–43  
[<https://doi.org/10.1016/j.jpowsour.2018.10.037>]
- [41] Yamamoto K, Yang S, Takahashi M, *et al.* High Ionic Conductivity of Liquid-Phase-Synthesized Li<sub>3</sub>PS<sub>4</sub> Solid Electrolyte, Comparable to That Obtained via Ball Milling. *ACS Appl. Energy Mater.* 2021; 4(3): 2275–81  
[<https://doi.org/10.1021/acsaem.0c02771>]
- [42] Stöffler H, Zinkevich T, Yavuz M, *et al.* Amorphous versus Crystalline Li<sub>3</sub>PS<sub>4</sub>: Local Structural Changes during Synthesis and Li Ion Mobility. *J. Phys. Chem. C* 2019; 123(16): 10280–90  
[<https://doi.org/10.1021/acs.jpcc.9b01425>]
- [43] Hayashi A, Hama S, Morimoto H, Tatsumisago M, Minami T. Preparation of Li<sub>2</sub>S–P<sub>2</sub>S<sub>5</sub> Amorphous Solid Electrolytes by Mechanical Milling. *Journal of the American Ceramic Society* 2001; 84(2): 477–9  
[<https://doi.org/10.1111/j.1151-2916.2001.tb00685.x>]
- [44] Luo X. Interface effects in solid electrolytes for Li-ion batteries. Karlsruhe Institut für Technologie (KIT); 2022.
- [45] Tsukasaki H, Morimoto H, Mori S. Ionic conductivity and thermal stability of Li<sub>2</sub>O–Li<sub>2</sub>S–P<sub>2</sub>S<sub>5</sub> oxysulfide glass. *Solid State Ionics* 2020; 347(6): 115267  
[<https://doi.org/10.1016/j.ssi.2020.115267>]

- [46] Nobuya Machida, Yuki Yoneda and Toshihiko Shigematsu. Mechano-chemical Synthesis of Lithium Ion Conducting Materials in the System Li<sub>20</sub>-Li<sub>2</sub>S-P<sub>2</sub>S<sub>5</sub>. J. Jpn. Soc. Powder Metallurgy 2003; 2003(Vol. 51, No. 2).
- [47] Lu S, Kosaka F, Shiotani S, Tsukasaki H, Mori S, Otomo J. Optimization of lithium ion conductivity of Li<sub>2</sub>S-P<sub>2</sub>S<sub>5</sub> glass ceramics by microstructural control of crystallization kinetics. Solid State Ionics 2021; 362: 115583  
[<https://doi.org/10.1016/j.ssi.2021.115583>]
- [48] Tsukasaki H, Mori S, Shiotani S, Yamamura H. Ionic conductivity and crystallization process in the Li<sub>2</sub>S-P<sub>2</sub>S<sub>5</sub> glass electrolyte. Solid State Ionics 2018; 317: 122–6  
[<https://doi.org/10.1016/j.ssi.2018.01.010>]
- [49] Wang S, Zhang W, Chen X, *et al.* Influence of Crystallinity of Lithium Thiophosphate Solid Electrolytes on the Performance of Solid-State Batteries. Adv. Energy Mater. 2021; 11(24)  
[<https://doi.org/10.1002/aenm.202100654>]
- [50] Takada K, Osada M, Ohta N, *et al.* Lithium ion conductive oxysulfide, Li<sub>3</sub>PO<sub>4</sub>-Li<sub>3</sub>PS<sub>4</sub>. Solid State Ionics 2005; 176(31-34): 2355–9  
[<https://doi.org/10.1016/j.ssi.2005.03.023>]
- [51] Tan DHS, Meng YS, Jang J. Scaling up high-energy-density sulfidic solid-state batteries: A lab-to-pilot perspective. Joule 2022; 6(8): 1755–69  
[<https://doi.org/10.1016/j.joule.2022.07.002>]
- [52] Zhou J, Chen Y, Yu Z, *et al.* Wet-chemical synthesis of Li<sub>7</sub>P<sub>3</sub>S<sub>11</sub> with tailored particle size for solid state electrolytes. Chemical Engineering Journal 2022; 429(5): 132334  
[<https://doi.org/10.1016/j.ccej.2021.132334>]
- [53] Kim M-J, Choi I-H, Jo SC, *et al.* A Novel Strategy to Overcome the Hurdle for Commercial All-Solid-State Batteries via Low-Cost Synthesis of Sulfide Solid Electrolytes. Small Methods 2021; 5(11): e2100793  
[<https://doi.org/10.1002/smt.202100793>][PMID: 34927966]
- [54] Gamo H, Nagai A, Matsuda A. Toward Scalable Liquid-Phase Synthesis of Sulfide Solid Electrolytes for All-Solid-State Batteries. Batteries 2023; 9(7): 355  
[<https://doi.org/10.3390/batteries9070355>]
- [55] Kano J, Chujo N, Saito F. A method for simulating the three-dimensional motion of balls under the presence of a powder sample in a tumbling ball mill. Advanced Powder Technology 1997; 8(1): 39–51  
[[https://doi.org/10.1016/S0921-8831\(08\)60478-1](https://doi.org/10.1016/S0921-8831(08)60478-1)]
- [56] Zou J, Yang X, Liu J. Study on Preparation of Superhard Nanopowder by Chaos Vibration with High Strength. Information Technology J. 2012; 11(4): 461–5  
[<https://doi.org/10.3923/itj.2012.461.465>]
- [57] Kwade A, Schwedes J. Wet Comminution in Stirred Media Mills. KONA 1997; 15(0): 91–102  
[<https://doi.org/10.14356/kona.1997013>]
- [58] Rosenkranz S, Breitung-Faes S, Kwade A. Experimental investigations and modelling of the ball motion in planetary ball mills. Powder Technology 2011; 212(1): 224–30  
[<https://doi.org/10.1016/j.powtec.2011.05.021>]

- [59] Schlem R, Burmeister CF, Michalowski P, *et al.* Energy Storage Materials for Solid-State Batteries: Design by Mechanochemistry. *Adv. Energy Mater.* 2021; 11(30): 2101022  
[<https://doi.org/10.1002/aenm.202101022>]
- [60] Burmeister CF, Hofer M, Molaiyan P, Michalowski P, Kwade A. Characterization of Stressing Conditions in a High Energy Ball Mill by Discrete Element Simulations. *Processes* 2022; 10(4): 692  
[<https://doi.org/10.3390/pr10040692>]
- [61] Daraio D, Villoria J, Ingram A, *et al.* Using Discrete Element method (DEM) simulations to reveal the differences in the  $\gamma$ -Al<sub>2</sub>O<sub>3</sub> to  $\alpha$ -Al<sub>2</sub>O<sub>3</sub> mechanically induced phase transformation between a planetary ball mill and an attritor mill. *Minerals Engineering* 2020; 155: 106374  
[<https://doi.org/10.1016/j.mineng.2020.106374>]
- [62] Petersen H, Reichle S, Leiting S, *et al.* In Situ Synchrotron X-ray Diffraction Studies of the Mechanochemical Synthesis of ZnS from its Elements. *Chemistry* 2021; 27(49): 12558–65  
[<https://doi.org/10.1002/chem.202101260>][PMID: 34062026]
- [63] Rathmann T, Petersen H, Reichle S, *et al.* In situ synchrotron x-ray diffraction studies monitoring mechanochemical reactions of hard materials: Challenges and limitations. *Rev Sci Instrum* 2021; 92(11): 114102  
[<https://doi.org/10.1063/5.0068627>][PMID: 34852549]
- [64] Weidenthaler C. In Situ Analytical Methods for the Characterization of Mechanochemical Reactions. *Crystals* 2022; 12(3): 345  
[<https://doi.org/10.3390/cryst12030345>]
- [65] Rietveld HM. A profile refinement method for nuclear and magnetic structures. *J Appl Crystallogr* 1969; 2(2): 65–71  
[<https://doi.org/10.1107/S0021889869006558>]
- [66] Dinnebier RE, editor. Powder diffraction: Theory and practice. Repr. Cambridge: Royal Society of Chemistry; 2009.
- [67] Lambert K, Geyter B de, Moreels I, Hens Z. PbTe|CdTe Core|Shell Particles by Cation Exchange, a HR-TEM study. *Chem. Mater.* 2009; 21(5): 778–80  
[<https://doi.org/10.1021/cm8029399>]
- [68] Liu Z, Suenaga K, Iijima S. Imaging the structure of an individual C<sub>60</sub> fullerene molecule and its deformation process using HRTEM with atomic sensitivity. *J Am Chem Soc* 2007; 129(21): 6666–7  
[<https://doi.org/10.1021/ja068516r>][PMID: 17474742]
- [69] Keen DA. A comparison of various commonly used correlation functions for describing total scattering. *J Appl Crystallogr* 2001; 34(2): 172–7  
[<https://doi.org/10.1107/S0021889800019993>]
- [70] Peterson PF, Olds D, McDonnell MT, Page K. Illustrated formalisms for total scattering data: a guide for new practitioners. *J Appl Crystallogr* 2021; 54(Pt 1): 317–32  
[<https://doi.org/10.1107/S1600576720015630>][PMID: 33833656]
- [71] Peterson PF, Keen DA. Erratum: Illustrated formalisms for total scattering data: a guide for new practitioners. *Corrigendum and addendum. J Appl Crystallogr* 2021; 54(Pt 5): 1542–5  
[<https://doi.org/10.1107/S1600576721007664>][PMID: 34667455]

- [72] Zea-Garcia JD, La Torre AG de, Aranda MAG, Cuesta A. A Comparative Study of Experimental Configurations in Synchrotron Pair Distribution Function. *Materials (Basel)* 2019; 12(8) [https://doi.org/10.3390/ma12081347][PMID: 31027173]
- [73] Dove MT, Li G. Review: Pair distribution functions from neutron total scattering for the study of local structure in disordered materials. *Nuclear Analysis* 2022; 1(4): 100037 [https://doi.org/10.1016/j.nucana.2022.100037]
- [74] Juhás P, Davis T, Farrow CL, Billinge SJL. PDFgetX3 : a rapid and highly automatable program for processing powder diffraction data into total scattering pair distribution functions. *J Appl Crystallogr* 2013; 46(2): 560–6 [https://doi.org/10.1107/S0021889813005190]
- [75] Tucker MG, Keen DA, Dove MT, Goodwin AL, Hui Q. RMCProfile: reverse Monte Carlo for polycrystalline materials. *J Phys Condens Matter* 2007; 19(33): 335218 [https://doi.org/10.1088/0953-8984/19/33/335218][PMID: 21694141]
- [76] Vadhva P, Hu J, Johnson MJ, *et al.* Electrochemical Impedance Spectroscopy for All-Solid-State Batteries: Theory, Methods and Future Outlook. *ChemElectroChem* 2021; 8(11): 1930–47 [https://doi.org/10.1002/celec.202100108]
- [77] Bloembergen N, Purcell EM, Pound RV. Relaxation Effects in Nuclear Magnetic Resonance Absorption. *Phys. Rev.* 1948; 73(7): 679–712 [https://doi.org/10.1103/PhysRev.73.679]
- [78] Huang B, Yao X, Huang Z, Guan Y, Jin Y, Xu X. Li<sub>3</sub>PO<sub>4</sub>-doped Li<sub>7</sub>P<sub>3</sub>S<sub>11</sub> glass-ceramic electrolytes with enhanced lithium ion conductivities and application in all-solid-state batteries. *Journal of Power Sources* 2015; 284: 206–11 [https://doi.org/10.1016/j.jpowsour.2015.02.160]
- [79] Mo S, Lu P, Ding F, *et al.* High-temperature performance of all-solid-state battery assembled with 95(0.7Li<sub>2</sub>S-0.3P<sub>2</sub>S<sub>5</sub>)-5Li<sub>3</sub>PO<sub>4</sub> glass electrolyte. *Solid State Ionics* 2016; 296: 37–41 [https://doi.org/10.1016/j.ssi.2016.09.002]
- [80] Phuc NHH, Maeda T, Yamamoto T, Muto H, Matsuda A. Preparation of Li<sub>3</sub>PS<sub>4</sub>-Li<sub>3</sub>PO<sub>4</sub> Solid Electrolytes by Liquid-Phase Shaking for All-Solid-State Batteries. *Electronic Materials* 2021; 2(1): 39–48 [https://doi.org/10.3390/electronicmat2010004]
- [81] Yamada T, Ito S, Omoda R, *et al.* All Solid-State Lithium–Sulfur Battery Using a Glass-Type P<sub>2</sub>S<sub>5</sub>-Li<sub>2</sub>S Electrolyte: Benefits on Anode Kinetics. *J. Electrochem. Soc.* 2015; 162(4): A646-A651 [https://doi.org/10.1149/2.0441504jes]
- [82] Yoshimoto M, Kimura T, Sakuda A, *et al.* Crystallization process of Li<sub>3</sub>PS<sub>4</sub> investigated by X-ray total scattering measurement and the reverse Monte Carlo method. *Solid State Ionics* 2023; 401: 116361 [https://doi.org/10.1016/j.ssi.2023.116361]
- [83] Parry KL, Shard AG, Short RD, White RG, Whittle JD, Wright A. ARXPS characterisation of plasma polymerised surface chemical gradients. *Surf. Interface Anal.* 2006; 38(11): 1497–504 [https://doi.org/10.1002/sia.2400]



- [84] Scofield JH. Hartree-Slater subshell photoionization cross-sections at 1254 and 1487 eV. *Journal of Electron Spectroscopy and Related Phenomena* 1976; 8(2): 129–37  
[[https://doi.org/10.1016/0368-2048\(76\)80015-1](https://doi.org/10.1016/0368-2048(76)80015-1)]
- [85] Tanuma S, Powell CJ, Penn DR. Calculations of electron inelastic mean free paths. IX. Data for 41 elemental solids over the 50 eV to 30 keV range. *Surf. Interface Anal.* 2011; 43(3): 689–713  
[<https://doi.org/10.1002/sia.3522>]
- [86] Price WS. Pulsed-field gradient nuclear magnetic resonance as a tool for studying translational diffusion: Part 1. Basic theory. *Concepts Magn. Reson.* 1997; 9(5): 299–336  
[[https://doi.org/10.1002/\(SICI\)1099-0534\(1997\)9:5<299::AID-CMR2>3.0.CO;2-U](https://doi.org/10.1002/(SICI)1099-0534(1997)9:5<299::AID-CMR2>3.0.CO;2-U)]
- [87] Popović L, Manoun B, Waal D de, Nieuwoudt MK, Comins JD. Raman spectroscopic study of phase transitions in Li<sub>3</sub>PO<sub>4</sub>. *J Raman Spectroscopy* 2003; 34(1): 77–83  
[<https://doi.org/10.1002/jrs.954>]
- [88] Mirmira P, Zheng J, Ma P, Amanchukwu CV. Importance of multimodal characterization and influence of residual Li<sub>2</sub>S impurity in amorphous Li<sub>3</sub>PS<sub>4</sub> inorganic electrolytes. *J. Mater. Chem. A* 2021; 12(11): 194  
[<https://doi.org/10.1039/d1ta02754a>]
- [89] Wu Y, Bensch W. Syntheses, structures, and spectroscopic properties of K<sub>9</sub>Nd[PS<sub>4</sub>]<sub>4</sub>, K<sub>3</sub>Nd[PS<sub>4</sub>]<sub>2</sub>, Cs<sub>3</sub>Nd[PS<sub>4</sub>]<sub>2</sub>, and K<sub>3</sub>Nd<sub>3</sub>[PS<sub>4</sub>]<sub>4</sub>. *Inorganic chemistry* 2008; 47(17)  
[<https://doi.org/10.1021/ic800143x>][PMID: 18686946]
- [90] Hayashi A, TADANAGA K, Tatsumisago M, Minami T, MIURA Y. Structural Change Accompanying Crystallization in the Lithium Ion Conductive Li<sub>2</sub>S-SiS<sub>2</sub>-Li<sub>3</sub>PO<sub>4</sub> Oxysulfide Glasses. *J. Ceram. Soc. Japan* 1999; 107(1246): 510–6  
[<https://doi.org/10.2109/jcersj.107.510>]
- [91] Seino Y, Nakagawa M, Senga M, Higuchi H, Takada K, Sasaki T. Analysis of the structure and degree of crystallisation of 70Li<sub>2</sub>S–30P<sub>2</sub>S<sub>5</sub> glass ceramic. *J. Mater. Chem. A* 2015; 3(6): 2756–61  
[<https://doi.org/10.1039/C4TA04332D>]
- [92] Glatz P, Comte M, Montagne L, Doumert B, Cormier L. Quantitative determination of the phosphorus environment in lithium aluminosilicate glasses using solid-state NMR techniques. *Phys Chem Chem Phys* 2019; 21(33): 18370–9  
[<https://doi.org/10.1039/c9cp03181b>][PMID: 31403647]
- [93] Brow RK. Review: the structure of simple phosphate glasses. *Journal of Non-Crystalline Solids* 2000; 263-264(11): 1–28  
[[https://doi.org/10.1016/S0022-3093\(99\)00620-1](https://doi.org/10.1016/S0022-3093(99)00620-1)]
- [94] Raguž B, Wittich K, Glaum R. Two New, Metastable Polymorphs of Lithium Pyrophosphate Li<sub>4</sub>P<sub>2</sub>O<sub>7</sub>. *Eur. J. Inorg. Chem.* 2019; 2019(11-12): 1688–96  
[<https://doi.org/10.1002/ejic.201801100>]
- [95] Massiot D, Fayon F, Capron M, *et al.* Modelling one- and two-dimensional solid-state NMR spectra. *Magn. Reson. Chem.* 2002; 40(1): 70–6  
[<https://doi.org/10.1002/mrc.984>]

- [96] Banerjee S, Holekevi Chandrappa ML, Ong SP. Role of Critical Oxygen Concentration in the  $\beta$ -Li<sub>3</sub>PS<sub>4-x</sub>O<sub>x</sub> Solid Electrolyte. *ACS Appl. Energy Mater.* 2022; 5(1): 35–41  
[<https://doi.org/10.1021/acsaem.1c03795>]
- [97] R. Zimmermanns, X. Luo, A. Hansen, M. Sadowski, Q. Fu, K. Albe, S. Indris, M. Knapp, H. Ehrenberg. Influence of oxygen distribution on the Li-ion conductivity in oxy-sulfide glasses - taking a closer look. *Dalton Transactions* 2024.
- [98] Klerk NJJ de, van der Maas E, Wagemaker M. Analysis of Diffusion in Solid-State Electrolytes through MD Simulations, Improvement of the Li-Ion Conductivity in  $\beta$ -Li<sub>3</sub>PS<sub>4</sub> as an Example. *ACS Appl Energy Mater* 2018; 1(7): 3230–42  
[<https://doi.org/10.1021/acsaem.8b00457>][PMID: 30057999]
- [99] Forrester FN, Quirk JA, Famprikis T, Dawson JA. Disentangling Cation and Anion Dynamics in Li<sub>3</sub>PS<sub>4</sub> Solid Electrolytes. *Chem. Mater.* 2022; 34(23): 10561–71  
[<https://doi.org/10.1021/acs.chemmater.2c02637>][PMID: 36530942]
- [100] Smith JG, Siegel DJ. Low-temperature paddlewheel effect in glassy solid electrolytes. *Nat Commun* 2020; 11(1): 1483  
[<https://doi.org/10.1038/s41467-020-15245-5>][PMID: 32198363]
- [101] Zhang Z, Nazar LF. Exploiting the paddle-wheel mechanism for the design of fast ion conductors. *Nat Rev Mater* 2022; 7(5): 389–405  
[<https://doi.org/10.1038/s41578-021-00401-0>]
- [102] TACHEZ M, MALUGANI J, MERCIER R, ROBERT G. Ionic conductivity of and phase transition in lithium thiophosphate Li<sub>3</sub>PS<sub>4</sub>. *Solid State Ionics* 1984; 14(3): 181–5  
[[https://doi.org/10.1016/0167-2738\(84\)90097-3](https://doi.org/10.1016/0167-2738(84)90097-3)]
- [103] Homma K, Yonemura M, Kobayashi T, Nagao M, Hirayama M, Kanno R. Crystal structure and phase transitions of the lithium ionic conductor Li<sub>3</sub>PS<sub>4</sub>. *Solid State Ionics* 2011; 182(1): 53–8  
[<https://doi.org/10.1016/j.ssi.2010.10.001>]
- [104] Kim J-S, Jung WD, Choi S, *et al.* Thermally Induced S-Sublattice Transition of Li<sub>3</sub>PS<sub>4</sub> for Fast Lithium-Ion Conduction. *J Phys Chem Lett* 2018; 9(18): 5592–7  
[<https://doi.org/10.1021/acs.jpcllett.8b01989>][PMID: 30207725]
- [105] Bron P, Dehnen S, Roling B. Li<sub>10</sub>Si<sub>0.3</sub>Sn<sub>0.7</sub>P<sub>2</sub>S<sub>12</sub> – A low-cost and low-grain-boundary-resistance lithium superionic conductor. *Journal of Power Sources* 2016; 329: 530–5  
[<https://doi.org/10.1016/j.jpowsour.2016.08.115>]
- [106] Shiba S, Miura A, Fujii Y, *et al.* Synthesis of lithium oxy-thiophosphate solid electrolytes with Li<sub>10</sub>GeP<sub>2</sub>S<sub>12</sub> structure by a liquid phase process using 2-propanol. *RSC Adv* 2023; 13(33): 22895–900  
[<https://doi.org/10.1039/d3ra03929c>][PMID: 37520098]
- [107] Suzuki K, Sakuma M, Hori S, *et al.* Synthesis, structure, and electrochemical properties of crystalline Li–P–S–O solid electrolytes: Novel lithium-conducting oxysulfides of Li<sub>10</sub>GeP<sub>2</sub>S<sub>12</sub> family. *Solid State Ionics* 2016; 288: 229–34  
[<https://doi.org/10.1016/j.ssi.2016.02.002>]
- [108] Kimura T, Inaoka T, Izawa R, *et al.* Stabilizing High-Temperature  $\alpha$ -Li<sub>3</sub>PS<sub>4</sub> by Rapidly Heating the Glass. *J Am Chem Soc* 2023; 145(26): 14466–74  
[<https://doi.org/10.1021/jacs.3c03827>][PMID: 37340711]

- [109] Schneider, Richard Hans, 68794 Oberhausen-Rheinhausen, DE, Stöffler, Heike, 75417 Mühlacker, DE, inventors; Karlsruher Institut für Technologie, 76131 Karlsruhe, DE, assignee. Behältnis zur Untersuchung von Feststoffelektrolyten. 2019 Feb 1.
- [110] Balach J, Linnemann J, Jaumann T, Giebeler L. Metal-based nanostructured materials for advanced lithium–sulfur batteries. *J. Mater. Chem. A* 2018; 6(46): 23127–68  
[<https://doi.org/10.1039/C8TA07220E>]
- [111] Jacobson AJ, Chianelli RR, Whittingham MS. Amorphous Molybdenum Disulfide Cathodes. *J. Electrochem. Soc.* 1979; 126(12): 2277–8  
[<https://doi.org/10.1149/1.2128950>]
- [112] Hofer M, Grube M, Burmeister CF, Michalowski P, Zellmer S, Kwade A. Effective mechanochemical synthesis of sulfide solid electrolyte Li<sub>3</sub>PS<sub>4</sub> in a high energy ball mill by process investigation. *Advanced Powder Technology* 2023; 34(6): 104004  
[<https://doi.org/10.1016/j.appt.2023.104004>]
- [113] Soravia S, Orth A. Design of Experiments. In: *Ullmann's Encyclopedia of Industrial Chemistry*. Wiley 2003; 176.